Linking Star Formation and Black Hole Mass Growth in External Galaxies

Inaugural-Dissertation

zur

Erlangung des Doktorgrades

der Mathematisch-Naturwissenschaftlichen Fakultät

der Universität zu Köln

vorgelegt von

Lukas Dominik Steiniger

aus Waldbröl

Köln

2023

Berichterstatter: (Gutachter)	Prof. Dr. Andreas Eckart
	Prof. Dr. J. Anton Zensus

Tag der mündlichen Prüfung: 19. Juli 2023

Abstract

An exciting topic in astrophysics revolves around active galactic nuclei (AGNs), as they count among the most extreme phenomena, with some objects easily outshining whole galaxies. At the heart of each AGN lies a black hole (BH) that is powered by accretion of orbiting material in the shape of a disk. Despite the humanly inconceivable mass of the central supermassive black hole (SMBH) M_{BH} in AGNs, it is still small in comparison to the mass of its host galaxy or even only that of the bulge component M_{bulge} of the host. The mass ratio is virtually always and often even by far $M_{\mathrm{BH}}/M_{\mathrm{bulge}} < 1\,\%$. Nevertheless, multiple connections between the mass of the SMBH and bulge properties have been found for inactive and active galaxies. One example for such a connection that holds for both types of galaxies is the $M_{\mathrm{BH}} - \sigma_*$ relation, where σ_* is the stellar velocity dispersion of the bulge. Hence, a co-evolution between the central BH and its host is assumed to exist, although the basis of this correlation is still debated.

From 2014 to 2016 a series of five papers was published, which analyzed some objects from the so-called low-luminosity type-1 quasi-stellar object (LLQSO) sample. Multiple properties of LLQSOs place them between local AGNs of low to moderate emission, and distant, but powerful quasars, both of which are covered by many studies. One of the most central topics of the paper series is the analysis of LLQSOs with respect to the correlation between the BH mass and the bulge luminosity, the $M_{\mathrm{BH}} - L_{\mathrm{bulge}}$ relation. The authors find that LLQSOs fall below different literature relations for inactive galaxies, corresponding to undermassive BHs and/or overluminous bulges. Based on the detection of molecular gas they attribute the deviation to star formation (SF), which causes overluminous bulges. This work builds upon the previous project by increasing the number of the analyzed LLQSOs and thus examining the objects in the context of an overall larger sample.

Observations of the additional LLQSOs took place in February and September 2019, utilizing the 3.6 m New Technology Telescope (NTT) equipped with the near-infrared (NIR) instrument Son of ISAAC (SOFI). Depending on each object, the relevant observation modes were long-slit spectroscopy and/or broad band filter imaging. This work has a special focus on K-band data.

Here, imaging is the basis to estimate the absolute K-band bulge magnitudes of the LLQSOs, which constitute substitutes for the respective bulge luminosities. The method of extracting BH mass estimates is based on the spectra, which are also used for the identification of diagnostic lines. Due to a translation of a BH mass estimation method

from the first broad Balmer emission line (Hα) to the Paschen-α (Pα) line, it is possible to use NIR spectroscopy for BH mass estimates. However, for LLQSOs the Pα line is often located outside the two atmospheric transmission windows, the H-band and the K-band. In other words, the area that likely contains the Pα line is expected to feature high level noise. A potential aid is the Brackett-γ (Brγ) line that lies outside the noisy region. Due to an assumed fixed ratio with the Pα line, the Brγ line can be used as its substitute. The combined use of both lines makes it possible to obtain BH mass estimates from all spectra.

The addition of 14 new LLQSOs to the previous sample of 16 objects in the $M_{\mathrm{BH}} - L_{\mathrm{bulge}}$ diagram shows results that are consistent with the previous studies. With only a few exceptions, objects from both samples are on average below the literature relations and show a similar scatter. Multiple spectra contain diagnostic lines, such as the shock tracer [Fe II] and lines from molecular hydrogen H_2, which indicates active SF within the bulges. This is in accordance with the notion that LLQSOs might experience an onset of SF, which shifts these objects in the $M_{\mathrm{BH}} - L_{\mathrm{bulge}}$ diagram towards higher luminosities and thus away from literature relations for inactive galaxies. A consequence of the SF in the bulge is a feeding of the central SMBH, which then grows in mass. Another effect is that the activity level of the AGN rises, which is indicative for duty cycles of AGNs, i. e., the concept of phases of lower and higher AGN activity. The higher activity leads in turn to a corresponding feedback from the center that might affect the bulge, which is an exemplary scenario of a co-evolution.

The inclusion of the redshift as an additional quantity in the $M_{\mathrm{BH}} - L_{\mathrm{bulge}}$ diagram points to a further aspect. Those LLQSOs that are close to or even agree with the literature relations appear to follow a trend, which can be generally expected, i. e., larger distances correspond to higher luminosities and also larger BH masses. In contrast to this, objects that deviate more from the relations for inactive galaxies appear more randomly placed with respect to their redshifts. It might be that the change of one parameter has influence on multiple other parameters, which results in the observed deviation. There are several scenarios that might initiate the evolution that leads to this deviation, including different merger events and secular evolution, but a definitive explanation is still missing.

Contents

Chapter 1

Motivation

The history of astronomy and astrophysics is coined by many changes of the worldview, some of these changes being drastically in contrast to beliefs that survived for centuries. For the largest part, humanity was and still is pinned to Earth. The last century has seen rapid advancements of technology and possibilities. Human-made satellites reached unprecedented distances and signaled their impressions back to Earth, as well as the first gravitationally bound steps of a human on another object than Earth took place. However, to this day, this is still considered exceptional.

A technological advancement of observational capabilities in combination with evolving physical models also had a great influence on astronomy and astrophysics. The resolving power of telescopes is increasing more and more and/or their sensitivities are heightened. Reasons are the increasing sizes of the primary mirrors of telescopes and larger baselines for interferometric observations. The advent of techniques, such as active and adaptive optics, helps increasing the image quality to new levels, in some cases allowing for diffraction-limited observations. Space-based telescopes, such as the James Webb Space Telescope (JWST), avoid atmospheric disturbances altogether. This makes facing the increased risk of irreparable failure worthwhile, as once these telescopes are launched, further maintenance is impossible.

One exemplary result from the advancements in the last century is that the initially only theoretical model of a black hole (BH) is supported by observations, leading to a wide acceptance of the existence of these objects. A recent culmination of observational advancements can be found in an event from 2019, which is the release of the first image of the shadow of a supermassive black hole (SMBH) by the Event Horizon Telescope Collaboration (EHTC), matching theoretical predictions remarkably well. In order to achieve this feat, a radio telescope with the virtual size of Earth is used, the Event Horizon Telescope (EHT). It combines multiple smaller radio telescopes around the globe. Even more recently, in 2022, an image of another SMBH was released, which lies at the center of our galaxy, the Milky Way (MW).

Mentioning SMBHs in an astrophysical context often leads to another, related topic, namely active galactic nuclei (AGNs). AGNs are part of the most extreme and fascinating astrophysical phenomena. There is a broad agreement that at the core of each galaxy

hosting an AGN, i. e., an active galaxy, lies a SMBH (e. g., Kormendy and Richstone 1995; Richstone et al. 1998; Ho 1999; Ho 2008). The SMBH is the heart of an engine, producing radiation on scales that can outshine whole galaxies. Hence, this radiation might be stronger than the combination of billions of stars. The source of this power is assumed to be an accretion process, usually modeled in form of an accretion disk around the SMBH (e. g., Kozlowski et al. 1979; Sakimoto and Coroniti 1981; Norman and Silk 1983).

Although the interest in AGNs grew into a large topic in astrophysics, many questions about the nature and properties of these objects remain unclear. Where do the vast differences between SMBHs at the centers of galaxies come from, as some show little to no activity, while others are extreme sources of radiation? The center of the MW is a great example for the former, and basically all quasars are examples for the latter. Are there correlations between the SMBH and its host galaxy, and if so, which relations and where do these come from? Some respective correlations have been found, where most of these hint at a connection between the central SMBH and the stellar bulge component of its host galaxy. However, even considering only the bulge component, the SMBH mass often makes up only much less than one percent of the bulge mass (e. g., Wandel 2004; Jiang et al. 2011). The corresponding sphere of influence of the central SMBH appears too small to have a large impact on the whole host galaxy or even its bulge only. As a result, an interdependent evolution of the SMBH and the host bulge is concluded. What are the details and implications of this?

When speaking of BH – bulge relations, these usually refer to the BH mass in combination with a property of the host galaxy. Famous examples for the second quantity in these relations include the bulge mass M_{bulge}, the bulge luminosity L_{bulge}, and the stellar velocity dispersion σ_*. It is not surprising that the basis for these relations is often found from inactive galaxies, i. e., galaxies that do not harbor an AGN, as these are the closest objects and accordingly most easily spatially well resolved. Some studies include considerations for the morphological nature of the host, e. g., early- vs. late-type galaxies, or classical bulges vs. pseudobulges. Numerous studies describe the correlations that are empirically found and described by models, as well as a connection between the nuclear activity and more host galaxy properties. These hint towards the aforementioned co-evolution of the central SMBH and the host galaxy, possibly via self-regulated BH feeding and feedback (e. g., McLure and Dunlop 2002; Somerville et al. 2008; Alexander and Hickox 2012; Heckman and Best 2014; de Nicola et al. 2019; Ding et al. 2020; Yesuf et al. 2020). Merger processes are thought to be related to the activity of the SMBHs. However, as nearby AGNs are often found in morphological late-type host galaxies, it is unlikely that these objects experienced major merger events. On the other hand, minor merger events could not only influence the central activity levels, they are also not easily identified, marking them as a viable option for activity regulation. Another source for regulation might be internal to the host galaxy, such as flows from bars or spiral arms, which leads to the conclusion that secular evolution should be the basis for the controlling principle (Kormendy and Ho 2013).

More studies seem to concentrate on the closest Seyfert galaxies and other local

AGNs of relatively low to moderate emission, as well as properties of powerful quasars at large cosmological distances. While morphologies of the former can be resolved and analyzed accordingly, these might not represent the whole population of AGNs. For higher redshifts the order of power of AGNs and star formation rate (SFR) is expected to increase. However, even modern technology does not allow for resolving very distant powerful quasars, including the assumed peak of activity for AGNs and star formation (SF) at $z \approx 2$ (Aird et al. 2015).

In contrast to these studies, a subsample is selected from the Hamburg/ESO Survey (HES) (Wisotzki et al. 2000), a wide-angle survey for bright UV-excess quasi-stellar objects (QSOs) and Seyfert-1 nuclei. The subsample is chosen with a limiting redshift of $z \leq 0.06$, which leaves the 99 closest low-luminosity type-1 quasi-stellar objects (LLQSOs) from the HES. Hence, given a telescope with appropriate capabilities, it should be possible to spatially resolve these sources. The LLQSO sample is farther away than close AGN samples of very low redshifts and moderate emission. Despite the higher distances, the objects from the LLQSO sample are more luminous, which partially compensates for the lower resolution. Accordingly, the objects from the LLQSO sample are supposed to form a connection between the local AGN population and distant, luminous quasars. Several parameters of LLQSOs support their placement in the spot between the other classifications.

A series of five publications between 2014 and 2016 analyzes some objects of the LLQSO sample (Busch et al. 2014; Busch et al. 2015; Tremou et al. 2015; Busch et al. 2016; Moser et al. 2016). One of the major results from the publications is based on near-infrared (NIR) observations and analyses of 16 objects from the LLQSO sample with respect to one of the BH – bulge relations, the SMBH mass M_{BH} – bulge luminosity L_{bulge} relation. Following a placement of these objects in a $\log - \log$ representation of a $M_{\mathrm{BH}} - L_{\mathrm{bulge}}$ diagram together with respective literature relations for inactive galaxies (Marconi and Hunt 2003; Vika et al. 2012; Graham and Scott 2013; Kormendy and Ho 2013), the authors find that on average the LLQSOs do not agree with the suggested relations, but show either undermassive BHs or overluminous bulges. Based on indications for SF, they propose overluminous bulges as the more probable explanation for the deviation. However, more objects from the LLQSO sample are needed to strengthen the finding.

This work builds upon the described project, with the major goal of enlarging the sample of LLQSOs that are analyzed with respect to the $M_{\mathrm{BH}} - L_{\mathrm{bulge}}$ relation. Two periods of NIR observations using the Son of ISAAC (SOFI) instrument mounted at the New Technology Telescope (NTT) took place in 2019, one in February and one in September. Each observation involves broad band filter imaging and long-slit spectroscopy acquisitions. The goal of the former is to find bulge luminosities, that of the latter to estimate BH masses and potential other characteristics from diagnostic lines in the spectra. Although problematic observing conditions reduced the number of objects that can be added to the previous sample in the $M_{\mathrm{BH}} - L_{\mathrm{bulge}}$ diagram, the total sample size is still approximately doubled.

Chapter 2

Theoretical Background

In this chapter I summarize the basic theoretical background for the rest of this thesis. Each section is a brief description of the respective topic and should not be considered exhaustive literature. However, an interested reader will find that the references therein do provide lots of reading material to an almost arbitrary degree of detail.

A common theme found in astronomy & astrophysics, is that many topics underwent a strong evolution over time, as theoretical knowledge spread and advanced faster, and technological developments opened doors that were shut before. While this still appears to be and keep being valid, it already led to initially well-working classifications and explanations for objects and phenomena becoming outdated and not as well-working as before. Some terms for certain classifications are used interchangeable by now, or sub-classifications were added as necessary. Depending on the exact topic, it is sometimes hard to keep naming conventions consistent, especially when considering different literature. In the following I try to keep classifications reduced to the most important ones, and descriptions and terms consistent with each other.

While this chapter is based on a multitude of literature sources, which are duly cited, there are three books that create a broad basis for essentially all topics covered in the following. These books are *An Introduction to Active Galactic Nuclei* (Peterson 1997), *The Physics and Evolution of Active Galactic Nuclei* (Netzer 2013), and *Extragalactic Astronomy and Cosmology: An Introduction* (Schneider 2015). Accordingly, citations of these books appear more often and refer to broader paragraphs.

2.1 Galaxies

Galaxies are universally described as very important building blocks in the universe as we know it. They are gravitationally bounded accumulations of stars, gas, dust, and more matter & objects, appearing in many shapes and having different properties. Often they contain more than hundreds of million of stars. By now it is widely accepted, that most galaxies harbor a SMBH at their centers. This is connected to one fundamental classification of galaxies into inactive & active galaxies. More on that topic can be found in Sect. 2.2, including some historical aspects in Sect. 2.2.1. Here, I want to focus more

on the description of a galaxy itself, rather than its center.

We are residing on planet Earth, which is part of the Solar System, orbiting around the Sun. The Sun, or rather the whole Solar System, is part of our Galaxy, the MW. It is classified as a barred spiral galaxy (cf. Sect. 2.1.1), mainly consisting of a thin and a thick disk, a central bulge and a bar, and an almost spherical halo. According to Schneider (2015), the latter contains not only gas and old stars, but also most of the globular clusters, which are luminous spheroidal and gravitationally bound accumulations of stars. At an estimated distance of about 8 kpc[(1)] from the center of the MW, the Sun travels at about 220 km/s. This velocity is significantly higher than the estimated velocity of about 160 km/s, based on visible matter only (Schneider 2015, p. 6). In order to explain this difference, as well as other phenomena related to the rotational velocities of objects in galaxies, dark matter was introduced. It is supposed to consist of material that is barely luminous, thus being invisible to us, and increasing the mass contained in galaxies to high enough levels that explain the observations. Its exact nature, and even its existence at all, is still a mystery to this day. Lately, alternative theories which modulate the established explanation for gravity, such as MOND (Modified Newtonian dynamics, Milgromian dynamics) (e. g., Banik and Zhao 2022), gain more traction. Being part of the MW, it is much harder to infer properties about it than observing other galaxies from the outside. Such observations revealed that many galaxies are part of even larger structures, galaxy clusters, where usually more than hundreds of galaxies are gravitationally bound. On even larger scales are the probably largest known structures in existence, galaxy filaments. These are then separated from comparatively large regions with nearly no galaxies at all, called voids[(2)].

In the context of galaxies and especially in the context of this work it makes sense to highlight one of the previously mentioned features of the MW, which can be relevant for almost all types of galaxies, the bulge. It is a central component of galaxies, usually assumed to consist of mainly old stars without much gas and dust that could fuel large-scale SF. In contrast to this, other areas of galaxies, such as for example the spiral arms in spiral galaxies, are typical places of SF. It depends on the galaxy type which part is assumed to be the bulge. For example the bulge component in elliptical galaxies is often associated with the whole galaxy. In case of the MW its bulge as assumed to be shaped like a peanut, with a characteristic scale-length of ~ 1 kpc and a scale-height of ~ 0.4 kpc (Schneider 2015, p. 64). There are different classifications of bulges, with the two most important categories being classical bulges and pseudobulges. Classical bulges are similar to elliptical galaxies, their name being connected to the historical assumption about the nature of bulges, that they are elliptical galaxies with a disk component. Stars in classical bulges follow basically random orbits, giving rise to the aforementioned elliptical shape of classical bulges, which can be seen as an indicator for merger events. Their formation process is assumed to be fast, potentially externally

(1) A parsec (pc) is a typical astronomical unit of distance, $1\,\mathrm{pc} \approx 3.086 \cdot 10^{16}$ m. It is based on another common distance, the astronomical unit (AU), $1\,\mathrm{AU} \approx 1.5 \cdot 10^{11}$ m, which corresponds roughly to the distance between Earth and Sun.

(2) More information on this topic can be found in Chapter 1.2.5 & Chapter 7, Schneider 2015.

driven, and to occur early in the galaxy formation (Athanassoula 2005). Although not a definite criterion, a large mass of the bulge in comparison to the disc is often a sign for a classical bulge. In contrast to this, pseudobulges are often on much smaller scales than their hosts, and their stars follow orbits in a disk structure, similar to spiral galaxies. Hence, these are also called disk-like bulges. There are different explanations that might describe the formation of these bulges, including a scenario where gas concentrates in the inner part of the galactic disk, eventually forming stars within this central area. While there are proposals for more classifications, only one more type of bulges is mentioned here, box/peanut bulges. These are thought to be connected to the natural evolution of barred galaxies, of which the bar is partially observed when seen nearly edge-on (Athanassoula 2005).

2.1.1 Galaxy Morphological Classifications

The advent of extragalactic astronomy can be associated with the famous astronomer Edwin Powell Hubble, who derived in 1925 a distance for Cepheids in the Andromeda galaxy of 285 kpc. While this does not match the more current estimate of its distance, it was seen as a proof for the existence of extragalactic objects (Schneider 2015, p. 101). The influence of Hubble on extragalactic astronomy & astrophysics is immense and can be seen in many aspects, including a famous classification scheme for galaxies based on their morphologies (Hubble 1926). This classification scheme is known as the Hubble sequence of galaxies or, especially when associated with a visualization, as the Hubble tuning fork, as can be seen in Fig. 2.1.

Although by now the Hubble classification scheme is seen as outdated, its general idea still holds. The basic distinction is between elliptical (E) and spiral galaxies. Spiral galaxies are subdivided into "normal" spirals (S) and barred spirals (SB), i. e., spirals with a central bar structure. Each group is divided into more specific classes of objects, either via a number or another letter. Trailing numbers indicate the level of ellipticity, that is observable by the isophotes[3] of ellipticals, where E0 is a circular galaxy[4] and E7 shows a highly elliptical shape. This trailing number n is based on the measurable ellipticity, $\epsilon = 1 - b/a$, where a is the semi-major axis and b the semi-minor axis of the elliptical shape. It is $n = 10 \cdot \epsilon$ (Schneider 2015, p. 103). Subgroups of normal and barred spirals are marked via the letters 'a', 'b', and 'c', with 'a' indicating tightly wound spiral arms and 'c' loosely wound spiral arms. Sometimes a class for the letter 'd' is included as well. In the context of this work it makes sense to note that a tighter spiral arm structure is often assumed to correlate with larger, and thus more luminous, central bulges. As an example, a typical luminosity ratio of bulge and disk for an Sa galaxy is $L_{\text{bulge}}/L_{\text{disk}} \approx 0.3$, whereas for an Sc gaalxy it is only ~ 0.05 (Schneider 2015, p. 116). A case for a third and even fourth class of galaxies can be made, for lenticular and irregular galaxies, respectively.

[3] Contour lines of constant surface brightness.

[4] It is important to note that projection effects play a crucial role in these morphological classifications. For example an actually highly elliptical galaxy might be oriented such that an observer from the MW only sees a circular shape.

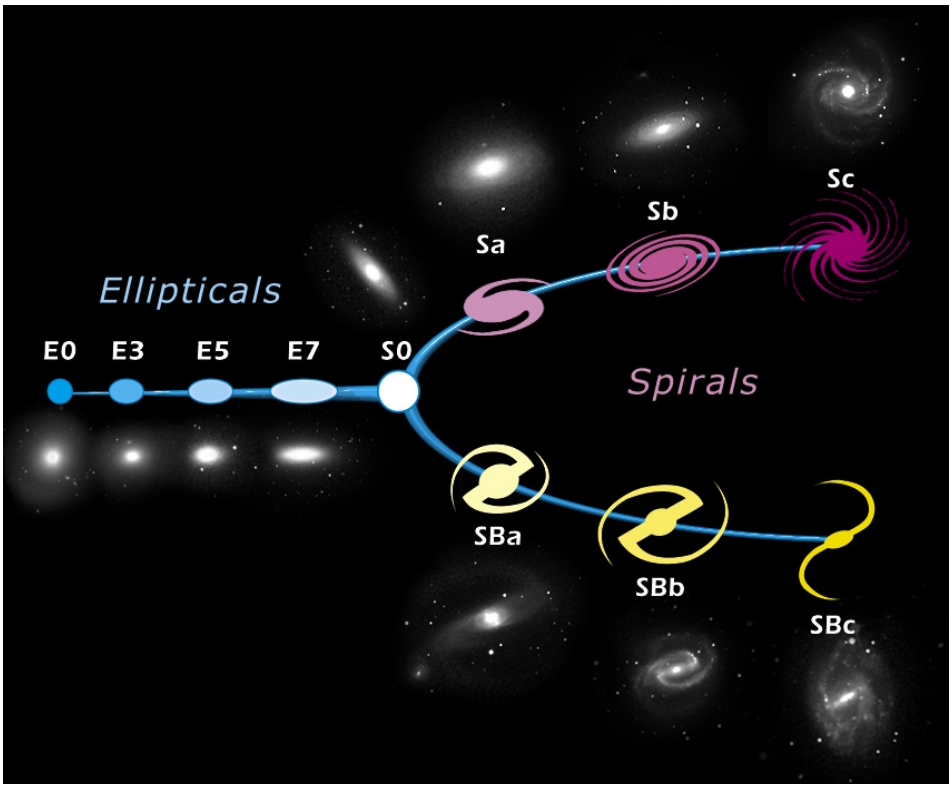

Figure 2.1: The Hubble classification scheme visualized as the Hubble tuning fork. It shows the principle idea behind the distinction between two classes of galaxies, ellipticals and spirals, of which the latter are again split into two categories, those with and those without a bar. Objects on the left are called early-type galaxies and accordingly objects on the right side are called late-type galaxies. This does not actually reflect any property related to their ages or evolution, but is based solely on historical reasons. The example sketches enhance the visibility of the principal shape, and images next to these sketches show how actual galaxies might look like. *Credit: NASA & ESA (CC BY 4.0) (In this version some text was removed from the upper left corner in comparison to the original image.)*

Lenticular galaxies are designated as S0 galaxies. They are an intermediate class between ellipticals and spirals, connecting the two-pronged spiral classification with the line of ellipticals in the Hubble tuning fork. These objects are often associated with a prominent bulge component, and have an outer disk without spiral arm structures. Irregular galaxies match their descriptive name and do not follow any of the mentioned classifications. Furthermore, all classes can be extended by even finer distinctions, and mixed cases such as barred lenticular galaxies (SB0) are possible. Historically, there is a naming scheme of early- and late-type galaxies, where elliptical and lenticular galaxies are early-types, and spirals are late-types. The same distinction is then again found within spiral galaxies, e. g., an SBa galaxy is an early-type barred spiral, whereas Sc is a late-type spiral. However, in either case this does not actually indicate any property related to the age or evolution of the galaxies.

Following the description by Schneider (2015), there is a multitude more of finer classes. In the case of elliptical galaxies a few of those are giant ellipticals (gE), intermediately luminous ellipticals (E), compact ellipticals (cE), dwarf ellipticals (dE), extremely luminous and large galaxies (cD galaxies), blue compact dwarf (BCD) galaxies, and dwarf spheroidals (dSph). As for spiral galaxies, it makes sense to also mention another sub-class, which is described as at least somewhat irregular. This class is denoted by an 'm', which stands for 'Magellanic', as known for example from the Large Magellanic Cloud. Spiral classifications are then extended for example by Sdm, SBm, or Sm, that might connect to classifications that are titled as irregular, such as Im or IBm. When describing the brightness profiles of some sub-classifications of ellipticals, especially considering normal ellipticals and the innermost part of cD galaxies, and that of classical bulges, these tend to follow a de Vaucouleurs profile[(5)]. In contrast to this, the brightness of pseudobulges and the disk component of spirals tend to follow exponential profiles.

The name de Vaucouleurs leads directly to another classification scheme, the de Vaucouleurs system (de Vaucouleurs 1959). This system is effectively an extended version of the Hubble classification scheme, based on the presence or absence of bars, rings, and spiral arms. Especially the introduced notation for spirals without bars (SA), and an intermediate class for weakly pronounced bars (SAB) can often be found in literature and databases. The presence of ring structures is indicated by '(r)', the absence of such by '(s)', and intermediate cases by '(rs)'. The previously known denotation as early-type ($^-$) or late-type ($^+$) objects is also applied within the groups of elliptical and lenticular galaxies.

Yet another classification system is the Yerkes system, which is mainly based on the stellar populations of galaxies (Morgan 1958, 1959). An important concept of this scheme is that of "Form Families", which are mainly denoted by single letter specifiers, and a few families being specified by two letters. One example is that of peculiar ellipticals

[(5)] The surface brightness I as a function of the (projected) distance r from the center is given by $\log\left(I(r)/I_\mathrm{e}\right) = -3.3307\left[(r/r_\mathrm{e})^{1/4} - 1\right]$, where r_e is the effective radius, i. e., the radius at which half of the emitted luminosity is contained, and I_e is the respective surface brightness at this radius, $I_\mathrm{e} = I(r_\mathrm{e})$ (Schneider 2015, p. 65).

(Ep) that contain dust absorption patches. Without explaining all remaining families, one specific Form Family has to be mentioned here as it appears later on this work, the family of D galaxies. These are galaxies that show a rotational symmetry, while having neither a spiral nor an elliptical structure.

2.2 The Active Galactic Nucleus

In the history of astronomy and astrophysics, observations of galaxies showed that there are different types of galaxies, where the spectral distribution of radiation varies a lot for different objects. The spectral energy distribution (SED) of a "normal", i. e., inactive, galaxy is dominated by spectra of its stellar populations, which are mainly intermediate to old stars. Their spectra depend on the surface temperatures of the stars and they are well presented by black body (BB) radiation, i. e., Planck curves (see Eq. 3.1). Usually, the temperatures reach from some thousand to a few tens of thousand Kelvin, which mainly covers the range of the NIR and optical spectrum, but also reaches into the ultraviolet (UV) regime (Schneider 2015, p. 105). Starburst galaxies show much higher star formation rates, possibly even by a factor of about 30 more. As a result, their spectra are affected by the larger amount of young stars, that are prominent in spectral sections from blue up to UV. However, most often this cannot be observed directly, as star formation is bound to its fuel, such as dense molecular clouds which also contain dust. This prevents the radiation from the young stars to be directly observable, while it does heat the dust and enables thermal emission in the infrared (IR) regime. A third type of galaxies are active galaxies, which harbor an active galactic nucleus (AGN) at their center. Their SEDs differ from those of inactive or starburst galaxies, as even a superposition of stellar spectra cannot describe their shapes, often showing large energies in all sections of the electromagnetic spectrum. The underlying processes count among the most energetic phenomena in the whole universe known to this day.

The probably shortest and simplest definition for an AGN describes its physical nature, stating that it is an object associated with a region that contains an accreting SMBH at its center. However, depending on the context, this might not be a practical definition. As an example, the SMBH at the center of the MW appears to be accreting matter, even showing flares, i. e., outbursts of larger luminosities than during quiescent phases. Despite this, it is seldom considered to be an AGN. The reason for that is its luminosity, which is much lower compared to other galactic cores or even just the stellar cluster at the Galactic Center, depending on the regarded wavelength regime. Literature provides different approaches to defining and using the term AGN. Netzer (2013) chooses a purely observational definition, and remarks in their work that an object is classified as an AGN in case it fulfills at least one of the following conditions, noting that this includes objects that others would not consider to be AGNs:

1. It contains a compact nuclear region emitting significantly beyond what is expected from stellar processes typical of this type of galaxy.
2. It shows the clear signature of a nonstellar contiuum emitting process

in its center.

3. Its spectrum contains strong emission lines with ratios that are typical of excitation by a nonstellar radiation field.
4. It shows line and/or continuum variations.

(Netzer 2013, p. 2)

Following this definition, objects are not fixed to be an AGN. For example, if their luminosity falls below an according threshold or rises from below to a luminosity above, these objects are not considered to be an AGN anymore or count from that moment as part of this AGN classification, respectively. Showing some overlap, but not exactly the same definition comes from Peterson (1997), who introduces AGNs as a reference "to the existence of energetic phenomena in the nuclei, or central regions, of galaxies which cannot be attributed clearly and directly to stars" (Peterson 1997, p. 1). Less of a direct definition and more of a description of the phenomenon of an AGN is that it is associated with a small central region of a galaxy, then called active galaxy, which is the source for a broad energy distribution that shows "significant emission in the full range from radio wavelengths to the X-ray and even gamma range" (Schneider 2015, p. 211). This also strengthens the important aspect, that an AGN is not restricted to only the SMBH, but a whole structured region, including different components. These components are mentioned in the following sections, matching the respective context.

2.2.1 History of Active Galactic Nuclei

The idea of a supermassive black hole (SMBH) at the center of each galaxy is, to a large extent, driven by the discovery of quasars. In order to explain these powerful sources, it is assumed that accretion of matter onto an extremely massive and at the same time very compact object takes place, with SMBHs being not the only, but rather likely candidates. Initially, potential candidates included very dense stellar clusters or boson stars, among other ideas. By now however, the existence of SMBHs is commonly accepted throughout the scientific community. In order to explain how it came to this, knowledge about the history of AGNs is helpful.

It is hard or likely even impossible to pinpoint each first occurrence of novel ideas with a large impact. An example for such an idea is that that Earth is part of the Solar System, which is in turn part of our galaxy, the MW, being made up of hundreds of billions of stars. Additionally, the existence of other, extragalactic objects, such as galaxies with similar or quite different morphologies as the MW needed time to consolidate. Examples for plenty of people with ideas and thoughts of this scale can be found in all documented history. However, these people were often ignored or even faced harsh consequences, especially in case their ideas conflicted with the world view of that time. In the context of AGN it is more sensible to skip directly to the 20th century, in order to reduce the risk of missing milestones and keeping it to the most directly relevant of them.

In 1999 Shields (1999) published an article, in which the history of AGNs up to the point of publication is briefly summarized. Based on this article and some further

sources, which are marked accordingly, here follows a summary of the historical milestones.

In the very early 20th century it was not certain yet, whether the objects that were called "spiral nebulae" at the time were close, gaseous objects, e. g., nebulae such as the Orion Nebula, or rather accumulations of many stars at a large distance, making these appear unresolved. To address this question, Fath (1909) aimed at testing a claim concerning the spectrum of these spiral objects. In case of a collection of stars the spectrum is expected to be continuous, while the spectrum of a gaseous nebula shows a line spectrum according to the atoms and molecules the gas consists of. After constructing a spectrograph and taking photographic spectra of multiple of these spiral nebulae, most of the resulting spectra showed a continuous form. Thus, they indicated accumulations of unresolved stars similar to the Sun. However, one object differed, as its spectrum showed a continuum, but also bright lines and absorption lines. The corresponding object is NGC 1068, which is a famous source as it is relatively close and well-studied by now. In the following years, more researchers found and examined the emission lines of NGC 1068 and more objects. For example, Slipher (1917) found the emission lines to cover a non-negligible range of wavelengths, while Hubble (1926) noted that some of his analyzed objects with stellar nuclei, which include NGC 1068 among other sources, show a planetary nebula-like spectrum.

The advent of a systematic analysis of emission lines from the nuclei of galaxies is attributed to Seyfert (1943), as Seyfert found that the spectra of six galaxies are of a stellar-like nature, while emission lines are on top of those. Each line profile turned out to be different from each other as well as between different objects, reaching widths of multiple thousands of $\mathrm{km\,s^{-1}}$, which Seyfert assigned to Doppler shifts. Not the least due to the names of very common classifications of certain types of galaxies, Seyfert is well known among astronomers and astrophysicists, especially in the context of active galaxies.

Despite these findings around the optical regime, another part of the electromagnetic spectrum was needed to strengthen AGNs as a focus of research. This leads directly to another famous person with a large impact on astrophysics, the physicist and radio engineer K. G. Jansky. While trying to find sources of static that affect trans-Atlantic radio communications, Jansky (1932) was able to build and make use of a rotating antenna and a receiver which works at a wavelength of about 14.6 m to systematically search for static from any direction. This allowed him to narrow the static to three sources, close thunderstorms, distant thunderstorms, and a faint but steady static, like a hiss, of which the origin was unknown. At first, Jansky attributed the hiss to the Sun, but after continued measurements over the course of the following year, Jansky (1933) found that the signal actually came from the center of the MW. In order to be able to reach this conclusion the long-term measurements were necessary, as these showed that the source moved along the azimuthal angle almost once a day, but not exactly every 24 hours, i. e., the time and direction of its maximum changed over the course of a year. According to Shields (1999), the impact of this finding within the circle of professional astronomers was still minuscule, and the free time project of an engineer, Grote Reber,

was necessary for further progress. After building a 31 foot ($\sim$ 9.45 m) reflector that operates at 160 MHz, Reber was able to create a radio sky map, making some special notes of maxima, a major one in the Sagittarius constellation and some minor maxima, including for example one in the Cygnus constellation (Reber 1940a,b, 1944).

After World War II ended, multiple radio engineers and groups of such were able to make use of the tools left from the war and advance radio astronomy even further. Attempting to find and analyze discrete sources, it was possible to limit the angular diameter of the aforementioned radio source in the Cygnus constellation from an initial upper limit of $\sim 2^\circ$ (Hey et al. 1946) later down to 6 arcmin (Ryle and Smith 1948). In combination with optical identifications of these discrete sources (Bolton et al. 1949), advancements started to accelerate. The use of interferometers grew more common and even structural measurements of radio sources became possible (e. g., Hanbury Brown et al. 1952). Further steps included the first categorizations of these sources, and more attempts at theoretical explanations and predictions, consolidating the notion of synchrotron emission as the basis of extragalactic discrete sources. The third Cambridge survey (3C), consisting of observations at 159 MHz (Edge et al. 1959), its revision a few years later at 178 MHz (Bennett 1962), and surveys following afterwards helped immensely providing more accurate radio positions, thus clearing up previous confusions and aiding optical identifications. With time AGN identifications also spread to other regimes of the electromagnetic spectrum, including the UV continuum, IR, and X-ray.

Although the notion of radio galaxies established itself with enough observational evidence (e. g., Minkowski 1960), the idea of AGNs took more time to develop. Multiple radio sources were found to be at the same positions as sources resembling stars in optical images, coining the term "quasar" (quasi-stellar radio source), also known as quasi-stellar object (QSO)[(6)].

An important discovery was made by Maarten Schmidt, based on their observations in late 1962 of a supposed foreground star. Its spectrum did not resemble an ordinary star, leading Schmidt to the idea that a redshift of $z = 0.16$ could explain some spectral features. In a collaboration with their colleagues, J. L. Greenstein and J. B. Oke, observations of the same object at other wavelengths as well as another object, of which the spectrum could be explained by the same idea, but with another redshift of $z = 0.37$, led to a promising solution to the question of the origin of quasars (Greenstein 1963; Hazard et al. 1963; Oke 1963; Schmidt 1963). However, the explanation for the redshift was still not certain, including other puzzling features, such as a very high luminosity and surface brightness for some objects. Although observations implied the possibility of a small, but very massive object, nowadays known as a BH, the idea appeared unlikely, especially including theoretical considerations from that time. Still, Greenstein and Schmidt (1964) elaborated further on different ideas, including one in which a high central mass gives rise to a glare that outshines a possible host galaxy.

The following years saw rapid advancements concerning AGNs, for example giving birth to new search techniques for quasars, finding more classifications of objects, and

[(6)] The terms quasars and QSOs are sometimes used synonymously, while at other times these refer to different objects. More information can be found in Sect. 2.2.2.

observations of larger redshifts. The accepted nature of the redshifts turned more and more towards a cosmological origin, i. e., a cosmological redshift instead of rapid motion or gravitational redshift (e. g., Gunn 1971). Eventually, it was also accepted that quasars are surrounded by host galaxies. Different classifications, such as Seyfert galaxies and quasars, were able to be connected via the now common name AGN. Some descriptions and explanations of certain AGN characteristics in the following sections contain information on further historical progress, which in some cases led to a wide consensus concerning AGNs.

However, two relatively recent publications that are linked to the context of SMBHs should not be missed here, as both can be considered modern milestones. These are based on two observations by the EHTC, a global consortium of different radio telescopes that effectively make up one Earth-sized telescope, the EHT. In April 2019 the EHTC released the first ever image of a SMBH, or rather of its shadow, as the BH is an entirely dark object. The SMBH lies at the center of galaxy Messier 87 (M87). About three years later, in May 2022, a similar image of the center of the MW was released by the EHTC, showing the object Sagittarius A* (Sgr A*), which is associated with a SMBH as well. Both images are shown in Fig. 2.2, including some more information. Given the size of these extremely massive objects, as well as their matching appearance compared with simulations, these images might be considered a final proof for the existence of SMBHs.

2.2.2 Classifications of Active Galactic Nuclei

Over time, the number of classes of AGNs grew and new designations were introduced. Some of these classifications share an overlap and the meanings of some classifications changed to some degree, or at least the way the respective terms are used. In order to avoid confusion, some authors resort to using only very broad terms, as for example in the publication by Netzer (2013), where they rely on only two categories, type-1 and type-2 AGN, as well as only a few names and abbreviations. These two classifications are generally distinguished by the presence or absence of narrow and broad emission lines, where type-1 AGNs contain broad emission lines, and type-2 AGNs only show narrow emission lines. The exact distinction differs in literature and in some cases special findings were coined as intermediate types, such as types 1.5, 1.8, or 1.9. As an example, Netzer (2013) gives slightly more detailed explanations for the two main types, describing type-1 AGNs as objects with broad, strong emission lines at optical and UV wavelengths, whereas type-2 AGNs have prominent narrow emission lines and in case there are traces of broad emission lines, these are at most very faint. A type-2 AGN is also expected to show a large column, which blocks especially X-ray emission. An according model that is a potential explanation for these differences, including short descriptions of the building blocks, is described in Sect. 2.2.3. Furthermore, there is another scheme for subdividing AGNs into two groups, which is their radio-loudness, i. e., whether a source is considered to be radio-loud or radio-quiet. Here, I introduce a few AGN classifications, which are probably the most important ones to mention.

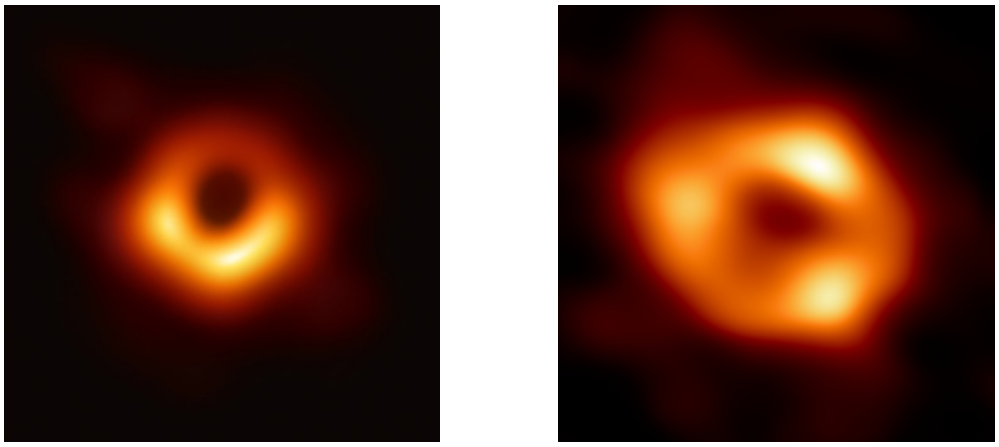

Figure 2.2: *On the left:* The center of the galaxy Messier 87 (M87) as seen with the Event Horizon Telescope (EHT) at a wavelength of 1.3 mm. This image is often referred to as the first ever image of a black hole (BH), although the BH itself is not actually visible, but only its shadow. The bright ring surrounding the BH at the center is associated with glowing gas from the accretion disk. It does not appear uniform due to events that create variations in the signal as well as distortion effects from the extreme gravitational environment. The size of the central, dark spot could easily contain the Solar System a few times. *Credit: EHT Collaboration (CC BY 4.0) (cropped image)* ; *On the right:* The BH at the center of the Milky Way (MW), Sagittarius A* (Sgr A*). Despite the similar appearance to the center of M87 in the left image, this BH is about 1000 times smaller, i. e., the outer edge of the bright ring has a similar size as the orbit of planet Mercury. However, as it is much closer to an Earth-bound observer, its size appears to be similar as on the right. While the gas orbiting the two BHs moves at similar velocities close to the speed of light, the gas around Sgr A* has a much shorter orbital period, related to the smaller size of the BH. Variations change accordingly on smaller timescales, leading to a different pattern of bright spots. *Credit: EHT Collaboration (CC BY 4.0)*

Quasars/QSOs

While sometimes treated as the same objects, quasars and QSOs are often distinguished (see also Sect. 2.2.1 for some historical context). The potentially distinctive characteristic between these two types of AGN is the respective radio-loudness. A quasar is essentially always considered to be a radio-loud AGN, whereas a QSO might be marked as a radio-quiet AGN, i. e., being barely or not at all detectable at radio wavelengths, which in turn depends on the sensitivity of the observations. Both types show blue colors, meaning here a low value of the $U - B$ color index[7], and their optical properties and SEDs are essentially the same. The latter point is related to the history of these objects, as one of the criteria for finding these objects was their blue color index (Schneider 2015, p. 221). In either case, these objects tend to be very luminous, potentially even in comparison to whole galaxies, and show strong and broad emission lines. When combining their high luminosities, where the nucleus might easily outshine the whole host galaxy, with their often high distances from the MW, these objects might appear like point sources in the optical. This led to their names as quasar (quasi-stellar radio source) and QSO (quasi-stellar object). According to Peterson (1997, p. 23), quasars have optical (blue) nuclear magnitudes of $M_\mathrm{B} < -21.5+5\log(h_0/100\,\mathrm{km\,s^{-1}\,Mpc^{-1}})$, where h_0 is the Hubble constant.

Seyferts

Similar to the previous classification, this one is already mentioned in Sect. 2.2.1. While the name "Seyferts" can indicate this class of AGNs, it is also often used to refer to Seyfert galaxies, i. e., galaxies that host such an AGN. The class of Seyferts is associated with AGNs of low-luminosities. Seyfert galaxies are usually found to be spiral galaxies with a bright core. The nuclear spectrum features strong emission lines, with a broader width than typical for velocities in galaxies. Their sub-division into Seyfert-1 and Seyfert-2 classes are a great example for the general distinction between type-1 and type-2 objects. Seyfert-1 have both, narrow and broad emission lines, while Seyfert-2 show only narrow lines. In both cases, even the narrow emission line widths are often around multiple hundreds of km/s, exceeding for example typical rotational velocities in galaxies (Schneider 2015, p. 222). Matching the criterion given by Peterson (1997) for quasars, Seyferts have central magnitudes of $M_\mathrm{B} > -21.5+5\log(h_0/100\,\mathrm{km\,s^{-1}\,Mpc^{-1}})$ (Schmidt and Green 1983). Depending on the exact criteria defining QSOs, particularly those that are radio-quiet, the transition between Seyfert-1 and these QSOs is smooth. There are suggestions that these two classes only differ by their redshifts (e. g., Weedman 1976). Observations of Seyferts showed that the broad emission lines are variable, and thus, changes of the classification might happen. If for example the AGN of a Seyfert-1 galaxy becomes fainter and the broad emission lines seem to disappear, an observation of such a source in the later state might have triggered a classification as a Seyfert-2. However, the broad emission line components do not actually vanish completely, but

[7] This color index is based on the magnitudes of an object using different filters. Here, these are the U and B filters, standing for Ultraviolet and Blue wavelengths, respectively.

only become very faint (Penston and Perez 1984). This also explains why the previously mentioned intermediate types of AGNs, namely objects of types 1.5, 1.8, and 1.9, are especially relevant for Seyfert galaxies.

There is an idea for another class of galaxies, the narrow-line X-ray galaxies. These were found in early X-ray surveys, exhibiting characteristics similar to Seyfert galaxies. They show high-excitation lines, just as Seyfert galaxies, but at lower luminosities (Ward et al. 1978). Later, these turned out to be Seyferts, of which the optical spectra are strongly influenced by dust in the galaxy, which dims and reddens radiation.

Radio Galaxies

As the name of this classification implies, these galaxies are characterized by strong signals at radio wavelengths from nucleus, i. e., these are radio-loud sources. Again, there is a distinction between type-1 and type-2 objects via broad-line radio galaxies (BLRGs) and narrow-line radio galaxies (NLRGs), respectively. Radio galaxies are associated with elliptical galaxies, that are usually very large. Otherwise these objects share a similar phenomenology with Seyferts, i. e., BLRGs and NLRGs might be considered radio-loud variants of Seyfert-1 and Seyfert-2 galaxies (Schneider 2015, p. 222).

LINERs

LINER is an acronym for low-ionization nuclear emission-line region, defined by Heckman (1980). These objects show very low luminosities when compared with other classifications of AGNs. Depending on the underlying criteria, low-ionization nuclear emission-line regions (LINERs) are not considered to be an actual type of AGN, as for example similar spectra to those of LINERs can be found in early-type galaxies that do not harbor an AGN. Thus, a possible explanation for their spectra might be star-formation, instead of an AGN. Other explanations include an accreting cooling flow of gas, possibly from the galactic halo, and shock-heated gas from collisions (Heckman 1987). The spectra of LINERs are similar to Seyfert-2 galaxies, but overall at the end of lower luminosities, which gives rise to another interpretation of LINERs as low-level Seyferts with a diluted non-stellar continuum. However, low-ionization lines are relatively strong in LINERs. These types of objects are also very common, as "at least one third of all nearby galaxies contain a LINER in their core, characterized by emission lines from neutral atoms or ions with rather low ionization energies" (Schneider 2015, p. 222). Their emission lines are even less broad than the narrow lines from Seyfert galaxies.

As Peterson (1997) describes, the spectra of LINERs, Seyfert galaxies, and H II-regions cannot be distinguished for certain via a single flux ratio of any two emission lines. It turns out that two ratios, i. e., two pairs of lines, can be used for such a distinction, as shown by BPT diagrams, named after the three people that published their finding, Baldwin, Phillips, and Terlevich (Baldwin et al. 1981). This enables the distinction between the aforementioned H II-regions, Seyferts, and LINERs, but also distinctions of other types of objects.

Blazars

While all AGNs show a continuum variability along the observed ranges of the electromagnetic spectrum, the variability of blazars is on shorter timescales and much larger, e. g., in only a day the magnitude in the visible regime might change by $\Delta m \geq 0.1\,\mathrm{mag}$, and they show larger fractions of polarization than other AGNs, namely a few percent against less than one percent (Peterson 1997, p. 43). Blazars are radio sources, i. e., they are all radio-loud, and they show strong highly energetic radiation, including γ-radiation, which exhibits fast and strong variations as well. Here, there is also a subdivision into two classes, but not based on type or radio-loudness. First, there are optically violent variables (OVVs)[8]. Their names imply an important characteristic, which is fast and strong variations in the optical regime. These sources include strong emission and absorption lines. This characteristic is an important factor to distinguish OVVs from the second class, called BL Lac objects. The designation comes from the observation of a paradigm for this class, the soure BL Lacertae, which was initially assumed to be a highly variable star. Given a very high signal-to-noise ratio (S/N), even in the case of BL Lac objects it might be possible to detect traces of stellar absorption or nebular emission lines, i. e., features of the host galaxy, allowing for otherwise problematic redshift estimates. The sub-classifications, OVVs and BL Lac objects, might be connected. According to Schneider (2015) BL Lac objects can appear like OVVs in epochs of relatively low luminosities, as emission lines might then be observable.

2.2.3 Unified Model

The idea behind the unified model, or rather unified models (also: unification models) in general, is that different classifications of AGNs can be explained by correlations between those. This is in turn based on the principle of Occam's razor, i. e., the thought that explanations should strive to contain only a small set of elements. In the case of AGNs this is applied by connecting different types of AGNs via the change of observational parameters, i. e., the same object might appear different to a respectively changing observer. After getting to know some classifications of AGNs in Sect. 2.2.2, some fundamentals for unified models are given already. A particular common theme should be obvious by now: the distinction between radio-loud and radio-quiet AGNs, and the distinction between type-1 and type-2 AGNs.

To understand the idea behind unification models, some further characteristics of AGNs are necessary to know. Here, I describe two important building blocks of an AGN, as they are widely found in literature, namely the narrow-line region (NLR) and the broad-line region (BLR). The following descriptions are mainly based on the respective sections of the books by Peterson (1997) and Netzer (2013).

NLR The NLR is a region of low density gas ($\sim 10^4\,\mathrm{cm}^{-3}$). Its column density is potentially low enough to be optically thin in some wavelength ranges, including

[8] Sometimes these are also called optically violently variables. Both terms are optionally followed by the word quasar.

the helium and hydrogen Lyman continuum, which then again boosts the overall ionization level. The size of the NLR can be of the order of kiloparsec, e. g., a luminous AGN might have a NLR that extends up to $\sim 3\,\mathrm{kpc}$. Thus, depending on the distance of the respective object, the NLR might be spatially resolved in the optical. Additionally, it is the largest region which is mainly ionized by the central engine of the AGN. The NLR is assumed to consist of gas clouds as well as dust in some regions, as the temperatures there can be below the dust sublimation temperature. That the NLR has a clumpy composition can be inferred from profile structures of high-resolution spectra. Spectra of the NLR include strong forbidden lines, as the respective transitions are not suppressed by high densities. This emission is assumed to be isotropic, because of the negligible amount of self-absorption in narrow lines.

The exact range for potential line widths of spectral lines from the NLR differs in literature. Based on the full width at half maximum (FWHM) of velocities associated with the lines the range and typical values, as given by Peterson (1997), appear to reflect a wide consensus. This range is given as $200\,\mathrm{km\,s^{-1}} \lesssim \Delta v_{\mathrm{FWHM}} \lesssim 900\,\mathrm{km\,s^{-1}}$ and typical values are expected to be around $350 - 400\,\mathrm{km\,s^{-1}}$. Due to stronger bases and potential asymmetries, narrow emission line profiles cannot be described accurately by a Gaussian. This is especially relevant for high-resolution spectroscopy, but less so at low resolutions. Emission lines from the NLR are used in diagnostic diagrams, such as the BPT diagram (see Sect. 2.2.2).

The morphology of a NLR is usually axisymmetric. If the source shows extended radio emission, this axis of symmetry coincides with the radio axis, which is suggestive for a connection between the thermal emission from the NLR and the non-thermal radio emission. The non-thermal, radio-emitting plasma interacts with the gas in the NLR, influencing the ionization levels, such that the total ionization level in the NLR is composite. A major amount is based on the central SMBH, but the plasma and the respective ionization via collisions contributes a non-negligible part (see also Viegas-Aldrovandi and Contini 1989). An additional note can be made that the radio axis, and by extension the NLR axis, seems to be oriented randomly with respect to the rotation axis of the host galaxy.

There is a concept called extended narrow-line region (ENLR), based on observations of cone-shaped ionization regions with anisotropic behavior. However, this region is assumed to be primarily ionized by stars, and thus should be distinguished from the NLR as described before. Its size can be more than $\sim 100\,\mathrm{kpc}$.

BLR In contrast to the NLR, the BLR shows broad line widths, just as its name implies. Broad emission line profiles are diverse, and cannot be described easily by one profile only. Again, line width specifications depend on the literature, especially the upper limit of broad lines. Following the scheme for line widths for the NLR, broad line widths from the FWHM of velocities are expected to be between $v_{\mathrm{FWHM}} \approx 500\,\mathrm{km\,s^{-1}}$, i. e., similar to some narrow line widths, and $v_{\mathrm{FWHM}} > 10^4\,\mathrm{km\,s^{-1}}$. The open end indicates some uncertainty as to an upper

limit. Typical values are stated to be around $\sim 3000 - 5000\,\mathrm{km\,s^{-1}}$. However, it is necessary to mention that emission line widths may vary even within the same spectrum, which is potentially linked to a dependence on the region it originates from. As an example, optical emission lines might come from a region at smaller radii than IR emission lines, leading to smaller line widths for the IR lines. This simplified picture is not a sufficient explanation for all differences, though. Another example for varying line widths is that the helium lines He II λ4686 and He I λ5876, which are around the same wavelengths as some hydrogen Balmer lines, are often broader than these Balmer lines, even at any relative intensity level. BLR spectra are based on photoionization by continuum radiation from the central SMBH, which can be inferred from the response of the emission lines to changes in the continuum (see also Sect. 2.4.1).

The width of the emission lines cannot be explained by thermal motion, as for example a model calculation for a gas at $10^4\,\mathrm{K}$ results in a line-of-sight (LOS) velocity dispersion of just $\sim 10\,\mathrm{km\,s^{-1}}$. Flipping the calculation around, to reach the typical broad emission line width of $\sim 5000\,\mathrm{km\,s^{-1}}$, the gas temperature would need to be $\gtrsim 10^9\,\mathrm{K}$. Thus, Doppler shifted gas is usually assumed to create the broad emission line widths.

Although the exact properties, such as the geometry and kinematics, are still unknown, in general the BLR is assumed to consist of gas clouds with high densities of for example $\sim 10^{10} - 10^{11}\,\mathrm{cm^{-3}}$. While even this density range is only valid for a quite specific scenario, it is sufficient to emphasize the vast difference to the NLR.

Despite its larger density, the BLR is assumed to be of order of magnitudes less massive than the NLR, which is related to the much smaller size of the BLR. However, as the BLR is by far more efficient concerning emission, the amount of emission lines from both of these regions is comparable. Individual gas clouds travel in bulk motions around the central source, which creates the range of velocities found in line profiles. The BLR is closer to the central source and thus, more affected by it than the NLR. The strong gravitational effects and the radiation pressure are in constant competition.

The size of a BLR is not certain, as it depends on the SMBH at the center. Thus, BLRs cover a range of sizes. A typical size estimate is of the order of 10 light days, with small BLRs around 1 light day and big BLRs around > 100 light days (e. g., Wandel et al. 1999; Peterson et al. 2004; Kaspi et al. 2005; Mandal et al. 2021). There are suggestions for a continuous transition between the BLR and the NLR, without a specific segregation. Another explanation for the transition between these regions relies on dust, and explains that the volume between the BLR and the NLR is filled with gas & dust.

There are two more building blocks related to an AGN, the accretion disk and the dusty torus. A short description of the accretion disk follows in another small section (see Sect. 2.2.3).

The dusty torus is at a further distance from the center than the BLR, but a smaller distance than the NLR. Following this assumption, Netzer (2013, p. 205) describes accordingly interpolated gas densities and a typically expected order of velocities in the toroidal region as $10^4 - 10^7\,\mathrm{cm}^{-3}$ and $1000\,\mathrm{km\,s}^{-1}$, respectively. However, details depend on the influence of the central SMBH on its surroundings, for example based on the BH size. The torus lies outside the dust sublimation area and hence, it is thought to contain dust and molecular gas. One very important characteristic, which gives the dusty torus sometimes also the name 'obscuring torus', is its high opacity at essentially all wavelengths. A possible exception could be the IR in combination with relatively small column densities, allowing for some transparency in that regime. The obscuration is especially important in the context of unified models, as can be seen in the following. While its exact structure is still unknown, e. g., a continuous model against a clumpy model, the toroidal shape with a small opening in the center and a much larger outer radius is commonly applied in models for this region. Still, other explanations cannot be ruled out, such as a warped disk, which might be connected to an inflow on large scales. The dusty torus might be connected to the anisotropy found for the ENLR, but even in that case, it is not clear how. On the one hand it could be that the torus blocks radiation in certain directions, while on the other hand collimated radiation from within might create the central opening and thus give the torus its shape as such. Lastly, the torus might not exist for all AGNs, as observations indicate that some objects might not contain such a dusty structure. With only one more component, that has been hinted at previously, and an additional detail about the building blocks of an AGN, unified models are more easily understandable: the continuum radiation comes from a central region right around the SMBH, the accretion disk, and some sources feature a strong jet coming from this central source.

The prior descriptions for parts of AGNs are all related to their morphologies and introduce a respective common theme in unified models. The analysis of AGN morphology might show that only a few parameters are needed to explain differences between different types of AGNs. In other words, different types of AGNs might be intrinsically the same, and observational parameters influence the resulting classification. Depending on the model, more or less parameters account for actual intrinsic differences in the sources. There are strong and weak unified models, where this "strength" accounts for the amount of unification via actual physical differences. A weak model unites only few types of objects via the assumed underlying physical traits, and thus leaves room for more inherently different classifications. In contrast to this stand strong models, which assume fewer intrinsic differences and base classifications more on external parameters. According to Peterson (1997), an example for such a weak model might rely on the optical and radio luminosity, so two intrinsic parameters, whereas a strong model might connect both luminosities via the total luminosity, a single intrinsic parameter. Both models explain any remaining distinctions via apparent differences, such as for example the viewing angle of an observer.

There are two examples for early identifications of such orientation effects. The first is given by Osterbrock (1978), trying to tackle the question why Seyfert-2 galaxies do

not show broad emission lines. The second comes from Blandford and Rees (1978), connecting blazars with an alignment between the observer and the radio axis. The premise of the former example addresses an important question, as the assumption that Seyfert-1 and Seyfert-2 galaxies should actually be united came early from a finding in observations of both types of sources. Seyfert-2 galaxies do not only miss broad emission lines, but also often show a lower ratio in AGN continuum to stellar continuum in comparison to Seyfert-1 galaxies. The dusty torus plays an important part in trying to explain this, as well as a medium that is able to scatter central radiation in other directions. Unified models that explain the difference between type-1 and type-2 objects based on the inclination between the observer and the source also help in understanding the emergence of intermediate types, as the previously mentioned types 1.5, 1.8, and 1.9. As an example, Netzer (2013, p. 141) mentions that the types 1.8 and 1.9 might emerge from heavy LOS reddening, connected to a stronger obscuration of the BLR.

One type of unified model is wide-spread and thus the most encountered in the subject, although it is not considered to be a final and detailed description for all AGN-type related phenomena. This unified model is depicted in Fig. 2.3. The basic assumption of this unified model is that there are two intrinsically different types of AGNs, which depend on the radio-loudness. A radio-loud AGN is thought to feature a jet, which in turn is missing in a radio-quiet AGN. The latter might still have a jet, but it would be of such low intensity that it cannot be observed. This unified model explains all remaining differences between types of AGNs as depending on the observer, in particular the viewing angle towards the source. In this model blazars are radio-loud sources for which the jet is aligned with or at least very close to the LOS of the observer, explaining the strength of these AGNs and their high variabilities. At a larger angle, i. e., not as much aligned with the jet anymore, an observer sees a quasar. Depending on the distinction between quasars and QSOs this might also be labeled explicitly as a radio-loud quasar. Increasing the angle from the jet even further shows a radio galaxy to an observer. However, as the center is not obscured by the dusty torus yet, the BLR is still visible and the radio galaxy would classified as a BLRG. For even larger angles the dusty torus blocks the view of the BLR and only signals from the NLR remain visible, resulting in a classification as a NLRG. Following this simplified scheme, the obfuscation of broad emission lines is rather obvious in case the viewing angle of the observer is within the plane perpendicular to the jet component, but also for slight deviations from that plane, depending on the size of the obscuring torus, i. e., its thickness. The same principle can be found for the radio-quiet AGNs. The counterpart to a NLRG is then a Seyfert-2 galaxy, where the BLR is again blocked from view by the dusty torus. Accordingly, if the BLR is visible to an observer, they would find the radio-quiet counterpart to a BLRG, wich is a Seyfert-1 galaxy. Finally, for a direct view on the center of a radio-quiet AGN an observer might see a QSO. If the terms quasar and QSO are used interchangeably, this might be labeled as a radio-quiet quasar.

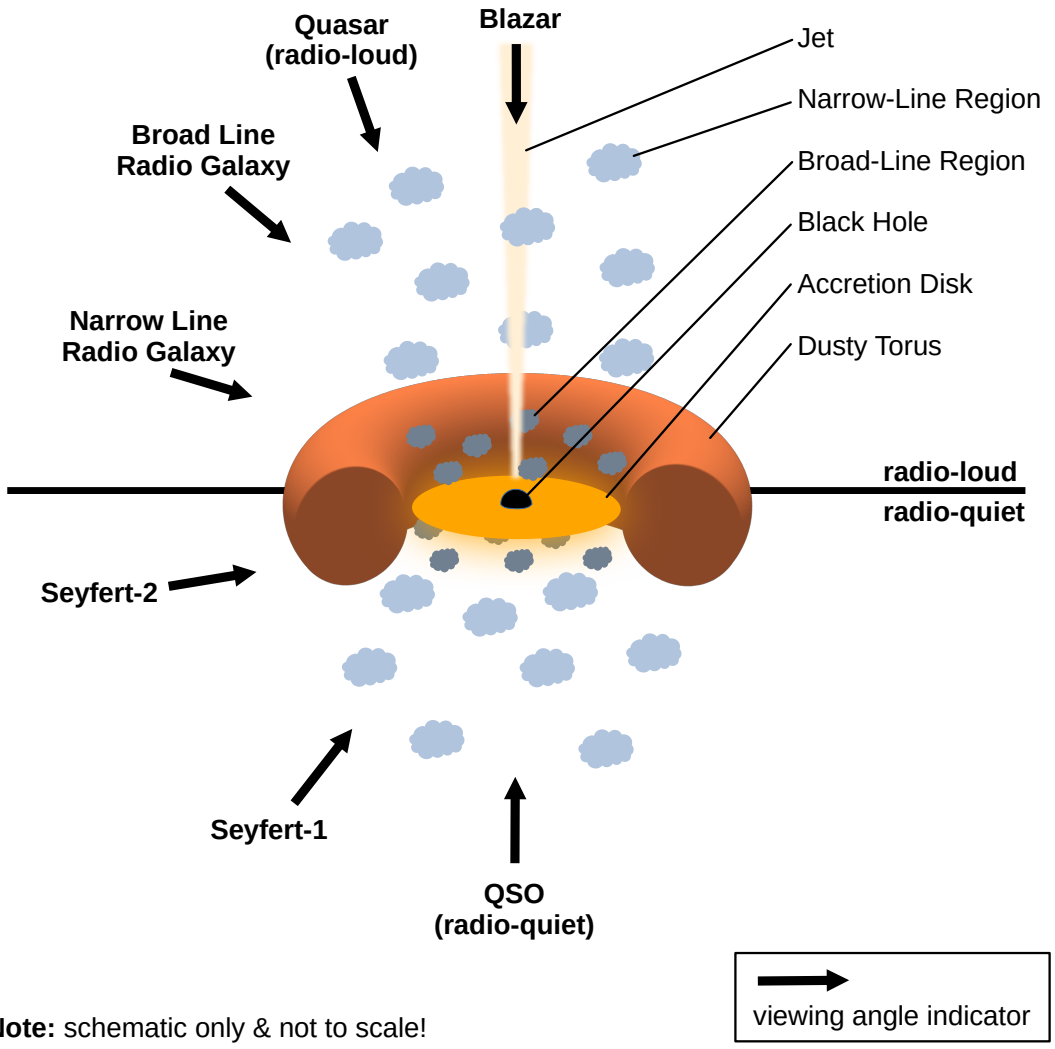

Figure 2.3: Visualization of a wide-spread unified model. The inherent characteristic that splits multiple types of AGNs into two classifications is the radio-loudness. Radio-loud sources, i. e., sources that feature a jet from the central region, are shown in the top half; radio-quiet sources are shown in the bottom half. The model is based on these 5 to 6 AGN components: dusty torus, accretion disk, central SMBH, BLR, NLR, and in case of a radio-loud source also a jet. As indicated in the lower left, this depiction is not to scale and only intends to visualize the schematic idea. *Inspired by a combination of the schematics from Urry and Padovani (1995, Fig. 1) and Emma Alexander* `https://emmaalexander.github.io/resources.html`.

Accretion

As it is a very central part of how an AGN is visible at all, a short description of the respective accretion process is reasonable. Previously it was hinted at that a SMBH is the central engine of an AGN. One question that may arise is why there is any signal at all coming from a BH, as these objects are famous for their high gravitational potentials, which do not let anything escape from within their event horizon[(9)]. The answer to this question is accretion, a basic process in astrophysics that can be encountered in many cases. In general the term refers to a gravitational accumulation of matter into a central massive object. Although this is relevant for many formation processes, including stars and planets, due to the context of AGN I concentrate here mainly on BHs. In essence, the first step is that gravitational potential energy is converted into kinetic energy. A straight fall into the central object should be the exception, as for almost all matter there is some angular momentum involved. Due to conservation of the angular momentum there needs to be another process involved, which makes the particles lose their angular momentum, as for example contact with, and momentum transfer to, other particles, i. e., friction. This heats the matter surrounding the central massive object. In turn, the internal energy can be a radiation source, which is observable.

The radiation creates a pressure that pushes against surrounding matter, which includes accreting particles. The accretion process can proceed as long as the gravitational force is larger than the force from the radiation acting outwards. If the forces are equal, there is a balance for which the luminosity is defined as the Eddington luminosity L_{Edd}. It is thus the maximum luminosity that an object can reach via steady accretion over long periods of time. Nevertheless, on short timescales, such as right after outbursts, the luminosity might exceed this limit. The accretion rate, i. e., the amount of mass swallowed in an accretion process over a certain period of time, depends on the given luminosity. A higher luminosity is connected to a higher accretion rate and the accretion rate given for the Eddington luminosity is called Eddington accretion rate, $\dot{M}_{\mathrm{Edd}}$. There are different types of accretion, including the probably simplest case: spherical accretion, which is also called Bondi accretion (Netzer 2013, p. 41).

However, a much more common assumption is that accretion occurs in a disk instead of a sphere. The mechanism that turns the potential energy into radiation is viscous dissipation within this disk. As the gravitational force should be much larger than the forces caused by friction, the particle velocities are expected to be of the order of local Kepler velocities. The velocities within the disk are differential, meaning that the angular velocity depends on the radius, which causes internal friction, i. e., a deceleration of particles (Schneider 2015, p. 225). Due to being slowed down the particles move inwards, i. e., the cycle of energy conversion starts over. According to the virial theorem 50 % of the gravitational potential energy is turned into kinetic energy, i. e., the rotational

[(9)] The event horizon is a boundary that encloses a region which cannot affect anything outside of this region. It is often described as that region around a BH from which not even light can escape, as gravity at this boundary is strong enough to bend light at such a curvature, that no distance from the central BH larger than the event horizon can be reached anymore. The Schwarzschild radius, also sometimes called gravitational radius, is the radius that defines the event horizon.

movement of the disk, whereas the other 50 % is turned into internal energy, i. e., heat. The emergence of radiation from the internal energy seems to be a very efficient process, as "[f]or a given mass, the accretion onto a black hole is about ten times more efficient than the nuclear fusion of hydrogen into helium" (Schneider 2015, p. 11). Complementary to this, Netzer (2013, p. 43) cites an efficiency from $\sim 4\,\%$ up to $\sim 42\,\%$ for the energy conversion into radiation.

Accretion disks can appear in different shapes, relating to their thickness, and with different opacities. The latter depend on the column or surface density and the ionization level. A common assumption about the accretion disk of a BH is that it is geometrically thin and optically thick. In order to get a feeling for the meaning of geometrically thin, Netzer (2013, p. 44) notes that this is the case for a thickness to radius ratio of potentially even much less than 0.1. It appears that only three fundamental parameters suffice to describe a few important characteristics of the accretion disk. The three parameters are the accretion rate of matter that is processed in the disk, the central BH mass, and the spin of this BH. The characteristics that these describe include the disk geometry, temperatures in the disk, the total luminosity, and the spectrum.

In an approximation the total spectrum of a geometrically thin, optically thick disk can be described as a superposition of BB spectra, where each single spectrum describes an isothermal ring at a respective radius. The low and high frequency end of the otherwise roughly flat spectrum of the disk depend on the lowest and highest temperature in the disk, resembled by its outer and inner radius, respectively. As the major part of radiation comes from smaller radii, the inner disk region and how far it reaches towards the central BH is important for the overall luminosity. This inner radius has a physical limit, as the disk would be ripped apart by the extreme gravitational pull at smaller radii. The outer disk radius might be connected to self-gravitational effects, i. e., the particles might form clumps at larger radii than the outer disk radius. One aspect that appears counter-intuitive is that the highest temperatures in accretion disks of more massive BHs are expected to be lower than in less massive BHs. For many AGNs radiation from the hottest regions is part of the UV regime, for some smaller BHs this is potentially the soft X-ray. However, considering that the average density of the region inside the event horizon decreases for larger BH masses, which is another example for a similarly counter-intuitive behavior of BHs, the lower temperatures do not appear as strange anymore. The effect of tidal forces on the accretion disk is simply weaker for a more massive BH.

The assumed geometrically thin, optically thick accretion disk is still just a simplified model. Actual disks might very well be non-uniform, potentially driven by strong and complex magnetic fields in the disk. These fields might also affect or even cause large parts of the viscosity in accretion disks. Another connection might be hot coronas, reaching temperatures that result in strong X-ray radiation. The topic of accretion disks is still evolving, with numerical simulations becoming better and more prevalent. Currently, though, there are still many unknowns and simplistic pictures need to suffice for lots of situations. However, advancements on this topic can be expected in the near future. In a very recent publication, Lu et al. (2023) find a connection between a jet and

the accretion flow of the SMBH at the center of M87, which is known from Fig. 2.2.

2.3 Central Black Hole – Host Galaxy Bulge Relations

Empirical analyses have shown that there can be multiple relationships assumed between the central SMBH and its host galaxy. Several studies have found that these correlations hold better when considering only the central bulge component of the host galaxy. Additionally, there is essentially a single BH property, which can be quantified for numerous objects with the current level of technology and knowledge, the BH mass. Put together, this is the reason why nowadays, when a relation between the central BH and its host galaxy is mentioned, it is often explicitly a reference to a BH mass – bulge property relation, i. e., a $M_{\mathrm{BH}}-$bulge relation. What exactly constitutes the bulge is a question of galaxy type. As described in Sect. 2.1.1, some galaxy classifications are expected to show a prominent bulge component, such as lenticular galaxies. Spiral galaxies might also feature a distinctive spheroidal bulge component, whereas elliptical galaxies themselves are considered to be the bulge. This could be seen as intuitive, because of the similarity between classical bulges and ellipticals, in contrast to pseudobulges, which is potentially relevant later on. Bulge properties that appear to scale with the BH mass are presented in this section.

An important aspect, which is implied by all these relations, is that there appears to be a co-evolution of the central SMBH and at least the bulge component of its host galaxy. Although SMBHs are extremely compact objects with inconceivable masses of more than $10^5\,\mathrm{M}_\odot$[(10)], in some cases even more than $10^9\,\mathrm{M}_\odot$, their spheres of influence, e. g., concerning gravity, appear small in comparison to the scale of their host galaxies. As was shown earlier, even the NLR, and especially the ENLR, can show a strong influence of surrounding stars and is thus much less dominated by the central SMBH as for example the BLR. With this in mind, it is already clear that the bulge component of the galaxy should not be dominated in any way by the central SMBH. In fact, considering only their total masses, it becomes quite puzzling why the central SMBH mass should scale at all with bulge properties, as the BH mass is virtually always less than 1 % of the total bulge mass, and often even much less than that. Examples for this are the studies by Wandel (2004) and Jiang et al. (2011). The former find in a sample of quiescent galaxies, that the BH masses are only about 0.2 % of their respective bulges. The latter find in their sample a factor of more than 1000 between the bulges and the BHs, i. e., the SMBH masses are even less than 0.1 % of the bulge masses. As a result, a joint evolution of the central SMBH and the bulge of its host galaxy is necessary for relations to develop between both. Some form of feedback that influences the growth of either, the SMBH and the bulge, has to take place, which connects both components and in turn leads to a question about the activity in the center of the galaxy. Are these correlations valid only for inactive or active galaxies, or possibly both? This question becomes even more important when considering that lots of relations have been found

[(10)] In astrophysics the mass of the Sun, $\mathrm{M}_\odot$, is a common unit of mass. It is $1\,\mathrm{M}_\odot \approx 1.99 \cdot 10^{30}\,\mathrm{kg}$.

empirically from samples of close, inactive galaxies.

One of the earlier findings and probably the most famous relation found between the central SMBH and the host bulge is the $M_{\mathrm{BH}} - \sigma_*$ relation, where σ_* is the stellar velocity dispersion of the bulge. Two papers about this relation were published within the same volume of the same journal, i. e., these were effectively published at the same time (see Ferrarese and Merritt 2000; Gebhardt et al. 2000). The relation has undergone a few adjustments over time (e. g., Tremaine et al. 2002; Gültekin et al. 2009) and it is considered as one of the most fundamental $M_{\mathrm{BH}}-$bulge relations. Based on the tight nature of this relation, as it shows only relatively small scatter of $\sim 0.25 - 0.3\,\mathrm{dex}$ (Tremaine et al. 2002), it was and is still used to gauge other $M_{\mathrm{BH}}-$bulge relations. Further analysis also revealed that this relation holds true for both, inactive and active galaxies, showing that here the level of activity of the central SMBH does not matter (e. g., Woo et al. 2010).

Two more $M_{\mathrm{BH}}-$bulge relations, which have been found even prior to the $M_{\mathrm{BH}} - \sigma_*$ relation and analyzed together in some publications, are the $M_{\mathrm{BH}} - M_{\mathrm{bulge}}$ relation and the $M_{\mathrm{BH}} - L_{\mathrm{bulge}}$ relation (for example Kormendy and Richstone 1995; Magorrian et al. 1998; Marconi and Hunt 2003; Häring and Rix 2004; Sani et al. 2011). The former relation connects the aforementioned mass of the central SMBH and the stellar mass of the bulge component, while sometimes the dynamical bulge mass is used instead of the stellar mass. The second relation considers the bulge luminosity instead of its mass. One reason why these two relations are sometimes analyzed jointly is that the two bulge properties are linked via another tight correlation, the $M_{\mathrm{dyn}} - L_{\mathrm{bulge}}$ relation. It connects the dynamical bulge mass with the bulge luminosity and shows only a small intrinsic dispersion of $\sim 0.1\,\mathrm{dex}$ (Sani et al. 2011).

There is another relation, which connects the BH mass with the Sérsic index n, the $M_{\mathrm{BH}} - n$ relation (Graham and Driver 2007). The Sérsic index is a parameter in the formula of a Sérsic profile, which is a generalized version of a de Vaucouleurs profile (Sérsic 1963). The intensity profile is given by $I(r) = I_0 \exp\left(-sr^{1/n}\right)$, where r is the distance from the center, and I_0 is the intensity at the center ($r = 0$). Often the parameter s is split into two parameters in order to consider the half-light radius. The Sérsic index n is used to account for the galaxy morphology, although the relation usually still refers to the central bulge component only. In contrast to this stands the $M_{\mathrm{BH}}-$*spiral arm pitch angle* relation. This is a measure of the tightness of a spiral structure, as possibly given in the case of disk galaxies, and thus a parameter of the host galaxy instead of a bulge component. The idea for the relation emerged from the discovery of AGNs in disk galaxies without a central bulge, where two possible, alternative factors that relate to the BH mass are halo concentration and virial mass in the host galaxy. As the mass concentration in the galaxy appears to determine the spiral arm pitch angle, the relation between the latter and the central SMBH mass can be assumed and was found accordingly (Seigar et al. 2008).

More relations between either the central SMBH mass or a property of its host galaxy and other quantities related to either of them are assumed to exist. An example for such a relation concentrates on the AGN only, as it connects the central BH mass and the

AGN luminosity (Peterson et al. 2004).

Another noteworthy correlation, although again not a $M_{\mathrm{BH}}-$bulge relation, is that the widths of narrow emission lines from the NLR appear to correlate with the bulge luminosity of the host galaxy, especially if no jet component is present. This indicates a virial origin of these lines, related to the stars in the bulge (Peterson 1997, pp. 104 sqq.).

2.4 Black Hole Mass Estimation Methods

Following the current understanding of BHs, these objects can be described by three independent parameters, which can be observed externally[(11)]: charge, spin (i. e., angular momentum), and mass. As mentioned in the previous section (Sect. 2.3), the BH mass is the most prominent quantity regarding an analysis based on observations. An obvious question following this statement is how to find a BH mass from observations. The main focus of this section addresses two methods in some detail and mentions some more possibilities. A special case of one method is important for this work, as it is applied in the analysis that follows later.

2.4.1 Reverberation Mapping

While reverberation mapping (RM) is only indirectly relevant to the work presented here, its importance within the general context of BH mass estimation methods is not to be underestimated. The term RM was introduced by Blandford and McKee (1982) as an indirect method, which allows the "mapping [of] the emission line regions of Seyfert galaxies and quasars having variable line intensities" (Blandford and McKee 1982). In essence, RM describes a response of the BLR to continuum variations from the nuclear BH. However, the principle has been used even earlier for studies of other objects. Blandford and McKee (1982) write that using a flash of radiation and its response from the ambient gas has been used as early as 1901 in order to explain the apparent expansion of Nova Persei, also known as GK Persei (Couderc 1939). The first verifiable time that someone analyzed reverberations in emission lines of Seyferts and quasars was done by Bahcall et al. (1972). Assuming a spherical distribution of gas, they calculated the response to the total line intensity. As mentioned before, while the principle of RM has been applied to other objects as well, it frequently refers to measurements of the BLR of an AGN. Additionally, it is often combined with spectroscopic measurements in order to apply Newton's law of gravity and find the mass of the central BH.

A slightly more detailed description of RM is as follows: each AGN shows a continuum spectrum, which is a central source of ionizing radiation that affects its host galaxy. However, the influence is especially concentrated to matter in the vicinity of the dense nuclear source, which is nowadays almost certainly believed, and in some cases even confirmed, to be a SMBH. As a result, emission line spectra from sources, such as quasars

[(11)] This is the so-called no-hair theorem, where other information about matter that formed the BH is metaphorically described as "hair". As this information is unavailable, the BH does not have "hair", leading to the naming of no-hair theorem.

and Seyfert-1 galaxies, are explained as gas from a region around the central source, that is irradiated by the very same source. At this point it is useful to remember the prevailing assumption about the morphology of galaxies hosting an AGN, i. e., especially one of the two major regions where emission lines originate, the BLR. All type-1 AGNs show variations in the optical-UV continuum luminosity, at least when given enough time and "[g]iven longer time, such a statement can also be made about the broad emission lines" (Netzer 2013, p. 158). These continuum variations can also be seen as line variations, which follow the former, e. g., an increase of the continuum luminosity is followed by an increase of almost all broad emission lines. If both variations can be observed, then the given time lag between them is an indicator for the size of the BLR. Some simplifying assumptions for RM are:

1. The light-travel times across the BLR are in the range of days to months.
2. The time scales for response of individual clouds to changes in the ionizing flux are given by the recombination and ionization times. Given the BLR typical density, this is of order 1 hour or less, that is, much shorter than the typical time scale for continuum variations.
3. The BLR structure and kinematics are constant over the duration of the RM experiment.
4. There is a known relationship between the observed UV or optical continuum and the ionizing continuum that is driving the emission-line variations.

(Netzer 2013, p. 158)

Comparison of the light curves for the continuum and emission lines can yield information about the gas & ionization distribution, and kinematics of the gas. The function that describes the mapping from the continuum light curve to that of the emission lines is called transfer function. A pulse of the continuum is evident from a response of the gas. Here, the gas is assumed to be in a distribution that resembles a thin shell. The transfer function then takes the shape of a box, limited by the two times $t_{\mathrm{start}} = 0$ and $t_{\mathrm{end}} = 2R/c$, where R is the radius of the gas distribution and c is the speed of light. Gas within the LOS is assumed to respond instantly, i. e., at $t = 0$, whereas the response of gas at the opposite side is delayed by $2R/c$. This simplified picture can be enhanced by refining the assumptions. As an example, the distribution of the gas can be extended such that an inner and outer radius are defined, R_{in} and R_{out}. The shape of the transfer function changes accordingly, e. g., a thick spherical shell can be represented by combining transfer functions of multiple thin shells. In this example the transfer function shows a decline from R_{in} to R_{out}. The shape of the declining transfer function depends on the respective gas emissivity at each radius (for more information see Netzer 2013, p. 160). Figure 2.4 shows a basic sketch of the idea behind the time delay τ in RM, where the LOS is within the orbital plane. This case enables the largest possible time delay. Then the extra distance d that a signal needs to travel, and the according delay τ, i. e., the

reverberation, is given by

$$\left.\begin{aligned} d = R + \cos(\theta) \cdot R = R \cdot \big(1 + \cos(\theta)\big) \\ c = \tfrac{d}{\tau} \end{aligned}\right\} \tau = \frac{R}{c} \cdot \big(1 + \cos(\theta)\big) \tag{2.1}$$

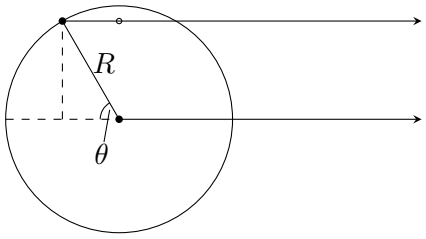

Figure 2.4: Sketch of the reverberation mapping (RM) scheme for the case that the LOS is within the orbital plane. The observer is assumed to be on the right side, which is indicated by the arrowheads. As a large distance between source and observer is assumed, the two shown lines towards the observer are effectively parallel. The three dots indicate the extra distance that signals have to travel in comparison to radiation directly from the central source. The connection between the two filled dots corresponds to the radius of the BLR clouds R. In combination with the hollow dot the additional distance which is parallel to the LOS is also marked.

Nowadays, RM is largely associated with the estimation of nuclear BH masses in galaxies. BH mass estimates from RM are considered to be a baseline for other mass estimation methods. The accuracy of BLR size measurements by their luminosity plays a large part in reaching this status, although the details of the geometry, kinematics, ionization structure, etc. of the BLR are still unknown and their influence on the BH mass estimates is not certain. However, other methods fall short in other ways, as for example the use of stellar kinematics appears promising, but due to limitations by instrumentation only has been applicable to objects inside the Local Group so far (Jiang et al. 2011). Probably the most important use case for stellar kinematics is the SMBH at the Galactic Center, i. e., at the center of the MW (e. g., Eckart and Genzel 1996). Other methods, such as BH mass estimators that use narrow emission lines, might be significantly affected by non-gravitational forces (Ho 1999). Effectively, RM is the only direct measurement of the BH mass, which makes other methods often not as highly regarded as RM. With all this in mind, the only remaining question is why would other BH mass estimation methods be used at all? This is related to a large downside of RM, namely the associated overhead. The continuum from an AGN typically varies in the optical/UV regime on timescales between days and months (Ho 1999). As a result, RM is very time-consuming, as it requires long-term spectroscopic observations, thus being expensive with respect to the usage of resources such as observation time, which is a critical point in astronomy.

2.4.2 Single-Epoch Measurements

In contrast to time-consuming RM there is a possibility to use the virial mass formula, which enables the estimation of BH masses based on single-epoch measurements. Based on the assumption that gas in the BLR obeys the virial theorem, RM is tightly connected to the virial mass (e. g., Peterson and Wandel 1999). This explains why RM is still considered as the baseline for BH mass estimation methods. Nevertheless, observations via single-epoch measurements are far easier to conduct and in turn provide a more appealing approach. As an example, the virial equation is given here for a BH mass M_{BH},

$$M_{\mathrm{BH}} = f \cdot M_{\mathrm{vir}} = f \cdot \frac{V^2 \cdot R_{\mathrm{vir}}}{G}, \tag{2.2}$$

where f is the virial factor, M_{vir} is the virial mass, V is the (circular) velocity at the virial radius R_{vir}, and G is the gravitational constant. If the virial factor f is fixed by certain assumptions (see Sect. 4.2.1), there are two unknown parameters left, the velocity V and the radius R_{vir}. Here, a connection to RM is useful, as BLR sizes are determined via RM measurements and then in turn used to calibrate a relation between the BLR size R_{BLR} and its luminosity, e. g., using L_{5100} (e. g., Kaspi et al. 2005). The radius – luminosity relation is then given in the form of $R_{\mathrm{BLR}} \propto L_{5100}^{\alpha}$, where α is a fitting parameter (e. g., $\alpha = 0.64$, Greene and Ho 2006). A basis for this relation can be found in Dibai (1977), where the author applies simplifying assumptions and finds that the characteristic size depends on two parameters, the electron density and the geometry of the gas. They come to the conclusion that the luminosity per energy relates to the cube of the effective radius, e. g., $L(\mathrm{H}\beta)/E(\mathrm{H}\beta) \approx R^3$ for the Hβ line. An even more simplistic approach is to scale the luminosity with the area of the luminous object, i. e., $L \propto R^2$ (e. g., Netzer and Laor 1993). In either case, the relation effectively takes the shape $R \propto L^{\alpha} \;\Leftrightarrow\; L \propto R^{\alpha'}$, where $\alpha' = 1/\alpha$. Different results have been found for the exact scaling. It is assumed that the function for AGNs that describes the effective ionization parameter might be decreasing with luminosity (Kaspi et al. 2000). To be able to make use of the virial mass formula a second quantity is needed, which is the velocity or, as with the luminosity, another quantity as its substitute. A candidate for this substitution is the FWHM of an emission line from the fast moving region. This FWHM is expected to be proportional to the velocity, $V \propto \mathrm{FWHM}$. With this knowledge the virial mass formula can be rearranged for easier recognition of fitting parameters,

$$M_{\mathrm{BH}} = f \cdot M_{\mathrm{vir}} = f \cdot \frac{V^2 \cdot R_{\mathrm{vir}}}{G} \tag{2.3}$$

$$\Leftrightarrow \qquad \log\left(M_{\mathrm{BH}}\right) = \log\left(\frac{f}{G}\right) + \log\left(V^2\right) + \log\left(R_{\mathrm{vir}}\right). \tag{2.4}$$

The aforementioned correlations between the parameters for substitution are accordingly

$$V \propto \mathrm{FWHM} \tag{2.5}$$

$$\Rightarrow \qquad \log\left(V\right) = \log\left(\mathrm{FWHM}\right) + const. \tag{2.6}$$

for the velocity and

$$L \propto R^{\alpha'} \tag{2.7}$$

$$\Rightarrow \qquad \log(R) = \alpha \log(L) + const. \tag{2.8}$$

for the radius. Inserting these substitutions into Eq. 2.4 yields

$$\log(M_{\mathrm{BH}}) = \log\left(\frac{f}{G}\right) + 2\log(\mathrm{FWHM}) + \alpha \log(L) + const. \tag{2.9}$$

Eq. 2.9 has the form of

$$\log(M_{\mathrm{BH}}) = \log(a) + b\,\log(L) + c\,\log(\mathrm{FWHM}) \tag{2.10}$$

$$\Leftrightarrow \qquad M_{\mathrm{BH}} = aL^b \mathrm{FWHM}^c. \tag{2.11}$$

There are only three parameters left, namely the overall normalization a, the exponent of the luminosity term b, and the exponent of the velocity term c. From the virial theorem a value for c is expected as $c = 2$, whereas b depends on α.

Greene and Ho (2005) find well-defined, empirical correlations between Balmer emission line luminosities and L_{5100}, as well as between the FWHMs of the two Balmer emission lines Hα and Hβ. By combining their findings the authors derive mass estimators that are based solely on properties of either the Hα or the Hβ emission line. Despite stating a clear preference for using the Hα over the Hβ emission line, the authors provide an equation for each case:

$$\frac{M_{\mathrm{BH}}}{\mathrm{M}_\odot} = (2.0^{+0.4}_{-0.3}) \times 10^6 \left(\frac{L_{\mathrm{H}\alpha}}{10^{42}\,\mathrm{ergs\,s^{-1}}}\right)^{0.55\pm0.02} \left(\frac{\mathrm{FWHM}_{\mathrm{H}\alpha}}{10^3\,\mathrm{km\,s^{-1}}}\right)^{2.06\pm0.06} \tag{2.12}$$

$$\frac{M_{\mathrm{BH}}}{\mathrm{M}_\odot} = (3.6 \pm 0.2) \times 10^6 \left(\frac{L_{\mathrm{H}\beta}}{10^{42}\,\mathrm{ergs\,s^{-1}}}\right)^{0.56\pm0.02} \left(\frac{\mathrm{FWHM}_{\mathrm{H}\beta}}{10^3\,\mathrm{km\,s^{-1}}}\right)^{2}. \tag{2.13}$$

Using the properties of a single emission line to get BH mass estimates is hugely advantageous in comparison to RM. The differences with respect to the needed overhead are vast and thus, single-epoch measurements are a powerful and practical tool in the context of AGNs. The principle of single-epoch BH mass estimators is found again in a part of the analysis, in Sect. 4.2.1, where a special use case for NIR spectra is described, including more information on the virial factor (see Sect. 4.2.1).

Chapter 3

Data Sets and Reduction

In this chapter I describe the data sets, which are the basis for this work. The foundation of this topic is the telescope and its instrument that is used to acquire the data. The accordingly used regime of the electromagnetic spectrum is a part of the near-infrared (NIR), and the reason why this can be beneficial is explained as well.

Although the reduction script for the long-slit spectroscopy data set is already a major part of my master thesis, it makes sense to repeat a general description of this script. This is due to a slight rework for general improvements and in order to make it applicable to the additional spectroscopy data set that is added to the set from the master thesis. Imaging data is also added in the scope of this work, which is why the respective reduction process for this data is described as well.

3.1 Telescope and Instrument

This section covers the technical part of the observations, including a description of the telescope, the NTT, as well as the instrument, SOFI, used for data acquisition for this work. Before that, the topic of the NIR regime of the electromagnetic spectrum is covered, as all data in this work is related to the NIR.

Unless there is an indication stating otherwise, the primary sources for the following discussions of the NIR, the NTT, and SOFI are the SOFI user manual (*SOFI User's Manual*), the websites for the NTT and SOFI including some links therein (*The ESO New Technology Telescope (website)*; *SOFI (website)*), and the according publication for the commissioning of SOFI (Moorwood et al. 1998).

3.1.1 The Near-Infrared

The NIR is a part of the infrared (IR), which in turn is a small part of the full electromagnetic spectrum. Electromagnetic radiation in general is usually characterized by either its wavelength λ or its frequency ν, while these quantities are effectively equivalent due to their connection via the speed of light c, where $c = \lambda \cdot \nu$. The energy of electromagnetic radiation scales linearly with the frequency. Radio waves cover a very

large range of wavelengths and reach the largest wavelengths of $> 100\,\mathrm{km}$, i. e., the lowest energies. The other end of the electromagnetic spectrum is populated by gamma radiation, which corresponds to wavelengths of the order of $\sim 1\,\mathrm{pm}$ and thus the highest energies. In between these regimes are – from lower to higher energies – microwaves, IR, visible light, UV, and X-ray.

The NIR covers the shortest wavelengths of the IR, in contrast to the other two parts of the IR, the mid-infrared (MIR) and the far-infrared (FIR). Exact values for the range of NIR wavelengths and frequencies vary in literature, just as for other parts of the electromagnetic spectrum, including the neighboring visible light. As an example, the wavelength range for visible light might be given as $350 - 780\,\mathrm{nm}$, which sets the shortest NIR wavelength accordingly to $0.78\,\mu\mathrm{m}$. However, other limiting wavelengths can be considered just as valid, e. g., $700\,\mathrm{nm} = 0.7\,\mu\mathrm{m}$ as the wavelength parting visible light and the NIR. For the upper wavelength limit of the NIR it makes sense to consider the astronomical context. There is a photometric system in astronomy, which designates letters to different passbands, just 'bands' for short. These letters help in communication, as for example when referring to wavelength ranges of telescope instruments. Depending on whether the L-band is included in the NIR or not, a wavelength of $\sim 4\,\mu\mathrm{m}$ or $\sim 2.5\,\mu\mathrm{m}$ can be considered as the upper wavelength limit of the NIR, respectively. There are three NIR bands which are encountered quite often, the J-band, H-band, and K-band. Yet again, the exact wavelength coverage of each band depends on the literature, and potentially even on variants of each band, such as for example the K_s-band as a slight variation of the K-band. These three aforementioned NIR bands span roughly from $1\,\mu\mathrm{m}$ to $2.5\,\mu\mathrm{m}$, which is relevant for the SOFI instrument later on (see Sect. 3.1.2).

The IR is commonly known from a thermal context, e. g., in heat lamps, medical thermometers, or thermal imaging. This is related to the BB spectrum, which can be expressed by a Planck curve, and accordingly Wien's displacement law. Planck's law is often expressed as the spectral radiance B_ν of a body[(1)],

$$B_\nu(\nu, T) = \frac{2h\nu^3}{c^2} \cdot \frac{1}{\exp\left(h\nu/k_\mathrm{B}T\right) - 1}, \tag{3.1}$$

where ν is the frequency, T the absolute temperature, k_B the Boltzmann constant, h the Planck constant, and c the speed of light. Wien's displacement law describes accordingly either the wavelength or frequency at which the spectral radiance of a BB peaks for a given temperature. However, it was found based on wavelengths and is still most often expressed as follows,

$$\lambda_\mathrm{max} = b/T, \tag{3.2}$$

where b is a constant of dimension $\mathrm{m}\cdot\mathrm{K}$. From this follows directly, that a temperature of about $16.5\,^\circ\mathrm{C} = 289.65\,\mathrm{K}$, which is a typical average temperature at inhabited places on Earth, corresponds to a maximum wavelength of $10\,\mu\mathrm{m}$. Another example of application for the IR is that of a considerable amount of remote controls, e. g., those for television

(1) When expressing the spectral radiance in terms of the wavelength λ instead of the frequency ν, it is important to consider the relation $B_\nu \mathrm{d}\nu = B_\lambda \mathrm{d}\lambda$, i. e., effectively the differential $\frac{\mathrm{d}\lambda}{\mathrm{d}\nu}$, or its inverse, depending on which spectral radiance is calculated.

devices usually operate in the NIR at wavelengths close to visible light. The sensors of many digital cameras are sensitive to these wavelengths, which is why such cameras allow humans to visualize the emission from respective remote controls. Coming back to the astronomical and astrophysical context, a prominent use case for NIR observations is if high extinction in other parts of the electromagnetic spectrum is encountered, which is given for example as soon as observations through dust are involved. A non-specific statement can be made that NIR radiation penetrates dust without much effect, i. e., there is barely interaction between the dust and the radiation. This is specifically true if compared to some other parts of the electromagnetic spectrum, as for example visible light. However, Earth-bound observations in the NIR suffer a much higher and more variable background than in visible light, as the atmosphere shows not only stronger absorption, but there is also telluric emission contributing to the overall noise. Fig. 3.1 shows the amount of atmospheric absorption for a part of the electromagnetic spectrum, including visible light and the IR. Those areas that show a low absorption, i. e., a high transmittance, are called atmospheric windows. Besides those shown in the diagram, there is another important atmospheric window for astronomers in the radio regime.

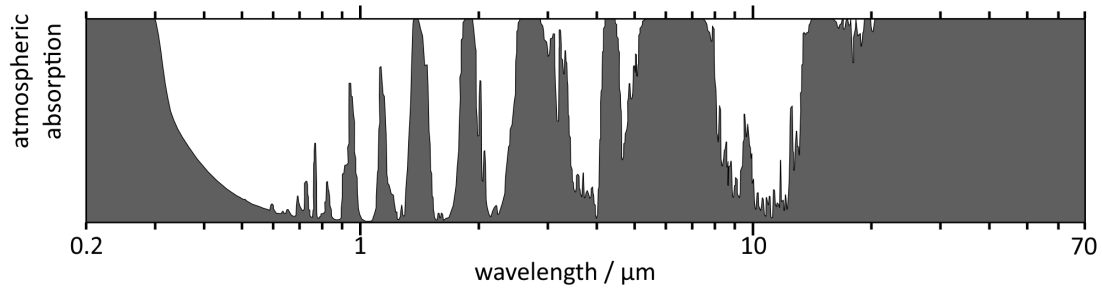

Figure 3.1: Atmospheric absorption between 0.2 and 70 µm. The filled, grey area indicates the amount of absorption at respective wavelengths. Regions of low absorption show a high transmission of respective electromagnetic radiation through the atmosphere. Starting on the left, it is evident that radiation of shorter wavelengths than 0.3 µm is fully absorbed, which corresponds to a part of the UV radiation. Larger wavelengths up to ~ 0.7 µm correspond to visible light, where the atmosphere shows a high transmittance. However, the major part of wavelengths covered here show a part of the IR. For wavelengths between ~ 0.7 µm and slightly larger than 10 µm, there are ranges of different sizes with either very low or high transmittance. This includes the NIR, and its respective passbands. All shown wavelengths larger than that, i. e., the far right of the diagram, are essentially completely absorbed, comparable to the UV on the left. *Credit: Adaptation of a work licensed under (CC0 1.0).*

The diagram shows that not all wavelengths between 1 and 2.5 µm have a high transmittance through the atmosphere. Two molecules are especially prominent with absorption features in this regime, water (H_2O, as vapor in the air) and carbon dioxide (CO_2). Both show variability and depend non-linearly on the airmass, which is a measure for the amount of air in the atmosphere that an observer has to look through for seeing any

object in the sky relative to the amount of air when observing right at the zenith. From the perspective of an observer the background can be split at a wavelength of 2.3 µm into two regions. For wavelengths below 2.3 µm non-thermal emission is dominating. Part of the background is driven by molecular emission lines, such as those from vibrational excitation states of the OH molecule. It is important to note that this emission is highly variable, changing in just a few minutes. Thermal emission dominates at wavelengths above 2.3 µm. Its origin can be the telescope and its components, sky emission, or other sources of thermal emission. According to *SOFI User's Manual*, changes of temperature between summer and winter influence the background of the K_s-band by a factor of 2, which is, however, still more stable than the background of the J-band and H-band, changing within a few minutes. Often there is high atmospheric absorption between bands. The corresponding areas are labeled here as "band gaps". This high absorption is also encountered in the band gaps between the J-band and H-band, and the H-band and K-band/K_s-band.

Previously, dust has been mentioned as a reason to observe in the IR, and dust is arguably the major reason for the amount of telescopes and respective observations in the IR. This is emphasized by Ian S. Glass in their book *Handbook of Infrared Astronomy*, as the author devotes one whole chapter out of just six chapters in total to dust. An example from their introduction of that chapter quantifies the importance of IR observations: An Earth-bound observer of the Galactic Center finds visible light to experience extinction of about 30 mag. This means that out of a number of 10^{12} photons, on average only about a single photon reaches the observer. Switching to the NIR, more specifically the center of the K-band at ~ 2.2 µm, this changes drastically. The extinction decreases to only about 2.5 mag, which corresponds to $\sim 10\,\%$ of all photons reaching the observer (Glass 1999, p. 105). Extinction is largely driven by scattering of radiation on these dust particles, whereas absorption of radiation also contributes, but less so than scattering. However, absorption does impact dust temperature, based on absorption of highly energetic radiation and the subsequent cooling via emission of IR radiation. For a qualitative description of both, absorption and scattering, the relation between wavelength λ of the radiation and particle size d is important. It appears that using a simplified model is successful at describing scattering of radiation by interstellar dust, if these particles are assumed to be spherical, of varying sizes, and show on average dielectric behavior. For the previously mentioned two regimes of the electromagnetic spectrum, visible light and the IR, two cases have to be considered. If the particle sizes and wavelengths are of a comparable order of magnitude, $\lambda \approx d$, the theory of Mie scattering works best for describing the processes, as it includes resonances between the radiation and the particles. This is valid for dust scattering of visible light. In contrast to this, IR wavelengths are larger, and thus $\lambda \gg d$. Another scattering theory works well at describing this case, the Rayleigh scattering theory, which results in an isotropic scattering (Glass 1999, pp. 107 sq.). As the Mie theory is more complete than that for Rayleigh scattering and especially the NIR includes some wavelengths very close to those of visible light, Mie scattering has been used to calculate extinctions of NIR bands.

Additionally, there appears to be a relation between the extinction and polariza-

tion. This might be related to a more realistic assumption concerning the shape of dust particles, that they are actually non-spherical and have a long axis. Considering their dielectric nature and a magnetic field in the interstellar medium, the particles can then align with the field lines. Radiation scattered from those oriented particles is accordingly linearly polarized.

Last but not least, another obvious reason for IR observations is in case that emission or absorption lines within this regime should be identified and analyzed, or the cosmological redshift of distant objects causes such lines from shorter wavelengths to be shifted to wavelengths in the IR.

3.1.2 The New Technology Telescope and Son of ISAAC

The European Organisation for Astronomical Research in the Southern Hemisphere is more commonly known as European Southern Observatory (ESO), and provides a number of observing facilities that are used by many groups of astronomers and astrophysicists. One of those facilities is the La Silla facility, located in northern Chile. This site still features two major ESO telescopes, the 3.6 m telescope and the New Technology Telescope (NTT), of which the latter is important for this work, as all observations were performed using the NTT. Son of ISAAC (SOFI) is an instrument mounted at the NTT. The name implies the existence of another instrument, 'ISAAC'. Both instruments are tightly connected, even though they were made for different telescopes. Infrared Spectrometer And Array Camera (ISAAC) was constructed for the Very Large Telescope (VLT), a telescope at the Paranal facility, while SOFI was constructed for the NTT with the intention to test some implementations of ISAAC before mounting this instrument at the VLT.

While ESO operates two major telescopes at the La Silla facility, the site hosts more telescopes that are not or only partially operated by ESO, such as the 2.2 m Max-Planck telescope, the 1.2 m Swiss Telescope, the 1.5 m Danish Telescope, the ESO 1 m Schmidt telescope, and some more. The facility is located at the southern part of the Atacama desert at an altitude of ~ 2400 m. The choice for this place is purposely remote from inhabited areas, in order to reduce influences that interfere with observations to a minimum. While light pollution is overall an increasing problem in many places of the world, showing impact on flora and fauna, the sensitivity of astronomical facilities magnifies the effect to another level. A night sky that is as dark as possible is an essential necessity to operate instruments as those from the La Silla facility. Additionally, the place is very dry and in combination with the relatively high altitude this minimizes influences as for example from water molecules in the air (see Sect. 3.1.1).

The NTT is built at an altitude of 2375 m and was commissioned in March 1989. ESO describes the telescope as "an Alt-Az, 3.58m Ri[t]chey-Chr[é]tien telescope which pioneered the use of active optics" (ESO 2014). The first important information from this is that the telescope is an alt-azimuth telescope, which means that the mount of the telescope allows for rotation along two axes — one to change the altitude, i. e., a vertical setting, and one to change the azimuth, i. e., a horizontal setting. The second information concerns the size of the primary mirror, quoting a diameter of 3.58 m. This

is an important characteristic that correlates with the sensitivity of a telescope, as a larger area for collecting radiation increases the chance to detect faint objects. Thirdly, the telescope follows the Ritchey-Chrétien design. These types of telescopes have at least two mirrors, a primary and a secondary mirror, which are both hyperbolic. The aim of this design is a reduction of optical errors, such as spherical and comatic aberration[(2)]. Finally, the quote indicates one of two major breakthroughs of the NTT, the introduction of an active optics system. While nowadays state-of-the-art telescopes also feature a similar technological characteristic, adaptive optics, the active optics system of the NTT is claimed to be the first of its kind. Active optics is a standard in big telescopes for over two decades by now, as it is a system that can compensate for deformation effects of a mirror. Reasons for these deformations are manifold, but can mostly be split into thermal influences and mechanical stress. Some possible causes include inhomogeneous temperatures that cause thermal expansion or contraction, wind, or even just gravity. The latter is especially relevant for telescopes with large size mirrors, as these cannot hold their shape for all orientations on their own. In comparison to an adaptive optics system, the deformation corrections from active optics happen on larger timescales of around 1 Hz. Thus, even with these corrections, active optics can only reach image quality of the ambient seeing. Adaptive optics is also a mirror deforming system, but much faster, with more than 100 Hz possible, in order to correct for atmospheric effects. Using adaptive optics can allow for diffraction limited image quality. Both systems rely on actuators that control the respective mirror shape. By using a detector for assessing the image quality, a feedback loop arises due to the combination with the actuator controls. The active optics system of the NTT controls the shape of the primary mirror using 75 actuators with three fixed points. Additional 24 actuators allow for lateral corrections. The secondary mirror can be moved in all three spatial dimensions. Movement in the plane perpendicular to the optical axis of the primary mirror is used to correct for comatic aberration, while movement along the optical axis sets the focus.

As previously hinted at, the NTT marks another important milestone. It was the first telescope with such an enclosure design, being placed in an octagonal housing, which allows for a very compact setup. The height of the dome is only about 18 m, while the diameter is about 17 m. This optimization is considered a large technological advancement. In combination with the overall reduced mass and a relatively light primary mirror, this allows for a rigid structure, which in turn enables more accurate pointing of the telescope. The whole building that contains the telescope is able to rotate, and initially this included the control room where observers resided and controlled the observation procedure. In 2003 the control room was moved to a new building close to the bottom of the ramp that leads to the NTT.

An improved quality of observations can also be reached by optimizing the air flow across the NTT. A ventilation system of the telescope chamber based on flaps has exactly this purpose. To reduce the internal thermal influence from telescope components, many parts have an active cooling system. For the motors of the telescope and hydraulic

[(2)] These are typical errors found in optical systems. If the system is spherical and/or incoming light is not aligned with the optical axis, then optical errors are introduced.

systems there is water cooling, while electronic boxes close to the telescope are insulated and cooled simultaneously.

Between July 1996 and July 1997 the NTT experienced a major upgrade, the so-called "NTT Big Bang". Many parts, including computers, controllers, motors, cameras for auto-guidance, and quality and analysis tools, were replaced and upgraded. Some of these upgrades are linked to identical components of the VLT, as the NTT was used to test some systems and features which were then also applied at the VLT.

In addition to the mentioned primary and secondary mirror of the telescope, there is a tertiary mirror. The main purpose of the third mirror is to switch between the two Nasmyth[3] focus platforms, as the NTT allows for mounting two instruments simultaneously. This means that the only two instruments remaining in operation to this day can take up these spots[4]. These instruments are EFOSC2 (ESO Faint Object Spectrograph and Camera (v.2)) and SOFI, mounted at the Nasmyth B and A focus of the NTT, respectively.

The SOFI instrument was installed at the NTT in December 1997. Just as the previously mentioned related instrument ISAAC, SOFI is essentially a focal reducing instruments with the same capabilities. These cover imaging, spectroscopy, and even polarimetry. Except for the latter, both, imaging and spectroscopy, are relevant for this work.

The intended purposes of SOFI at commissioning encompassed the creation of deep field surveys for galaxies at high redshifts and low mass stars. Fitting the context of this work, spectroscopy of galactic nuclei is also mentioned. Additional spectroscopy includes that of supernovae and other sources, especially those that can be found in the Deep Near-Infrared Survey of the Southern Sky (DENIS).

In the case of imaging, SOFI offers two plate scales, each with a respective mode, the $0.288''$/px Large Field and the $0.273''$/px Spectroscopic Field[5]. The band filters exist as narrow and broad variants, covering wavelengths between 0.9 & 2.5 µm. There is fast imaging and a burst mode available, which corresponds to detector integration times of around only a few tens of milliseconds. In that case hardware windowing is used to significantly reduce the detector array size to the order of a few tens of pixels per side.

Spectroscopy is offered in form of long-slit spectroscopy for two low resolution grisms and a medium resolution grism[6]. The resolving power is given as $R = \lambda/\Delta\lambda \approx 600$ and $R \approx 1500$, respectively, where in both cases more precise resolution estimates depend

[3] Nasmyth is a type of telescope design, where after the primary and secondary mirror follows a tertiary mirror that reflects the collected light to the side of the telescope.

[4] Former instruments, that are decommissioned by now, are SUSI-1 (Superb Seeing Imager/Instrument), SUSI-2 (Superb Seeing Imager/Instrument - 2), EMMI (ESO Multi-Mode Instrument), and IRSPEC (Infrared Spectrometer).

[5] This work follows a standard notation for angles, using $'$ to denote arcminute ($1' = 1/60\,^\circ$) and $''$ for arcsecond ($1'' = 1/60'$). These might also appear in words as their shorter variants "arcmin" and "arcsec", respectively. Additionally, pixel might be shortened as "px".

[6] Grism is the short term for a grating prism, i. e., the two optical components diffraction grating and optical prism, both used for the diffraction of light. A grism combines the optical properties of both components.

on the exact wavelength (see also Tab. 3.1 for more information). In either case, the slit length is $4.92' \approx 290''$ and the slit width can be chosen as 0.6, 1, or $2''$. For the medium resolution mode, spectroscopy is limited to the H-band and K-band, whereas the low resolution mode offers an overall wavelength range of $0.93 - 2.52\,\mu\text{m}$. Only one of the low resolution grisms is important for this work, the 'red' grism (see Tab. 3.1). The given wavelength range of the red grism roughly covers the H-band and K_s-band, as well as the band gap in between those.

Table 3.1: Basic information about the two low resolution grisms, including each wavelength range and resolution for the $0.6''$ slit width. As the resolution scales inversely with the slit width, for example the red grism GRF has a respective resolving power of ~ 590 when using the $1''$ slit and $\lesssim 300$ for the $2''$ slit. *Taken from* SOFI User's Manual*, p. 9.*

Grism Number	Order Sorting Filter	Wavelength Range (μm)	Resolving Power	Dispersion Å/px
Blue	GBF (Grism Blue Filter)	$0.95 - 1.64$	930	6.96
Red	GRF (Grism Red Filter)	$1.53 - 2.52$	980	10.22

Instead of a complete description of the optical layout, here I mention only a few components. SOFI's optical layout is based to a large extent on using wheels. From the point of view of incoming radiation, the first encountered component that is mentioned here is a mask wheel. This wheel includes for example the three slit masks of different widths for long-slit spectroscopy. Two filter wheels contain each different band filters, in total 5 broad band filters and 16 narrow band filters, excluding the two low resolution grisms. More details about the broad band filters related to this work can be found in Tab. 3.2. Additionally, the filter wheels feature a fully open and a fully closed position, and even a few more options. Then follows a grism wheel and finally an objective wheel. The pixel scale depends on the used objective, as for example in imaging mode there are the aforementioned Large Field Objective and the Spectroscopic Objective. As a reminder, the former has a pixel scale of $0.288''$/px, which ultimately results in an according field of view (FOV) of $4.92' \times 4.92'$, and the latter has a pixel scale of $0.273''$/px, and a respective FOV of $4.66' \times 4.66'$.

For the calibration of spectroscopic observations there is a designated calibration unit inside the telescope adaptor. The unit includes different lamps, either with the purpose of flat fielding, which is done by a halogen lamp, or for the calibration of wavelengths based on known emission lines, which works using a xenon and a neon lamp. The xenon and neon lamps are also called arc lamps. Even though both lamps are used for medium resolution spectroscopy, the xenon lamp alone is sufficient for low resolution spectroscopy. In the case of imaging, flat fielding is done using the respective dome flat field lamp.

The heart of any instrument is its detector. In the case of SOFI, this is an IR bolometer of array type Hawaii Hg:Cd:Te (Mercury:Cadmium:Tellurium) in a 1024×1024 format, that is split into four quadrants. Some general array properties can be found in

Table 3.2: Three of the SOFI filters relevant to the imaging observations connected to this work. All shown filters here are broad band filters, as can be seen by their filter widths. The remaining two broad band filters are Z and J_s. There are 16 available narrow band filters, having widths of $0.010 - 0.031\,\mu m$. However, as these are not important in the context of this work, they are not listed here. *Taken from* SOFI User's Manual*, p. 7.*

Filter Name	Central Wavelength [μm]	Filter Width [μm]	Peak Transmission [%]
J	1.247	0.290	n/a
H	1.653	0.297	83
K_s	2.162	0.275	88

Tab. 3.3. A few of these properties have been re-evaluated a few times in the past. The *SOFI (website)* includes a section about detector characteristics, where this evolution can be seen. The readout noise for all four quadrants of the array changed effectively only little between 2005 and 2012, showing a slight tendency towards lower Analog-Digital Unit (ADU) values. A similar situation is given for the gain, that also roughly kept its average value in the same time frame. The non-linearity of the detector even decreased between 2005 and 2010, from $< 1.5\,\%$ between 50 and 10000 ADU to $< 0.5\,\%$ in the same range of ADU. Only the total number of bad pixels increased by a noticeable amount between 2003 and 2012. While this can be expected due to degradation of the detector, the number is also based on the shape of the vignetted detector region. This vignetted area changed since the earlier dates. Additionally, the evaluation of the number of bad pixels is independent of previous assessments and a different choice of limiting accuracy naturally leads to a different number of bad pixels. The total number of bad pixels for 2003 is given as 9666 and for 2012 as 14884, but the previous arguments need to be considered for a meaningful comparison.

In order to avoid external and internal thermal influences, such as those mentioned earlier, the detector is cooled by a cryo-mechanical system. For this purpose, it is positioned in a vacuum tank, that is cooled to a temperature of around $77\,K \approx -196\,°C$ by using a closed-cycle cooler. This low temperature is reached using a circuit of liquid nitrogen, that helps with the initial cooling down from higher temperatures.

There is a possibility for different readout modes of the detector, as each of its pixels can be read out independently and columns are individually reset. In case of SOFI there are two available readout modes:

1. **Double Correlated Read**:
   Following the implication of its name, the voltage is read out two times. The first readout is at the beginning of the integration, the second readout at the end of it. An application scenario is given for a high background, i. e., when the background is the most prominent source of noise, and accordingly short integration times are connected with this readout mode. However, there is a minimum integration time

Table 3.3: Properties of the detector array that is a key component of the SOFI instrument. These detector properties are based on information of the manufacturer, Rockwell Scientific, which has been acquired in 2006 by another company, Teledyne. Some values depend on the context, as for the example the readout noise depends on the applied readout mode. By now the stated numbers are in some cases only rough indications, as these values changed due to degradation or other changes concerning the instruent. *Taken from the* SOFI (website) *(2023-03-26).*

Array Format	Hawaii HgCdTe 1024×1024
Pixel Size	$18.5\,\mu m$
Quantum Efficiency	$\sim 60\,\%$
Gain	$\sim 5.4\,e^-/ADU$
Readout Noise	$\sim 2.1\,ADU$
Bad Pixels	~ 10000
Non-Linearity	$< 1.5\,\%$ over 0 to 10000 ADU
Dark Current	$< 0.1\,e^-/s$

of 1.182 s.

2. **Non-Destructive Read**:
   The procedure of this readout mode follows the principle of Fowler sampling and is only applicable to spectroscopic modes. Here, the voltage is sampled multiple times after a reset, i. e., multiple times during each integration time. A linear fit is made for each pixel using the sampled voltages as a function of time. The slope of the linear fit represents the average photon rate for this pixel, and is then used in combination with the total integration time to find a respective final voltage for this integration. This causes heat from the reading at the array borders, which means the number of samples has be kept under a certain threshold (*here:* 60), on order to avoid the noise from this effect to dominate. An additional measure to reduce the influence of noise is to sample the analogue signal multiple times for each reading. This method creates a larger overhead per integration. Accordingly, it is more advantageous for larger exposure times. The shortest integration time can be calculated by the factor 1.64 times the number of samples per integration.

Overall, the NTT with SOFI cannot compete with bigger, modern telescopes and more sophisticated instruments, that operate at the same wavelengths and offer similar features. Some other instruments and telescopes have already been decommissioned, even though these were younger than the NTT and/or SOFI. However, observation time with a telescope and instrument of a higher or even similar class is incredibly valuable to lots of astronomers and astrophysicists, and as long as both stay operational, the NTT and SOFI will keep on acquiring important data.

3.2 The Sample and Observations

This work treats a sub-sample of a larger, specific kind of object sample, the so-called low-luminosity type-1 quasi-stellar object (LLQSO) sample. Based on knowledge from previous sections, the name of the sample gives a rather clear picture of what it constitutes. Starting at the end, the objects from this samples are considered to be QSOs. Based on the previously presented unified model (see Sect. 2.2.3, Fig. 2.3), these objects are thought to be radio-quiet AGNs that are viewed essentially face-on. Considering the first part of the name of the LLQSO sample as well, i. e., QSOs of low luminosities, it makes sense to see this only as a rough classification. The fact that this sample is expected to consist of type-1 objects underlines the assumed face-on view. However, radio-quiet type-1 objects do not necessarily need to be viewed strictly face-on, as Fig. 2.3 shows that the Seyfert-1 classification could be valid as well. In the context of low-luminosity QSOs this makes even more sense, as Seyferts show rather low luminosities in comparison to almost all other types of AGNs. Thus, it is not surprising that a considerable amount of objects from the LLQSO sample is classified in literature as Seyfert-1 objects.

All objects of the LLQSO sample are chosen from, and are thus a part of, the Hamburg/ESO Survey (HES), or more accurately in this context its flux-limited sample of 415 QSOs and Seyfert-1 galaxies (Wisotzki et al. 2000). The HES covers a large part of the southern hemisphere, in total close to $\sim 10000\,\mathrm{deg}^2$. Observations were done with the ESO Schmidt telescope, which is also known as the ESO 1-metre Schmidt telescope, hosted at the La Silla observatory, just like the NTT. Objective-prism photographs were taken with the ESO Schmidt telescope and then subsequently digitized and analyzed. The HES is a wide-field survey for bright QSOs, which here means that their optical magnitudes are within an interval of $13 \lesssim B_J \lesssim 17.5$ in the B_J passband. The redshifts of these objects are limited to $0 < z < 3.2$. AGNs that satisfy these criteria and that show broad emission lines with FWHM $\geq 1000\,\mathrm{km\,s^{-1}}$ are included in their sample of QSOs. According to the authors, based on the flux and redshift limits, their QSO sample is spectroscopically 99 % complete and well-defined, i. e., it includes all AGNs for the given criteria. The inclusion of low-redshift QSOs is described as particular, since many other surveys discriminate against extended sources.

The LLQSO sample is essentially based on a selection of Bertram et al. (2007). The authors choose all objects from the previously mentioned HES sample after applying a limiting redshift of $z = 0.06$. This choice of a redshift limit should principally ensure that a certain feature can be found in NIR spectroscopic data – the CO band heads, or more specifically the diagnostic CO(2−0) rotation vibrational band head absorption line. However, the characteristic and especially the detectability of this band head absorption line depends on each object and the observation, including aspects like S/N. In case a detection of the line is possible in the K-band, the stellar population of the AGN host can be analyzed. By applying the redshift range of $0 \leq z \leq 0.06$ to the HES sample of QSOs and Seyfert-1 galaxies, a total of 99 objects are considered part of the LLQSO sample. Bertram et al. (2007) call the sample "nearby low-luminosity QSO sample", while arguing

that the objects are not necessarily classified as QSOs. They state that judging by a traditional boundary between QSOs and Seyfert-1 galaxies from literature, which is in their case an absolute magnitude of $M_B \approx -22$ (see also Sect. 2.2.2), their selected sample consists of rather lowly luminous QSOs, showing absolute B_J magnitudes that are larger than -22, i. e., less bright. The label of the sample slowly evolved, via a mention of "low-luminosity type 1 quasi-stellar objects (QSOs)" (König et al. 2012), to "low-luminosity type-1 QSO sample" (Busch et al. 2012), which was then finally abbreviated as the LLQSO sample. This name stuck when a series of papers was published, in which some of the objects of this sample are analyzed (Busch et al. 2014; Busch et al. 2015; Tremou et al. 2015; Busch et al. 2016; Moser et al. 2016). The total number of 99 objects in the LLQSO sample also made it convenient to introduce a two-digit identifier (ID) for each object, which is often much shorter and more practical than the full name of a source according to HES.

This work constitutes the continuation of the analysis of a certain aspect from the paper series, the $M_{\mathrm{BH}} - L_{\mathrm{bulge}}$ relation (see also Sect. 2.3). Including the last paper of the series, Busch et al. (2016) analyze a total of 16 objects from the LLQSO sample with respect to the $M_{\mathrm{BH}} - L_{\mathrm{bulge}}$ relation. Here, I expand this analysis by adding more objects from the LLQSO sample.

Observations for data acquisition took place in 2019. Two different time frames of observations are given, one in February and one in September. These observations are tagged by a respective program identifier (PID). The PID of the observations in February is `0102.B-0114(A)`. While the total time frame of observations for this program is from February 14 to 24, there is a gap of one day at February 20, i. e., two nights, which means the time frames with observations each night are February 14 to 19 and February 21 to 24. This corresponds to a total of 8 nights of observations. For the observations in September the PID is `0103.B-0055(A)`. Overall this program took even longer, from September 7 to 24, but the time frames with observations during each night are different, namely September 7 to 11, September 12 to 13, and September 21 to 24. In total this corresponds again to 8 nights of observations. However, during the nights from September 8 to 9 and from September 22 to 23 the telescope stayed closed, such that only calibration files were taken and no observations of science objects took place, reducing the effective number of observation nights down to 6. Weather conditions also did not allow for all planned observations, such that for example some objects might only have imaging files and no corresponding spectroscopic files. In other cases the observation block (OB), i. e., data acquisition of multiple files that belong together, could not be finished and the respective data sets for some objects are incomplete. Whether an incomplete data set can still be processed in some way, to be able to make meaningful measurements, depends on each situation and has to be decided individually. More information on this can be found in the respective sections about the reduction procedures for imaging and spectroscopy files.

All raw files are accessible in the ESO archive[(7)] for raw data[(8)]. Arguably the easiest

[(7)] `https://archive.eso.org/`

[(8)] `https://archive.eso.org/eso/eso_archive_main.html`

method to find all relevant files is to use each PID in the respective search fields, i. e., `0102.B-0114(A)` for the February observations and `0103.B-0055(A)` for the September observations.

Here, both applied modes of SOFI, i. e., spectroscopy and imaging acquisitions, have the same pixel scale of $0.288''$/px. For imaging the Large Field Objective is used, resulting in a FOV of $4.92' \times 4.92'$. Each object observed in imaging mode is supposed to be covered using the J-band, H-band, and the K_s-band filter (see Tab. 3.2). For spectroscopy the slit mask, which corresponds to a width of $1''$, is applied. Its slit length is fixed as $4.92'$. In combination with the red grism GRF, the resolving power is given as about 600, and the dispersion is 10.22 Å/px (see also Sect. 3.1.2 and Tab. 3.1). The xenon lamp alone is sufficient for acquisition of spectroscopic calibration files.

3.3 Reduction Procedures

The following two sections are descriptions of the reduction procedures for spectroscopic data as well as imaging data. The intended way of reduction is to use software provided by ESO, so-called recipes, which effectively make up a pipeline for data reduction.

In case of the spectroscopic data set, the respective recipe does not work properly – a situation that was already encountered and needed to be overcome when other data from the same telescope and instrument had to be reduced for the paper series about the LLQSO sample (see Sect. 3.2). Accordingly, a script was created in order to reduce the data semi-manually and extract spectra from the reduction output. This turned out to be a boon and a bane, as can be seen in Sect. 3.3.1. In contrast to this, the ESO pipeline does work for the imaging data and the description of this reduction procedure is accordingly shorter.

As is often the case for astronomical data, files are given in the Flexible Image Transport System (FITS) format. This format can store many different other data formats, especially tables and multidimensional image arrays, e. g., even data cubes from integral field spectrographs. Each file consists of at least one Header/Data Unit (HDU), the Primary HDU, which might contain any of the mentioned data formats. An arbitrary amount of HDUs can be appended to each file in form of extensions that follow the format of the Primary HDU. While the name of an HDU implies the existence of both units, only a Header Unit is necessary for each HDU, whereas the additional Data Unit is optional. The Header Unit contains keywords with respective values and potentially also comments. It is analogous, or at least very similar, to Exif (Exchangeable image file format), and stores metadata. In essence, the Data Unit is self-explanatory, as it can store any of the permitted data formats. The FITS files, which are important for this work, can all be displayed as 2-dimensional arrays, i. e., similar to classical photos. For imaging this comparison is not far off, while for spectroscopy it is a bit more complicated. The following sections provide some exemplary visualizations and according explanations.

3.3.1 Long-Slit Spectroscopy

The following describes a reduction script that is a major part of my master thesis. As previously described, the pipeline provided by ESO does not work for the data sets that this work is based on. In particular, the recipe that reduces raw spectroscopy files does not work, while the reduction of calibration files is possible. This is also the case for earlier work on the LLQSO sample using SOFI data, which is why it was possible to recover an incomplete version of a substitute reduction script. Accordingly, the script was modified multiple times. It was essentially rebuilt for the spectroscopy data from February 2019 within the scope of my master thesis. This work includes a smaller modification in order to make the script applicable to the spectroscopy data from September 2019 as well. As a result, the following description of the reduction procedure is similar to the respective description in my master thesis.

The reduction script is written in the high-level programming language PYTHON[(9)], and it makes frequent use of IRAF[(10)] via the PYTHON package PYRAF[(11)]. In order to display FITS files I mainly use SAOIMAGEDS9 (Joye and Mandel 2003), often referred to as DS9 for short, a software written at the Smithsonian Astrophysical Observatory. As DS9 is easily connected to IRAF, occasionally both are used together to work on files.

In this case, an important aspect of the data acquisition of long-slit spectroscopy files is that a nodding pattern is used. An object is observed multiple times during one OB, where the position of the object can be changed for example between different integration times. One integration time can be treated as one raw image, as these images here are created by a single integration. A possible nodding pattern, which is encountered here, is to change the orientation of the telescope only after n integration times at the same position. Then, the telescope is moved, i. e., nodded, between different positions along the slit, while keeping the object within the slit coverage. The positions of the object are typically denoted as A and B, and the combination of observations at both positions is called a cycle. In other words, one cycle might consist of observations with the telescope nodded from A to B (AB), or the other way around, first B and then A (BA). For $n = 3$ images at each position A and B, the respective cycle would be

$$\mathrm{A}_1\,\mathrm{A}_2\,\mathrm{A}_3\,\mathrm{B}_1\,\mathrm{B}_2\,\mathrm{B}_3.$$

In turn, a full OB consists of multiple cycles. The previous nodding position is kept before switching again, as this avoids an unnecessary overhead of readjusting the telescope, i. e., a pattern of AB BA AB BA ..., with an essentially arbitrary amount of cycles. An

(9) Python Software Foundation, `https://www.python.org/`

(10) Image Reduction and Analysis Facility (IRAF) was initially developed by the National Optical Astronomy Observatory (NOAO) and constitutes a software system for reducing and analyzing astronomical data. Maintenance by NOAO ended in 2013. By now it is maintained as community software on the hosting service GitHub, `https://iraf-community.github.io/`.

(11) PYRAF is a command language developed at the Space Telescope Science Institute (STScI), until development and support stopped in 2019. The language is now maintained within the framework of the IRAF community, `https://iraf-community.github.io/pyraf.html`.

example observation pattern for a full OB of 40 images consists of $n = 4$ images at each position, which corresponds to cycles of 8 images, and 5 cycles in total in this exemplary OB.

The reason for using a nodding technique is of practical nature. Sensitive observations, especially those with a scientific aim such as finding accurate flux densities, suffer from external and potentially even internal influences. A description of some environmental influences, as well as sources of noise from the devices themselves, can be found in Sect. 3.1.1 and Sect. 3.1.2. The contribution of radiation from the sky is usually not only non-negligible, but can in fact be easily dominating. Removing sky contribution is an accordingly essential step during data reduction. One possibility to do this is using sky images, i. e., observations of supposedly empty fields in the sky that do not contain any sources. The respective sky contribution can then be accounted for in the images that contain the scientifically interesting target(s), i. e., "science objects". By using the nodding pattern it is possible to circumvent the overhead of acquiring sky images. The FOV that contains a science object usually encompasses large, empty areas. When a nodding pattern is applied, these empty areas are purposely used to serve as substitutes for the sky images. Moving the science object around within the FOV results in different sky areas, potentially in all available directions from the science object. With enough different images, the sky areas can even contain other, nearby sources, as well as bad pixels and other image artifacts, as any impact from these is removed when applying an average. An example for the view of an observer on two of the galaxies covered in this work and potential respective slit positions can be found in Fig. 3.2.

To maximize the impact of a nodding pattern between different positions, such as A and B from before, these positions are not fixed, but allow for a small random offset. It makes sense, and is very close to the actual reality for these observations, to imagine the science object being at position A as the object actually being at an arbitrary, fixed place in one half of the image, while position B corresponds to another arbitrary, fixed place in the other half of the image. Consequently, one cycle corresponds to two offsets, one for position A and one for position B, respectively. After acquisition of a full cycle that contains $2n$ images, i. e., n images at each position with their fixed offsets, the next cycle reuses the offset from the last n images that share the same position, but changes the offset when switching to the other position. An example might make this more clear. The following exemplary pattern $\mathrm{P}^{N}_{n,\,\mathrm{off}i}$ for different positions P is given for $n = 3$ images , two cycles ($N = 2$), and includes offsets marked via indices "off" with a trailing number i that indicates different offsets:

$$\mathrm{A}^{1}_{1,\,\mathrm{off1}}\,\mathrm{A}^{1}_{2,\,\mathrm{off1}}\,\mathrm{A}^{1}_{3,\,\mathrm{off1}}\,\mathrm{B}^{1}_{1,\,\mathrm{off2}}\,\mathrm{B}^{1}_{2,\,\mathrm{off2}}\,\mathrm{B}^{1}_{3,\mathrm{off2}}\;\mathrm{B}^{2}_{1,\,\mathrm{off2}}\,\mathrm{B}^{2}_{2,\,\mathrm{off2}}\,\mathrm{B}^{2}_{3,\,\mathrm{off2}}\,\mathrm{A}^{2}_{1,\,\mathrm{off3}}\,\mathrm{A}^{2}_{2,\,\mathrm{off3}}\,\mathrm{A}^{2}_{3,\,\mathrm{off3}}.$$

The introduced exponent indicates the current cycle to help differentiating between images from different cycles, although these are taken at the same position. In principle the first two offsets "off1" and "off2" can be omitted, such that the positions $\mathrm{A}_{i,\mathrm{off1}}$ and $\mathrm{B}_{i,\mathrm{off2}}$ ($i \in [1, n]$) are treated as the points of reference for the positions A and B, respectively. In that case only subsequent cycles show actual offsets from these reference points. An example for this nodding pattern as it is actually applied can be found in

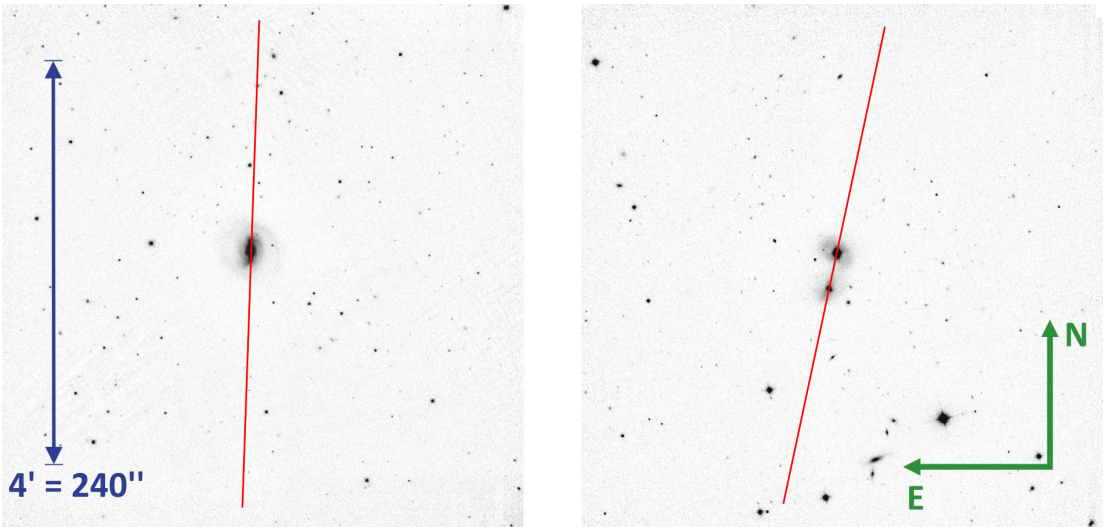

Figure 3.2: 2-dimensional images of two objects, which show the positioning of the slit for long-slit spectroscopy. The slit is indicated by the red line, which is for scale, i. e., the length corresponds to 290″ and its width is $\sim 1''$. Both images show the actual angle of the slit for which these objects have been observed. The slit position on the left shows two reasons for choosing a certain angle of the slit. First, other nearby, extraneous sources are avoided. Second, the slit roughly follows the shape of the galaxy. On the right, the slit is chosen at an angle that purposely includes another nearby source, which is located close, south-southeast to the main target. In order to create the nodding observation pattern, the slit is moved along its long axis. The compass in the lower right and the ruler on the left are valid for both images. More information on these objects can be found in Sect. 4.1. For completeness, their names are still given here: object 64 (HE1108-2813) is on the left, and object 67 (HE1143-1810) is on the right.

Fig. 3.3, which is simultaneously a general example for a 2-dimensional visualization of slit-spectroscopy files, i. e., slit-spectroscopy images.

Previously, indications for problems during observations are described. If problems arise while observing, i. e., during an OB, and the current cycle is subsequently aborted, the intended number of images in an OB might not be reached. As a result, cycles might be fully or partially missing at the end of an OB, potentially also giving rise to an incomplete number of images m at the respective position A or B, where $m < n$. In some cases such problems arose during an observation, which was aborted and then as soon as possible continued, giving rise to incomplete cycles and/or an irregular number of images $m \neq n$ at position A or B during an OB. Such a case might even cause $m > n$, i. e., more images at one position than originally planned. Additionally, the offsets might become irregular, especially in such a case as resuming the observations after an interruption, but also simply because the telescope stops moving at one position instead of following the designated pattern. All raw files were manually examined and the observation pattern accordingly noted, such that as many files as possible can be used in the reduction process, independently of regular or irregular patterns.

Based on this knowledge it is possible to find different approaches at reduction procedures – those that work for complete, regular OBs and those that work around incomplete and/or irregular OBs. An according description can be found at the respective step in the reduction process. The different steps are described in the following.

Step 1 – Rectification: Science & Calibration Images

Although it is not immediately evident from a quick look at the 2-dimensional visualization of slit-spectroscopy images (see Fig. 3.3), these images suffer from a distortion, similar to a photograph taken with a fisheye lens. A schematic visualization can be found in Fig. A.1, which shows the problem in an exaggerated manner. The first step is mainly addressing this problem.

Each first image at position A and B is used for the rectification of all images from the same OB. As an example, if the number of images at one position is $n = 5$, then the first image and the sixth image is used, as these two images correspond to the positions A and B, respectively. These two images are combined two times. For one combined image, pixels below and above certain thresholds are rejected while calculating a weighted average image using the IRAF task `imcombine`. The other combined image is found by the same task, i. e., a weighted average of both images, but without rejecting any values. After this, the combined image with rejected pixels is subtracted from the combined image without rejecting any pixels, resulting in a new image that effectively shows both positions, A and B, of the object. This image can be used to trace these positions, i. e., find their position as well as the curvature, that is expected to exist in the image. The user is expected to help with finding the initial, rough positions of the object by marking these interactively in a diagram. These positions are effectively two values on the x-axis, as the y-axis corresponds to the dispersion axis, and the rectification should follow the y-axis. Based on the initial guesses of the user, another IRAF task automatically re-identifies the object at both positions along the dispersion axis and

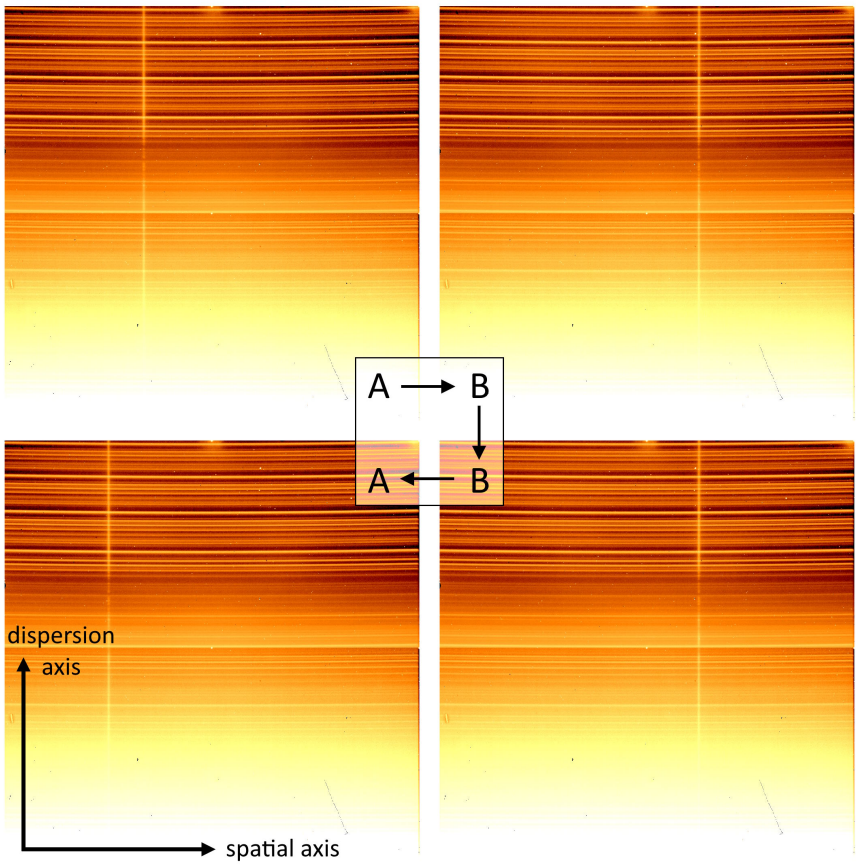

Figure 3.3: Examples for visualizations of raw slit-spectroscopy files via a heat color map. The axes indicator in the lower left is valid for all four images, i. e., the classical x-axis corresponds to the spatial axis, while the y-axis shows the dispersion. Each image spans a total of almost 295″ along its spatial axis, while the wavelengths range from 1.53 to 2.52 µm. Longer wavelengths are at the lower parts of the images, which can be recognized by the increasingly strong contribution of thermal effects. As these images show raw observation files, there are many image artifacts and other unwanted influences. The bright vertical line in each image is the target galaxy, which is here object 29 (HE0253-1641). When viewing the images in a clockwise rotation, starting from the top left, as indicated by the letters and arrows in the middle, the nodding pattern for different offsets can be seen. In reference to the variables from the text, for this object there are $n = 3$ images created at each of the four positions. The top row corresponds to the first cycle, where the left shows position A_{off1}, and the right position B_{off2}. The bottom row shows the second cycle, that starts on the right where the second position, B_{off2}, is kept for the first half of this cycle, i. e., the next three images. The other half of the second cycle is again at position A, but for a different offset, A_{off3}.

notes respective x-values, i. e., the spatial center of the object for each wavelength. An according diagram displays the found x-coordinates along the dispersion axis and the task lets the user assess and, if deemed necessary, tweak or accept the results. These coordinates are the basis for correcting any possible distortion. In form of a coordinate map, they can be applied to and thus transform all images from the OB, which is called rectification here.

Before actually applying the coordinate map and transforming all images, another correction needs to be done, the flat field correction. Even when illuminating the detector with perfectly homogeneous light, the result deviates from a respectively homogeneous image. This can be simply due to different sensitivities for each pixel, but also from other influences during image acquisition. In case of SOFI, a halogen lamp is used to create a flat field (see Sect. 3.1.2). The raw flat field images directly created by SOFI are not the same as the flat field that should be applied to raw files. Here, a pattern for flat fielding is used, where four images are needed to create one final flat field. In two of those images the halogen lamp is switched on, in two of those images it is switched off. While this is in general a good practice, it might even be necessary, in order to account for thermal signals that are especially relevant for wavelengths above 2.3 µm. Then the flat field image accounts for this thermal component and can correct raw images accordingly. However, atmospheric features play only an insignificant role here, as the lamp is relatively close to the detector, and respective corrections for these effects should be found another way.

A part of the full ESO pipeline for reducing raw spectroscopy files from SOFI is a recipe that extracts a 'master' flat field from the aforementioned raw flat field images. This part of the pipeline works as expected, and thus creates according, normalized master flat fields. Coming back to the previous topic, all raw images are divided by the master flat field before the transformation based on the coordinate map takes place. This rectification is also applied to the arc file, i. e., a file taken with a lamp of known emission lines that helps calibrating the wavelengths (see Sect. 3.1.2). Here, this is a xenon lamp that shows distinct emission lines at wavelengths of 1.54226 µm, 1.60577 µm, 1.67327 µm, 1.73305 µm, 1.87932 µm, 2.02678 µm, 2.14759 µm, 2.31996 µm, and 2.48315 µm. An intensity diagram in *SOFI User's Manual*, p. 63 displays the according spectrum, which can be used in combination with the created arc file to detect the positions of multiple emission lines. Using the same principle as before, the user provides an initial guess for these positions and an automated re-identification is executed. Again, the result can be evaluated and potentially adjusted by the user. After performing the respective fit, certain pixels are connected to respective wavelengths. From this, any wavelength can be identified along the dispersion axis, provided it is within the given range of wavelengths. The accuracy of wavelength detection is also limited by the spectral resolution of the instrument, which is 10.22 Å/px for the red grism used here. This correction might also be considered as a rectification.

The final part of this step is to subtract images within one cycle from each other, where one image has the object at position A and the other at position B. This makes use of the previously described advantages of the nodding technique, i. e., removing

sky contribution and other image artifacts. Here, the irregularity of some observations becomes relevant. Based on the previously introduced notation for an image at each position in a cycle, $\mathrm{P}^N_{n,\,\mathrm{off}i}$, it makes sense to show the scheme of an arbitrary cycle N. The offsets can be omitted as these are not relevant within a single cycle. Then the cycle looks like this,

$$\mathrm{A}^N_1\,\mathrm{A}^N_2\,\ldots\,\mathrm{A}^N_n\,\mathrm{B}^N_1\,\mathrm{B}^N_2\,\ldots\,\mathrm{B}^N_m,$$

where in case of an uninterrupted, regular cycle $m = n$. Whether the order of positions is AB or BA does not matter and is interchangeable, effectively just depending on whether N is even or odd. Based in this information, the script is built to allow for two options:

1. For this option, each image k at position A^N_k has a partner image $l = k + n$ at B^N_l and vice versa. These two images are subtracted from each other, such that all $2n$ images from a cycle have a new image, where the object is still at the same position as in the original image, but also a "negative" object from the other position is apparent in this subtraction image. This option is only available in case of complete and regular cycles, as only then each image has one specific partner image that it does not share with any other image. For the previous schematic this can be seen here,

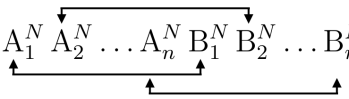

   where $m = n$ as the cycle is regular.

2. This option connects all images at either position A or position B with a single image from the respectively other position, in order to execute the same subtraction as in the former option. Expressed via the previous notation, this means that all images $k \in [1, n]$ at position A^N_k share their partner image, which is image 1 from the second position, B^N_1. Accordingly, all images $l \in [1, m]$ at position B^N_l share the image at position A^N_n as their partner image. The two images A^N_n and B^N_1 are chosen, as these are chronologically closest to the images of the same cycle that are at the respectively other position. Again, for the given schematic this can be seen here,

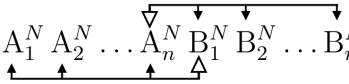

   where it is possible that $n \neq m$. The large, empty arrowhead indicates, which image is used as a partner for the images at the other position. As the number of images at positions A and B does not need to be the same, this option can also be applied to irregular cycles.

The advantage of option 1 is that one single image does not influence multiple other images, and thus its overall impact is smaller. In case the observations did not experience

any problems and all images follow the expectation, this does not matter much. However, it does happen that a single image may randomly show much stronger artifacts than other images. In that case option 1 helps to mitigate the influence. The largest drawback of this option is that it relies on regular cycles, which are not always given. Option 2 on the other hand does work on irregular cycles as well, potentially even cases where there is an arbitrary number of n images at position A, but only a single image at position B. The potential disadvantage of this has just been described, as if that single image at position B has bad quality, it affects all n images at position A.

Here, it turns out that the influence of relying on a single image per position in a cycle does have only a negligible impact. Option 1 is a good measure against unwanted side effects, but option 2 is necessary to use in cases of irregular cycles during an OB. Overall, the given data sets allow for option 2 in all cases. At this point, for all images there is a respective subtraction image, in which the sky-subtracted object is at an unchanged position and a "ghost" is found at the position of the partner image.

Step 2 – Rectification: Standard Star Images

Accurate measurements of quantities like for example flux or flux density are very challenging. This procedure is much easier and thus, more applicable to many situations, when a reference object can be used to gauge these measurements. Another very important point for IR spectroscopy, or here more accurately NIR spectroscopy, is the impact of the atmosphere of Earth, which can change significantly even on timescales of minutes. Although far from perfect, there is a solution which enables both, gauging measurements via a reference object and reducing atmospheric effects in the final spectroscopic image. Standard stars come into play for this, sometimes also called telluric standard stars, as they are used for the correction of telluric contamination.

Due to the fast changes, observations of a standard star are expected to take place right before and right after observing the scientific target. In order to describe the atmosphere as accurately as possible, standard stars are chosen to be close to the actual target. This results in a similar airmass with similar atmospheric conditions as for the target observations. However, these standard star observations can be much shorter than those of the science object and still be sufficient for corrections. In the scope of the observations for this work, there is one cycle before and one after the science observations per standard star. Additionally, each cycle consists in total of two images, i. e., only one image at position A and one at position B. In short, for each OB of a scientific target there are two OBs of the standard star, each consisting of one cycle of $A_1\,B_1$ only. Then the same rectification procedure as described in step 1 is also applied to the standard star images, i. e., all science images are in principle replaced by the standard star images.

Step 3 – Combination: Standard Star Spectra

This step is based on the spectra of the standard stars, which means that these have to be extracted from the files first. In order to extract a spectrum it is necessary to choose a spatial segment around the object of interest and find the object in there. The choice for the size of this segment is tricky. In a best case scenario, the point spread

function (PSF) is known and can be used for that. The PSF is a function that describes how an astronomical point source looks like when being observed with a telescope. It consists mainly of two components. The first component is diffraction, a quantity that is physically inherent for any finite aperture and gives rise to an Airy disk pattern, a concentric pattern of minima and maxima, of which the latter decrease in intensity for larger distances from the center. The second component is aberration, a previously introduced concept of errors in geometrical optics. In a model best case, for example of perfect weather and ideal optics conditions, these types of errors would not exist. Meanwhile, in reality, they do exist, but to a very different extent that depends on the given parameters. Some telescopes use systems that effectively allow them to work at the diffraction limit, given the environment does not interfere too much.

Although it is related to atmospheric effects as well, astronomical seeing is not to be confused with the PSF. Seeing is the effect caused by the atmosphere that perturbs signals from the outside, which affects all Earth-based detectors, especially including telescopes. A perfectly planar wave that passes the atmosphere is subject to perturbations, such that an observer does not register a planar wave anymore. The underlying conditions in the atmosphere typically change on timescales shorter than a second. Albeit not the case for the NTT, some telescopes are equipped with adaptive optics to counter this effect (see Sect. 3.1.2). A measurement of the seeing via a differential image motion monitor (DIMM) is a typical standard for astronomical observations, as is also the case for the data here. In this particular case, the header of each FITS file contains two keywords that describe the measured seeing in arcseconds, once at the start and once at the end of creating the respective file, i. e., image. It appears that in some cases the DIMM might not have worked or other problems were involved, as values are given as '-1.0', which is not a sensible number in the context of seeing. These values are avoided in further steps of reduction and analysis.

This step starts with finding the mean seeing from all seeing measurements for all files involved here, i. e., the standard star images before and after the science target observations. Although not a perfect substitute for the PSF, this measure is used to estimate the spatial scale, i. e., the aperture, for the extraction of a spectrum. This choice is supported by a circumstance that becomes more apparent later on, but for completeness is described here. Most seeing measurements are above $1''$ with some even above $2''$, while the smallest single seeing measurement is $\gtrsim 0.5''$. As the NTT does not have an adaptive optics system, the size of the PSF is impacted by atmospheric conditions, which are in turn estimated by the seeing measurement. After converting the seeing measurement via the pixel scale given here, i. e., $0.288''$/px, and applying a ceiling function for a sensible amount of pixels, even the smallest seeing values result in aperture widths larger than most FWHM measurements from each PSF in imaging data of the same observations. Put differently, the seeing-based aperture size as it is chosen here is expected to be larger than a PSF measurement. For the extraction of standard star spectra the impact of the sky-subtracted background surrounding the source is low. In case of extended sources, such as the host galaxies of the AGNs that are the actual scientific targets here, a respective justification can be found in the description of the

next step (see step 4).

The procedure described here is applied to the two images of the standard star from before and after the scientific target observations. In both subtraction images the expected spatial position, i. e., the x-value, of the standard star is found via an offset value from a respective FITS header keyword. This value follows yet again the principle, that it only constitutes a first estimate of the position. It is used in combination with the fit of a Gaussian profile to find a more accurate position estimate. The Gaussian profile G is fitted based on four parameters, a, b, c, and d, as the intensity along the spatial axis, i. e., the x-axis,

$$G_{a,b,c,d}(x) = \frac{a}{\sqrt{2\pi c^2}} \cdot \exp\left(-\frac{(x-b)^2}{2c^2}\right) + d, \tag{3.3}$$

where the parameter b corresponds to the position of the profile maximum. The intensity values, i. e., the y-values, that are necessary for such a fit are found via taking the median value along the dispersion axis for each pixel along the spatial axis. Based on the fitted position of the standard star it is possible to shift its position to the center of the spatial axis. As the shift from the fitting result to the new position might not be an integer value, an interpolation algorithm takes care of finding respective new values per pixel. While this cuts off a part of the image and adds an artificial area, these parts do not influence any following procedures, provided the object is not very close to one end of the spatial axis before being shifted to the center. This is done for both subtraction images.

From these two new images, in which the standard star is centered, spectra are extracted. The aperture size that defines the spatial extent used for the extraction is based on the seeing, as described previously. The seeing is converted from arcseconds to pixels, multiplied by a factor for manual control of the aperture size, and finally applied to a ceiling function, i. e., rounded up to the closest larger integer. Correlating spectral features with each other can be sensitive with respect to even small misalignments. Thus, the user is shown both spectra that are extracted from the two images in a single diagram, where the dispersion axis, i. e., the previous y-axis, is now the new x-axis. It is then possible to spot a slight misalignment of spectral features and correct for this by providing shifts, possibly again on sub-pixel scales, until both spectra appear aligned. Although it is not necessary yet, as the source object is the same in both spectra, the spectra are normalized for this step. The cumulative shift found by the user is applied to the respective spectrum, that is not normalized, and both spectra are added here. This step is important to note, as it combines the integration times of both images. A conversion of pixels as the spectral x-values to wavelengths is done via the specifics given for the SOFI instrument. These values are also found in the header of the FITS files.

As a reminder, this procedure is applied to each set of two standard star images from before and after the scientific target observations. Hence, there are two spectra, each created by combining two prior spectra. The last part of this step is the combination of these two spectra. Again, they are normalized, shifted as necessary, and added onto each other. This resulting standard star spectrum combines four initial spectra, each

corresponding to an integration time of 10 s. The combined spectrum can be treated accordingly as conforming to an integration time of 40 s.

Step 4 – Extraction: Science Object Spectra

This step is similar to step 3. The goal here is to extract a spectrum for the scientific target, i. e., the AGN, and potentially some more information from off-center spectra.

As a first step, a seeing value is chosen which defines the aperture size for the extraction of spectra. In order to be consistent with respect to calibrations based on the standard star, the same seeing is chosen as previously, i. e., the average seeing that is measured for all standard star acquisitions before and after the target observations. As before, the subtracted images are taken and the position of the object in each image is fitted, based on respective offset values from the headers of the FITS files as an initial guess. Similar to the previous procedure for each spatial pixel, i. e., along the x-axis, the median of the values along the dispersion axis is taken, creating a substitute intensity profile in which the object can be found. Again using Eq. 3.3, a more accurate position of the object is found by the Gaussian fit. This position is being fed into an interpolation algorithm to shift the object from the subtraction images to the center. Accordingly, each raw file has not only a corresponding subtraction image, but also a shifted image in which the target is centered. A difference between this step and the previous step is that there is no extraction of a spectrum for each of those shifted images, but the shifted images are all combined. The combination is done by taking the median, which overall improves the S/N of the output image, based on the number of images that are combined. Effectively, all raw files from the respective OB are merged to create a single image, from which spectra can be extracted.

For the extraction of a spectrum the unit of the dispersion axis is again converted from pixels to wavelengths. The choice of aperture is partially different than for the standard star. A spectrum that is calibrated can only be extracted when using the same aperture as for the standard star. As the standard star is expected to be an unresolved point source, just as the AGN at the center of the galaxy, the aperture size is also the very same. The seeing is converted from arcseconds to pixels, multiplied by the same factor as before, and applied to a ceiling function. Previously, it was discussed why an aperture that is expected to be slightly larger than the PSF should still work for extracting the standard star spectrum. Here, the situation is different, as the AGN is not surrounded by a sky-subtracted background, but its host galaxy. Still, the same aperture size can be assumed to work here as well, because the contribution from light of the host galaxy is expected to be low enough that it is negligible, even when considering an analysis of contaminated emission line fluxes (Kim et al. 2010). As the host galaxy should be spatially extended, it is possible to extract more spectra. In this case an off-center spectrum might be of interest, as it represents a spectrum of the host galaxy of the AGN. The script places two apertures at a manually defined distance to the left and right of the AGN position, and extracts spectra from both apertures. These off-center spectra are averaged and result in an according mean off-center spectrum. It is important to note that the choice of aperture size can be different than the aperture

for the standard star and AGN. While this prevents a meaningful calibration of the flux density levels, the spectrum can in principle still show the course of flux density levels in arbitrary units. An according spectrum thus allows for the identification of emission and absorption lines, at least if the wavelengths are corrected for a respective redshift of each object.

Step 5 – Spectra Alignment: Standard Star & Target
This step is essentially a part of the procedure found in step 2. Previously, the extracted spectra from the different standard star images have been aligned. The same procedure is applied here, but for the combined standard star spectrum and the scientific target spectrum of the AGN. To allow for meaningful redshift corrections of the AGN spectra later on, these are fixed and treated as the basis. A comparison of the spectra is only possible if these are on similar levels. Thus, both are normalized and displayed to the user. By showing visual feedback within a looped process, the user shifts both spectra possibly even on sub-pixel scales, until spectral features are aligned. As these are two different types of objects, not all features are comparable, and according parts of the spectra have to be found, where this is possible. The cumulative shift is then applied via interpolation to the actual, i. e., non-normalized, spectrum of the standard star.

Step 6 – Spectra Alignment: Standard Star & Sun
In this step another spectrum is introduced, that of the Sun. The Sun spectrum, or solar spectrum, is important for the following step, where a more detailed explanation of the reasoning can be found. For this step here it suffices to say that the necessary Sun spectrum, that is converted to match the required resolution of these spectra, is only available for the H-band and K-band. The wavelengths covered by the available spectra are $\sim 1.497 - 1.799\,\mu\text{m}$ and $\sim 1.942 - 2.468\,\mu\text{m}$, leaving a gap between the two bands. A BB curve is approximated and scaled, such that it can be used as a substitute for the Sun spectrum within this gap. The approximation is based on a typical surface temperature of a type G2V star, i. e., the spectral classification of the Sun, which is around 5770 K.

With the solar spectrum and the standard star spectrum from the previous step being available, these two spectra are aligned here, following the same procedure as in step 5. Involved procedures include displaying the normalized spectra, ask the user for shift estimates in form of a feedback loop, and then shifting the Sun spectrum to match the standard star spectrum.

Step 7 – Calibration
Finally, the spectra from all previous steps can be offset against each other. The procedure for standard star corrections follows the method described by Maiolino et al. (1996). The authors argue that a simple division of the spectrum of an object by the spectrum of a standard star is insufficient, and they show an alternative procedure based not only on a standard star, but also the Sun. In order to be able to apply this procedure, the standard stars need to be comparable to the Sun. According to the authors their

suggested procedure works for early GV or late FV stars, as the characteristics of stars with these spectral classifications are close enough to G2V stars. The observations that this work is based on follow the instructions from the publication, e. g., observing the standard star before and after the target observations, and using standard stars of the mentioned spectral classifications. Here, these classifications range from F5V to G5V for the observations in February and from G1V to G3V for the September observations. However, Maiolino et al. (1996) also mention limitations based on "blind" sections in the solar spectrum, i. e., parts of the spectrum where atmospheric effects are too strong to be considered properly. This matches the reality found in step 6. Another influence of the low transmission within the gap between transmission bands can be seen in the extracted spectra, as the noise at respective wavelengths is often dominating the spectrum. This band gap noise cannot be considered completely and its amount and scale depends on the specific conditions during the observations as well as the relative S/N per source. The suggested procedure corrects for the influence of a BB curve within the calibrated spectrum and those lines, that are introduced by the standard star spectrum. The respective equation is shown later in the description of this step.

The spectra as they are present from the previous steps have calibrated wavelengths, which can be accounted for accordingly. Nevertheless, the intensity values are effectively still counts of the detector, except for the solar spectrum, which is scaled to the standard star spectrum. In order to convert the target spectrum to show a more physical quantity, such as a flux density, a calibration is necessary. The other spectra are effectively tools to gauge the target spectrum.

A general calibration principle in astronomy is based on the relation between the absolute magnitude M and the luminosity L of a source of radiation. For a target object the equation that connects its absolute magnitude M_{obj} and its luminosity L_{obj} to the reference values of a known object, M_{ref} and L_{ref}, is given as

$$M_{\mathrm{obj}} = M_{\mathrm{ref}} - 2.5 \log_{10} \left(\frac{L_{\mathrm{obj}}}{L_{\mathrm{ref}}} \right). \tag{3.4}$$

However, these quantities are usually not directly available from observations, such that substitutes have to be used instead. Usually these are the apparent magnitude m and the flux F, or often the flux density f. In that case the equation is

$$m_{\mathrm{obj}} = m_{\mathrm{ref}} - 2.5 \log_{10} \left(\frac{f_{\mathrm{obj}}}{f_{\mathrm{ref}}} \right) \tag{3.5}$$

$$\Leftrightarrow \quad f_{\mathrm{obj}} = f_{\mathrm{ref}} \cdot 10^{-0.4(m_{\mathrm{obj}} - m_{\mathrm{ref}})}. \tag{3.6}$$

In order to apply such an equation here, it is necessary to know the respective values for a reference object and either the target flux density or its apparent magnitude. A typical reference source is the star Vega, as it already has been extensively analyzed and is even used to define the zero point for the apparent magnitude in some photometric systems. Considering that the Two Micron All-Sky Survey (2MASS) is a typical source for literature values of sources in the NIR, which is also the case for this work, it makes sense to base the Vega reference values on the according 2MASS photometric system.

Vega is also used to define the 2MASS zero magnitude (Cohen et al. 1992, 2003). An online tool[(12)] for a conversion between magnitudes and flux densities in different photometric systems provides for the 2MASS zero point magnitude in the K_s-band a flux density of $\sim 4.29 \cdot 10^{-10}\,\mathrm{W\,/\,(m^2 \mu m)}$. It is important to note that this value is valid for the K_s-band and a calibration factor needs to be applied accordingly at the central wavelength of this band, which is at 2.159 µm. The apparent magnitudes of the standard stars in this work are known from the 2MASS catalogue. Their flux densities can be found from applying Eq. 3.6, using $m_{\mathrm{ref}} = 0$ and $f_{\mathrm{ref}} = 4.29 \cdot 10^{-10}\,\mathrm{W\,/\,(m^2 \mu m)}$ in combination with each respective literature magnitude m_{obj}. As a result, the corresponding flux density of the telluric standard star f_{telluric} at the center of the K_s-band can be considered as known at this point.

The solar spectrum might affect the flux density levels when being involved in the calibration, such that a respective scaling needs to be taken care of. For this, the median of ten values around the K_s-band center at 2.159 µm of the Sun spectrum is found and stored in a variable c_{Sun}. Division of the solar spectrum by this factor results in a scaled spectrum, that does not change the values at the calibration point of the K_s-band, as can be seen in the final equation below.

Finally, the spectra need to be weighted according to each detector integration time (DIT). The total DIT that corresponds to the standard star spectrum is given before as 40 s. For almost all AGNs that are part of these observations, the DIT is 150 s for each raw image. As neither the images nor their spectra are added, but combined differently, the DIT of the final image and spectrum from this image corresponds to 150 s as well. Objects with different DITs have to be scaled accordingly.

A combination of all information and spectra from above yields the following equation

$$\text{spec-}f_{\mathrm{target}} = \frac{\text{spec-c}_{\mathrm{target}}}{\mathrm{DIT}_{\mathrm{target}}} \cdot \frac{\mathrm{DIT}_{\mathrm{telluric}}}{\text{spec-c}_{\mathrm{telluric}}} \cdot f_{\mathrm{telluric}} \cdot \frac{\text{spec-c}_{\mathrm{Sun}}}{c_{\mathrm{Sun}}}, \tag{3.7}$$

where spectra given in counts are indicated by 'spec-c' with the subscript denoting the respective object, DIT are the respective integration times in seconds, f_{telluric} is the flux density of the standard star at the wavelength of the calibration point given in $\mathrm{W\,/\,(m^2\ \mu m)}$, c_{Sun} is the number of counts in the solar spectrum at the calibration point, and 'spec-f_{target}' denotes the resulting flux density spectrum in $\mathrm{W\,/\,(m^2\,\mu m)}$. In order to offset the spectra against each other, their wavelength ranges are adjusted to match each other. As described earlier, applying this equation is not sufficient to calibrate the off-center spectrum of the target AGN, as long as its aperture size does not correspond to that of the standard star. However, this is the case for the AGN spectrum itself, such that this spectrum is finally calibrated.

(12) "Magnitude/Flux Density Converter", provided by NASA/IPAC-Caltech (National Aeronautics and Space Administration (NASA); Infrared Processing and Analysis Center (IPAC)) within the scope of the Infrared Science Archive (IRSA), `https://irsa.ipac.caltech.edu/data/SPITZER/docs/dataanalysistools/tools/pet/magtojy/index.html`

3.3.2 Imaging

The Data Unit of imaging FITS files is closer related to photography as it is known from everyday life. Probably the strongest similarity is that both axes, the x- and y-axis, are spatial axes. However, where most cameras create images that imitate human vision by using detectors that gather signals from the whole optical regime – and in some cases even a bit more of the electromagnetic spectrum, as described in Sect. 3.1.1 – astronomical imaging is often purposely constrained to a narrow band of wavelengths. Here, the according band of interest, which is used for the imaging data of this work, is the K_s-band. In case of the SOFI instrument the respective band filter is centered at a wavelength of 2.162 µm, and has a width of 0.275 µm (see also Tab. 3.2). When looking at a visualization of such an image, the according information that is conveyed equals the registered amount of radiation from within the range of that band filter. A possible way to visualize this, is to denote the strongest signals using white and the lowest with black, whereas signals in between are respective shades of gray. Humans usually have a better perception even for small differences when using a color map instead of gray scale. Therefore, a common method is using a heat map, as for example done in Fig. 3.3. Any figures in this section that show FITS files use the same visualization as just described. Nevertheless, other display parameters, such as contrast and scaling, influence the appearance and render qualitative comparisons between the visualizations meaningless. In order to make measurements it is necessary to have access to the FITS files.

Here, the reduction procedure for the imaging data is much more straightforward, at least from the perspective of the user. This is because of the SOFI data reduction pipeline provided by ESO, which in contrast to the spectroscopy files works as expected for the imaging files. Some steps included in this reduction procedure are similar to those for the spectroscopy files. Hence, explanations can be much shorter here.

Although there are more recipes for SOFI files from its imaging mode, whether these can be applied depends on the available files, such as different optional calibration files. Only two recipes are of importance for the observations here. The first recipe is called `sofi_img_domeflat`, the second `sofi_img_jitter`. The name of the recipe `sofi_img_domeflat` includes a keyword, that was already an important aspect in the previous section about reducing spectroscopy data, which is “flat”. Just as before, there are different raw flat field files that correspond to the calibration lamp being switched on or off. A mix of both cases is combined within the given SOFI pipeline recipe, which creates a master flat field image. An example for such a master flat field image and a raw imaging file can be seen in Fig. 3.4.

Prominent features in the master flat field image, which are already apparent in the raw flat field images, are a hard transition between detector halves, which appears like a step between different levels, structures at intermediate scales of $\lesssim 10$ px, and large structures that span hundreds of pixels. Potential reasons for these effects might be the missing removal of a zero level offset, pupil ghosts and moving dust grains, and scattered light, respectively. Simple variations of the pixel sensitivities, i. e., a non-uniform detector efficiency, can be seen as well. An example for these features are the

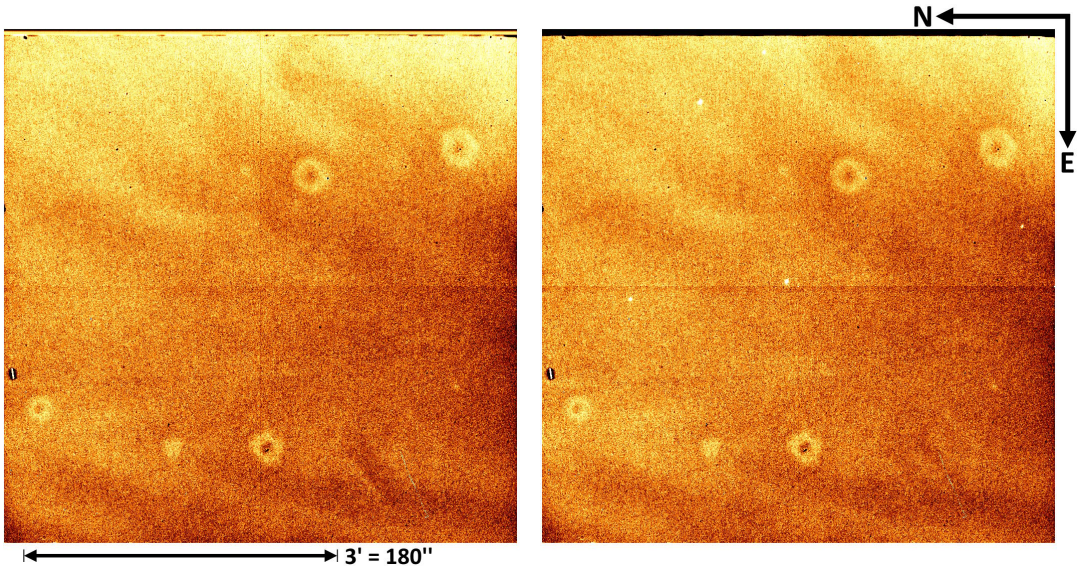

Figure 3.4: On the left is the display of an exemplary master flat field image. It is easily noticeable, that the image does not look uniform at all, even though the illumination that this image is based on is supposed to be as homogeneous as possible. This underlines the importance of the flat field correction, as well as the potentially strong influence of bad pixels and other image artifacts. As in the case of spectroscopy, the deviations come from different effects, as for example different pixel sensitivities. The image on the right displays an example of a raw imaging file, which is the first raw file for object 01 (HE0003-5023). From a first glance it looks remarkably similar to the master flat field image. Only a few bright spots in the raw image on the right indicate the different natures of these two files as they are displayed here. However, it is important to note that their scaling is vastly different, as the pixel values in the flat field image are all around unity (~ 1.0), whereas the values in the case of this raw image span a range of the order of 10^3. The compass and the ruler are valid for both images.

ring-like structures, that are found at different spots in the master flat field and even in raw images. Although it is possible to estimate flat field effects from simple sky observations or possibly even directly from observations of a science target, the *SOFI User's Manual* recommends using dome flats, i. e., creating designated raw flat field images, in order to better account for array sensitivity variations at low frequencies.

The second recipe, `sofi_img_jitter`, is the counterpart to the long procedure for spectroscopy files, described in the previous section. What is the nodding for spectroscopic observations is the jittering for imaging observations. By applying small shifts between successive raw files, a correction for many effects as well as an estimate of the sky background is possible. The recipe can process different input files, where some are optional. As hinted at earlier, the master flat field is one of the optional inputs, as flat field corrections can be estimated from other images as well. However, as the effect from its correction capability is often desired and the designated calibration files are more reliable, it is good practice to use the dome flat images.

One of the effects associated with SOFI observations is the "cross talk" effect. This effect is encountered for bright sources and shows a difference between the upper and lower part of the detector. The whole line in which the source is located, or more realistically all lines, as the object appears likely broader than 1 pixel in the image, are affected from this. Additionally, all lines that are at a distance of half the image size from the lines with the object are affected as well. With an image size of 1024 pixels per side, half of the image size corresponds to 512 pixels. Assuming that a bright object affects the lines $100-110$, then also lines $612-622$ show an impact. This effect is observable in both directions, i. e., the bright object could also be at lines $612-622$ and accordingly affect lines $100-110$. The cross talk effect creates a ghost, which corresponds to the integrated flux of the affected line times a factor of $1.4 \cdot 10^{-5}$. It can only be corrected for, if the source does not saturate the detector. This is an example for an effect, that is corrected for when applying the `sofi_img_jitter` recipe. In fact, the removal of this effect is listed as the first basic step in reducing imaging data.

The second effect mentioned depends on another type of calibration files, the dark frames. These files are not present for the observations here, which is why their role is only mentioned very briefly. Dark frames are essentially detector exposures without any direct illumination, and they consist of different components. One such component is the heat that emerges from the readout amplifiers. However, even an inevitable physical principle contributes to this, which is the random creation of electron/hole-pairs.

A third step is the flat field correction. This is described above, as part of the description of the SOFI pipeline recipe `sofi_img_domeflat`. Thus, it is not repeated here.

The fourth effect consists of bad pixels. These need to be flagged and if possible replaced by sensible values. There is a distinction between four different kinds of bad pixels.

1. **Dead pixels:** These pixels show very low values, corresponding to their name, as if the respective spot of the detector is dead, i. e., unresponsive. In case of SOFI, flat field images are used to find a distribution of all pixel values. This is fitted by

a Gaussian. Dead pixels are those that are 4σ below the mean value.

2. **Hot pixels:** These pixels are essentially the counterpart to dead pixels. Here, the pixel value distribution is taken from dark frames. Again, a Gaussian fit and the mean value are used to mark these bad pixels. However, these pixels have values that are 4σ above the mean value.

3. **Noisy pixels:** Recognizing these pixels is based on the average of the images used for the dead and hot pixels. These correspond to deviations found from the distribution of pixels in the average image.

4. **Frame pixels:** This type of bad pixels is based on masking. For SOFI observations it is possible to use different masks, which show corresponding influences at the edges of their focal planes. Those pixels that are affected by this masking are marked as frame pixels.

The fifth step is about the sky subtraction, which is also introduced in the section about the reduction of spectroscopic data (see Sect. 3.3.1). Each input image of the target is corrected for sky contribution. If these are available, this contribution is estimated from designated sky images. Otherwise, the sky contribution is estimated for each target image and respectively subtracted from it. Similar to the previously described nodding technique for spectroscopy images, the corresponding jittering technique for imaging observations here helps with this estimate. Due to the multitude of shifts, any pixel is expected to not be at the position of a source most of the time. As a result, the average value of a pixel corresponds to its sky value. Outliers are paid attention to via rejection. Depending on the input parameters, and especially when the number of input files is sparse, the sky estimate might be simplified by creating a median image from the input files.

Step 6 is finding a common reference of the input images, that are corrected by application of the previous steps, and stacking these. Again, this reminds of the procedure applied to the spectroscopy files, where the target is centered in order to combine all images. In case of the recipe here, a 2-dimensional cross-correlation function uses initial estimates from the header of the FITS files to find offsets between images with an accuracy of a fraction of a pixel. Images are registered via re-sampling to the previously found sub-pixel offsets. The following alignment is usually based on the first image as a reference. The algorithm that finds the average of the images automatically recognizes and rejects outliers.

The last step of this recipe treats the removal of residual bias variations. These are small steps, or jumps, between pixel values along the columns of an image. A correction of these is done via finding the average value along each row, which results in an averaged image of 1 pixel height. To avert an impact on the levels of the resulting image, the highest and lowest values ($N = 200$) are not considered in the following computation. This 1 pixel image is subtracted from each column of the input image for this step.

An example for one raw image as well as the corresponding final image after applying the `sofi_img_jitter` recipe is shown in Fig. 3.5.

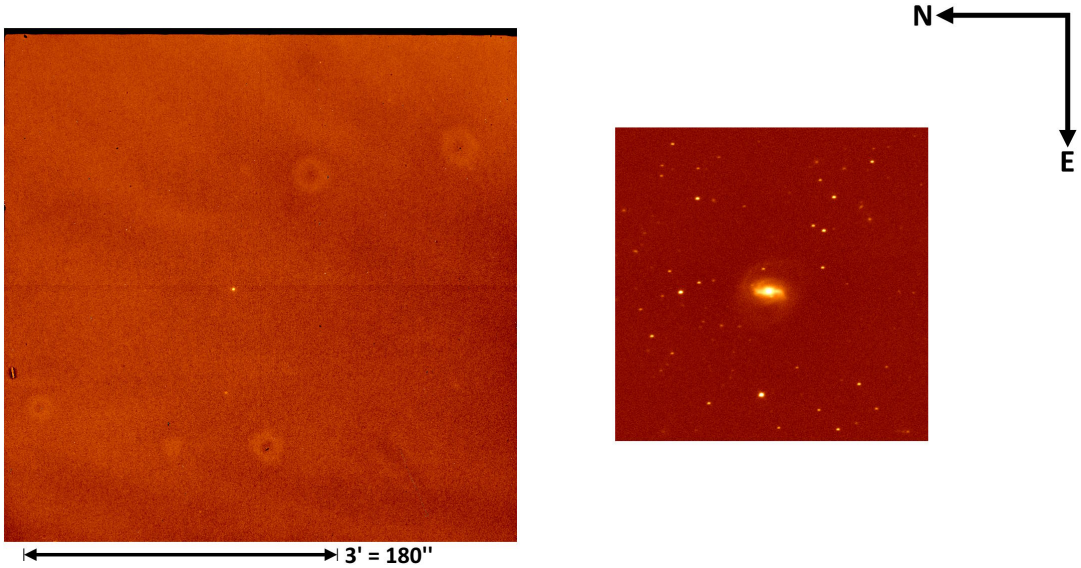

Figure 3.5: Example for a raw image on the left and the according final image after the reduction procedure on the right. In this case, object 64 (HE1108-2813) from K_s-band filter imaging acquisitions during the night from February 23 to 24, there are a total of 20 raw target images that are passed as input to the pipeline recipe. The image shown on the left is the first raw image from that night. If compared with Fig. 3.4, it is evident that a different scaling is used to display these images. Due to this, even the raw image here looks less noisy, although visible effects and artifacts are similar to the previous raw image. The final image on the right is cropped, in order to highlight the target galaxy. The compass and ruler are valid for both images.

Chapter 4

Data Analysis and Results

Although the data reduction is often heavily time consuming, especially in case of problems with the data and/or the reduction pipeline, the actual heart of astrophysical work lies in the analysis of the data. This chapter covers the data, their analysis, and according results.

As described in Chpt. 1, the goal of this work is to enlarge the sample of analyzed LLQSOs with respect to the $M_{\mathrm{BH}} - L_{\mathrm{bulge}}$ relations for inactive galaxies provided by literature. In case of agreement with former results, reasons for the found deviation should be provided, potentially supporting previous explanation scenarios. The BH masses for the objects are found via analysis of the spectroscopy data. If the quality of the spectra is sufficiently well, i. e., not too noisy, emission and/or absorption lines can be identified, providing an insight into potential effects that cause a deviation from the literature. The K_s-band bulge magnitudes are extracted from respective imaging data.

This work assumes a standard ΛCDM cosmology of $\Omega_{\mathrm{m}} = 0.3$ and $\Omega_{\Lambda} = 0.7$, with a Hubble constant of $H_0 = 67.74\,\mathrm{km/(s\,Mpc)}$ (Planck Collaboration et al. 2016, Tab. 4, rightmost column). Oftentimes literature provides $H_0 = 70\,\mathrm{km/(s\,Mpc)}$, including some publications closely related to this work. The small difference does not appear striking and no remarkable effect can be found. In fact, tests that adjust results of this work, such as luminosities and mass estimates, to the latter value of H_0 find relative deviations of about 3 %. Given the context of accuracy here, as is described in the following sections, these small deviations are overall negligible.

4.1 Observational Data Details

This section provides more concrete information about the objects of the LLQSO sample, that are a part of this work. Although the observations partially included a few more objects, not all of the respective files can actually be analyzed here. The reason for this lies in incomplete observations. Both, imaging and spectroscopy of an object, is needed for a complete analysis within the scope of this work. In a few cases, it still makes sense to analyze the spectroscopic data, despite a missing imaging counterpart from the given observations. This is based on the availability of partial results from the previous

work on the LLQSO sample, i. e., the previously mentioned paper series. An additional consideration is the distinctly larger effort for the reduction of the spectroscopy files. Even if the imaging counterpart and a result from a previous analysis is missing, the spectroscopic analysis of already reduced data does not appear meaningless.

Some examples for objects from the LLQSO sample that are part of this work are already mentioned in Chpt. 3. This includes the fact that these sources can all be found within the scope of the HES, and that the complete LLQSO sample contains 99 objects. Accordingly, the two-digit IDs are a practical shorthand reference to objects.

Table 4.1 shows the objects of the LLQSO sample that are a part of this work, i. e., the list is already reduced with respect to incomplete observations of objects that cannot be considered within the given scope here. Tables A.1 and A.2 include more observational information on spectroscopy and imaging, respectively. Furthermore, Tab. 4.2 contains general and observational information about the standard stars that are used to calibrate the spectroscopy data, including each connection with the science targets. Any information about the standard stars that is used in the reduction and analysis, such as spectral classifications and magnitudes, is taken from the "SIMBAD Astronomical Database - CDS (Strasbourg)", or in short "SIMBAD"[(1)] (Wenger et al. 2000). An exception to this is the star S852-C, for which the information is taken from Persson et al. (1998) and Leggett et al. (2006).

Several problems during the observations have an impact on handling the data. As mentioned earlier, some observations were aborted. The observations for a few of those objects have been repeated at a later time or another observation night, while other observations remain at an incomplete stage. Although the reduction procedure for spectroscopy data is written in a way that tries to include as many files as possible, some files still cannot be made use of. The same can be found for imaging data, i. e., incomplete and or faulty files render the use of all files impossible. However, in the case of spectroscopy, even problems relating only indirectly to the galaxy observations can influence the possibility to reduce and thus use files. For example, if an observation of a respective standard star is missing, no calibration can be done. Then a chronologically close observation of another standard star might be used instead, where in that case the calibration procedure is not expected to be as accurate as for a designated standard star.

An example for a fixable problem is given for Hip063985, where the star is centered in both images after the science target observations. Then the subtraction, which is necessary to sky-subtract the images, does not work as intended. In this specific case it is possible to manually shift the object in the two images by a certain offset to the left and to the right, respectively. This is possible as the impact of the artificially created regions at the side of each shifted image is small.

Another example for a problem that can be fixed is wrong meta-data in the file headers that is supposed to indicate the spatial position of the object. For spectroscopy this might manifest as a sudden constant offset between the expected position according to the file header and the actual position of the object (e. g., object 95), or even a changing offset during the same OB (e. g., object 22). In the case of imaging a similar

[(1)] Set of Identifications, Measurements and Bibliography for Astronomical Data (SIMBAD)

Table 4.1: List of objects, their classifications & redshifts, and data availability. Column (1): Object ID with respect to the LLQSO sample. Column (2): Name of each object according to the HES. Column (3): Classification of the activity type of the AGN. Column (4): Redshift of the object. Column (5): Morphological classification of the host galaxy. Column (6) and (7) show which observation in 2019 covered spectroscopy and imaging of each object, respectively.

ID	Name	AGN Class.	Redshift	Morphology Class.	Observation Set Spec.	Imag.
(1)	(2)	(3)	(4)	(5)	(6)	(7)
01	HE0003-5023	Sy1	0.0334	S0 D[2]	Sept.	Sept.
13	HE0108-4743	Sy1	0.0239	E[1]	Sept.	Sept.
20	HE0149-3626	Sy1	0.0335	SAb[1]	Sept.	Sept.
22	HE0203-0031	Sy1.9	0.0424	S0[1,3]	Sept.	Sept.
29	HE0253-1641	Sy1.9	0.0320	—	Sept.	—[a]
53	HE0535-4224	Sy1	0.036	—	Febr.	Febr.
54	HE0608-5606	(NL)Sy1	0.032	—	Febr.	Febr.
58	HE0949-0122	(NL)Sy1	0.0197	E−S0[1,3]	Febr.	Febr.
64	HE1108-2813	Sy1	0.024	SBab[1,3]	Febr.	Febr.
66	HE1136-2304	Sy	0.027	—	Febr.	Febr.
67	HE1143-1810	Sy1.5	0.033	Irr/Sc[1,3]	Febr.	Febr.
70	HE1256-1805	—	0.014	—	Febr.	—[b]
71	HE1310-1051	Sy1	0.034	—	Febr.	—[a]
74	HE1330-1013	Sy1	0.022	SBb/SABc[1,2,3]	Febr.	—[b]
76	HE1346-3003	Sy1.2	0.0161	SA0+/S0-a[1,3]	Febr.	Febr.
77	HE1348-1758	(NL)Sy1	0.0122	(E)[3]	Febr.	—[a]
78	HE1353-1917	Sy1	0.035	Sbc[3]	Febr.	Febr.
89	HE2236-3621	Sy1	0.0600	—	Sept.	—[b]
95	HE2322-3843	Sy1	0.0359	S0/E[1,2,3]	Sept.	Sept.
99	HE2354-3044	Sy1	0.0307	Sb[1]	Sept.	Sept.

[1]: from NASA/IPAC Extragalactic Database (NED); [2]: from SIMBAD; [3]: from Lyon-Meudon Extragalactic Database (LEDA); [a]: Results are available from previous imaging. [b]: Only spectroscopy analysis possible, as neither imaging nor previous results are available.

Table 4.2: Observational and general information on the standard stars that are available for spectroscopy data. Column (1): Name of each standard star. Column (2): Object IDs of the science targets that are calibrated using this standard star. Column (3): Date of observation, i. e., the night in 2019 in which each star was observed. Column (4): Average seeing from the file headers in arcseconds. Column (5): Spectral classification of each standard star. Column (6) and (7): Apparent magnitude in the H-band and K-band, respectively.

Name	ID	Observation Date	Seeing	Class	Magnitude	
					H	K
(1)	(2)	(3)	(4)	(5)	(6)	(7)
Hip001552	01	Sept. 21 – 22	2.35	G3V	6.667	6.568
Hip007121	13	Sept. 21 – 22	1.56	G2V	8.039	8.006
Hip007167	20	Sept. 12 – 13	1.25	G2V	7.606	7.540
Hip010649	29	Sept. 12 – 13	1.67	G3V	7.630	7.530
Hip012951	22	Sept. 21 – 22	2.08	G1V	7.921	7.817
Hip025190	53	Febr. 16 – 17	1.18	G5V	6.841	6.733
Hip031279	54,70	Febr. 17 – 18	0.96	F5V	7.507	7.453
Hip054149	66,77	Febr. 22 – 23	0.78	F6V	6.790	6.706
Hip054804	67	Febr. 16 – 17	0.79	G3V	6.667	6.559
Hip057421	64	Febr. 18 – 19	2.07	G0V	6.396	6.351
Hip063985	78	Febr. 21 – 22	0.69	F8V	7.511	7.411
Hip064670	76	Febr. 21 – 22	0.64	F5V	7.264	7.218
Hip065116	71,74	Febr. 18 – 19	2.07	G5V	6.805	6.747
Hip109444	89	Sept. 07 – 08	1.60	G3V	7.564	7.508
Hip115519	95	Sept. 21 – 22	1.57	G2V	7.045	6.972
Hip117581	99	Sept. 23 – 24	1.36	G2V	7.326	7.283
S852-C	58	Febr. 21 – 22	1.25	G	11.041	10.981

problem of wrong header information can be encountered for objects 20, 64, and 67. However, in contrast to the spatially 1-dimensional nature of the slit-spectroscopy files this affects more header keywords that correspond to the two dimensions.

The information provided in the previously mentioned tables, in particular the total integration time, already considers any lost data that was not recoverable within the scope of this work.

One important aspect about imaging and spectroscopy is related to the resolution of the NTT and SOFI. Data here is effectively seeing limited and dominated, i. e., the diffraction limit of the telescope is lower than the effects based on the seeing. The diffraction-limited angular resolution θ in radians is typically calculated via $\theta \approx 1.22\frac{\lambda}{D}$, where λ is the wavelength and D the physical diameter of the aperture. The latter is usually the size of the primary mirror of a telescope, at least as long as no interferometry is involved. For an exemplary calculation for the NTT it makes sense to choose roughly the upper end of the wavelength range of $\sim 2.5\,\mu\text{m}$, as a larger wavelength results in a larger angular resolution, i. e., a worse resolving power. Then it is $\theta_{\text{NTT}} \approx 0.175''$, which is a considerably smaller angle than the provided seeing measurements. The previously mentioned tables show that the average seeing is measured as $\gtrsim 0.6''$ for the best conditions during observations, and often it is even above $1.0''$. Thus, in case of this data the seeing is dominating the image quality with respect to the spatial resolution.

The spectral resolving power $R = \lambda/\Delta\lambda$ for the given observations with SOFI, as introduced in Sect. 3.1.2, is $R \approx 600$. Another way to express the resolving power is $R = c/\Delta v$, where c is the speed of light and Δv is the smallest distinguishable difference between velocities, as for example coming from the Doppler effect. The basis for this is Doppler broadening in the non-relativistic limit, where the emitted frequency ν_{emit} and the observed frequency ν_{obs} for a radial velocity Δv are related via $\nu_{\text{obs}} = \left(1 + \frac{\Delta v}{c}\right)\nu_{\text{emit}}$. Frequency and wavelength are approximately connected via $\frac{\nu_{\text{obs}}-\nu_{\text{emit}}}{\nu_{\text{emit}}} = \frac{\Delta\nu}{\nu_{\text{emit}}} \approx \frac{\Delta\lambda}{\lambda_{\text{emit}}} = \frac{\lambda_{\text{obs}}-\lambda_{\text{emit}}}{\lambda_{\text{emit}}}$, or expressed more generally, $\frac{\Delta\nu}{\nu} = \frac{\Delta\lambda}{\lambda}$. From this follows directly $\frac{\Delta\lambda}{\lambda} = \frac{\Delta v}{c}$. For SOFI it is $\Delta v \approx 500\,\text{km/s}$, which is an important quantity within the scope of the analysis of emission lines.

4.2 Spectroscopy Data

This whole section deals with the analysis of the spectroscopy data, that is based on the red low-resolution grism, long-slit observations with SOFI. The main purpose of the analysis is to find BH mass estimates of the nuclear SMBHs. A short description of the method to find these estimates precedes the actual application and according results. Before all of this a testing scheme is shown, which treats the reliability of the calibration procedure. At the end of this section follows the description of further line identifications and corresponding possible conclusions.

An analysis of the Paschen-α emission line, and if possible the Brackett-γ emission line as well, is a part of my master thesis. However, in the master thesis this is again restricted to only long-slit spectroscopy observations from February 2019. Additionally, not only the reduction procedure experienced slight changes between the master thesis

and this work, but this also applies to the analysis as well. Some potentially even strong similarities between the descriptions are unavoidable, as the theoretical principle of the analysis did not change. On the other hand, the following directly describes a difference with respect to the previous work.

The reduction procedure from Sect. 3.3.1 includes the possibility to choose a factor that controls the aperture size which is used for the extraction of spectra. As the spectroscopy data effectively features one spatial dimension, the aperture size is accordingly a length or a width. Although not the most accurate term, here, half of the width is called 'radius'. For each object this radius r in pixel is based on the seeing s in arcseconds and the factor a. It is calculated via

$$r = \mathrm{ceil}\,(a \cdot s/0.288) = \lceil a \cdot s/0.288 \rceil, \tag{4.1}$$

where 'ceil' is a ceiling function, also denoted by $\lceil \dots \rceil$, and the factor 0.288 is the given pixel scale for SOFI in arcesconds per pixel. Each spectrum is read for all wavelengths from the spatial center of an object and going the radius r in both possible directions.

The previous work is based on an aperture size factor of 1.5, i. e., $a = 1.5$, which results in an aperture width of ~ 3 times the measured seeing. Following the earlier reasoning as for why the seeing is expected to work as a basis for the extraction of spectra, using a factor of 1.5 results in large aperture widths that are likely to include much more than the galactic nucleus only. Due to the nature of narrow long-slit observations, the impact of the host galaxy in comparison to the AGN is still expected to be low (e. g., Glikman et al. 2006). Nevertheless, I tested more factors that control the aperture size, concentrating especially on the additional factor of 0.5, which results in an aperture width that is a bit larger than the seeing measurement. This aperture size is still expected to include a whole point source, such as a standard star or an AGN, but reduces the impact of other influences, such as the background around a standard star or the host galaxy of an AGN. The sub-pixel shifts during the calibration process to align different spectra likely introduce small differences between each application of the reduction procedure. Consequently, no qualitative measurement of the impact of different aperture sizes is done here, as it requires a statistically relevant number of tests. While the smaller aperture size factor seems to decrease the apparent noise, this result is mainly based on a subjective perception.

I test the robustness of the reduction procedure, with particular emphasis on the calibration procedure, by applying a cross-calibration between some standard stars. Multiple sets of two standard stars are chosen, where each pair of stars is observed during the same night, which is supposed to result in a better comparability. However, observational conditions, like the seeing, can change during the same observation night. Thus, this choice cannot emulate the same conditions as designated standard star observations before and after observing a galaxy target. Tests were done for both mentioned characteristic aperture size factors, i. e., 0.5 and 1.5 (quantity a in Eq. 4.1). Results are expected to be similar for both aperture sizes. The reasons for this are especially the similar classes of different standard stars and that spectra from large apertures include less impacting background sky around the object. In all cases the shapes of the extracted

spectra remind of BB curves, which matches the expectation.

The tests encompass the comparison of literature values for the apparent magnitudes and the respective flux densities with their counterparts from measurements in the reduced files. A conversion between magnitudes and flux densities is done using the same online tool as before (see Sect. 3.3.1). It is again taken care of using the same photometric system as for the literature values, i. e., the 2MASS system. The comparison includes multiple quantities, which are supposed to assess the overall calibration levels as well as find a possible distortion of the shape of the spectrum with respect to different wavelengths. These quantities include the deviations between the expected and measured flux density levels of the continuum at the center of the H-band (1.662 µm) and the K-band (or rather K_s-band, 2.159 µm), the ratio between these two flux density levels, and the respective conversions to magnitudes. For an aperture size factor of 1.5 the largest deviation between an expected and a measured continuum flux density level is found to be $\sim 50\,\%$, while other measures are between $< 10\,\%$ and $\sim 40\,\%$. In contrast to this, a smaller aperture size factor of 0.5 shows the largest deviation at $\sim 40\,\%$, with other values between $< 10\,\%$ and $\sim 30\,\%$. Considering the expected ratios of flux densities at each band center, H/K, this situation is slightly changed. The larger aperture size shows differences from the expectations at $\gtrsim 0-9\,\%$, while for the smaller aperture this is $\sim 2-7\,\%$. Respective magnitudes vary in all cases less than 0.5 from the expectation, in some cases even less than 0.1. Difference values between expectations and results for the $H-K$ magnitudes are all below 0.1.

On the one hand, this still shows that differences of factors up to ~ 2 can occur. While the aforementioned possible changes in observing conditions, in particular the seeing, can be used to attempt an explanation, other factors might still not be accounted for. Closely related to the seeing can be the airmass. For a galaxy the standard star is chosen to be close to the target and thus have a similar airmass. The comparison of different standard stars here does not take this into account. On the other hand, the overall results of the cross-calibration tests show that in most cases the procedure is stable. Not only do the levels of the resulting spectra often match the expectation within reasonable limits, the general shape of the spectrum appears to be unimpaired, as shown by the small deviations of the $H-K$ values. Hence, the reduction and calibration procedure is assumed to work as intended.

4.2.1 Black Hole Mass Estimates

Single-Epoch Mass Estimator in the Near-Infrared

As described in Sect. 2.4.2, it is possible to estimate BH masses from single-epoch measurements. The described and largely accepted method relies on spectral features in the optical/UV regime of which the spectral diagnostics are well established. As the data in this work is based on the NIR regime, a connection has to be made between these different parts of the electromagnetic spectrum before being able to apply single-epoch BH mass estimation methods to NIR data. In a publication by Kim et al. (2010) exactly this was done.

The work of the authors is based on a sample of 37 unobscured type-1 AGNs, of which the central SMBH masses, M_{BH}, are known either via the reverberation mapping method (see Sect. 2.4.1) or the single-epoch measurement method using Balmer lines (Hα, Hβ, etc., Greene and Ho 2005) and potentially the 5100 Å continuum luminosity (Kaspi et al. 2000). Kim et al. (2010) use this sample in order to derive mass estimators based on the velocity widths and luminosities of the NIR hydrogen emission lines Paschen-α (Pα, HI(4-3), $\lambda = 1.87561\,\mu$m) and Paschen-β (Pβ, HI(5-3), $\lambda = 1.28216\,\mu$m). A part of the authors' motivation is that the NIR is considered especially useful, as the AGN population is estimated to consist of more than 50 % so-called red or dusty AGNs, and NIR radiation can be used to look through dust with a very low suppression (see also Sect. 3.1.1). This fact combined with a given luminosity L of either the continuum or an emission line, for which it is $M_{\mathrm{BH}} \propto L^{0.5}$, the according BH mass uncertainties are only about "a factor of 2 or less, even without correcting for the dust extinction with the Paschen decrement" (Kim et al. 2010). In contrast to the optical lines, this is a much smaller impact from extinction.

The authors assume the virial factor f to be 5.5 (see Sect. 4.2.1 for a respective discussion). They adjust literature BH mass estimates to this value of the factor in case another one was used. A basis for their work is the assumption that the line profile shapes of Paschen lines follow those of Balmer lines. Their single component Gaussian fits and double component fits agree in most cases.

In the context of emission line analysis, especially considering hydrogen recombination lines, contamination of respective lines by the host galaxy has to be considered. Kim et al. (2010) find only a negligible contamination of respective measurements. While they state that a contamination of the line flux from the host galaxy is possible, a narrow slit from slit-spectroscopy observations results in very low contributions of less than 8 %.

As part of their analysis, the authors investigate the correlation of properties between Paschen and Balmer lines. Based on the supposedly shared origin, Kim et al. (2010) use a difference between the FWHM values of the Pα and the Pβ emission lines by more than a factor of 1.5 as a sign that at least one of them is erroneous. The authors derive equations that relate the properties of Balmer and Paschen lines, with their findings suggesting that the broad lines for both emission line types originate from similar regions in the BLR. The broad Balmer lines are expected to be from a more central region of the BLR than the broad Paschen lines. This is important with respect to the widths of these emission lines, as material that is more distant from the center can be expected to have lower velocities. Hence, the broad Paschen lines are on average narrower than the broad Balmer lines.

Following the description from Sect. 2.4.2, the authors find that the luminosity of a Paschen line is closely connected to the radius of the BLR, i. e., they measure the size of a BLR via $L_{\mathrm{P}\alpha}$ and $L_{\mathrm{P}\beta}$. Additionally, the FWHM of the respective Paschen line describes the velocity term. As a result, their mass estimators are based on Paschen line properties only. Within the scope of their work they cover a mass range of $10^{6.4} - 10^{9.5}\,\mathrm{M}_{\odot}$.

The aforementioned fitting parameters from Eq. 2.10 and 2.11, a, b, and c, are fitted by the authors for three different assumptions. As a reminder, a is the overall

normalization, b the exponent of the luminosity/BLR size term, and c the exponent of the FWHM/velocity term. Their different assumptions are described here:

1. The authors use the equation provided by Greene and Ho (2007a) for optical emission lines, which is a slightly altered version of the same authors previous finding (Greene and Ho (2005), see Sect. 2.4.2). The Balmer line properties are replaced by the line luminosities and FWHMs of the respective Paschen lines, derived from relations they found between Hα and the Paschen lines.

2. The exponent of the velocity term c is fixed to a value of 2, as this is expected from the virial relation, while setting a and b as free parameters.

3. All three coefficients a, b, and c are treated as free parameters.

Kim et al. (2010) argue that the scatter in the M_{BH} estimates is intrinsic, for example from the uncertainty that arises from input mass values, rather than being dominated by measurement errors concerning the FWHM and line luminosity measurements. They compare the three methods for determining M_{BH} based on their different assumptions and find the smallest scatter for the method based on the third assumption. However, that method is missing a physical explanation for the FWHM exponent. Therefore, the authors prefer method 2, as it can be justified on a physical basis. For completeness the resulting BH mass formulae for all 3 methods are shown here. Method 1, which is based on the equation given by Greene and Ho (2007a), gives the following two equations for the Paschen lines, Pα and Pβ:

$$\frac{M_{\mathrm{BH}}}{\mathrm{M}_\odot} = 10^{7.29\pm0.10} \left(\frac{L_{\mathrm{P}\alpha}}{10^{42}\,\mathrm{erg\,s^{-1}}}\right)^{0.43\pm0.03} \left(\frac{\mathrm{FWHM_{P}}\alpha}{10^{3}\,\mathrm{km\,s^{-1}}}\right)^{1.92\pm0.18} \tag{4.2}$$

$$\frac{M_{\mathrm{BH}}}{\mathrm{M}_\odot} = 10^{7.33\pm0.10} \left(\frac{L_{\mathrm{P}\beta}}{10^{42}\,\mathrm{erg\,s^{-1}}}\right)^{0.45\pm0.03} \left(\frac{\mathrm{FWHM_{P}}\beta}{10^{3}\,\mathrm{km\,s^{-1}}}\right)^{1.69\pm0.16} \tag{4.3}$$

For method 2, where the exponent of the velocity term is fixed to a value of 2, the two equations are:

$$\frac{M_{\mathrm{BH}}}{\mathrm{M}_\odot} = 10^{7.16\pm0.04} \left(\frac{L_{\mathrm{P}\alpha}}{10^{42}\,\mathrm{erg\,s^{-1}}}\right)^{0.49\pm0.06} \left(\frac{\mathrm{FWHM_{P}}\alpha}{10^{3}\,\mathrm{km\,s^{-1}}}\right)^{2} \tag{4.4}$$

$$\frac{M_{\mathrm{BH}}}{\mathrm{M}_\odot} = 10^{7.13\pm0.02} \left(\frac{L_{\mathrm{P}\beta}}{10^{42}\,\mathrm{erg\,s^{-1}}}\right)^{0.48\pm0.03} \left(\frac{\mathrm{FWHM_{P}}\beta}{10^{3}\,\mathrm{km\,s^{-1}}}\right)^{2} \tag{4.5}$$

Method 3 leaves all parameters as free parameters and results in these two equations:

$$\frac{M_{\mathrm{BH}}}{\mathrm{M}_\odot} = 10^{7.31} \left(\frac{L_{\mathrm{P}\alpha}}{10^{42}\,\mathrm{erg\,s^{-1}}}\right)^{0.48\pm0.03} \left(\frac{\mathrm{FWHM_{P}}\alpha}{10^{3}\,\mathrm{km\,s^{-1}}}\right)^{1.68\pm0.12} \tag{4.6}$$

$$\frac{M_{\mathrm{BH}}}{\mathrm{M}_\odot} = 10^{7.40} \left(\frac{L_{\mathrm{P}\beta}}{10^{42}\,\mathrm{erg\,s^{-1}}}\right)^{0.46\pm0.02} \left(\frac{\mathrm{FWHM_{P}}\beta}{10^{3}\,\mathrm{km\,s^{-1}}}\right)^{1.41\pm0.09} \tag{4.7}$$

Each denominator of the luminosity term can also be expressed in watts instead of $\mathrm{erg\,s^{-1}}$ as it is $1\,\mathrm{erg} = 10^{-7}\,\mathrm{J}$, i. e., $10^{42}\,\mathrm{erg\,s^{-1}} = 10^{35}\,\mathrm{W}$.

Virial Factor

The virial factor f is introduced in Eq. 2.2 for calculating a BH mass via the virial mass approach. It is the factor that connects the virial mass M_{vir} and the BH mass M_{BH}. While the details of what exactly the factor includes vary in literature, it is often described as factoring in the general morphology of the BLR by describing its kinematics, geometry, and inclination.

There have been different attempts at theoretical predictions for this factor. In practice it is often set by using the correlation between the BH mass and the stellar velocity dispersion of the bulge component of the host galaxy, the $M_{\mathrm{BH}} - \sigma_*$ relation (see Sect. 2.3). Here, the virial factor f is assumed to be 5.5, which follows the description for the mass estimator by Kim et al. (2010), i. e., the adopted mass estimator in this work (see Sect. 4.2.1). However, this choice for the virial factor of $f = 5.5$ is not trivial, especially considering the two publications that Kim et al. (2010) refer to, namely Onken et al. (2004) and Woo et al. (2010).

According to Onken et al. (2004), earlier works typically express the velocity V from the virial mass formula (Eq. 2.2) via the FWHM of an emission line. In contrast to this, Peterson et al. (2004) find their virial products to be more consistent when using the line dispersion σ_{line} instead, i. e., the second moment of the line profile. In order to differentiate between using the line FWHM V_{FWHM} and the line dispersion σ_{line}, Onken et al. (2004) use two different factors as the virial factor, ϵ (for V_{FWHM}) and f (for σ_{line}), i. e., $M_{\mathrm{BH}} \propto \epsilon \cdot V_{\mathrm{FWHM}}^2 = f \cdot \sigma_{\mathrm{line}}^2$. While the ratio $V_{\mathrm{FWHM}}/\sigma_{\mathrm{line}}$ is generally expected to cover a range of values, Onken et al. (2004) follow a typical assumption and set the relation to $\sigma_{\mathrm{line}} = V_{\mathrm{FWHM}}/2$. As the velocity appears squared in the virial mass formula, a conversion between the virial factors f and ϵ works via a factor of 4, i. e., here $\epsilon \cdot V_{\mathrm{FWHM}}^2 = f \cdot \sigma_{\mathrm{line}}^2 \;\Leftrightarrow\; f = 4 \cdot \epsilon$.

During most of the earlier stages of using the virial mass approach for BH mass estimates, a very common and arguably one of the most simplistic models for the BLR is a spherical, isotropic velocity field, which yields $\epsilon = 3/4$, i. e., $f = 3$. However, other models change the virial factor based on their underlying assumptions. As the BLR parameters, such as morphology and kinematics, are still unknown, there is currently no way to predict the virial factor from first principles (e. g., Woo et al. 2010). Consequently, fitting the virial factor to samples with known BH masses is still the favored approach. Onken et al. (2004) find their best average scaling factor to be $\langle f \rangle = 5.5$ when applied to virial products that use the dispersion σ_{line}, and accordingly $\langle \epsilon \rangle = 1.4$ when using FWHM measurements instead. It appears that this was mixed up by Kim et al. (2010) as they use the FWHMs of their emission lines *and* a virial scaling factor $f = 5.5$, although the virial factor should be the ϵ from earlier instead, i. e., then $f_{\text{Kim et al.}} = 1.4$. That Kim et al. (2010) might erroneously refer to the virial factor is emphasized by another of their references, Woo et al. (2010), where the authors also refer to Onken et al. (2004) and furthermore emphasize that the virial factor of 5.5 is only valid when used in combination with the line dispersion, σ_{line}. Woo et al. (2010) describe this result as incompatible with the simplistic spherical BLR, which has been described before ($\epsilon = 3/4$, $f = 3$).

In spite of all these findings I keep using the factor of 5.5 in this work for multiple reasons:

1. Despite the explicit indications to differentiate between the usage of V_{FWHM} and σ_{line} in the publications of Onken et al. (2004) and Woo et al. (2010), Kim et al. (2010) apparently overlooked this. The authors even re-scaled previous results they reference to reflect their choice of a factor of 5.5. Still, there might be an oversight on my part. For example, their fitting methods might correct for any deviation caused by the different choice of virial factors. The results are then effectively correct, at least considering their data set of BH masses, which comes from widely used and accepted publications.

2. Busch et al. (2016) use the same mass estimator and find a well agreement between their analyzed objects and other mass estimation methods, e. g., using optical/UV spectra in combination with a different virial factor. This strengthens the previous assumption, that the fitting procedure by Kim et al. (2010) might remove, or at least mitigate, potential differences in virial factors.

3. According to Collin et al. (2006) a smaller virial factor has to be used for AGNs with larger V_{FWHM}, which means in turn that smaller V_{FWHM} correspond to larger values of the virial factor, whereas no such change of the virial factor is required if the line dispersion σ_{line} is used instead. This is connected to the previously mentioned ratio $V_{\mathrm{FWHM}}/\sigma_{\mathrm{line}}$ not being fixed, but actually covering a range. Most of my objects show relatively small broad line widths, i. e., $V_{\mathrm{FWHM}} \lesssim 2000\,\mathrm{km/s^{-1}}$, which then implies the use of a rather large virial factor.

4. As a correction for using another virial factor is effectively a conversion between two fixed virial factors, the deviation is also fixed to a respective factor. Here, this is $\Delta \log M_{\mathrm{BH}} = 0.6$, and an according adjustment of the mass estimates is straightforward. Even if the choice of virial factor by Kim et al. (2010) turns out be an actual error, the BH mass estimates can not only be easily adjusted, but they are currently higher than they should be. This is important in the context of an argument that is used later on in the analysis in this work, which implies potentially undermassive BHs. When I switch to a smaller virial factor the BH mass estimates decrease accordingly. Using the larger factor and still being able to find the same result is a stronger argument for the point that is made later on.

The mass difference that is given for exchanging the virial factors ϵ and f, i. e., $\Delta \log M_{\mathrm{BH}} = 0.6$, is roughly the same as the uncertainty for BH mass estimates from single-epoch measurements ($\sim 0.5\,\mathrm{dex}$), not including potential systematic errors yet (Woo et al. 2010). Given the additional transition from largely accepted single-epoch measurements in the optical/UV to the NIR regime, uncertainties are expected to be at least around the same, if not even higher. To put this differently, the mass estimates are only rough estimates of the order of magnitude and much less exact measurements, such that the order of magnitude of the virial factor is currently more important than its exact value.

Hydrogen Emission Line Fitting

The mass estimator described in Sect. 4.2.1 can be used in accordance with the data of this work to estimate BH masses. Special emphasis lies on the method that is based on the second assumption. Not only do the authors of the mass estimator argue themselves that this method is favored (Kim et al. 2010), but it has also been applied successfully in the previous work about the LLQSO sample (Busch et al. 2016). As the Pβ emission line is located in the J-band at a wavelength of $\lambda_{\mathrm{P}\beta} = 1.28216\,\mu\mathrm{m}$, it is not included in the spectra that are available for this work. Consequently, following the given mass estimator, only the Pα line can be used here.

The emission line is expected to be found at a wavelength of $\lambda_{\mathrm{P}\alpha} = 1.87561\,\mu\mathrm{m}$ in the spectra, if these are corrected for their respective redshift. A critical point is the transmission of the atmosphere in the band gap between the H-band and the K-band (see Sect. 3.1.1 and 3.3.1). In the case of SOFI, variations can be expected to be especially strong for wavelengths between about $1.8\,\mu\mathrm{m}$ and $2.0\,\mu\mathrm{m}$ (see *SOFI User's Manual*, pp. 8–9). Thus, a higher redshift of an object shifts the Pα emission line in the observed spectra from within the noisy region in the band gap towards the outer parts, where the noise is less dominating. However, the redshift alone is not the only one indicator for the detectability of the Pα line, as the noise levels may vary due to different reasons. Weather conditions and the comparability of observing conditions for the galaxy target and its corresponding standard star influence the amount of noise that remains in the extracted spectrum. This can be seen in Fig. A.2, which features example spectra for four cases:

1. The noise in the band gap is dominating and the Pα line is not easily apparent.
2. The band gap noise is strong, but the Pα feature is still recognizable.
3. The noise in the band gap is only slightly larger than the noise found in the whole continuum. Despite this, the Pα line cannot be found easily.
4. The band gap noise is slightly larger than noise in the rest of the spectrum, while the Pα emission line is the dominating feature in the spectra and thus very distinct.

These examples highlight the noise within the band gap as a potential problem when analyzing the Pα emission line. If the Pα line is drowning in noise and cannot be analyzed properly, a respective BH mass estimate is harder to find. One potentially helpful factor is that the mass estimator depends only on the broad component of the emission line. This line component might be visible despite some overlaying noise, if the noise manifests as rather narrow spikes. In such a case, the noise does influence the emission line, but its overall shape might be recognizable. For broad and stronger noise, the impact on the Pα line can still be overwhelming and render a sensible BH mass estimate impossible.

However, there is a possibility to circumvent the noise in the band gap by using another hydrogen recombination line, the Brackett-γ emission line (Brγ, HI$(7-4)$) at a rest wavelength of $\lambda_{\mathrm{Br}\gamma} = 2.16612\,\mu\mathrm{m}$. Although there is no mass estimator for this

emission line, under certain circumstances a fixed ratio between this line and the Pα line can be assumed. Following Osterbrock and Ferland (2006), based on a case B recombination scenario, and a low electron density limit with a typical temperature of $T \approx 10\,000\,\mathrm{K}$, the ratio is given as Pα/Brγ= 12.5. This is also used by Busch et al. (2016). However, this line ratio introduces a new problem. The Brγ emission line is much weaker than the Pα line. If the Pα line is barely or not detectable, it is improbable that the Brγ line can be detected instead. This is also illustrated in Fig. A.2. With a rest wavelength of 2.16612 µm, all redshifts between ~ 0.16 and ~ 0.6 place the observed Brγ emission line between 2.2 and 2.3 µm. This range of redshifts matches the objects from the LLQSO sample very well, and Fig. A.2 shows that an emission feature can be seen for some objects in the mentioned wavelength range, especially if the Pα line is already very strong, e. g., for objects 01, 29, and 67.

As a result, I tried fitting both recombination lines, the Pα and the Brγ emission line. The ideal case is to find two components for each emission line, a narrow and a broad component. This is based on the assumption that all objects from the LLQSO sample are expected to be type-1 AGNs, that show narrow and broad emission lines. However, the low spectral resolution of SOFI when applying the red grism ($\Delta v \approx 500\,\mathrm{km\,s^{-1}}$, see Sect. 4.1) might result in non-resolved narrow lines, especially if their width is below the instrument resolution and/or they show only low fluxes.

The BH mass estimator relies on a fit of the broad emission line only, where the quantities, that are necessary to be applied to the chosen BH mass estimator from Sect. 4.2.1, are the line luminosity and its FWHM. An unresolved narrow line might influence the broad component, especially for relatively narrow line widths of broad emission lines, e. g., $\lesssim 1500\,\mathrm{km\,s^{-1}}$. Such a broad line might appear boosted to higher levels around its center by an overlapping, unresolved, and thus potentially indistinguishable narrow component. This would increase the estimate of the broad line luminosity in comparison to a pure broad line, that is not contaminated by the narrow line. Hence, the BH mass found from such a contaminated broad emission line might be larger. However, this argument relies on other parameters to stay the same or increase as well, including the FWHM of the broad line. In contrast to this, the contamination of a broad line component by a narrow line creates elevated levels especially around the line center, which boosts the maximum and thus might decrease the corresponding FWHM in comparison to a pure broad line. The decreased FWHM then mitigates or even negates any effect from a boosted line luminosity concerning a BH mass estimate.

For that reason I treat the additional fitting of the expected narrow line component as a best practice, independent from any visual cues for the existence of such a narrow line. Accordingly, an unconvincing fit of the narrow component, e. g., when it results in a tiny flux or it does not closely follow the spectrum, does not make the overall fit of both lines ineffectual. The impact on the analysis in the context of this work is expected to be small, as long as a strong influence on the broad emission line component can be averted, which is done by forcing a fit of both components.

For each, the narrow and the broad line component, I presume a line shape that can be fitted via a Gaussian profile. Following the analysis by Kim et al. (2010), the

continuum background can be locally well described by a linear offset. A corresponding single Gaussian line profile then takes a similar form as Eq. 3.3, but includes an additional linear equation instead of a fixed offset. The new context makes a change of some parameter names sensible as well,

$$G(\lambda) = \frac{F}{\sigma \cdot \sqrt{2\pi}} \cdot \exp\left(-\frac{1}{2} \cdot \frac{(\lambda - p)^2}{\sigma^2}\right) + m \cdot \lambda + n, \tag{4.8}$$

where F is the line flux, σ is the standard deviation and σ^2 the according variance, p is the center or peak wavelength of the profile, and m and n are the linear equation parameters for the slope and the constant offset, respectively. A double Gaussian profile, which can describe the narrow and the broad line component simultaneously, is just another Gaussian profile with its own set of parameters, e. g., F', σ', and p', that is added to the previous Gaussian, but sharing the same linear offset. The standard deviation σ and the FWHM of the profile are related via

$$\mathrm{FWHM} = 2\sqrt{2\ln(2)} \cdot \sigma \approx 2.35482\sigma. \tag{4.9}$$

The spectra are given as the flux density f in $\mathrm{W}\,/\,(\mathrm{m}^2\,\mu\mathrm{m})$ for different wavelengths λ in µm, i. e., $f(\lambda) = G(\lambda)$ from Eq. 4.8. According units of the parameters are $[F] = \mathrm{W}\,/\,\mathrm{m}^2$, $[\sigma] = [p] = \mu\mathrm{m}$, $[m] = \mathrm{W}\,/\,(\mathrm{m}^2\,\mu\mathrm{m}^2)$, and $[n] = \mathrm{W}\,/\,(\mathrm{m}^2\,\mu\mathrm{m})$. From this, the unit of the FWHM would be the same as for σ. The conversion between the standard deviation in units of a wavelength to a Doppler shifted velocity is done via

$$\sigma = \frac{v_{\mathrm{FWHM}}}{2.35482} \cdot \frac{p}{c}, \tag{4.10}$$

where c is the speed of light in vacuum, that dictates the unit of the velocity v_{FWHM}. The value of c is exact[(2)] and given as $299\,792.458\,\mathrm{km\,s^{-1}}$. The basis for Eq. 4.10 is Doppler broadening, which is effectively given as $v_{\mathrm{FWHM}} = 2\sqrt{2\ln(2)} \cdot \sigma \cdot c/\lambda_0$, where λ_0 is the rest wavelength, i. e., here this corresponds to the parameter p.

The broad emission line luminosity L is still missing, but can be calculated from the line flux F. Their relation is given by

$$L = 4\pi D^2 \cdot F, \tag{4.11}$$

where D is the distance of the respective source. The distance can be inferred from the redshift z of each object (see Tab. 4.1). From the two relations $v = H_0 \cdot D$ (Hubble's law) and $1 + z = \sqrt{\left(1 + \frac{v}{c}\right) / \left(1 - \frac{v}{c}\right)}$ it follows that

$$D = \frac{c}{H_0} \cdot \frac{2z + z^2}{2 + 2z + z^2}. \tag{4.12}$$

[(2)] According to the National Institute of Standards and Technology (NIST): "The NIST Reference on Constants, Units, and Uncertainty", value for 'speed of light in vacuum', `https://physics.nist.gov/cuu/Constants/`, date: April 17, 2023

The common units for c and H_0, i. e., $\mathrm{km\,s^{-1}}$ and $\mathrm{km\,s^{-1}\,Mpc^{-1}}$ cancel partially, such that Mpc (mega-parsec) remains as the unit of the distance D. After finding these quantities from a fitting procedure, all that is needed for a BH mass estimate following Eq. 4.4 is present.

The fitting algorithm is based on the Levenberg-Marquardt (LM) algorithm and connected to a visual feedback loop to potentially apply iterative changes to the input parameters. This is in contrast to what I did in the scope of my master thesis, i. e., emission line fitting of the spectroscopy objects from February 2019, where I used a few different sets of input parameters with different limits and applied these to all objects. The LM algorithm aims at solving non-linear least squares problems, which is a typical problem in curve fitting. A comparison with related algorithms shows an advantage of the LM algorithm, namely that it is often able to find a sensible minimum as a solution even for initial parameters, which are far off from this solution. Thus, in principle the algorithm is a very good match with the given problem of curve fitting. However, as in some cases the noise is strong enough to drown any potential emission line, even this algorithm might not find a sensible solution to a respective problem. Especially in these cases the iterative feedback loop might help finding a better matching fit. In contrast to this, the previous application of fixed parameter sets in my master thesis only worked reliably for clearly distinct emission lines. Then all sets converged to the same solution, whereas cases with high noise levels resulted in fits that do not follow the emission line, but potentially the background only.

Following the descriptions from this section and Sect. 2.2.3, the most important input parameters with their respective initial limits for the narrow and broad emission line components are given in Tab. 4.3.

Based on a similar physical reasoning as Kim et al. (2010), I choose a restriction for the difference between values of the FWHM between the analyzed emission lines. Previously, it is mentioned that Kim et al. (2010) limit this difference between the Pα and Pβ emission lines to a factor of 1.5, as both lines are expected to share their origin. Although the two lines of interest here are not from the same spectral series of hydrogen recombination lines, the assumption and according limiting factor can also be applied to the Pα and Brγ lines. This is especially helpful, if one of the emission lines can be fitted more easily than the other one. The "good" fit helps finding restraints for the FWHM of the "worse" fit. Combined with earlier findings about the difference between the narrow and broad line component, it is sufficient to apply this restrictive factor only to the broad components of the two emission lines.

If not indicated otherwise, the following descriptions are valid for spectra that are extracted for an aperture size factor of 0.5. Different examples for better and worse fits of the Pα and Brγ emission lines, each with a broad and a narrow line component, are shown in Fig. 4.1. The figure shows in particular three different cases.

1. The overall fits of both hydrogen recombination lines work well and their results agree. This includes a factor of < 1.5 between the FWHM values of the broad components and BH mass estimates that overlap within the internal scatter.

Table 4.3: Input parameters with their initial boundaries. Column (1): Descriptive name of the input parameter. Column (2): Initial value of a parameter at the start of applying the fitting procedure. Column (3): Lower and upper boundaries of each input parameter. Column (4): Unit of the parameter and, if applicable, also a scaling factor. The scaling helps the algorithm to deal with numbers that are easier to handle, whereas the units are practically irrelevant for the fitting procedure. Except for the wavelength range around the central wavelength, which is fixed after its initial setting, all of these values as well as their boundaries can be adjusted afterwards, i. e., within the iterative feedback loop.

Parameter Name (1)	Initial Value (2)	Boundaries (3)	Scaling & Unit (4)
Central Wavelength Pα	1.87561	± 0.02	µm
Central Wavelength Brγ	2.16612	± 0.02	µm
Narrow Line FWHM	500	$[0, 900]$	$\mathrm{km\,s^{-1}}$
Broad Line FWHM	1800	$[900, 10\,000]$	$\mathrm{km\,s^{-1}}$
Narrow Line Flux	1.0	$[0, \infty]$	$10^{-15}\,\mathrm{W\,m^{-2}}$
Broad Line Flux	1.0	$[0, \infty]$	$10^{-15}\,\mathrm{W\,m^{-2}}$
Linear Slope m	0	$[-\infty, \infty]$	$10^{-15}\,\mathrm{W\,m^{-2}\,\mu m^{-2}}$
Linear Offset n	-1.0	$[-\infty, \infty]$	$10^{-15}\,\mathrm{W\,m^{-2}\,\mu m}$

2. The fit of the Pα line is good, whereas that of the Brγ is not. This can be followed by disagreeing BH mass estimates for both lines, although the broad FWHM values are connected by not more than a factor of 1.5, such that the difference is not necessarily large.

3. The Brγ emission line fit appears to be better than that of the Pα line. This might be related to the broad component in particular, which results in a respective impact on the BH mass estimates. As the Brγ FWHM helps in finding constraints for the Pα line, the difference between mass estimates might not be large, similar to the previous point.

However, other cases can be encountered as well, including no or only weak indications for the emission lines and accordingly bad fits. Figure A.3 shows the fits of the Pα and Brγ emission line for all remaining objects. It is evident that for some objects the two emission lines are not easily apparent. While they might drown in noise, these lines might not be intrinsically pronounced enough or at all, such that even low noise data would not yield good fits (e. g., object 20 and 95). In some cases there is an indication for an emission line, but the shape does not remind of a single- or double-Gaussian (e. g., object 13 and 70). I assume that the largest impact is from high level noise very close to the expected emission lines, which influences the shape of the feature to deviate from a (multi-component) Gaussian. This makes it harder to differentiate between the actual line and noise, resulting in less accurate fits.

Additionally, literature sometimes provides multiple values for the redshift that vary by a small extent, such that a line identification might be impacted from this. Section A.2 includes a short discussion of a potential influence and why the line identifications here appear to not be affected from this scatter in redshift values.

Important results for fitting parameters of the narrow and the broad line component for the Pα line are shown in Tab. A.3, whereas the same results for the Brγ line are shown in Tab. A.4. It should be noted that the fit procedure is supposed to produce error estimates as the standard deviation of each fit parameter. However, in most cases the fit does not show such error estimates. This is often the case after applying any change within the iterative feedback loop to the initial input values, either by changing a parameter value itself or its boundaries. Nevertheless, even if no changes are applied, some fits do not have corresponding error estimates. Those few cases that do include error estimates are shown in Tab. A.5.

At this point the chosen mass estimator (Eq. 4.4) can be used to get SMBH mass estimates for all AGNs. Respective results for the 20 LLQSOs that are analyzed via their spectra can be found in Tab. 4.4. When choosing between using either the BH mass estimate from the Pα emission line or the estimate from the Brγ emission line, the Pα line should be the preference in most cases. The mass estimator is based on this emission line and thus, per definition the Pα line is supposed to be the better choice. This situation might change if the Brγ line appears more distinguished in the spectrum, yielding a significantly more trustworthy fit, at least based on visual inspection. This can be found for three objects, 58, 64, and 77, where object 58 is a limiting case, as both line fits appear to be on a similar quality level, with the Brγ line slightly in the lead. The Brγ line is still chosen as it results in a slightly larger mass estimate, which becomes more important in Sect. 4.4. In fact, the other two cases also show an increased BH mass estimate based on the Brγ line fit in comparison to the respective Pα-based mass estimate.

Another noteworthy object in this context is 71, for which both line fits immediately converge to a good match with the spectrum. However, their mass estimates do not overlap considering the internal scatter of the mass estimator. This shows that a fit which appears reliable from visual inspection does not automatically fulfill this criterion of reliability. The assumed line ratio might not work for all objects and could be wrong in some cases, depending on the underlying parameters. Thus, there is another reason to prefer the Pα line over the Brγ line as a substitute whenever possible.

When comparing the BH mass estimates via the Pα line with those from the Brγ line, 50 % of the objects show no overlap between the respective ranges of scatter. The other half of the objects show either an overlap or the lowest estimate from one line corresponds to the highest estimate from the other line. The latter is the case for two objects. It is noteworthy that, as the scatter corresponds to the internal uncertainty of the BH mass estimator method, when including a visual inspection and assessment of the emission line fits, the actual uncertainties might be larger, depending on each object and its corresponding fits. Another factor of uncertainty is the fixed setting of the virial factor, as this implies a certain geometry for the BLRs of all objects here.

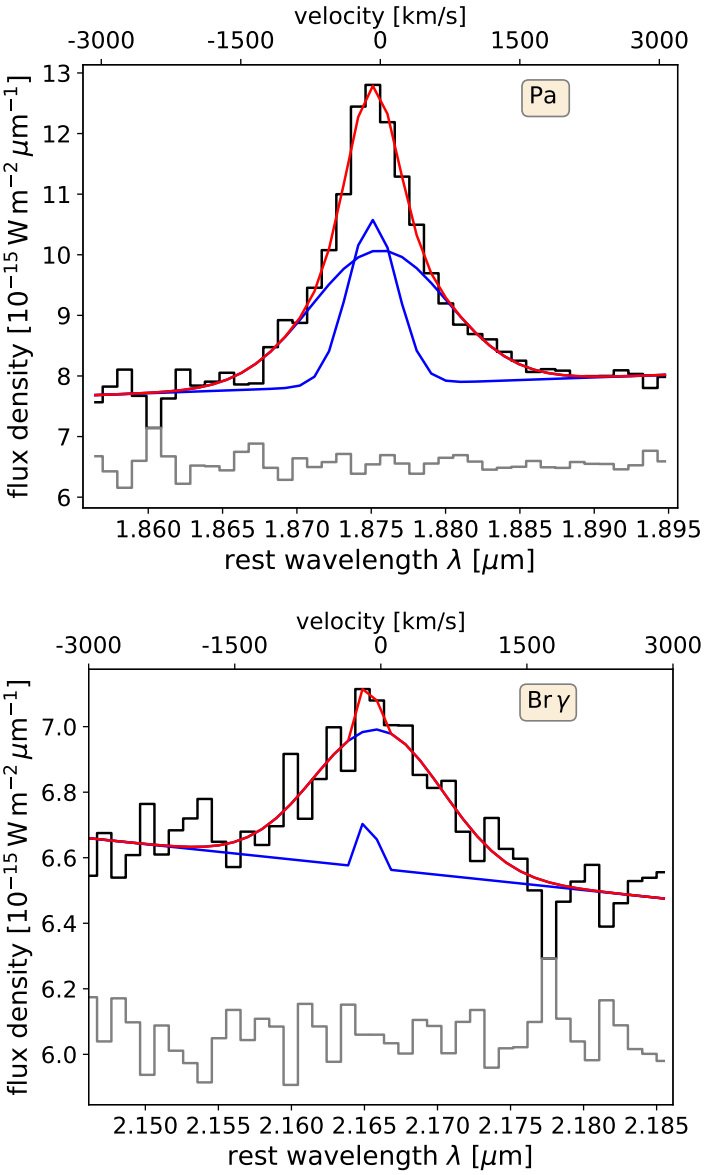

Figure 4.1: Emission line fits of the Pα and Brγ line for object 29 (HE0253-1641). Wheat-colored boxes indicate the emission line in each diagram. The extracted spectrum is shown as a black step plot. The two blue lines show the Gaussian fits of the narrow and broad line component that share the same linear offset. On top of these is their combination in red, i. e., the full double Gaussian fit. The grey step plot indicates the difference between the full fit and the actual spectrum. For visualization purposes, the difference is levelled by an offset. The fit results and corresponding BH mass estimates from both lines agree well for this object.

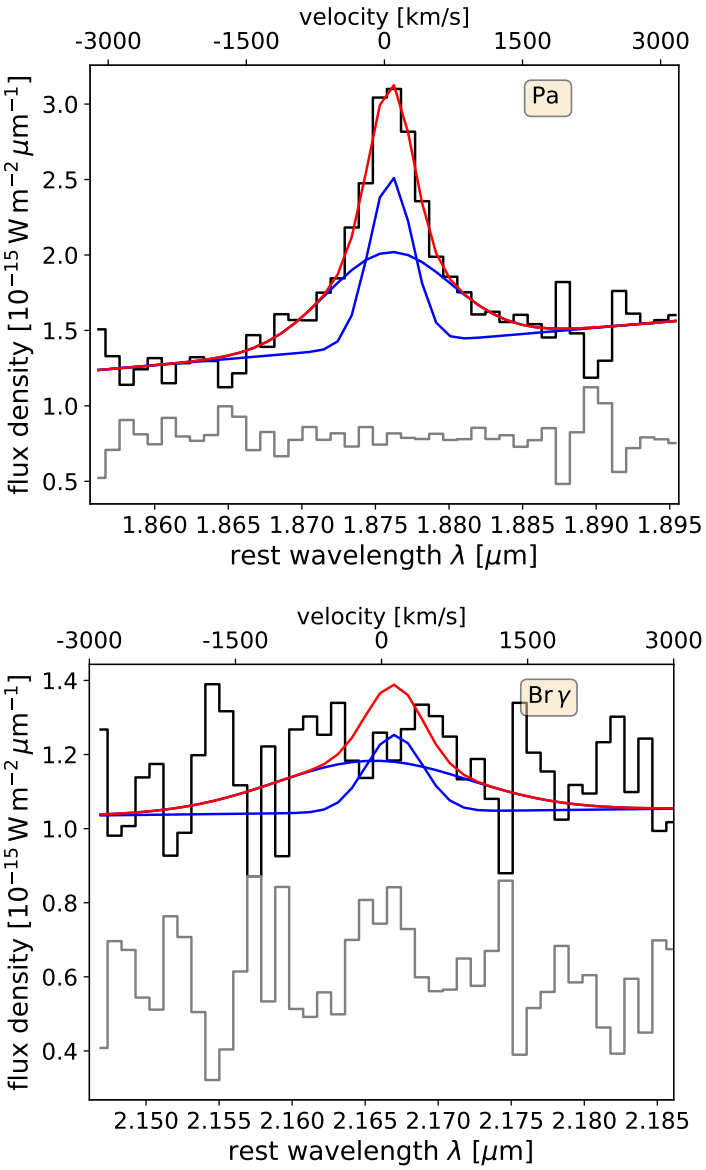

Figure 4.1: (Cont.) Line fits of the Pα and Brγ line for object 89 (HE2236-3621). All components of the graphs have the same meaning as previously. It is evident that the fit of the Pα emission line easily follows the spectrum, while the fit of the Brγ line does not. There is hardly any indication for the existence of the Brγ line in the spectrum as it drowns in noise. Respective results from the Brγ fit do not appear trustworthy. The Pα line is by far the better candidate for a BH mass estimate for this object.

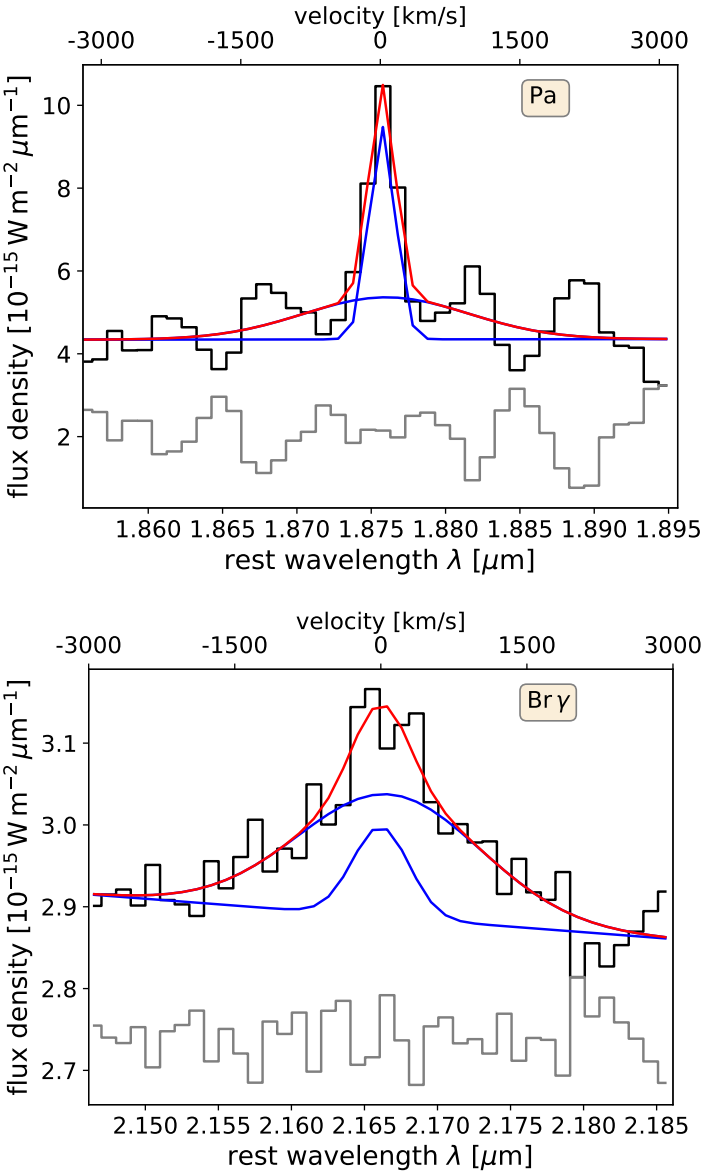

Figure 4.1: (Cont.) Line fits of the Pα and Brγ line for object 77 (HE1348-1758). All components of the graphs have the same meaning as previously. This object is a paradigm for the reason of fitting the Brγ emission line, despite the Pα-based mass estimator. While the spectrum shows a clear indication for the Pα line, the algorithm initially found effectively only a narrow component. Based on the fit of the Brγ line, the broad component of the Pα line can be constrained via tighter boundaries, leading in turn to an overall better fit of the Pα line. Still, the Brγ line fit appears as the better choice for a BH mass estimate.

Table 4.4: The resulting BH mass estimates from the chosen mass estimator (Eq. 4.4) for the Pα and Brγ broad emission line fits. All values are given as $\log(M_{\rm BH}/{\rm M}_{\odot})$. Column (1): Object ID from the LLQSO sample. Column (2): Name of each object according to the HES. Column (3): BH mass estimate from the broad Pα line fit. Column (4): Mass scatter for the broad Pα line fit. Column (5): BH mass estimate from the broad Brγ line fit. Column (6): Mass scatter for the broad Brγ line fit. The scatter range is based on the variations that are introduced by the uncertainties in the mass estimator, i. e., the internal scatter of the estimator only.

ID	Name	Pα Emission Line		Brγ Emission Line	
		BH Mass	Scatter	BH Mass	Scatter
(1)	(2)	(3)	(4)	(5)	(6)
01	HE0003-5023	7.08	6.97 – 7.18	6.97	6.87 – 7.06
13	HE0108-4743	6.37	6.21 – 6.54	6.78	6.64 – 6.92
20	HE0149-3626	7.36	7.21 – 7.50	7.86	7.76 – 7.95
22	HE0203-0031	7.04	6.90 – 7.17	7.64	7.55 – 7.73
29	HE0253-1641	7.03	6.91 – 7.14	7.05	6.96 – 7.14
53	HE0535-4224	7.04	6.92 – 7.16	6.82	6.71 – 6.92
54	HE0608-5606	6.83	6.71 – 6.96	7.08	6.96 – 7.20
58	HE0949-0122	7.35	7.26 – 7.44	7.61	7.53 – 7.68
64	HE1108-2813	6.36	6.17 – 6.54	6.56	6.44 – 6.67
66	HE1136-2304	7.78	7.69 – 7.88	7.91	7.83 – 7.99
67	HE1143-1810	7.62	7.56 – 7.69	7.52	7.47 – 7.58
70	HE1256-1805	6.43	6.28 – 6.57	6.76	6.62 – 6.91
71	HE1310-1051	7.39	7.29 – 7.49	7.69	7.61 – 7.77
74	HE1330-1013	6.78	6.63 – 6.94	7.04	6.91 – 7.17
76	HE1346-3003	7.39	7.29 – 7.49	7.20	7.09 – 7.31
77	HE1348-1758	6.67	6.49 – 6.85	6.80	6.64 – 6.96
78	HE1353-1917	7.76	7.65 – 7.86	7.36	7.23 – 7.49
89	HE2236-3621	6.93	6.82 – 7.05	7.51	7.43 – 7.59
95	HE2322-3843	6.86	6.70 – 7.01	7.45	7.34 – 7.56
99	HE2354-3044	6.63	6.48 – 6.78	6.96	6.82 – 7.09

It is intriguing that the subjective assessment of the fits does not necessarily correspond to matching BH mass estimates, as is described for object 71 before. In that case, both fits appear to follow the spectrum well, but the mass estimates do not overlap. The reverse situation can also be encountered, as for example object 64 shows a nice fit of the Brγ line and an almost non-existent fit of the broad Pα line, but the mass estimates do overlap within their scatter. A possible reason for this might be the influence of the broad Brγ line fit on finding constraints for the broad Pα line fit.

These results show that the Brγ line, and an according fit of its broad component, can act as a substitute for the Pα line if necessary. As a rule of thumb, this substitution is expected to be slightly more reliable if both lines are actually pronounced in the respective spectrum. However, in that case it makes more sense to directly use the Pα line instead of the Brγ line. A fit of the broad Brγ emission line might also be used as a validation or restriction for the FWHM of the broad Pα line, especially if the latter is harder to identify than the former.

BH mass estimates have also been found for spectra that are extracted using an aperture size factor of 1.5. Based on estimates for well distinguishable emission lines, such as the Pα line of object 67, the differences are small to non-existent. I also tested a slit-correction that is based on a consideration of the redshift and angular size of each object, and applied a respective factor of the order of unity to each spectrum. While in some cases this has a noticeable impact on the continuum levels, the differences for corresponding line fits are negligible. Other factors that might contribute to a slit-correction and have been considered are the airmass and seeing. As no significant change can be found in fitting results and according mass estimates, any slit-correction is ignored in later results, i. e., as they are shown here. Additionally, the earlier finding that the reduction procedure with a smaller aperture size factor appears to result on average in less noisy spectra, the results for the aperture size factor of 0.5 are preferred.

For some objects there are BH mass estimates provided in literature. These can be found in Tab. A.6, where the caption contains more information. For one object, 95, there are two masses provided in literature, where one of these masses is higher than my estimate and the other mass matches my value. When counting this for both cases, then my estimates are too low in two cases, too high in four cases, and match the literature estimates in four cases. This shows that there does not appear to be a systematic offset of my BH mass estimates. Additionally, the uncertainty of the literature values is unknown and they should not be treated as irrefutable results. The previous example, object 95, shows this fact, as one literature mass estimate is considerably larger than the other, $\Delta \log (M_{\mathrm{BH}}/\mathrm{M}_{\odot}) \approx 1.3$. Moreover, object 67 is good example for a very stable emission line fitting routine with an accordingly consistent mass estimate, even considering both, the Pα and the Brγ emission line fits. As this estimate deviates by about 0.9 dex from the literature value, at least one estimate appears to be erroneous, or there is a hidden error in the method. Given the previous finding that there does not appear to be a systematic error, the latter seems less likely.

Most of the mass estimates can be encountered again in Sect. 4.4, where they are applied to the $M_{\mathrm{BH}} - L_{\mathrm{bulge}}$ relation.

4.2.2 Identifications of More Lines

The spectra are expected to contain more diagnostic lines than only the Pα and the Brγ emission lines. Some of the other lines that might be found in the range of wavelengths for these spectra are rotational-vibrational lines of molecular hydrogen (H_2), a forbidden [Fe II] line, CO absorption bands, and the coronal line [Si VI]. The latter is considered a common tracer of an AGN signature (e. g., Riffel et al. 2006; Mason et al. 2015). Similar to the Pα and the Brγ lines, the [Fe II] line might be excited by the AGN, while other excitation mechanisms are possible as well. For [Fe II] this is shock tracing and the estimation of supernova rates (e. g., Calzetti 1997; Alonso-Herrero et al. 2003). Other shock tracers are the rotational-vibrational lines of molecular hydrogen, which can also be seen as a basis that enables SF. The Pα and Brγ lines are also indicators for young SF, but the strong influence of the AGN, especially considering their broad components, probably exceeds that of the SF. Nevertheless, in principle NIR hydrogen recombination lines such as Pα and Brγ trace ionizing photons that are produced by massive stars. Due to their short lifespans, this is related to recent ($< 10\,\mathrm{Myr}$) star formation in a galaxy (Li et al. 2013). Emission lines of CO and the aforementioned CO absorption bands (band heads) include more information about the stellar populations.

I searched for any signs of emission and absorption lines in all spectra. An extensive list of NIR lines can be found in Tokunaga, A. T. (2002), which served as a reference for the potential recognition of spectral features here. For this step I analyzed the spectra extracted for the aperture size factor of 0.5, as well as for a factor of 1.5, which is supposed to include a larger stellar contribution from the host galaxy. Additionally, I searched the extracted off-center spectra for the same features. A list of the accumulated identifications can be found in Sect. A.3.

Essentially all line features are less pronounced in the off-center spectra, with only few exceptions. This is an expected finding, especially in case of features that are connected to the AGN, and it is related to the distance of the apertures from the center of the host galaxy. Each aperture is centered at a distance of two times the converted seeing value, once to the right and once to the left of the center, where the AGN resides. The apertures have widths of two times this seeing value, such that the central region, that is omitted here, also corresponds to a width of two times the value. This might leave out some contribution of the central bulge in the off-center spectra. However, even if the bulge is included within a centered aperture, effects of the host galaxy are expected to not be as strong as from the AGN itself.

In contrast to this, the off-center spectra should contain no or only minimal contribution from the AGN. Based on the AGN tracer line [Si VI] this statement cannot be fully supported. In some cases, such as for object 58, the line is still visible in off-center spectra. The glare from the nucleus is apparently strong enough to influence even the off-center spectra. Other cases do not show this effect, as for example the indication for [Si VI] disappears in the off-center spectrum of object 67. A simple explanation might lie in the overall damping of line features in the off-center spectra, as the [Si VI] line is not very strong in the spectrum of 67 even for a centered aperture.

In total there are 20 spectra for different objects analyzed here. The overall iden-

tifications include multiple potential line candidates, and especially other hydrogen recombination lines. A prominent example is the Brackett-δ line, which is found in almost half of the sample here (9/20), being quite distinct in some cases. Here, I concentrate on the abundance of three particularly interesting lines. The AGN tracer [Si VI] can be found in 10 spectra, where it is rather distinctive in some cases. Another AGN tracer, but also shock tracer, is the [Fe II] line, that can be found in 9 spectra. This can be combined with other shock tracers, such as lines from molecular hydrogen H_2. These can be found for 13 objects, but are often only associated with weak features in these spectra. Possible implications from this are discussed in Sect. 4.4.

4.3 Imaging Data

This section describes different methods and tests which I used for extracting absolute K-band bulge magnitudes for each available object. In contrast to the spectroscopy data, the amount of objects for which data from imaging observations can be used here is smaller, i. e., 20 objects for spectroscopy, but only 14 objects for the K-band imaging. As shown in Tab. 4.1, for three objects that are missing in imaging (29, 71, and 77) there are bulge magnitudes available in literature that can be used instead of omitting the object from a follow-up analysis. However, the latter is the case for the remaining three objects (70, 74, and 89), which cannot be considered in further analysis.

4.3.1 Choosing an Aperture Radius

Similar to the choice of an aperture for spectroscopy (Sect. 4.2), the aperture radius is also important in the context of photometry. Busch et al. (2015) use a circular aperture with a radius of about three times the FWHM they measured for the PSF in order to calibrate their data. Based on some tests I find that this choice works well as a default aperture radius, that can be adjusted if necessary.

By using an IRAF task, which can apply either a Moffat or a Gaussian fit to a source within a specified aperture radius, I test the impact of multiple different settings. A Moffat distribution is often used when a Gaussian does not fit the PSF well. Its intensity I as a function of the distance r can be written as

$$I(r) = I_0 \cdot \left(1 + (r/R)^2\right)^{-\beta}, \tag{4.13}$$

where I_0 is the intensity at the center of the source, R is a width parameter (half width at half maximum), and β is a constant coefficient that represents atmospheric scattering (Moffat 1969).

In this work I choose to fit Moffat instead of Gaussian distributions. This is partially supported by Busch et al. (2015, Sect. 3.1), where the authors model the AGN component of their data via a Moffat function with a width that is fixed to their measured PSF. However, their PSF measurements are based on Gaussian profiles. To assess the difference between using Gaussian and Moffat profiles, I did test measurements on some sources in my data. Based on previous measurements I found that two images are

particularly interesting cases for this test, as one shows a large average PSF measurement for multiple sources, whereas the other results in a relatively small average PSF measurement. The former situation is given for the reduced, final image for object 58, which is observed during the night February 23 to 24, the latter for the respective image of object 76 from the same observation night. Some relevant results from measurements are shown in Tab. 4.5.

Table 4.5: Comparison of results for measurements of fitting a Moffat and a Gaussian profile to different sources. Respective lines indicate for which object the measurements, that are shown below, are valid. The unit of the peaks is counts (ADU) and that of the radius is pixel, which is effectively irrelevant as they can be arbitrary for the comparison. Column (1): Type of object. Column (2): Peak of the Moffat profile fit. Column (3): FWHM of the Moffat profile fit. Column (4): Peak of the Gaussian profile fit. Column (5): FWHM of the Gaussian profile fit.

Object Type	Moffat		Gaussian	
	Peak	FWHM	Peak	FWHM
(1)	(2)	(3)	(4)	(5)
58 HE0949-0122 (February 23 – 24)				
star	162.8	5.67	165.2	5.54
star	712.8	5.57	724.9	5.43
star	44.77	6.42	44.69	6.45
galaxy[1]	14702	5.61	14805	5.56
76 HE1346-3003 (February 23 – 24)				
star	1208	2.76	1210	2.59
star	228.1	2.11	225.5	2.17
star	200.2	2.40	200.4	2.31
star	1265	2.29	1257	2.31
galaxy[1]	24025	2.37	23603	2.44

[1]: The aperture is centered at the nucleus of the active galaxy.

In both cases the measurements of the galaxy do not show noticeable differences to measurements of stars with respect to the different fit profiles, except for the higher intensities in these specific cases. The deviations are calculated using the Moffat values as a baseline, i. e., Gaussian/Moffat. Deviations of the peak values are only between $< 0.1\,\%$ and $< 1.8\,\%$. For the values of the FWHM measurements, deviations are between $< 0.5\,\%$ and $< 6.2\,\%$, where the largest deviation is an outlier, being more than twice as large as the second largest deviation of $< 3\,\%$. With the differences between measurements being clearly below $10\,\%$, the choice of a Moffat or a Gaussian profile does not appear to matter for the further analysis here.

The agreement with the previously mentioned aperture radius of about three times the Moffat FWHM comes from another test, in which I applied multiple apertures of

different sizes to the same object, and compared the differences in flux measurements. Respective measurements are applied to the reduced image of object 01 from the observation night September $10 - 11$, by choosing a relatively bright point source from the FOV of the image (2MASS J00054407-5005245). The PSF in this image, as a median of the FWHM measurement for multiple point sources, is $\sim 4.62\,\mathrm{px}$, i. e., $\sim 1.33\,''$. Flux measurements for different aperture radii are shown in Tab. 4.6.

Table 4.6: Exemplary flux measurements for different aperture radii on a point source. Column (1): Aperture radius in pixel. Column (2): Description of the radius, where the median Moffat FWHM is valid for the image that these measurements were conducted on. Column (3): Measured flux within the aperture in arbitrary units.

Radius / px	Descriptive Size	Flux (arb. unit)
(1)	(2)	(3)
2.31	half median Moffat FWHM	17393.8
4.62	median Moffat FWHM	34902.6
9.24	double median Moffat FWHM	42994.7
13.83	triple median Moffat FWHM	44636.2
18.48	quadruple median Moffat FWHM	45549.3
23.1	quintuple median Moffat FWHM	46129.7

The aperture radius correlates with the flux at all times. However, after reaching three times the median Moffat FWHM for the respective image, further changes for larger apertures appear insignificant. The difference between the largest tested aperture and the triple median Moffat FWHM is only about $\sim 3.3\,\%$. In contrast to this, the difference with respect to smaller radii is much larger. Even when using the median Moffat FWHM as the aperture radius, the difference to triple that radius is $\sim 22\,\%$. For smaller radii this difference grows accordingly even more.

The background around a source is obviously a big factor for the choice of an aperture size, as a strong background influences larger apertures much more than a well subtracted background. However, this exemplary test shows that the choice for the given data here of about three times the Moffat FWHM from according measurements in the image should include the necessary flux, but not much more. It is effectively the sweet spot for the aperture radius for most measurements on point sources, as for example calibration measurements. Another benefit from this choice of aperture radius is that the chance of including other sources than the intended source at the center of the aperture is smaller than for larger radii. This situation might change for extended sources, such as the bulge component of the host galaxy of an AGN. Then corresponding considerations for other aperture radii have to be taken into account. The applied IRAF task can automatically apply an aperture that is close to three times the median Moffat FWHM, which I call '3M-fit radius' for simplicity. As an example, the difference in flux for the same object as in Tab. 4.6 between using three times the median Moffat FWHM and using the 3M-fit radius is $< 0.05\,\%$. This is due to the small difference in radii of $< 1\,\%$. Thus, in the following I refer to the 3M-fit radius instead of three times the median Moffat FWHM.

Similar to the spectroscopy data, I also applied cross-calibration tests to imaging data. To further test and strengthen the choice of the 3M-fit radius as a default aperture radius, I included different sizes of the apertures. Based on another method of calibration, that I tested before switching to what is effectively presented in this section, the image of object 67 from observation night February $15-16$ is of particular interest for this test. The reason for this is that it showed the largest deviations when applying the previous method that I aborted later on. Thus, it makes a good candidate for follow-up cross-calibration tests using the method shown here. The median Moffat FWHM for the image of 67 is given as $2.57\,\mathrm{px} \approx 0.74''$, which is a relatively small size of the PSF with respect to all given imaging files here. Originally, four stars were chosen with one reference star. However, it turns out that one of these objects (2MASS J11454313-1827073) might actually consist of two sources that are very close to each other. This is not apparent in the literature 2MASS image, while this assumption is supported by an elongated shape at the core of the source for certain scaling and contrast settings in the given image here. Cross-calibration results for all tested aperture radii are largely off for this object ($\sim 30-52\,\%$). A list of results for the other three stars can be found in Tab. 4.7.

Table 4.7: Cross-calibration results within the reduced image of object 67 for one reference star (2MASS J11454095-1829402) and three stars for the testing procedure ("obj1": 2MASS J11454837-1827433; "obj2": 2MASS J11453600-1828533; and "obj3": 2MASS J11454329-1828361). The table is split into three sections that correspond to different radii, which are indicated above of each section. Column (1): Identifier of the object as given in this caption. Column (2): Measured flux for the current radius of each section in arb. unit. Column (3): Expected flux for the current radius of each section in arb. unit. Column (4): Difference between measured and expected flux in percent. Column (5): Difference between measured and expected magnitude, based on the flux values.

ID	Measured Flux	Expected Flux	Flux Diff.	Magnitude Diff.
(1)	(2)	(3)	(4)	(5)
1.285 px radius (half median Moffat FWHM)				
obj1	1978.9	2286.7	−13.5 %	0.157
obj2	98970.1	117167.2	−15.5 %	0.183
obj3	16197.4	15346.4	+5.5 %	0.059
2.57 px radius (median Moffat FWHM)				
obj1	4523.7	4669.3	−3.1 %	0.034
obj2	230189.9	239250.6	−3.8 %	0.042
obj3	31642.3	31336.7	+1.0 %	0.011
7.45 px radius (3M-fit radius)				
obj1	5689.7	5898.1	−3.5 %	0.039
obj2	294127.6	302211.1	−2.7 %	0.029
obj3	40338.8	39583.2	+1.9 %	0.021

It is evident that the median Moffat FWHM or a larger measure as the aperture radius is more favorable than a smaller radius. However, it is noteworthy that using either the median Moffat FWHM or the 3M-fit radius does not show large variations for this image, as both cross-calibrations result in deviations of $< 4\,\%$. Due to aforementioned reasons concerning total flux measurements, choosing the 3M-fit radius for the aperture size is still preferred.

4.3.2 Procedure Description and Testing

The extraction of a bulge magnitude is most accurate for an elaborate, sophisticated morphological decomposition of an active galaxy into its different components, including a subtraction of the central AGN. Within the scope of this work I apply a much simpler and more straightforward approach for estimating the bulge magnitudes. This section deals with a trial for this procedure, to assess whether it is working as intended and to roughly test its accuracy.

In order to test the procedure I used four objects with known bulge magnitudes from previous publications (Busch et al. 2014; Busch et al. 2015). For three of those objects I tested the procedure using the files from previous observations, that are partly used for results of the mentioned publications. These objects are also part of the LLQSO sample. Their IDs and names according to the HES are 11 HE0103-5842, 29 HE0253-1641, and 83 HE2204-3249, where the reader might recognize object 29 from the spectroscopy sample of this work. The additional, fourth object is 62 HE1029-1831. This object is part of the imaging set from the observations in February 2019, which is missing its counterpart in spectroscopy, such that it is not mentioned previously. However, Busch et al. (2015) analyze object 62 using another telescope, the VLT, and accordingly also another instrument. As a part of their analysis, the authors find the absolute K-band bulge magnitude for object 62, such that the imaging files here can be used to add this image to the pool of test objects for the procedure of this work.

The other three objects, 11, 29, and 83, are chosen as they cover a wide range of different parameters. This includes the absolute K-band bulge magnitudes found by Busch et al. (2014), as these objects cover a range of $\sim -25\,\mathrm{mag}$ to $\sim -22\,\mathrm{mag}$, which is almost the whole range of magnitudes that the authors find for their full sample. Additionally, they list the luminosity fractions for these objects, including that for the bulge to total luminosity. The objects show values from relatively small (~ 0.17) to large (~ 0.78) fractions of the bulge luminosities. Their morphological types are noteworthy as well, as two objects are considered as barred spirals, and the third one as an elliptical galaxy. Finally, the visible, angular size of the objects in the SOFI images, in relation to the sources presented in this work, covers the range from rather small to medium-large. Together with object 62 the small sample of just four test objects shows a wide scatter of properties that might influence the measurements.

For the sake of completeness I also applied cross-calibration tests to the images of the two objects 11 and 83. Each test consists of the cross-calibration of just two stars, but again for different aperture radii. Results in a similar format as in Tab. 4.7 can be found in Tab. 4.8.

Table 4.8: Cross-calibration results within the reduced images of objects 11 and 83. The table is split in respective sections for each LLQSO object. For object 11 the reference star is 2MASS J01051798-5825446, the "object" star is 2MASS J01051960-5827109. For object 83 the reference star is 2MASS J22074439-3234420, the "object" star is 2MASS J22074648-3235184. The radii follow the same scheme as in Tab. 4.7, i. e., first half the median Moffat FWHM, then the median Moffat FWHM, and lastly the 3M-fit radius. Column (1): Aperture radius in pixel. Column (2): Measured flux for the current radius of each section in arb. unit. Column (3): Expected flux for the current radius of each section in arb. unit. Column (4): Difference between measured and expected flux in percent. Column (5): Difference between measured and expected magnitude, based on the flux values.

Radius (1)	Measured Flux (2)	Expected Flux (3)	Flux Diff. (4)	Magnitude Diff. (5)
object 11				
2.435	11249.7	10665.5	+5.5 %	0.058
4.87	20112.1	19810.1	+1.5 %	0.016
14.33	26315.1	25625.2	+2.7 %	0.029
object 83				
2.835	55493.3	53638.3	+3.5 %	0.037
5.67	110751.9	110208.6	+0.5 %	0.005
16.74	138303.3	137976.9	+0.2 %	0.003

The results confirm the earlier finding, that a larger aperture radius than half of the median Moffat FWHM is preferable. Again, the difference between the 3M-fit radius and the median Moffat FWHM as the radius is negligible. Thus, the conclusion is the same as before.

The idea behind the procedure to extract bulge magnitudes, that is applied in this work, lies in the 3M-fit radius as a default aperture size indicator, and potential adjustments. The adjustments are based on the morphological type of each galaxy, the visible angular size in the SOFI images, and a visual inspection of each galaxy for different scaling and contrast settings, accounting for the size of its central luminous parts, that individually depend on each source. As a reminder, for an elliptical galaxy the whole object is assumed to make up the central spheroid or bulge. Their neighbors in the Hubble tuning fork, lenticular galaxies, are also thought to feature large, prominent bulges, whereas (barred) spirals tend to have smaller bulges.

In order to find the 3M-fit radius, as well as the median Moffat FWHM for potential adjustments, multiple measurements are made on point sources in each image. Then at least two stars are chosen, if possible even more, for which there is an apparent magnitude in the K-band from 2MASS in literature. In a best case scenario these stars are close to the galaxy, but also isolated enough from other sources nearby, that there is no or only as minimal contamination as possible in any measurements. From a simple visual inspection this is given for the reference stars that are chosen here. As a result from taking measurements on multiple stars the influence from possibly contaminated measurements is further mitigated.

A potential problem that arises from this procedure is that the resulting apparent magnitudes, one for each reference star, cannot be easily averaged, due to the logarithmic scale. It is possible to derive a formula that can be used to get an average apparent magnitude $\overline{m}$. Probably the most straightforward way to calculate such an average magnitude is to calculate the arithmetic mean of n input fluxes $\overline{f} = \frac{1}{n}\sum_{i=1}^{n} f_i$ and calibrate the resulting apparent magnitude via a reference source with known f_{ref} and m_{ref}, using Eq. 3.5. However, this is not applicable to the situation here, as there are N reference sources in combination with a single flux measurement of the object of interest. In order to find an average reference source with a respective flux density $\overline{f}_{\mathrm{ref}}$ and apparent magnitude $\overline{m}_{\mathrm{ref}}$, the average of all available apparent magnitudes $[m_{\mathrm{ref},1}, m_{\mathrm{ref,N}}]$ has to be found, which leads back to the initial problem. Based on the upper equation that describes the average flux $\overline{f}$ in combination with the scaling from Eq. 3.6, it is possible to derive a respective formula for the average $\overline{m}$ from n different input magnitudes,

$$\overline{m} = 2.5 \cdot \log_{10}\left(\frac{n}{\sum_{i=1}^{n} 10^{-0.4 \cdot m_i}}\right). \tag{4.14}$$

Using the distance of an object, that can be inferred from its redshift (see Eq. 4.12), together with $\overline{m}$, it is possible to find a respective average absolute magnitude $\overline{M}$. In this specific case here, these magnitudes are given for the K-band, i. e., $\overline{m}_K$ and $\overline{M}_K$.

The first step of testing the procedure overall are according measurements on multiple point sources in each image, to find the 3M-fit radius and the median Moffat FWHM.

Then I started by simply applying an aperture, of which the size is based on the 3M-fit radius, to each central region of the galaxies. Afterwards, I used the aforementioned parameters to adjust the 3M-fit radius accordingly for each object. These measurements are supposed to include the bulge component of each source. However, at each center also lies an AGN. In order to only include the flux of the bulge, the contribution from the AGN needs to be subtracted. This is done using a smaller aperture that is centered on the AGN, choosing an aperture width that corresponds to the median Moffat FWHM. This modeling of the AGN contribution is the same procedure as applied by Busch et al. (2014). Results for the application of the procedure to each test object are shown in Tab. 4.9.

Table 4.9: Literature values and results for measurements on the sample of test objects. Column (1): Object ID from the LLQSO sample. Column (2): Number of reference stars for the respective object that are used for flux measurements. Column (3): Average absolute K-band bulge magnitude from measurements on all reference stars, where the aperture size is set using the 3M-fit radius. Column (4): Average absolute K-band bulge magnitude from measurements on all reference stars, where the aperture size is set using the adjusted radius. Column (5): Absolute K-band bulge magnitude from literature.

ID	Nr. of Ref.s	$\overline{M}_{K,\text{3M-fit radius}}$	$\overline{M}_{K,\text{adj. radius}}$	$M_{K,\text{lit}}$
(1)	(2)	(3)	(4)	(5)
11	2	-23.62	-23.62	$-23.78^{[a]}$
29	2	-23.03	-22.86	$-22.13^{[a]}$
62	4	-23.82	-23.66	$-23.57^{[b]}$
83	3	-24.45	-24.74	$-25.00^{[a]}$

[a]: According to Busch et al. (2014, Tab. 7). [b]: According to Busch et al. (2015, Sect. 3.1).

For object 11 (HE0103-5842) the 3M-fit radius is kept as the aperture, i. e., there are no further adjustments. The object is roughly of medium size in comparison to other objects from this work. It is classified as a barred spiral (SB) and its luminosity fraction for the bulge is given as ~ 0.48. The visual inspection, including a comparison of an aperture that is based on the 3M-fit radius with the appearance of the galaxy, shows that this default choice for the aperture size fits the object well. The resulting absolute K-band bulge magnitude differs from the literature value by 0.16 mag, which appears as a good result, given the difference between this procedure and an elaborate morphological decomposition of the galaxy.

Object 29 (HE0253-1641) is also a barred spiral galaxy, but has a much smaller luminosity fraction of the bulge of ~ 0.17, resulting in the smallest absolute K-band bulge magnitude from the test sample. Additionally, the object has a smaller angular diameter than object 11, which can be seen in a comparison of the objects. In fact, this object is small in comparison to most objects of this work. My estimated absolute K-

band bulge magnitude from the 3M-fit radius is about 0.9 mag lower than the literature value, i. e., I overestimate its brightness by almost 1 mag. The correction of the aperture size uses two times the median Moffat FWHM, but the respective result is still ~ 0.7 mag off from the literature value. This is a large deviation, which is probably based on the low luminosity fraction of the bulge, and it is not evident from the visual inspection, such that this object shows the largest deviation between my estimate and the literature value.

Yet another barred spiral is object 62 (HE1029-1831). It is also relatively small in angular size, similar to object 29, but even a bit smaller. The corrected aperture size is accordingly again two times the median Moffat FWHM, while the PSF is slightly smaller for 62 than for 29. While the result for the 3M-fit radius deviates from the literature value by 0.25 mag, which is already significantly better than the results for 29, the adjusted radius reduces this deviation to 0.09 mag. This result shows an even better agreement with literature than is given for object 11, which is already relatively close to the reference value, given the simplicity of the approach.

In contrast to the previous three objects, object 83 is associated with an elliptical galaxy. Accordingly, the full host galaxy is considered to contribute to the bulge luminosity and its luminosity fraction of the bulge is the largest in the test sample at about 0.78. The choice of a size for the aperture deviates accordingly from the 3M-fit radius to include the full host galaxy. If the galaxy is not very small and the PSF relatively large, the expected aperture size for an elliptical galaxy increases in comparison to the 3M-fit radius. This is also the case here. When using the 3M-fit radius the corresponding absolute K-band bulge magnitude is off by about 0.55 mag from the literature value. Here, my result is showing an underestimation of the bulge luminosity. The increased aperture size of 42 px, which is approximately 7.5 times the median Moffat FWHM for the given image, decreases the deviation to 0.26 mag, which is a much closer estimate with respect to the literature value. However, a problem for this object lies in nearby foreground stars, which are included if the radius is chosen large enough to guarantee an inclusion of the full host. By testing different aperture sizes centered on this object I find that the only way to reach the literature magnitude is for even larger aperture radii, which include foreground objects. The given context of a fast, simplistic procedure for finding bulge magnitudes does not include the modeling of potential foreground stars, which can then be subtracted from the galaxy in order to eliminate their contribution. Hence, the smaller choice of an aperture radius results in an expected underestimate of the bulge brightness for this object.

The overall deviations from literature values for the final results in the test sample cover a range of about $0.09 - 0.7$ mag. It is important to note that all of the adjusted aperture radii improve the results in comparison to literature magnitudes, some even significantly. The observed deviations agree with the interpretation of each source in the context of further information that is available here. However, this additional information is missing for the other imaging objects that are analyzed in Sect. 4.3.3, such that a consideration of it would break the meaning of the test sample. The test emphasizes that the simplistic approach here cannot compete with an elaborate morphological decom-

position. In contrast to this stands the significantly reduced complexity and according time that it takes to apply the described procedure to different sources. Based on this, and including considerations such as the foreground stars for object 83, the procedure is deemed to work well enough for rough estimates of the bulge magnitudes, such that these can be used for an additional analysis in Sect. 4.4.

4.3.3 Bulge Magnitude Estimates

This section deals with the application of the previously described procedure for extracting absolute K-band bulge magnitudes (see Sect. 4.3.2) to all imaging objects from the observations that this work is based on. One aspect from the procedure relies on the morphological classification of the host galaxy. However, this is not given for all objects here (see Tab. 4.1), such that a visual inspection has to suffice in these cases. Results for all objects can be found in Tab. 4.10, including a split view of those that have been observed during two observation nights.

Those sources, that have a respective image for each of two observation nights, are described here in more detail. The first object is 58 (HE0949-0122) with two quite different values for the median Moffat FWHM in both images. Accordingly, the 3M-fit radius for both cases is different as well, being 6.50 px in the image from the night February 14 to 15 and 16.86 px for February 23 to 24. Despite this, the 3M-fit radius is chosen to define the aperture size in both cases. A reasoning for this can be found in a discussion below. It is noteworthy that the results for the bulge magnitudes are not far off from each other, with a difference of 0.15 mag. The resulting average magnitude is -24.53.

The other three objects with two observation nights show even smaller differences in estimated bulge magnitudes between those two nights. For object 64 (HE1108-2813) the choices of aperture radii are slightly different. In the first night it is the median Moffat FWHM multiplied by a factor of five, whereas this factor is only four in the second night. These choices are related to the consideration of all available information about this source, and the different values for the median Moffat FWHM per image. The resulting area, that the apertures cover, is similar in both cases. Hence, it is less surprising that the estimated bulge magnitudes agree very well for both observation nights. For the first night it is -23.57, while for the second it is -23.59, resulting in an average value of -23.58.

The difference between the values for the 3M-fit radius of each observation night for object 66 (HE1136-2304) is not large. As a result, the choice of five times the median Moffat FWHM covers a similar part of the relatively small galaxy in both images. Considering the differences between images from two different observation nights for the other objects, this object shows probably the smallest differences. The estimates for the bulge magnitudes are -23.04 and -23.11, i. e., a deviation between the estimates of 0.07 mag. While this is a stronger deviation than for object 64, it is still relatively small. The resulting average estimate of the K-band bulge magnitude is -23.08.

The last object with two observation nights, which is 76 (HE1346-3003), also shows a good agreement between the respective results. This is not self-evident, as all objects

Table 4.10: Results for the extraction of K-band bulge magnitudes for all imaging objects according to Tab. 4.1. Those objects, that are observed during two different nights are accordingly listed twice. Column (1): Object ID from the LLQSO sample. Column (2): Date of the night of observation. Column (3): Descriptive size of the radius that is chosen for the aperture, where "m.M.$_{\mathrm{FWHM}}$" is an abbreviation for the median Moffat FWHM. Column (4): Number of reference stars for the respective object that are used for flux measurements. Column (5): Average absolute K-band bulge magnitude from measurements on all reference stars, where the aperture size is set using the adjusted radius.

ID (1)	Obs. Night (2)	Choice of Radius (3)	Nr. of Ref.s (4)	$\overline{M}_K$ (5)
01	Sept. 10-11	3M-fit radius	2	−23.50
13	Sept. 07-08	$\sim 6\times$ m.M.$_{\mathrm{FWHM}}$	2	−23.44
20	Sept. 07-08	$\sim 5\times$ m.M.$_{\mathrm{FWHM}}$	2	−24.14
22	Sept. 09-10	$4\times$ m.M.$_{\mathrm{FWHM}}$	3	−24.47
53	Febr. 15-16	3M-fit radius	4	−23.27
54	Febr. 15-16	3M-fit radius	5	−22.78
58	Febr. 14-15	3M-fit radius	2	−24.60
58	Febr. 23-24	3M-fit radius	2	−24.45
64	Febr. 15-16	$5\times$ m.M.$_{\mathrm{FWHM}}$	4	−23.57
64	Febr. 23-24	$4\times$ m.M.$_{\mathrm{FWHM}}$	4	−23.59
66	Febr. 15-16	$5\times$ m.M.$_{\mathrm{FWHM}}$	3	−23.04
66	Febr. 23-24	$5\times$ m.M.$_{\mathrm{FWHM}}$	3	−23.11
67	Febr. 15-16	$4\times$ m.M.$_{\mathrm{FWHM}}$	4	−23.72
76	Febr. 16-17	3M-fit radius	2	−24.21
76	Febr. 23-24	$6\times$ m.M.$_{\mathrm{FWHM}}$	2	−24.25
78	Febr. 16-17	3M-fit radius	3	−23.42
95	Sept. 09-10	$\sim 6\times$ m.M.$_{\mathrm{FWHM}}$	4	−24.53
99	Sept. 07-08	$2\times$ m.M.$_{\mathrm{FWHM}}$	4	−22.75

in the image from the night February 16 to 17 show the same warped shape of the PSF, where the cores of all sources appear slightly elongated and curved. The 3M-fit radius from that image is also larger than for the second night. As is the case for objects 64 and 66, the effective choices for the radii result in apertures that cover similar parts of the host galaxy. The two nights result in absolute K-band bulge magnitudes of -24.21 and -24.25, which differ by only 0.04 mag, giving an average magnitude of -24.23. Despite the strong similarity of the results I choose to ignore the estimate for the first night, as the warped shape of the PSF appears strange. The small difference between the estimates means at the same time that ignoring one result does not impact the overall outcome for this object.

While a completely blind application of the procedure is impossible, I try to treat different observation nights as if they are observations of unrelated objects. Despite the effectively different choices of aperture radii, the deviations between two nights for the same object are relatively small, $0.02 - 0.15$ mag. Taking into account the differences between observation nights, the deviation between bulge magnitude estimates for object 66 with 0.07 mag appears most intriguing. The similarity of both images implies the expectation of a negligible difference, especially when compared to the other objects. However, as the approach here is expected to result rather in rough estimates than precise measurements, a difference of 0.07 mag does appear immaterial. Overall, this points towards a robustness of the procedure as it is applied here.

Further noteworthy cases are those objects that are ellipticals or at least potential candidates for this class, in case their classification is not clear as either E or S0. Both classifications are associated with large, prominent bulges, especially in case of ellipticals. Similar to object 83 the candidates for ellipticals here, 13, 58, and 95, also have foreground stars nearby, which might influence measurements for large apertures. In all cases the assumed radii might be too small and the according bulge brightness is likely underestimated.

For object 13 the choice of aperture radius is relatively straightforward in comparison to the other two sources as the maximum radius that does not include two obvious foreground sources. However, it cannot be excluded that there are more sources even closer to the galaxy nucleus, especially as a contour plot indicates at least one bright blob within the chosen aperture size. Although the galaxy appears to extend a bit further out, the contribution of the remaining part should be low. Object 13 is classified as an elliptical only, which supports the assumption that the whole galaxy should be included and the overall bulge brightness is probably slightly underestimated here.

For object 58 the assessment depends on whether the source is an elliptical or a lenticular galaxy. As described earlier, there are two observation nights for this object with different choices of aperture radii, i. e., the covered region of the source is different for both images. If 58 is actually an elliptical, then the aperture choice for the first night is much too small, even when considering nearby sources that could influence measurements, whereas the aperture for the second night is only slightly too small. Using the 3M-fit radius is more of a lower limit here, potentially even for a S0 classification in the first image. For the first night, the 3M-fit radius coincidentally matches with a central

part of the object at the boundary of which a step of change in brightness can be found for certain visualization settings. The 3M-fit radius of the second night of observing 58 is much larger and encloses most of the source, coming even close to the apparent area of influence from another source nearby. Considering the large difference of areas included in the apertures, the difference in estimated bulge magnitudes of ~ 0.15 mag is rather small. On the one hand, this might be related to the accordingly different apertures used on the central AGN in both images. On the other hand, the influence of the outer parts of the galaxy show a much smaller contribution to the overall luminosity than the inner parts.

Object 95 is special in comparison to the previous two objects, as it is not clear whether the adjacent feature is a close, faint source or actually a part of the galaxy, e. g., a tail from a perturbation such as a merger event. This galaxy is classified as either E or S0. The feature is excluded from the chosen aperture, partly due to its unknown origin and partly because it is questionable whether it can be counted as part of the bulge component, which is valid for either morphological classification from literature. Still, the estimated absolute K-band bulge magnitude is probably a lower limit of the bulge brightness.

4.4 The LLQSO Objects and the M-L Relation

This section describes the objects from the LLQSO sample in the context of a $M_{\mathrm{BH}} - L_{\mathrm{bulge}}$ diagram and in comparison to respective literature relations. Accordingly, the results from the previous sections (Sect. 4.2 and 4.3) are important here. In order to quantify the placements in the diagram, the errors of the quantities have to be discussed.

The errors of the BH mass estimates from the broad emission line fitting could simply be based on the internal scatter of the estimator, as shown in Tab. 4.4. This scatter depends on the broad emission line that is used as a basis for the final BH mass estimate, i. e., either the Pα or the Brγ line, which is the same for some cases, but varies in others. As expected, for most objects the fit of the broad Pα emission line is used as a basis for the final BH mass estimate. The only exceptions are objects 58, 64, and 77, where the Brγ line fit appears more promising than that of the Pα line (see Sect. 4.2.1).

Another point that is made before is that the formal, internal scatter might not reflect the actual errors, as these can be expected to be larger in some cases. Without going more into detail of considerations like the fixed virial factor, the following choice of errors combines the internal scatter with a subjective assessment of the fit. This factors in aspects like the spectral noise that surrounds the fitted emission line and the amount of adjustments within the feedback loop to reach the final fit. If the fitting of the respective emission line appears to work well and noise is low, the internal scatter might be kept. Otherwise the error is accordingly increased (see also Fig. A.3). Table 4.11 shows the respective error values. Those objects that cannot be considered in this section, as a respective bulge magnitude is missing, are already excluded, i. e., objects 70, 74, and 89 are missing in the table.

As described in Sect. 4.3, the method for finding the absolute K-band bulge mag-

Table 4.11: The effectively chosen BH mass estimates for each object and their respective errors. The basis for the adjustments is described in the text. Column (1): Object ID from the LLQSO sample. Column (2): Chosen BH mass estimate, either from the broad Pα or Brγ line. Column (3): Maximal deviation based on the internal scatter as listed in Tab. 4.4. Column (4): Adjusted error for the mass estimate.

ID	BH Mass	Max. Scatter	Adjusted Error
(1)	(2)	(3)	(4)
01	7.08	0.11	0.11
13	6.37	0.17	0.27
20	7.36	0.15	0.30
22	7.04	0.14	0.34
29	7.03	0.12	0.12
53	7.04	0.12	0.32
54	6.83	0.13	0.13
58	7.61	0.08	0.28
64	6.56	0.12	0.22
66	7.78	0.10	0.10
67	7.62	0.07	0.10
71	7.39	0.10	0.10
76	7.39	0.10	0.25
77	6.80	0.16	0.21
78	7.76	0.11	0.11
95	6.86	0.15	0.35
99	6.63	0.15	0.20

nitudes is relatively simplistic. Accordingly, it is less accurate than for example finding the value from a sophisticated morphological decomposition of the host galaxy. It is hard to quantify an error per object from this method, such that the description here concentrates on the choice of a generic error for all estimated bulge magnitudes. The test of the procedure from Sect. 4.3.2 shows that the deviations with respect to literature magnitudes lie in a range of $0.09 - 0.7$ mag. However, it has to be considered that the second largest deviation is 0.26 mag, i. e., less than 40 % of the largest deviation, which does not even consider the logarithmic scale. Thus, it makes sense to take a closer look at the largest deviation of 0.7 mag, which is given for object 29.

While it cannot be ruled out that the method from this work might result in similarly large deviations from more accurate bulge magnitude estimates when applied to the full imaging sample, object 29 appears to be an outlier. Not only is it a barred spiral, which is often associated with a less pronounced central spheroidal component than for example in the case of lenticular galaxies, but it also shows a small angular diameter. The corresponding result is the given small bulge to total luminosity fraction for this object. An overestimate of the bulge magnitude using the procedure of this work can be expected for this object, although the scale of deviation is even larger than anticipated. With a small caveat, that is explained later, this object is considered as an outlier.

The argument of using object 29 from the test sample as an outlier leaves the remaining deviations in a range of $0.09 - 0.26$ mag. In order to be on a safer side and not underestimate the uncertainty by a huge amount, I find it more sensible to choose the new upper limit of deviations in the test sample as an exemplary error. Hence, each estimated bulge magnitude has the error 0.26 mag. However, further discussions of specific objects are not ruled out.

Three objects of the full sample here are missing values for their bulge magnitudes, which still leaves 17 LLQSOs in the sample of this work. While only 14 of these have estimates for bulge magnitudes following the procedure of Sect. 4.3, the three remaining objects have bulge magnitudes provided by literature. These objects are 29, 71, and 77, where the reader probably recognizes object 29 from the previous discussion. For completeness, all three objects with their literature values for the absolute K-band bulge magnitude are listed in Tab. 4.12.

Table 4.12: Values of the absolute K-band bulge magnitudes for three objects as provided by Busch et al. (2014). Column (1): Object ID with respect to the LLQSO sample. Column (2): Name of each object according to the HES. Column (3): Absolute K-band bulge magnitude.

ID	Name	$M_{K,\,\mathrm{bulge}}$
(1)	(2)	(3)
29	HE0253-1641	−22.13
71	HE1310-1051	−23.25
77	HE1348-1758	−21.99

As described in Chpt. 1, a major goal of this work is an increase of the number of

analyzed objects from the LLQSO sample with respect to an earlier series of publications. There is a particular focus on the $M_{\mathrm{BH}} - L_{\mathrm{bulge}}$ relation. Busch et al. (2016) analyze 16 objects from the LLQSO sample in the context of the $M_{\mathrm{BH}} - L_{\mathrm{bulge}}$ relation and plot these objects in an according diagram with some literature relations for inactive galaxies. These 16 objects and the literature relations are also found in the diagram below together with the LLQSOs from this work.

However, while this work adds 17 data points, only 14 are actually new objects in the diagram. The three overlapping objects between the previous and the new sample are those that are listed in Tab. 4.12. Accordingly, their bulge magnitudes are the same for both sets, but their mass estimates are different. As shown in Tab. A.6, the previous SMBH mass estimates are based on fitting the Hβ emission line. For objects 29 and 71 I use the broad Pα line fit for the BH mass estimate, whereas for object 77 I choose the broad Brγ line instead. This results in a small increase of the mass estimate when compared with my broad Pα line fit for this object.

Figure 4.2 shows the $M_{\mathrm{BH}} - L_{\mathrm{bulge}}$ diagram, which includes both samples and four literature relations that are found for inactive galaxies according to Marconi and Hunt (2003), Vika et al. (2012), Graham and Scott (2013), and Kormendy and Ho (2013). A larger version with the included object IDs next to each data point can be found in Fig. A.4.

From a first glance it is already evident that the overall scatter of the data points is similar for both samples. There are no strong outliers in the diagram, i. e., all objects cover similar ranges of BH masses and bulge magnitudes. A few objects appear to agree with the relations for inactive galaxies that are provided by literature, while the largest part of both samples lies systematically below these relations. As the objects are below the literature relations, either the BH masses are lower or their bulges are more luminous in the NIR than the expectation that is based on inactive galaxies. The nature of this deviation is one of the leading questions that the series of publications about the LLQSO sample approached.

When looking more into the details of some specific data points, there are multiple conspicuous aspects. The two leftmost objects are part of the previous and new sample of LLQSOs. Thus, they are connected. In fact, these are objects 77 (leftmost) and 29 (second to leftmost). It is evident that the error bars of my SMBH mass estimates do not include the mass estimates from the previous sample. However, the previous sample features other objects with two different mass estimates that show on average even larger differences than given here between the previous and my mass estimates. If the objects from the previous sample had have error bars, they might actually overlap with the estimates shown here. Switching the mass estimate for object 77 from using the Brγ line to the estimate based on the Pα line, the mass would be closer to the previous estimate, although not much. Additionally, there is a reason that I switched to using the Brγ line fit instead (see Sect. 4.2.1). The third object that is part of both samples, object 71, shows a great agreement with the BH mass estimate from the previous sample, despite the rather small error bars (see also Tab. A.6).

Intriguingly, the new BH mass estimates for objects 29 and 71 shift the data points

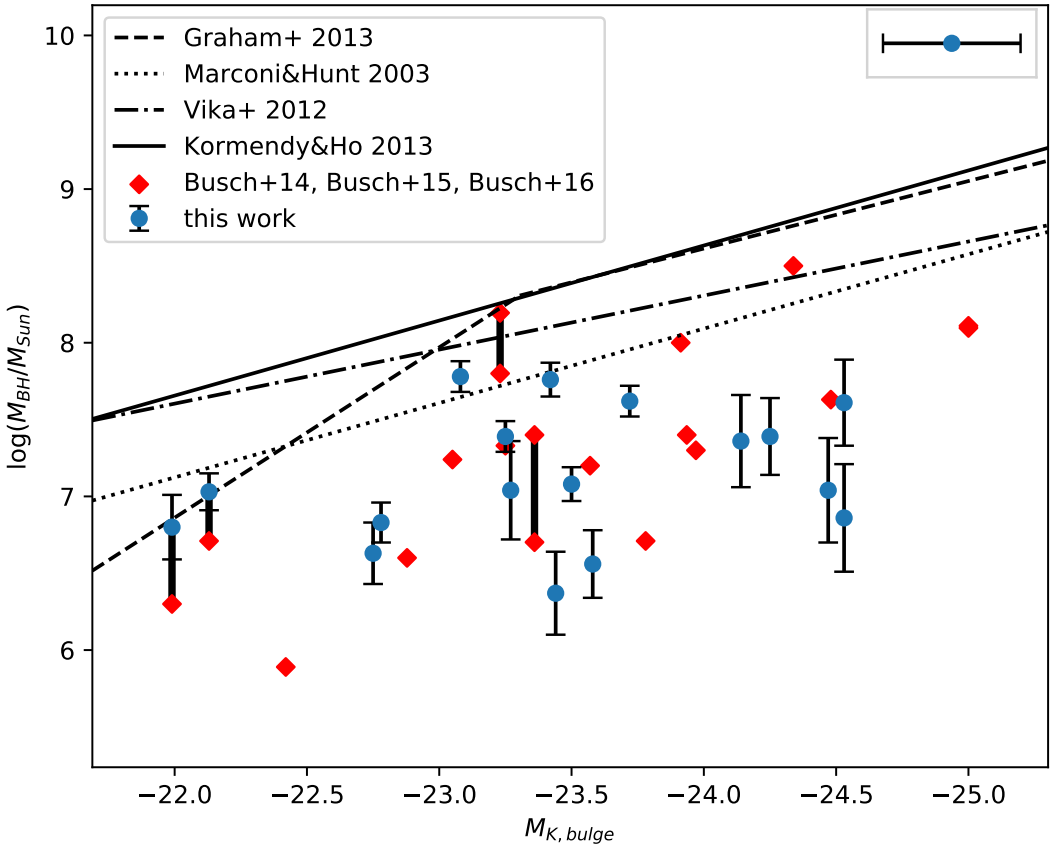

Figure 4.2: $M_{\mathrm{BH}} - L_{\mathrm{bulge}}$ diagram, where the bulge luminosity is substituted by the absolute K-band bulge luminosity. The diagram features four literature relations for inactive galaxies. The x-axis is inverted, such that brighter objects appear further right in the diagram. Objects from the series of publications about the LLQSO sample are included as red diamonds, whereas the objects from this work are added as blue circles. The data point in the box at the top right of the diagram does not correspond to an object, but shows the exemplary error for the bulge magnitudes (see the text for more information). For six objects there are two different mass estimates, where both estimates are connected via a thick vertical black bar. In the case of two objects the mass estimates are so close to each other, that the black bar is effectively not visible.

in comparison to the previous sample to lie almost exactly on the relation as suggested by Graham and Scott (2013). A special aspect about their relation is the bent, which originates from a differentiation between core-Sérsic and Sérsic galaxies that might be based on different merger scenarios, such as dry or wet merger processes. Part of their work is related to feeding of the central SMBH that supposedly results in a different scaling than for dry mergers, where the BH feeding is likely related to the level of AGN activity. In other words, their sample is less restricted to inactive galaxies than the other literature relations. Considering the AGN nature of the objects presented here, this connects the LLQSO sample with the relation. Together with more findings from these authors (Scott et al. 2013; Graham and Scott 2015), it is suggested that the steeper relation for lower mass BHs ($M_{\mathrm{BH}} \lesssim 10^8\,\mathrm{M}_\odot$) is related to a faster BH growth with respect to the bulge luminosity than is expected from the other relations.

Despite the earlier reasoning why the uncertainty of object 29 is considered an outlier, an open question is the implication of a similar deviation for objects from this work, i. e., a shift of about 0.7 mag towards lower bulge luminosities. On the one hand, in that case more objects would agree with the literature relations, although not all. Additionally, the similarity of the scatter between the previous and the new sample would decrease, showing the new sample to feature on average much lower luminosities. On the other hand, the previous reasoning shows that it is unrealistic to expect the same overestimated brightness from object 29 for all other objects as well. For some objects, such as 13, 58, and 95, the estimated bulge brightness shown here is probably rather a lower limit than a highly overestimated luminosity (see the discussion in Sect. 4.3.3). One exception from this is object 99, which can be found as the third object from the very left. If concentrating on the galaxy only, the image of object 99 is astonishingly similar to 29. For many visualization settings of the images the sources appear almost the same. Hence, the question arises whether the bulge magnitude of 99 is overestimated the same way as it is for 29. As mentioned earlier, I tried to apply the method "blindly", i. e., concentrating on the given information per image and object, while avoiding influences for example from the observation of the same object in another night. The robustness of the procedure that I found from this is described in Sect. 4.3.3. Accordingly, the chosen aperture size for objects 29 and 99 turns out to be in principle the same in both cases, which is two times the median Moffat FWHM. This supports the assumption that the brightness of the bulge of object 99 might be overestimated on a similar scale as it is for 29, i. e., possibly even around a value of 0.7 mag. However, it should be noted that even a correction for such a large deviation shifts the object in the $M_{\mathrm{BH}} - L_{\mathrm{bulge}}$ diagram only so far left, that it is still barely below all literature relations. Obviously, the deviation of object 99 from the literature correlations would then be much smaller than for the current estimate, especially considering the relation by Graham and Scott (2013).

The final publication of the series about the LLQSO sample (Busch et al. 2016) contains an argument of the authors that the host spheroids are overluminous in contrast to the explanation of the deviation via undermassive BHs. In principle both possibilities can be explained via a co-evolution of the central SMBHs and the bulges of their host galaxies. It is argued that there is no need for merger events, but secular evolution

is sufficient, i. e., internal mechanisms such as the feeding of the central AGN and its according feedback. Busch et al. (2016) also target the nature of the excitation mechanisms that lead to the overluminous bulges. Not surprisingly they find overall similar emission lines as I do (see Sect. 4.2.2 and A.3), e. g., the AGN tracer line [Si VI], the shock tracer and supernova rate estimator [Fe II], and multiple lines for molecular hydrogen H_2. Likely based on an abundance of molecular gas in LLQSOs (Bertram et al. 2007), many of their objects are found to be forming stars in the bulges. This stands in contrast to the assumption that bulges mainly consist of old stars and SF is typically not expected. Molecular gas is a basis for SF (e. g., Kennicutt 1998), but the connection to AGNs is not clear. Busch et al. (2016) mention that the findings related to the flow of molecular gas show outcomes that still need to be connected, e. g., out-flowing feedback contains molecular gas (García-Burillo et al. 2014), while an inflow of H_2 from the galactic plane towards the center fuels the AGN (Riffel et al. 2015).

A large open question is about duty cycles of AGNs, i. e., whether there are phases of more and less activity in the galactic nuclei, and if so, whether these cycles are regular or not. Related to this are merger scenarios, that are often associated with a change in SF and AGN activity. These are not bound to only happen within a specific time frame, but might occur in the past, present, and future. Combined with this is the overall question about distance-specific stages of evolution in AGNs, e. g., the finding of a peak AGN activity at $z \approx 2$. This is one of the signs that indicate an expectancy of certain AGN characteristics for respective distances. In the context of duty cycles, Busch et al. suggest the following scheme: First, an onset of SF results in brighter bulges, i. e., the data point of a galaxy travels to the right in a diagram as shown in Fig. 4.2. This is followed by stronger feeding (and feedback) of the central SMBH, which results in a faster growth of the BH mass than the respective bulge luminosity. The object travels up in the diagram and back onto the relation as suggested for inactive galaxies. An object that travels along this path shows an increase in AGN activity, as the BH feeding is connected to its activity level.

The enlarged sample of 30 different LLQSOs might well agree with this scenario. Given the findings by Busch et al. (2016) and the agreement between the previous and the new sample of LLQSOs, all parameters match the suggested description. The different distances of each data point from the literature relations, including the objects that are close or even on the relations, can be explained by their different stages on the path. The objects close and on the relations correspond to those that might start or end their trajectory following the previous description. Objects further away might then travel even further out, redirect their path, or follow a returning trajectory towards the relation for inactive galaxies. Indications for this can be found when considering the spectra of the LLQSOs from the new sample that are furthest right in the diagram, i. e., objects 20, 22, 58, 76, and 95. Although it cannot be ruled out that these objects might travel even further right, it is more likely that they follow a trajectory which points back towards the literature relations. In fact, all of their spectra contain the AGN tracer [Si VI], with the exception of the rather noisy and feature-less spectrum of object 95. Turning the argument around, then the objects further left in the diagram

might be expected to show more signs for SF and shocks. However, as the starting point for the path of all objects is uncertain it is less meaningful to make a statement similar to that for the objects on the right of the diagram. In agreement with this uncertainty the spectra that contain more hints towards shocks and molecular gas seem randomly spread in the diagram. Based on the existence of the AGN tracer in the spectra of the objects on the right, the proposed idea of the trajectories is still strengthened.

Subsequently, it makes sense to analyze the placements of objects with respect to groups that might show a systematic behavior. This might be based on certain properties of the host galaxy and/or the AGN. The relatively low amount of available information here makes such an analysis difficult, and simply from the diagram as it is shown in Fig. 4.2 no grouping of objects can be found. However, one property that is known relatively certain for each object is the redshift. A respective introduction of the redshift into the diagram can be seen in Fig. 4.3.

Although not a strictly followed rule, there appears to be a slight trend between the redshift and the placement of each object along the diagonal from the lower left to the upper right. In fact, this trend becomes stronger for the objects that are close to or even on the literature relations for inactive galaxies. There is a rule of thumb that more distant AGNs are likely to be more powerful, which is partially based on the peak of AGN activity at $z \approx 2$ (see above), but also related to selection effects, as Earth-bound observers cannot detect faint sources at large distance. From this rule the observed trend in the diagram seems expected. However, the particularity that the trend grows weaker for the objects that show larger deviations from literature relations might be connected to the nature of the deviation. It could be argued that as soon as a change of one parameter results in a deviation from the expected behavior, this spreads to other parameters, and the whole evolution of the object is thrown off its regular course. An even larger sample of LLQSOs and many more object characteristics are needed for a more detailed analysis.

Different findings with respect to the $M_{\mathrm{BH}} - L_{\mathrm{bulge}}$ relation itself can be found in many publications in literature. As an early example Woo and Urry (2002) do not find a correlation between the BH mass and its host luminosity. In contrast to this, McLure and Dunlop (2002) analyze a sample consisting of AGNs as well as local inactive galaxies, where they do not find a difference between these sub-samples, and only a small scatter for their combined sample. Thus, they even suggest to use the relation for BH mass estimates of high-redshift galaxies. However, especially for distant galaxies the case of a cosmological evolution might need to be considered. While Bennert et al. (2010) conclude that the $M_{\mathrm{BH}} - L_{\mathrm{bulge}}$ relation evolves with the redshift, the authors find that the $M_{\mathrm{BH}} - L_{\mathrm{total}}$ relation does not, leading them to the conclusion that the bulges might grow via a redistribution of disk stars. Schulze and Wisotzki (2011) and Schulze and Wisotzki (2014) find no evidence for a general cosmological evolution of BH – bulge relations after taking selection effects into account.

If an evolution of the host galaxy luminosity or its bulge component exists, it has to be considered especially in the context of the $M_{\mathrm{BH}} - L_{\mathrm{bulge}}$ relation. Without an assumption about a passive luminosity evolution Ding et al. (2017) find that their data

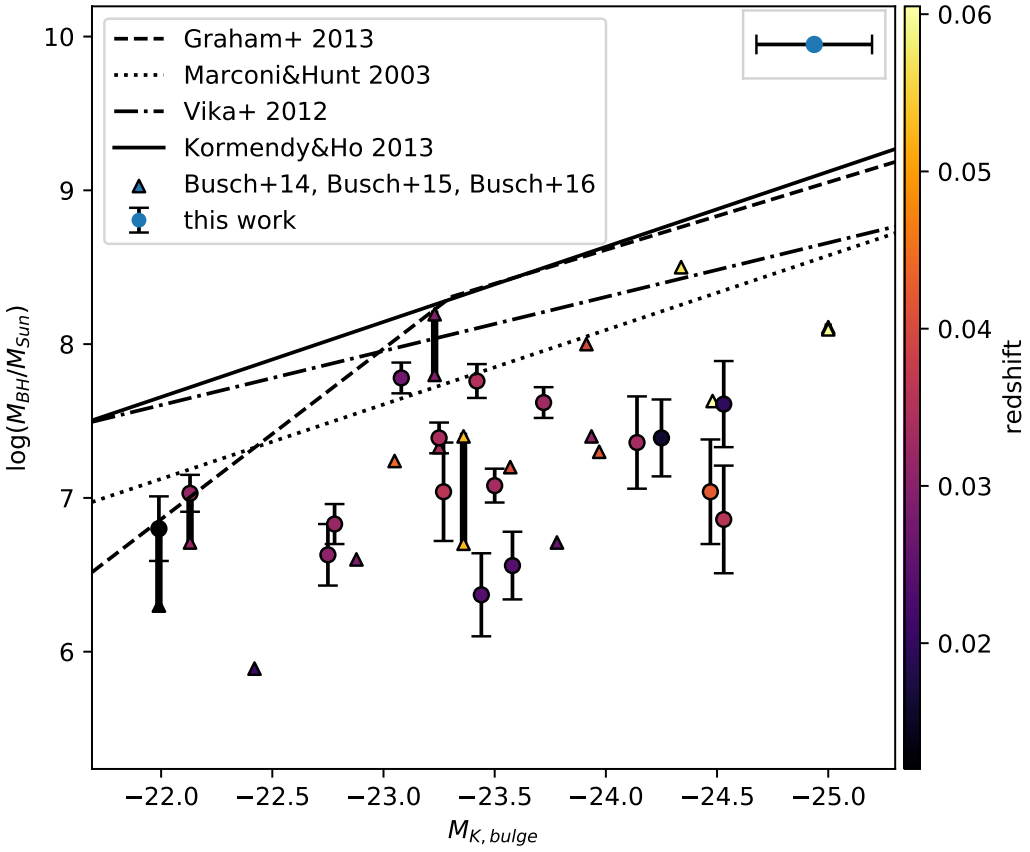

Figure 4.3: $M_{\mathrm{BH}} - L_{\mathrm{bulge}}$ diagram similar to Fig. 4.2, but including the redshift as a color-coded filling for each object. For an easier distinction between samples, the LLQSOs from the previous publications are shown as triangles here. Other diagram properties are the same as in the previous figure, i. e., the data point in the box at the upper right only indicates the exemplary error of the bulge magnitudes.

for high-redshift objects (up to $z \approx 4.5$) match the local relations for L_{bulge} or L_{total}. However, after correcting for a passive luminosity evolution, they even find that the BHs appear to reside in less luminous galaxies than locally observed. Their result is consistent with a scenario where the BH growth predates that of the host galaxy, which has been predicted from simulations (Croton 2006). Similar results are found by Peng et al. (2006a,b). Ding et al. (2020) show results for closer objects ($1.2 < z < 1.7$), which are in agreement with local samples. Some outliers tend towards higher BH masses, but they state that no strong conclusions can be made. These cases that stand directly in contrast to the findings of this work are partially explained by a respectively switched evolution trajectory based on a cosmological evolution, i. e., the BH growth is found to precede that of the bulge component of its host (Bennert et al. 2010; Ding et al. 2017).

Based on the often larger distances of the objects in these publications that stand in contrast to the findings here, an effect based on the redshift might come into play, much stronger than the previously discussed implication for Fig. 4.3. However, it should be noted that the observation of undermassive BHs and/or overluminous bulges is not restricted to the LLQSO sample. Other AGNs that lie below local relations have been found in the optical, whereas the interpretations are slightly different. Nelson et al. (2004) and Bennert et al. (2011b) attribute their finding to overluminous host bulges, similar to the interpretation in this work, while Kim et al. (2008) tend towards undermassive BHs. Merloni et al. (2010) agree with either explanation, brighter hosts or smaller BH masses. However, after considering a passive evolution of stellar populations, the deviation vanishes and the authors find a broad agreement with local relations where some objects even show BH masses above local relations. An interpretation that potentially matches the finding of this work is given by Urrutia et al. (2012), as the authors describe that objects might be below the local $M_{\mathrm{BH}} - L_{\mathrm{bulge}}$ relation due to a bulge growth first, which is followed by the growth of the BH.

Jiang et al. (2011) find that lower mass SMBHs ($\sim 10^5 - 10^{7.6}\,\mathrm{M}_\odot$, with most masses $<\sim 10^6\,\mathrm{M}_\odot$) are below the $M_{\mathrm{BH}} - L_{\mathrm{bulge}}$ relation, which agrees with the bent in the literature relation by Graham and Scott (2013). Other authors describe a flattening in the low-mass region, i. e., a shallower slope especially for $< 10^6\,\mathrm{M}_\odot$ (Greene and Ho 2006), which emphasizes the debatable nature of the topic. However, Jiang et al. (2011) argue that their results might be connected to a differentiation between pseudobulges and classical bulges, and they mention the idea that pseudobulge luminosities might not scale with BH masses at all (see also Kormendy et al. 2011).

More support for the results and interpretation from the LLQSO paper series and this work comes from different observations of SF in the hosts of AGNs, which is thought to depend on the overall luminosities of the host and the AGN (e. g., Kauffmann et al. 2003; Jahnke et al. 2004; Hickox et al. 2009; Merloni et al. 2010; Bongiorno et al. 2014). According to Jahnke et al. (2009) SF is not even necessary for shifting objects towards the higher bulge luminosities, as a redistribution of stars from the host galaxy into its bulge component is sufficient. This agrees with the result mentioned previously for Bennert et al. (2010). Bennert et al. (2011a) argue that the bulge growth might be mediated via secular evolution and/or minor merger events. The redistribution of stars

into the central spheroid requires another component that is distinctive from the bulge, such as the disk from a late-type galaxy. In that case the combination of a redistribution of stars into the bulge, as well as an onset of SF would lead to the respective objects likely showing an overluminous bulge component relative to a given BH mass for local $M_{\mathrm{BH}} - L_{\mathrm{bulge}}$ relations.

It is yet unclear why there might be such differences in observations. A cosmological evolution might be a significant factor, as the relatively close LLQSOs show a clear trend that is not universally confirmed. As mentioned before, there is a possibility of duty cycles for AGNs that are roughly dependent on the age of a galaxy. From this follows that many galaxies are expected to show similar deviations at certain evolutionary stages. The details are not certain and might depend on essentially all parameters, such as host galaxy and bulge morphologies, major and minor merger events, secular evolution that includes a possible redistribution between disk and bulge stars, Eddington ratios, and many more parameters.

Chapter 5

Summary, Conclusion, and Outlook

In this work I increased the number of analyzed objects from the LLQSO sample with respect to the BH mass M_{BH} – bulge luminosity L_{bulge} relation by almost a factor of two in comparison to the sample analyzed by Busch et al. (2014) and Busch et al. (2016). LLQSOs are found as a part of the HES by application of a limiting redshift, $z \leq 0.06$. Based on their properties, the objects from the LLQSO sample fill a gap between local Seyferts of low to moderate AGN activity levels and distant, powerful quasars. One important finding by Busch et al. (2016) is that the LLQSOs do not follow $M_{\mathrm{BH}} - L_{\mathrm{bulge}}$ relations from literature as they are suggested for inactive galaxies. On average, the LLQSOs that the authors analyze are found to fall below these relations, indicating either undermassive BHs or overluminous bulges of the AGN host galaxies. The main objective of this work was to enlarge the number of LLQSOs that are analyzed with respect to the $M_{\mathrm{BH}} - L_{\mathrm{bulge}}$ relation. From this, I reinvestigated their findings in the larger sample to identify parallels and possibly differences with respect to previous results.

This work builds upon two NIR data sets of external galaxies from respective observation periods, one in February 2019 and one in September 2019. Both data sets originate from observations with the NTT using the SOFI instrument. The applied observation modes are broad band filter imaging and long-slit spectroscopy, which extend across multiple bands. Here is a particular emphasis on K-band observations.

Based on a rewritten reduction script for the raw spectroscopy files from my master thesis, and the provided data reduction pipeline for SOFI imaging files, I included as many files as possible in each reduction procedure. For this I adjusted the reduction script for the spectroscopy files, such that it can include irregular observation sets. Depending on the nature of the problems I repaired faulty files for imaging data as well. I tested the extraction of spectra for different aperture widths and found a corresponding default choice for the spectra that were analyzed afterwards.

The estimation of SMBH masses using NIR spectra is based on a method described by Kim et al. (2010). A common mass estimation method from single-epoch measurements

uses the broad emission line of the first spectral line from the Balmer series, the Hα line. The authors translated this estimation method into respective estimators that make use of the NIR emission lines Paschen-α (Pα) and Paschen-β (Pβ). Since the Pβ emission line is not part of the spectra here, the mass estimation method relies on the broad Pα emission line only. However, the area between the atmospheric transmission windows, the H-band and the K-band, features strong, high-level noise in most spectra, which covers the expected position of the Pα emission line. As this line is often a powerful, distinct feature in the respective spectra, mass estimates might still be possible. Furthermore, I made use of the Brackett-γ (Brγ) emission line, as it is expected to be connected to the Pα line for a specific line ratio. Although the spectra here feature the Brγ line within the less noisy K-band, it is much weaker than the Pα line. Thus, even a lower noise level can still interfere with an identification and respective fitting of the line. I tried to fit each emission line, Pα and Brγ, with a double Gaussian that corresponds to two components, a narrow and a broad line component. This was done by applying a fit procedure to both lines in all spectra, using an iterative feedback loop for fit adjustments. A presumed similar origin of both broad lines helped in finding boundaries for corresponding fit parameters, which is important in the context of estimating BH masses. I found BH mass estimates for all LLQSOs from the new sample using either the broad Pα or Brγ line. The choice of emission line for the estimate is based on an assessment of all fits, for example with respect to the noise level at the base of each emission line and the difference between the total line fit and the spectrum.

The method for extracting bulge magnitudes is more simplistic than using an elaborate morphological decomposition, but consequently much faster. This is especially evident when applied to multiple different objects. It relies mainly on a visual inspection of each galaxy in combination with its angular size and, if available, its morphological classification. By testing the procedure on a small sample of objects with known absolute K-band bulge magnitudes from a sophisticated morphological decomposition (Busch et al. 2014; Busch et al. 2015), I found that the faster procedure from this work produces results that behave as rough estimates. The quality of the results is adequate, while also showing limitations that have to be considered under specific circumstances.

In total 17 data points were added to a log – log representation of a $M_{\mathrm{BH}} - L_{\mathrm{bulge}}$ diagram that features the previous sample of LLQSOs together with four literature relations for local inactive galaxies. This corresponds to the addition of 14 new objects, enlarging the total sample of analyzed LLQSOs from 16 to 30 objects. I found that the addition of more LLQSOs to the previous sample results in a similar scatter, which can be expected based on the selection criteria for the whole LLQSO sample. Busch et al. (2016) argued that the deviation of LLQSOs from the relations for inactive galaxies is based on overluminous bulges, as they found signs for SF in the LLQSOs. My findings agree well with this. In particular, I found in multiple spectra indications for the same lines as Busch et al. (2016). This includes the AGN tracer [Si VI], the shock tracer [Fe II], and different lines that are associated with molecular gas, specifically H_2. Molecular gas is considered a basis for SF and it appears that LLQSOs might be forming stars in their bulges, which is not self-evident, as a common assumption is that bulges are mainly

devoid of gas and consist of old stars.

A potential interpretation of the deviation between LLQSOs and the literature relations for inactive galaxies is based on duty cycles of AGNs. In order to reach their placements below the suggested relations, the objects might start with an onset of SF, which increases the brightness of their bulges, i. e., an effective shift of the objects in the $M_{\mathrm{BH}} - L_{\mathrm{bulge}}$ diagram towards higher luminosities. From this follows an increased feeding of and likely also feedback from the central SMBH. The level of AGN activity increases and the BH mass grows. Accordingly, objects are shifted back towards the literature relations. Their trajectory, especially the phase of BH mass growth, then corresponds to the idea of duty cycles for AGNs. A question that remains open is the origin of the trigger event that puts objects on the suggested path. The onset of SF might be based on merger processes, secular evolution, or potentially even both, as well as other factors. One example suggested in literature is a redistribution of stars for example from a disk into the bulge component.

When including the redshift in the diagram as an additional quantity, a trend can be seen. Due to selection criteria, more distant objects are expected to be more luminous and show on average larger BH masses. Here, the crux of the matter lies in a differentiation between objects very close to the literature relations for inactive galaxies and those that deviate further from these relations. The former objects appear to follow the expected trend more rigorously than the latter. Although the nature of the trigger for the deviations is still unclear, it might be that the change of a single parameter exerts an influence on other parameters as well, which results in the overall deviation.

This work achieved a large increase of the sample of analyzed LLQSOs in comparison to the sample from the previous project by almost doubling the number of objects with respect to the $M_{\mathrm{BH}} - L_{\mathrm{bulge}}$ relation (Busch et al. 2014; Busch et al. 2015; Tremou et al. 2015; Busch et al. 2016; Moser et al. 2016). Nevertheless, the topic allows for more analyses, as there are many more options that cover different branches of ideas. The application of an elaborate morphological decomposition to the imaging data would open up new possibilities, while probably improving the error margins of the estimated bulge magnitudes. As a result, missing classifications of the host galaxies could be added and existing classifications upgraded. Including these in the analysis of the deviations of the LLQSOs from the relations of inactive galaxies would allow to put emphasis on a differentiation between different types of bulges. Depending on each bulge type, namely ellipticals, classical bulges, and pseudobulges, objects might show a grouping behavior that cannot be seen yet. This is especially relevant as pseudobulges might be the reason that some objects do not follow BH – bulge relations as expected (e. g., Kormendy et al. 2011).

As described in Sect. 3.2 and 4.1, the data sets that this work is based on are partially incomplete. Reasons for this can be related to bad weather or problems with the telescope, which resulted in a disruption of the respective observation. Hence, some objects are missing either observations via long-slit spectroscopy or the imaging counterpart. In the case of spectroscopy data, all files for objects that can be reduced using the respective reduction procedure from Sect. 3.3.1 are included in this work. The following

analysis of the spectra of these LLQSOs results in BH mass estimates for all respective objects. In contrast to this, there are more LLQSOs from imaging observations that are not considered yet, as they are missing in the spectroscopy data. This includes J-band and H-band filter imaging files. Despite their missing counterparts in spectroscopy, an analysis of these imaging files is possible.

Some spectroscopy files still contain more that can be analyzed. As an example, in some cases the slit position is chosen to include another object as well, such as the nucleus of a nearby galaxy. This is given for objects 67 and 99 (see Fig. 3.2 for an example). An analysis of the second object along the slit is still pending in both cases.

As described in Sect. 4.2.2 (and accordingly Sect. A.3), the Pα and Brγ emission lines are not the only features that can be recognized in the spectra. In some cases these line identifications have to be treated with caution, as the respective features are hardly distinct from the noise that can be seen in the spectra, and they were only noted as they might correspond to a line that is listed in literature. However, other lines are strong and distinctive. Depending on the nature of these easily recognizable lines, applying a fitting procedure might make sense as well (see also Busch et al. 2016). The limiting redshift of the LLQSO sample is supposed to ensure the inclusion of CO absorption band heads. This is especially true for the CO(2-0) band head in the K-band, as it can be used for an analysis with respect to the stellar populations and stellar kinematics (Gaffney et al. 1995; Fischer et al. 2006). However, the identification of CO band heads appears relatively problematic. While there are indications for these lines in the spectra of some objects, they do not appear to be distinct and might be heavily influenced by noise. Due to their importance it might still make sense to analyze these lines in more detail.

Another possibility that makes use of emission lines in the spectra is to put the objects in a diagnostic diagram. A version of a diagnostic diagram that is based on narrow NIR lines uses the $H_2(1-0)S(1)\,/\,\mathrm{Br}\gamma$ ratio on the x-axis and the [FeII]1.257µm / Pβ ratio on the y-axis. The low resolution of the spectra might impede the fitting of these lines, especially if these are inherently weak features in the spectra. Another issue is that both lines from the second ratio, i. e., for the y-axis, are not even available in the spectra here. However, the two lines can be substituted via line conversions ([FeII]1.257µm = [FeII]1.644µm / 0.744 and Pβ = Pα / 2.05). The groundwork for this exists already, as I tried to create an according diagnostic diagram based on an automated fitting procedure. As the automated fitting of lines turned out to be highly sensitive to surrounding noise, a slight adjustment is still necessary. The implementation of a fitting approach similar to the one described in this work would yield more compelling results.

It is clear that there is potential for more analyses here. More properties are hidden within the current data sets and the applied procedures can be compared to established alternatives, e. g., by applying a morphological decomposition to each imaging object. The addition of missing data would increase the sample size even more, potentially revealing new findings that are currently impossible to see. While this is the conclusion of this work in particular, the project and overall topic is far from finding an end.

Appendix A

A.1 Further Figures and Tables

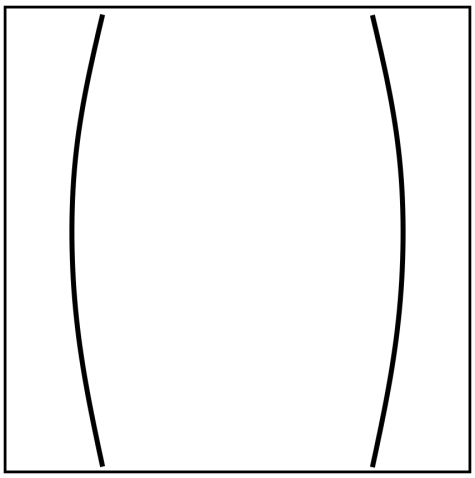

Figure A.1: Schematic sketch that shows a principally possible, but exaggerated distortion of the slit-spectroscopy images. As in a previous figure, the x-axis corresponds to the spatial axis, while the y-axis is the dispersion axis. The two curved lines correspond to an image that combines either two sources or one source at two different positions. Without the distortion effect, both lines would be straight and parallel to the y-axis.

Table A.1: Observational information for the available spectroscopy data in this work. Column (1): Object ID. Column (2): Date of observation, i. e., the night in 2019 in which each object was observed. Column (3): The total integration time in seconds that is used to create a final reduced image. Column (4): Average seeing from the file headers in arcseconds.

ID (1)	Observation Date (2)	Integration Time (3)	Seeing (4)
01	Sept. 21 – 22	7200	2.350
13	Sept. 21 – 22	3600	1.185
20	Sept. 12 – 13	7200	1.188
22	Sept. 21 – 22	5400	1.640
29	Sept. 12 – 13	4500	1.026
53	Febr. 16 – 17	7200	0.858
54	Febr. 17 – 18	8400	0.669
58	Febr. 21 – 22	6720	1.006
64	Febr. 18 – 19	7280	2.070
66	Febr. 22 – 23	8100	0.887
67	Febr. 16 – 17	7200	0.898
70	Febr. 17 – 18	8400	1.060
71	Febr. 18 – 19	8400	2.070
74	Febr. 18 – 19	5100	2.070
76	Febr. 21 – 22	7200	0.595
77	Febr. 22 – 23	9450	0.852
78	Febr. 21 – 22	6750	0.629
89	Sept. 07 – 08	4500	1.600[1]
95	Sept. 21 – 22	6300	1.363
99	Sept. 23 – 24	5400	1.360

[1]: Seeing values from the file headers are stuck at a single value and thus probably erroneous, but the only available information.

Table A.2: Observational information for the available imaging data in this work. Four objects appear twice, as each of these objects has two different nights of observations. Column (1): Object ID. Column (2): Date of observation, i. e., the night in 2019 in which each object was observed. Column (3): The total integration time in seconds that is used to create a final reduced image. Column (4): Average seeing from the file headers in arcseconds.

ID	Observation Date	Integration Time	Seeing
(1)	(2)	(3)	(4)
01	Sept. 10 – 11	200	1.600[1]
13	Sept. 07 – 08	200	1.600[1]
20	Sept. 07 – 08	180	1.600[1]
22	Sept. 09 – 10	200	1.600[1]
53	Febr. 15 – 16	210	1.017
54	Febr. 15 – 16	210	1.011
58	Febr. 14 – 15	315	0.964[2]
58	Febr. 23 – 24	140	1.028
64	Febr. 15 – 16	155	2.674
64	Febr. 23 – 24	100	4.167
66	Febr. 15 – 16	150	2.608
66	Febr. 23 – 24	100	4.194
67	Febr. 15 – 16	170	0.770
76	Febr. 16 – 17	70	0.782
76	Febr. 23 – 24	60	0.894
78	Febr. 16 – 17	175	0.835
95	Sept. 09 – 10	200	1.600[1]
99	Sept. 07 – 08	250	1.600[1]

[1]: Seeing values from the file headers are stuck at a single value and thus probably erroneous, but the only available information. [2]: All provided seeing values here are invalid. The given seeing is the average from observations directly before and after this object.

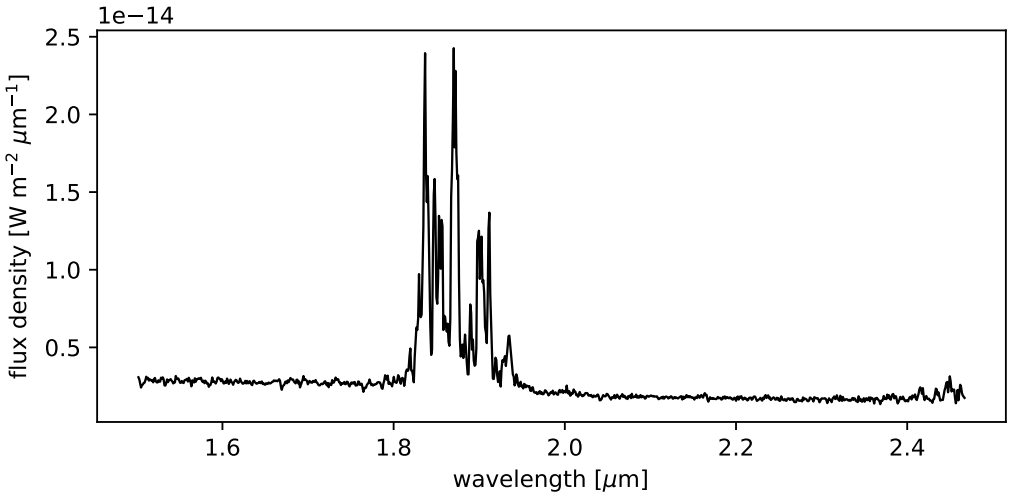

54 HE0608-5606

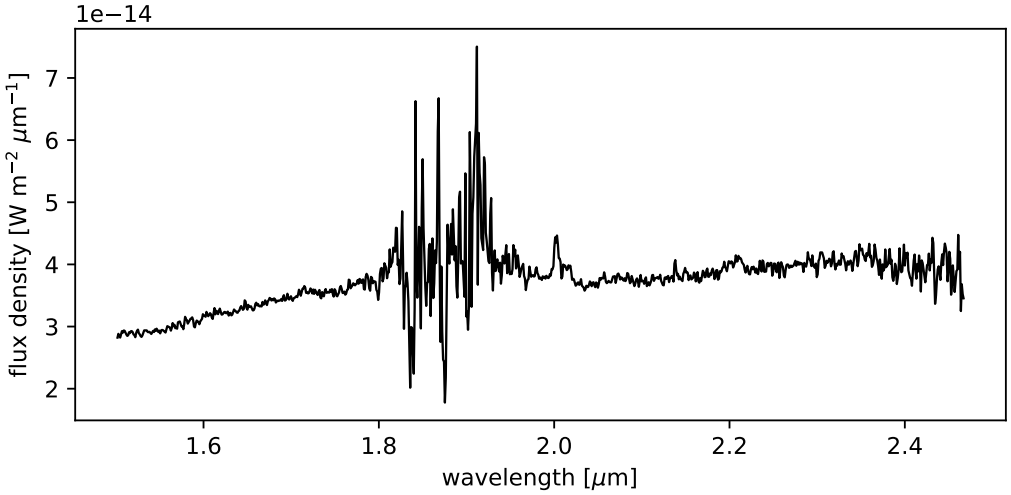

58 HE0949-0122

Figure A.2: All spectra of this figure are not corrected for respective redshifts and correspond to raw extractions. The two exemplary spectra shown here feature particularly strong noise in the band gap between the H-band and K-band. In both cases the noise is dominating the overall flux density levels. Although there are indications, the Pα emission line is not easily apparent in these spectra.

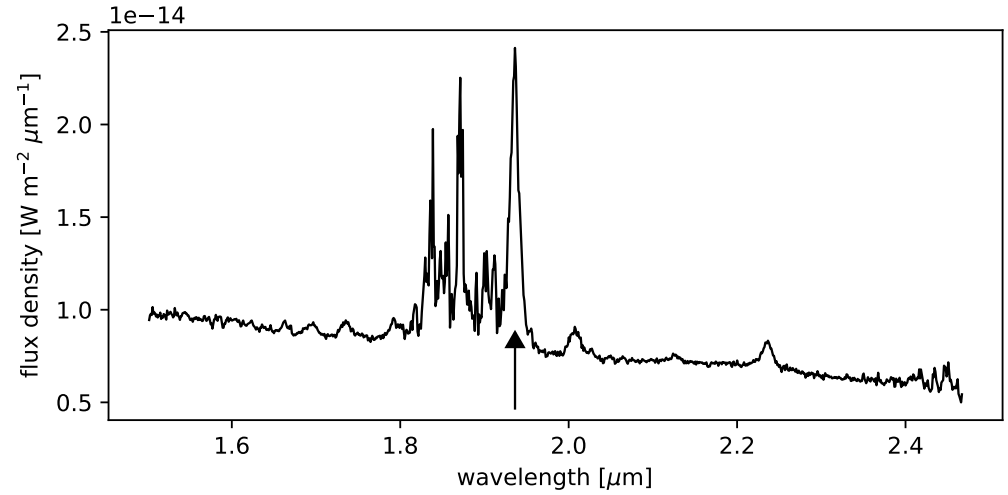

67 HE1143-1810

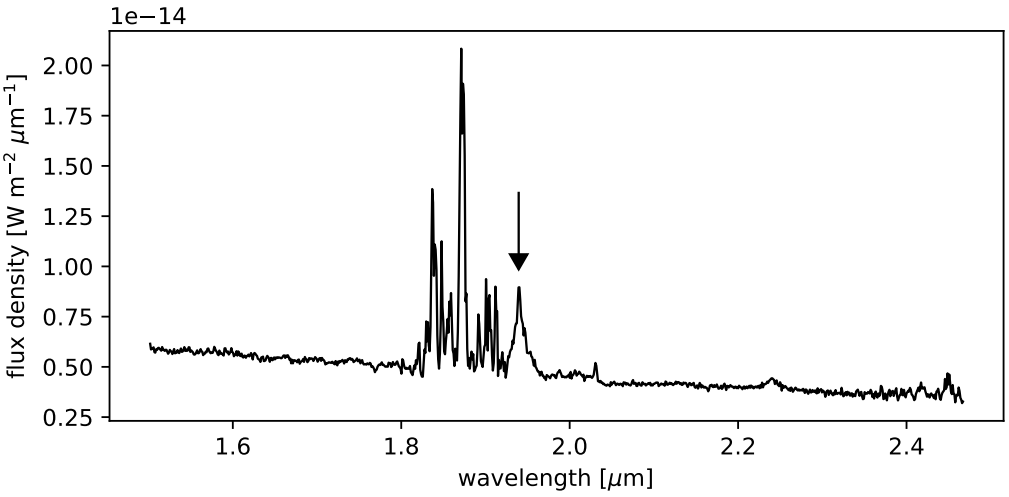

71 HE1310-1051

Figure A.2: (Cont.) Two more examples with relatively strong noise in the band gap. However, in both cases here the Pα feature is strong enough to be easily recognized, as indicated by the arrows.

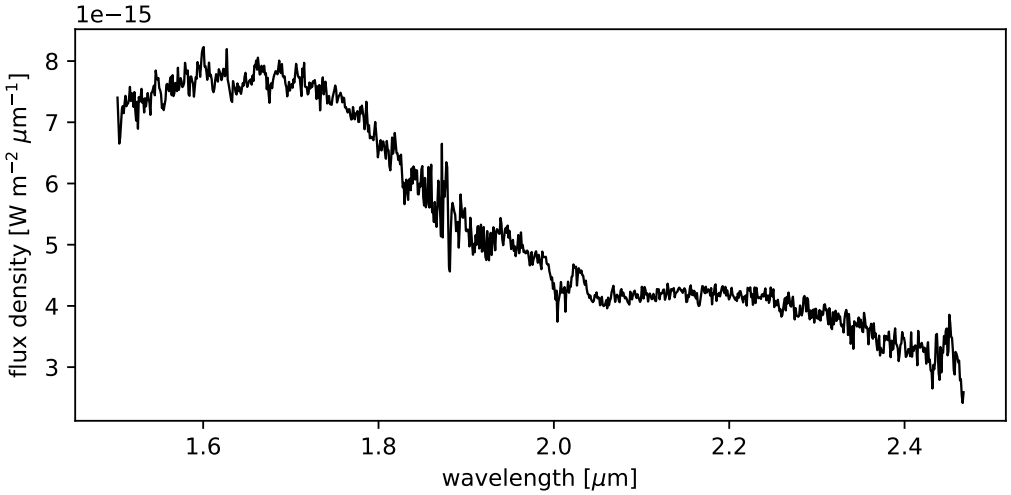

20 HE0149-3626

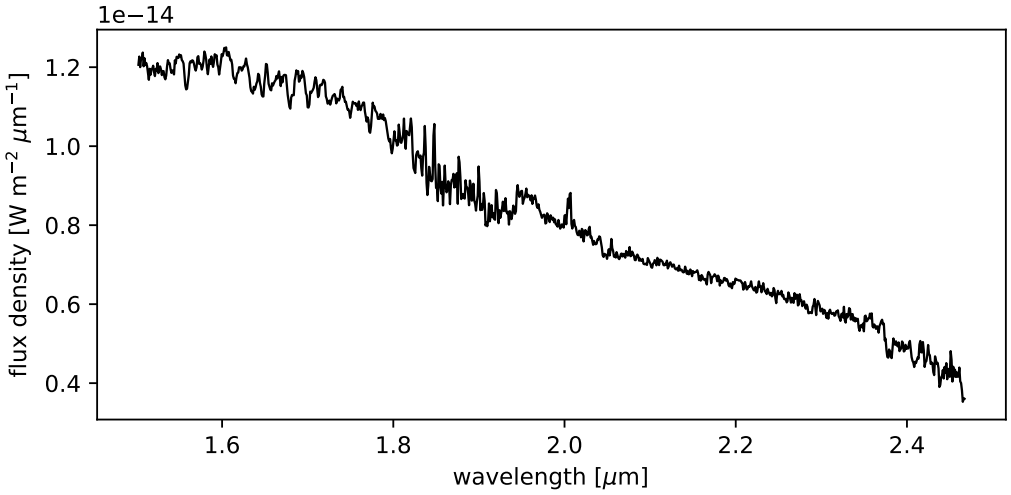

95 HE2322-3843

Figure A.2: (Cont.) These two examples show much lower noise levels in the band gap. Most likely the observation conditions are much better than for the previous objects of this figure. Still, any potential features within the region of the band gap need to be treated with great caution. It is important to note that the Pα emission line is not easily apparent for these objects.

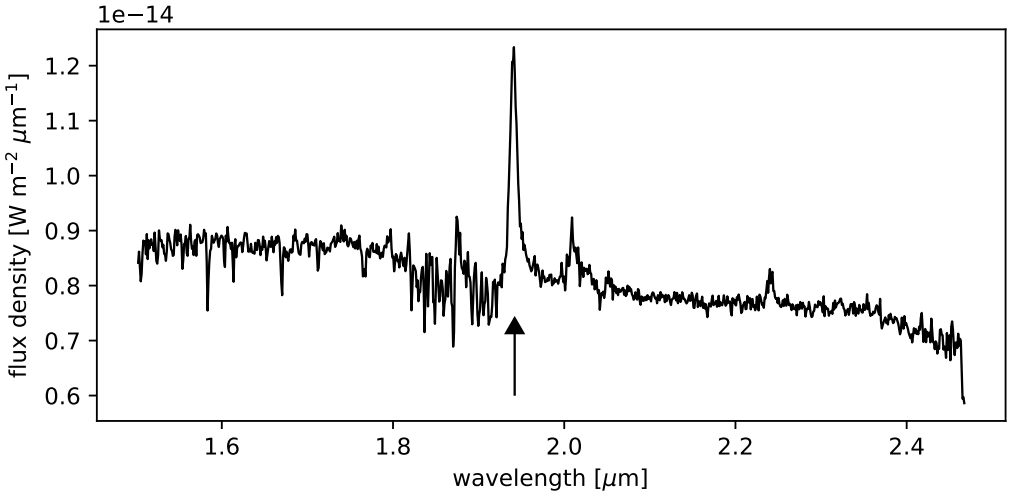

01 HE0003-5023

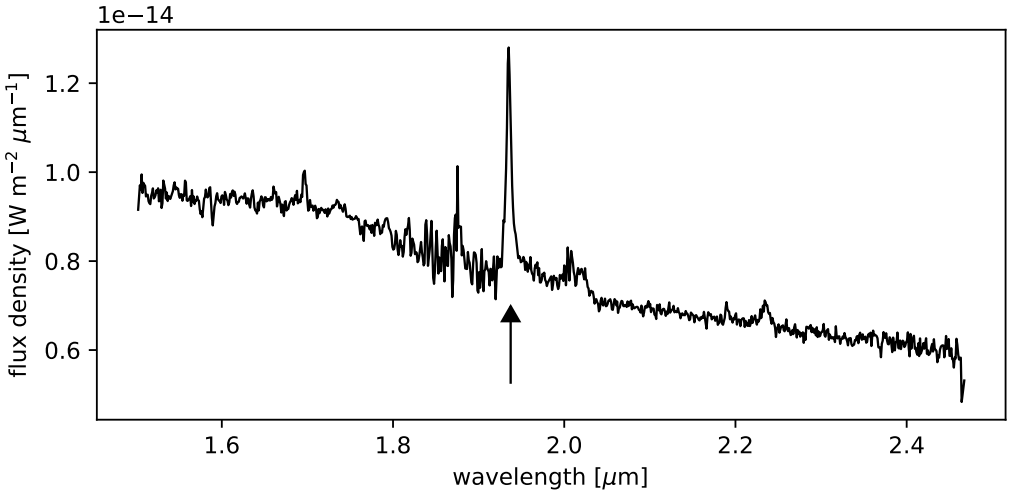

29 HE0253-1641

Figure A.2: (Cont.) Yet two more examples for spectra with a relatively low noise in the band gap. In contrast to the previous two spectra the Pα emission line (marked by the arrows) is easily apparent and the overall dominating feature in each spectrum.

Table A.3: Important line parameters from fitting simultaneously a narrow and broad component to the Pα emission line. The expected central wavelength is 1.87561 µm, but small deviations from this are possible. Column (1): Object ID from the LLQSO sample. Column (2): Narrow line position, i. e., the central wavelength at the peak of the fit profile in µm. Column (3): Narrow line width, i. e., the FWHM of the fit profile in $\mathrm{km\,s^{-1}}$. Column (4): Narrow line flux of the fit profile in $10^{-20}\,\mathrm{W\,m^{-2}}$. Column (5): Broad line position (see Col. (2)). Column (6): Broad line width (see Col. (3)). Column (7): Broad line flux (see Col. (4)).

ID	Narrow Line Component			Broad Line Component		
	Position	FWHM	Flux	Position	FWHM	Flux
(1)	(2)	(3)	(4)	(5)	(6)	(7)
01	1.87760	650.0	303.9	1.87797	1634.5	3590.3
13	1.87550	750.0	75.0	1.87570	1314.2	622.6
20	1.87660	250.0	40.1	1.87700	3388.3	685.2
22	1.87733	250.0	40.0	1.87550	2100.0	672.6
29	1.87507	626.3	1136.7	1.87553	1715.5	2536.9
53	1.87200	607.0	510.4	1.87400	1850.0	1602.5
54	1.87516	503.2	517.2	1.87350	1557.4	1516.5
58	1.87500	500.0	2740.1	1.87561	1968.0	17201.7
64	1.87547	106.9	594.2	1.87500	1540.0	300.0
66	1.87675	737.5	2279.7	1.87508	3455.8	7150.9
67	1.87424	641.4	1643.6	1.87386	2152.6	15673.7
70	1.87331	350.0	1000.0	1.87561	1150.0	4000.0
71	1.87605	430.6	472.9	1.87660	2326.0	3652.9
74	1.87583	500.0	345.8	1.87425	1850.0	1250.0
76	1.87415	389.9	1603.6	1.87500	2350.0	15253.1
77	1.87574	330.5	1129.4	1.87600	2100.0	1420.9
78	1.87563	327.3	113.1	1.87539	3706.0	2868.7
89	1.87604	553.8	412.3	1.87588	1591.3	654.3
95	1.87786	275.0	71.2	1.87790	2125.0	378.2
99	1.87441	182.7	34.6	1.87497	1538.8	671.9

Table A.4: Important line parameters from fitting simultaneously a narrow and broad component to the Brγ emission line. The expected central wavelength is 2.16612 µm, but small deviations from this are possible. Column (1): Object ID from the LLQSO sample. Column (2): Narrow line position, i. e., the central wavelength at the peak of the fit profile in µm. Column (3): Narrow line width, i. e., the FWHM of the fit profile in $\mathrm{km\,s^{-1}}$. Column (4): Narrow line flux of the fit profile in $10^{-20}\,\mathrm{W\,m^{-2}}$. Column (5): Broad line position (see Col. (2)). Column (6): Broad line width (see Col. (3)). Column (7): Broad line flux (see Col. (4)).

ID	Narrow Line Component			Broad Line Component		
	Position	FWHM	Flux	Position	FWHM	Flux
(1)	(2)	(3)	(4)	(5)	(6)	(7)
01	2.16700	750.0	100.0	2.16850	1350.0	378.4
13	2.16550	500.0	39.1	2.16690	1618.9	143.6
20	2.16770	255.1	14.9	2.16770	3850.0	338.1
22	2.16655	348.1	92.1	2.16650	2750.0	300.0
29	2.16533	84.7	42.2	2.16594	1437.7	468.5
53	2.16811	309.2	100.0	2.16925	1250.0	220.0
54	2.16650	650.3	72.6	2.16600	2000.0	139.8
58	2.16700	750.0	363.8	2.16600	2305.9	2402.8
64	2.16528	312.5	65.0	2.16573	1033.5	309.9
66	2.16698	481.2	58.5	2.16638	3488.2	1000.3
67	2.16562	86.4	33.6	2.16468	1794.3	1639.5
70	2.16600	600.0	100.0	2.16612	1720.0	300.0
71	2.16625	586.1	81.8	2.16697	2648.7	681.7
74	2.16700	450.0	100.0	2.16700	2100.0	200.0
76	2.16600	697.8	474.1	2.16500	1950.0	1060.6
77	2.16612	629.6	53.2	2.16669	2039.9	235.8
78	2.16700	374.5	46.4	2.16600	3000.0	84.4
89	2.16700	625.0	100.0	2.16550	2150.0	229.4
95	2.16682	225.0	40.0	2.17000	2650.0	200.0
99	2.16721	221.6	20.3	2.16750	1900.0	104.5

Table A.5: All errors that the fitting algorithm finds for the different parameters of Tab. A.3 and A.4 shown here in the upper and lower part, respectively. According to the description in Sect. 4.2.1, this affects only a few objects. It is important to note the different scaling of some parameters in comparison to the other tables. If necessary, an additional scaling is found directly at the respective value. Column (1): Object ID from the LLQSO sample. Column (2): Narrow line position error, in $10^{-4}\,\mu$m. Column (3): Narrow line width error, in $\mathrm{km\,s^{-1}}$. Column (4): Narrow line flux error, in $10^{-20}\,\mathrm{W\,m^{-2}}$. Column (5): Broad line position error (see Col. (2)). Column (6): Broad line width error (see Col. (3)). Column (7): Broad line flux error (see Col. (4)).

ID	Narrow Line Errors			Broad Line Errors		
	Position	FWHM	Flux	Position	FWHM	Flux
(1)	(2)	(3)	(4)	(5)	(6)	(7)
Pα (according to Tab. A.3)						
29	1.12	72.6	266	2.54	174	249
66	2.77	135	550	9.40	446	728
67	2.18	129	571	1.66	115	668
71	1.83	87.5	122	3.62	214	338
78	2.93	118	44.5	3.62	214	338
89	1.65	106	152	5.35	374	145
99	9.05	240	48.8	6.11	294	121
Brγ (according to Tab. A.4)						
29	$1.64 \cdot 10^4$	$2.57 \cdot 10^6$	$32.6 \cdot 10^5$	5.03	207	65.9
64	3.43	163	56.8	4.64	224	62
66	3.59	138	19.1	4.25	185	37.2
67	$1.27 \cdot 10^4$	$1.34 \cdot 10^6$	$12.5 \cdot 10^5$	2.09	92.1	91
71	6.54	302	62.4	12	801	237

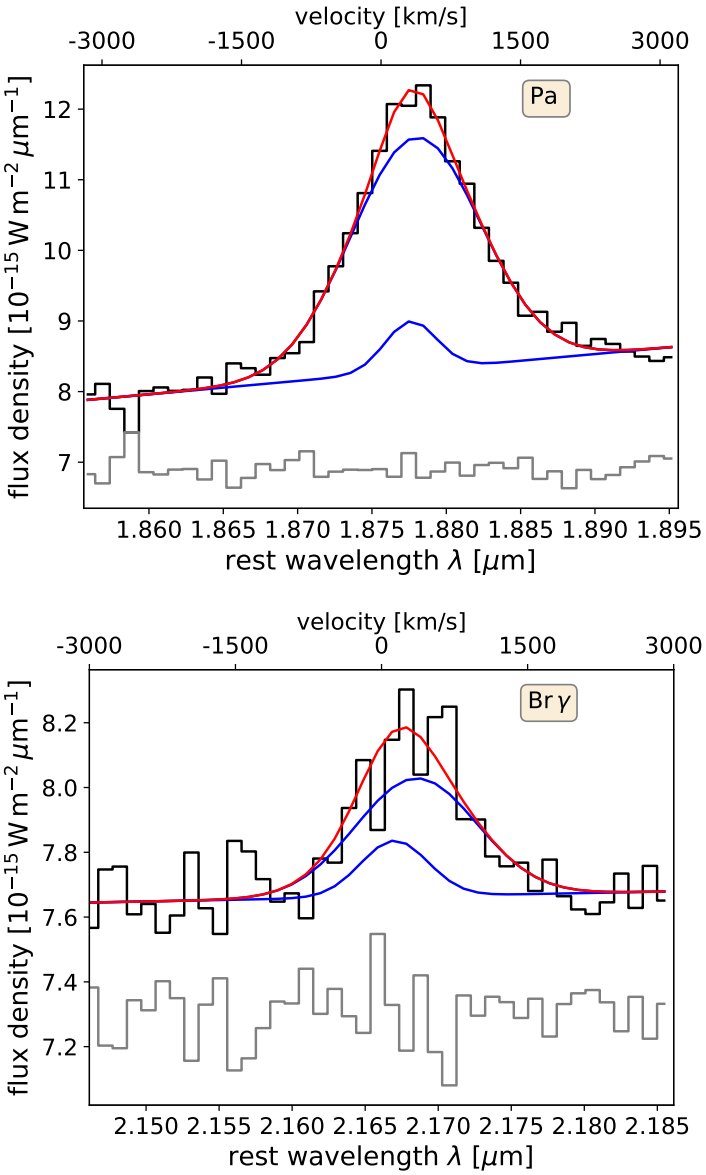

Figure A.3: Line fits of the Pα and Brγ line for object 01 (HE0003-5023). All components of the graphs have the same meaning as in Fig. 4.1.

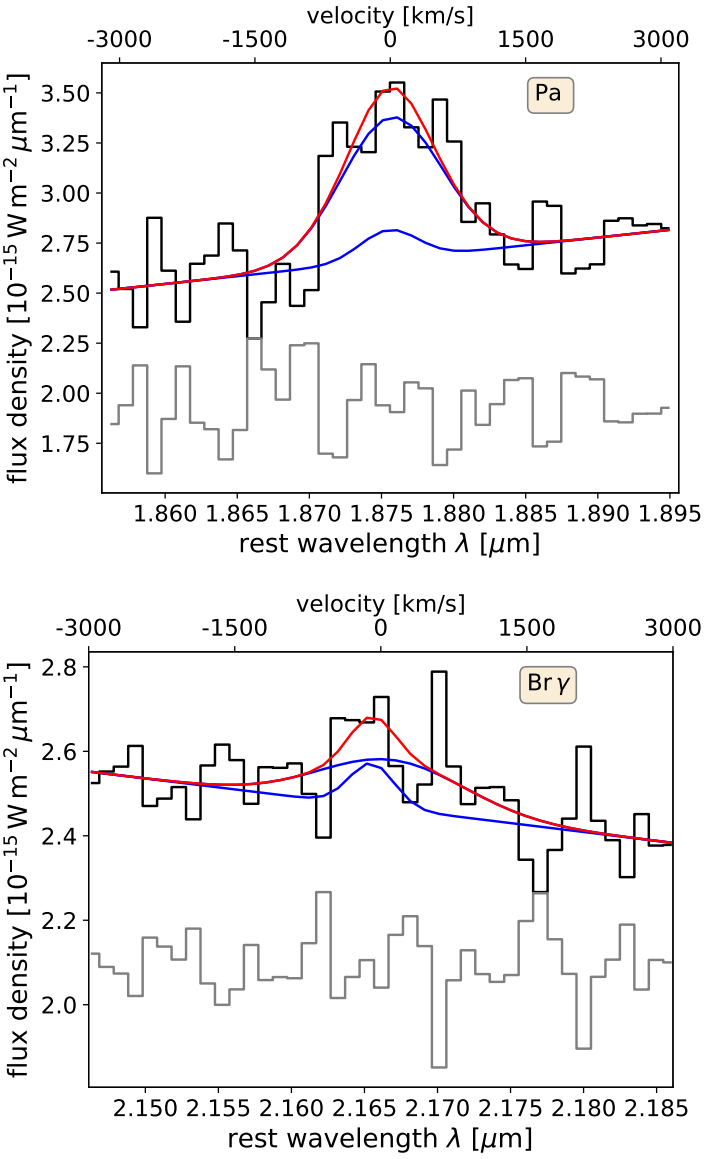

Figure A.3: (Cont.) Line fits of the Pα and Brγ line for object 13 (HE0108-4743). All components of the graphs have the same meaning as previously.

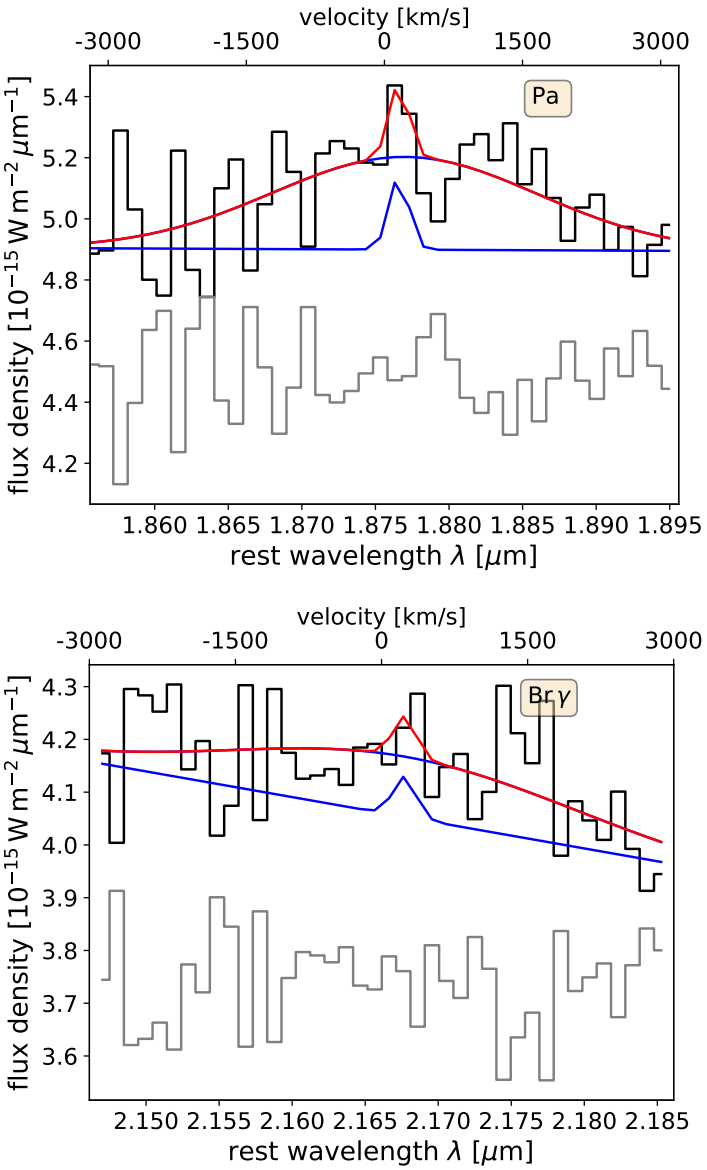

Figure A.3: (Cont.) Line fits of the Pα and Brγ line for object 20 (HE0149-3626). All components of the graphs have the same meaning as previously.

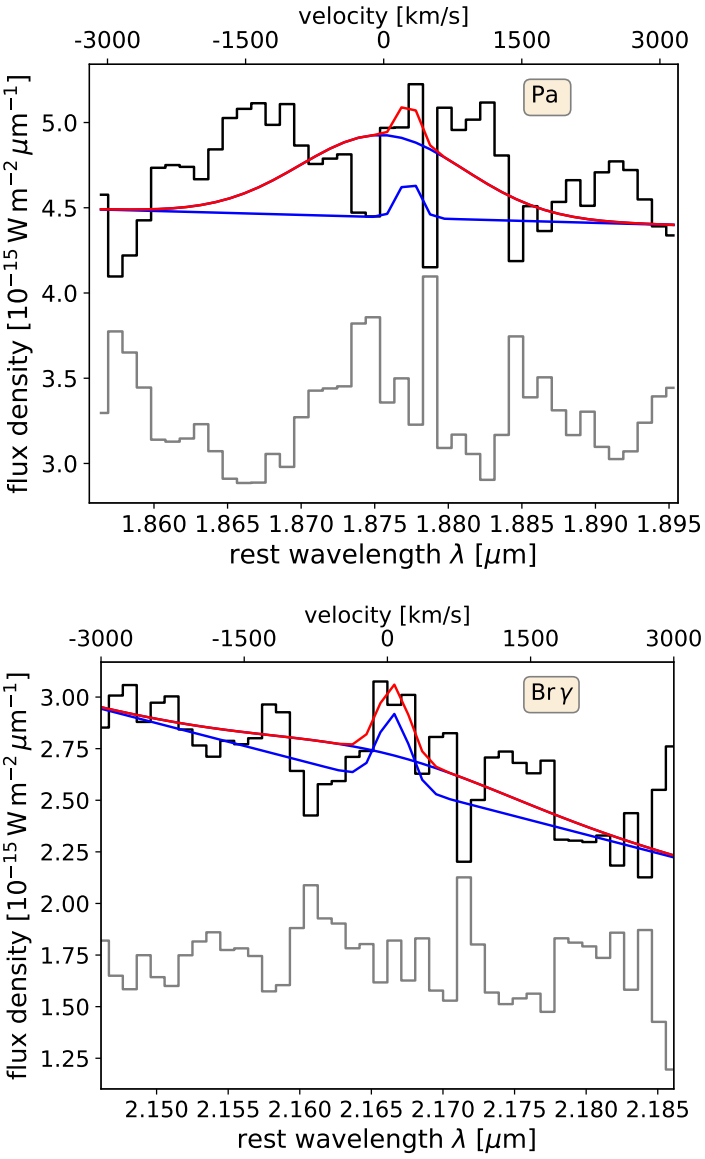

Figure A.3: (Cont.) Line fits of the Pα and Brγ line for object 22 (HE0203-0031). All components of the graphs have the same meaning as previously.

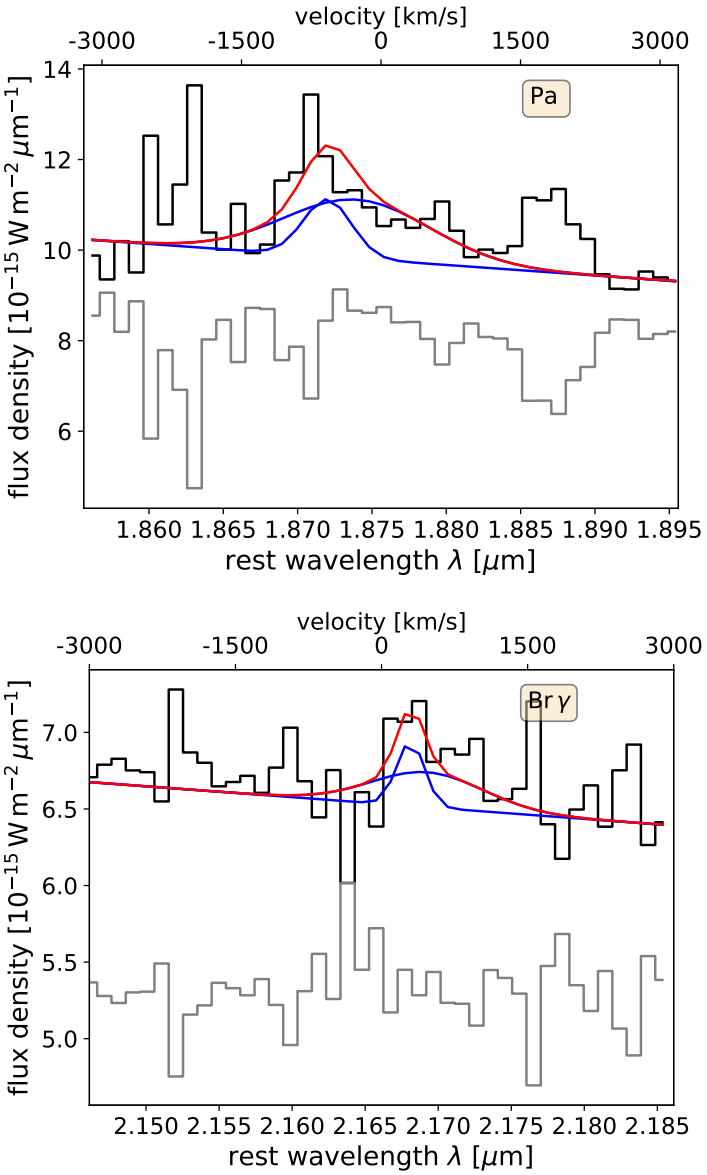

Figure A.3: (Cont.) Line fits of the Pα and Brγ line for object 53 (HE0535-4224). All components of the graphs have the same meaning as previously.

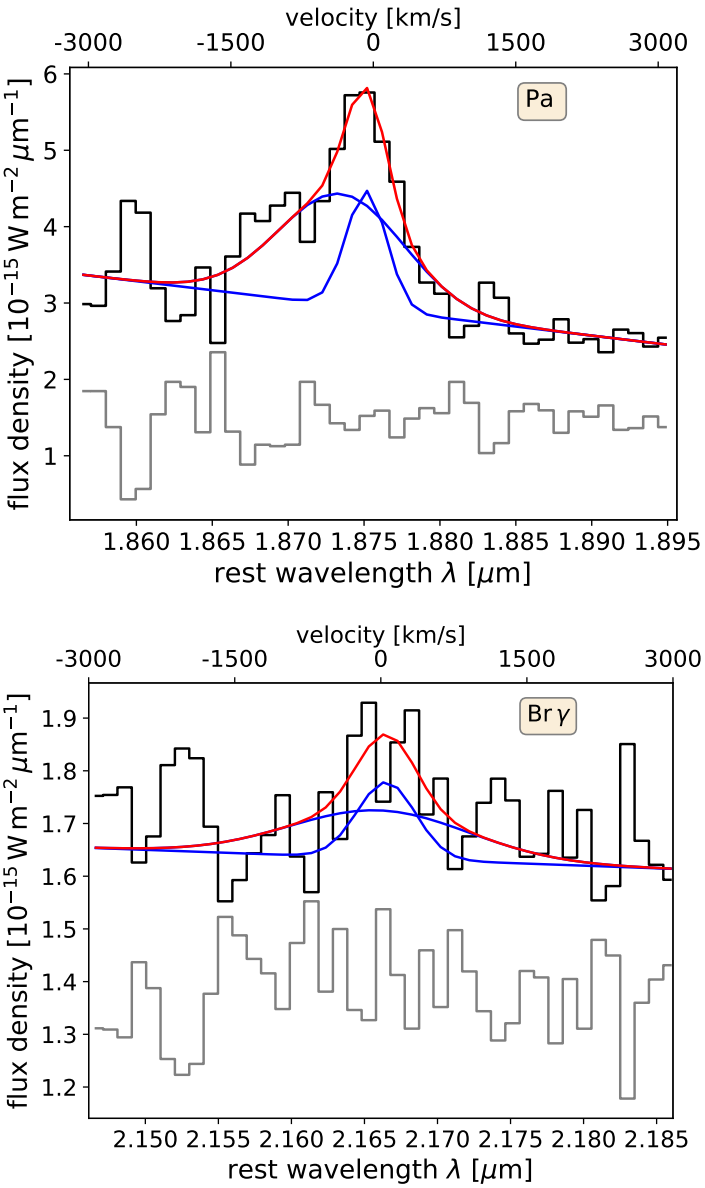

Figure A.3: (Cont.) Line fits of the Pα and Brγ line for object 54 (HE0608-5606). All components of the graphs have the same meaning as previously.

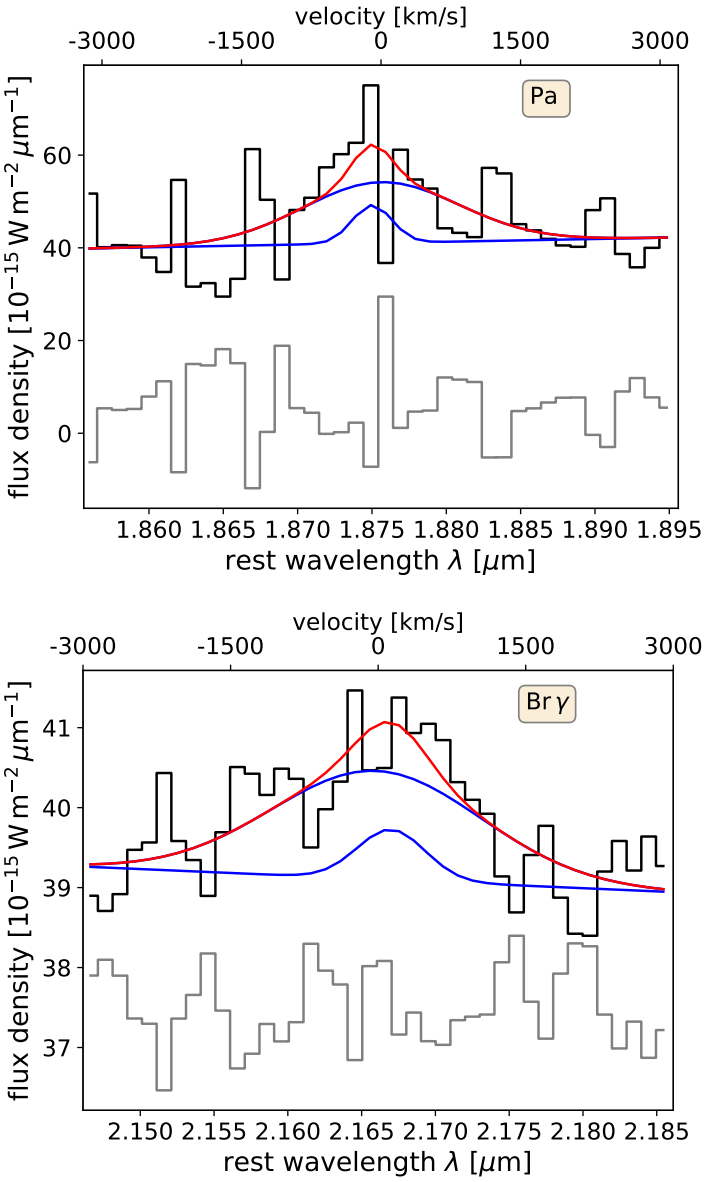

Figure A.3: (Cont.) Line fits of the Pα and Brγ line for object 58 (HE0949-0122). All components of the graphs have the same meaning as previously.

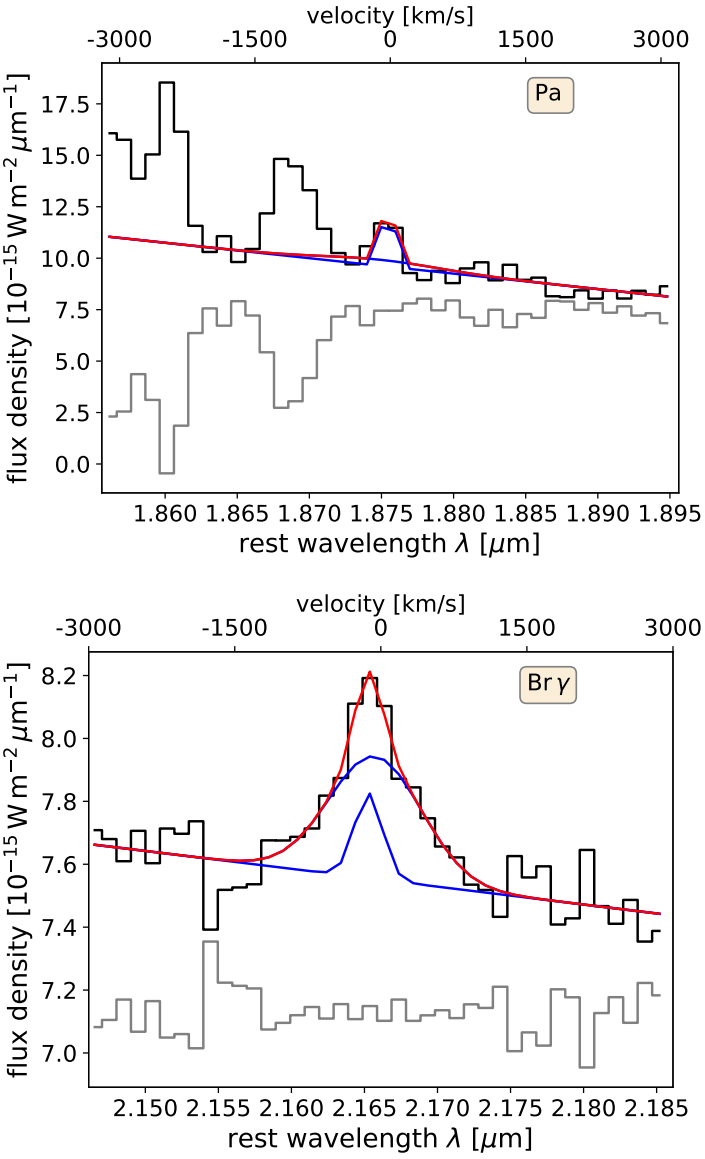

Figure A.3: (Cont.) Line fits of the Pα and Brγ line for object 64 (HE1108-2813). All components of the graphs have the same meaning as previously.

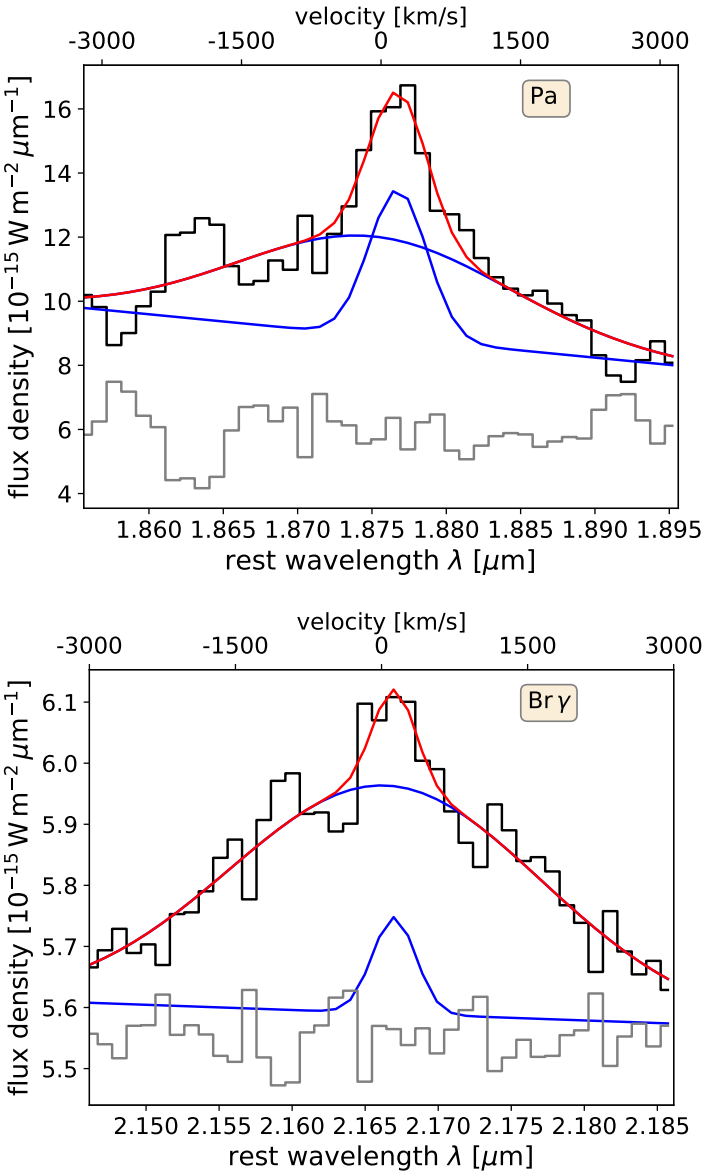

Figure A.3: (Cont.) Line fits of the Pα and Brγ line for object 66 (HE1136-2304). All components of the graphs have the same meaning as previously.

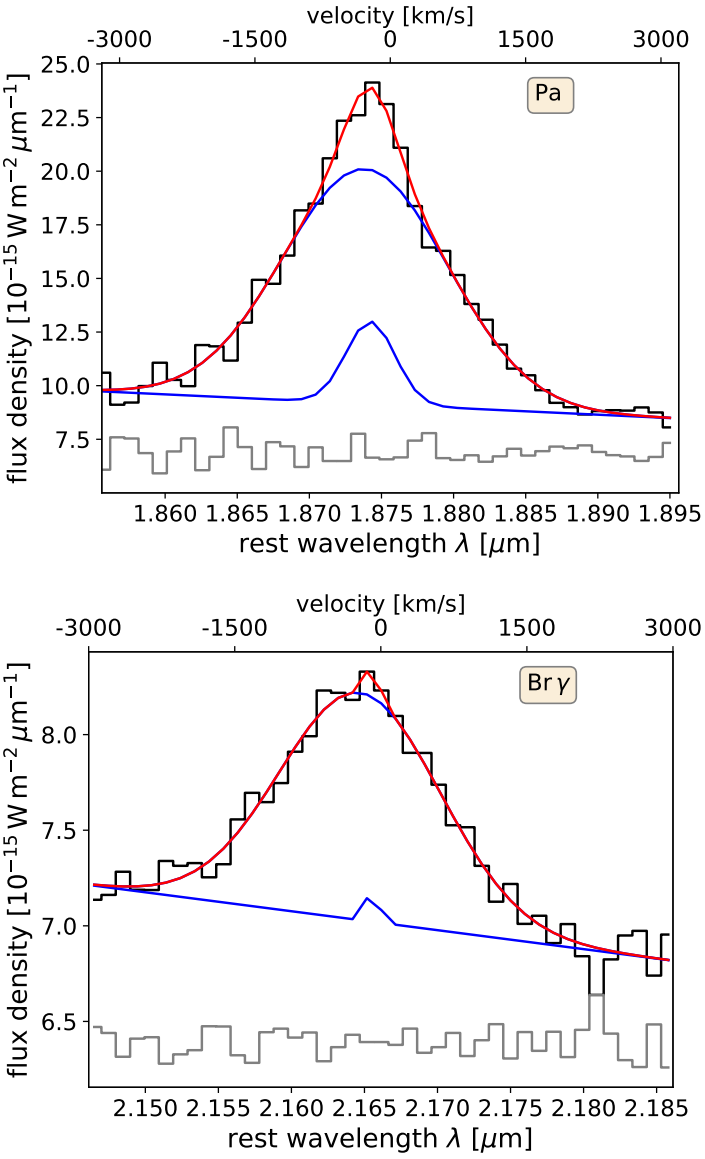

Figure A.3: (Cont.) Line fits of the Pα and Brγ line for object 67 (HE1143-1810). All components of the graphs have the same meaning as previously.

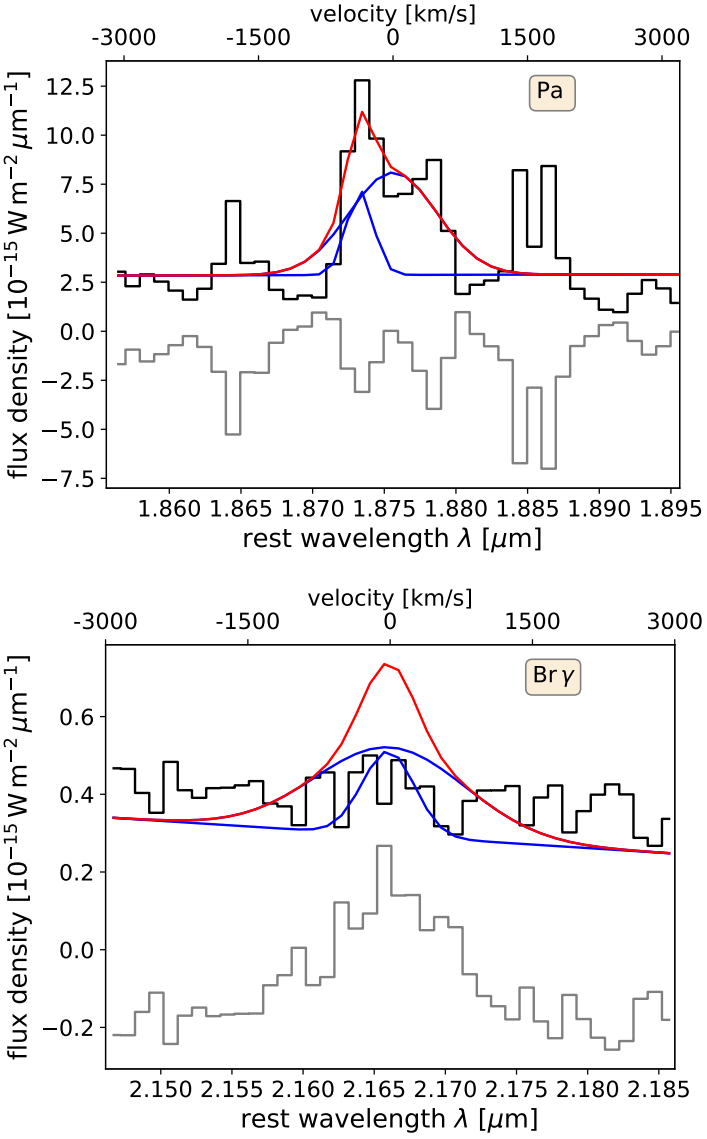

Figure A.3: (Cont.) Line fits of the Pα and Brγ line for object 70 (HE1256-1805). All components of the graphs have the same meaning as previously.

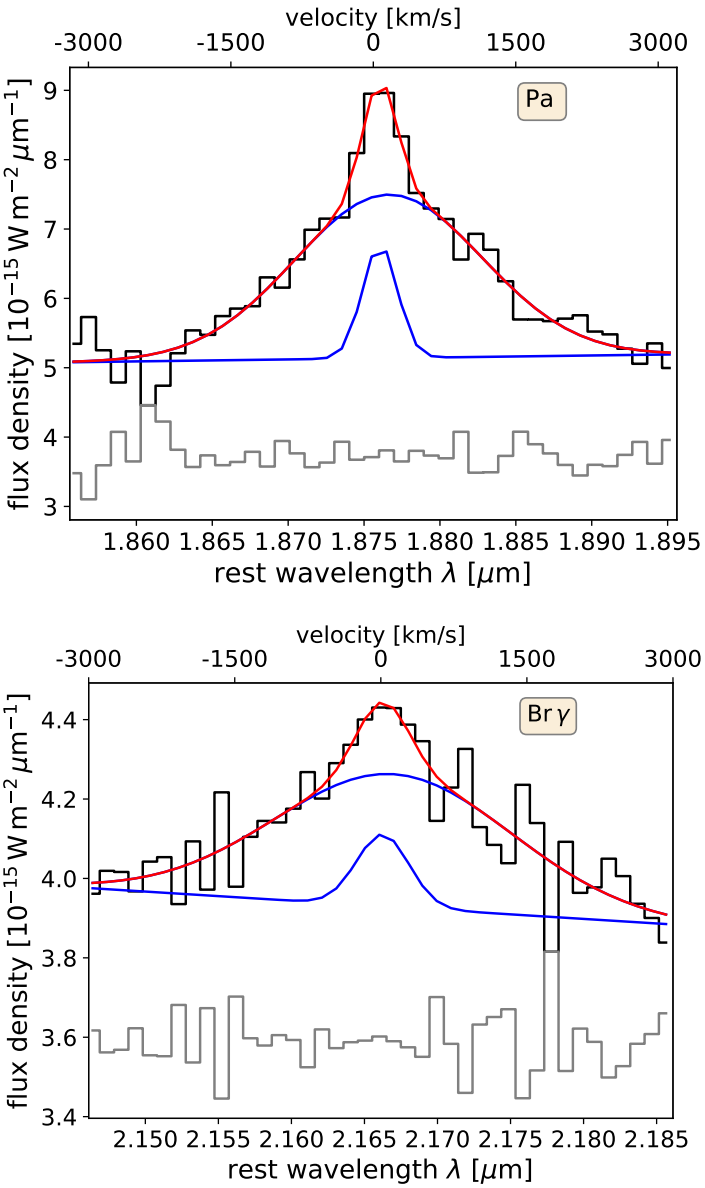

Figure A.3: (Cont.) Line fits of the Pα and Brγ line for object 71 (HE1310-1051). All components of the graphs have the same meaning as previously.

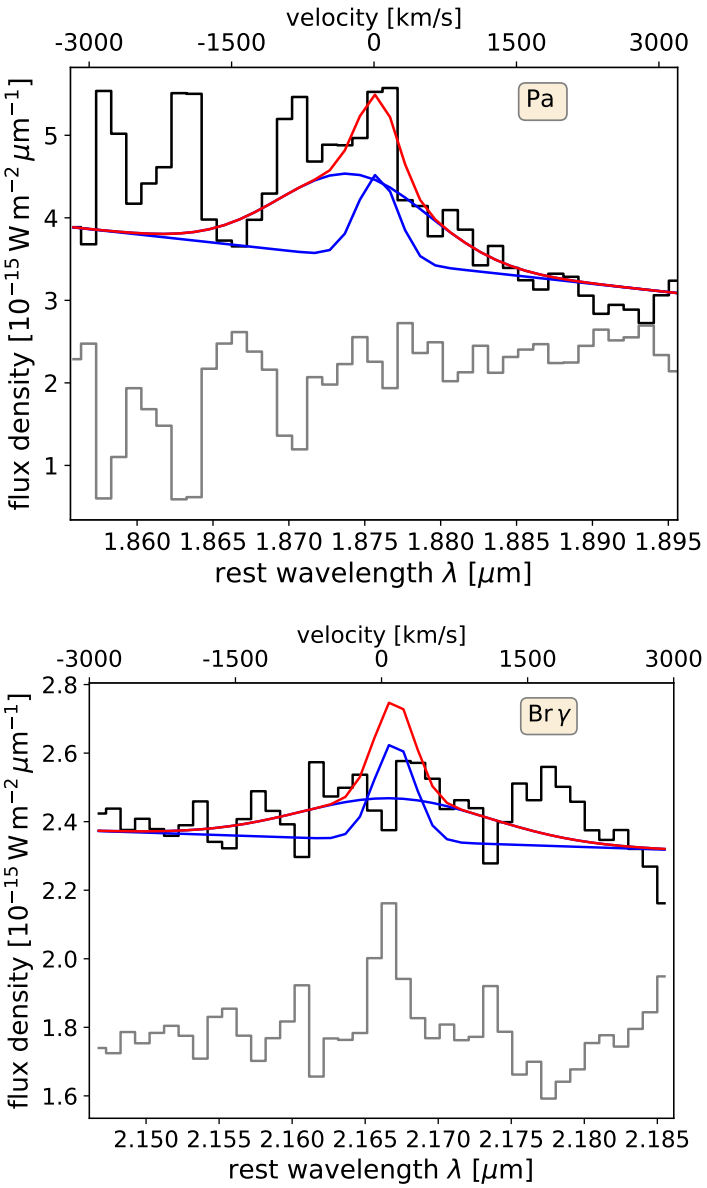

Figure A.3: (Cont.) Line fits of the Pα and Brγ line for object 74 (HE1330-1013). All components of the graphs have the same meaning as previously.

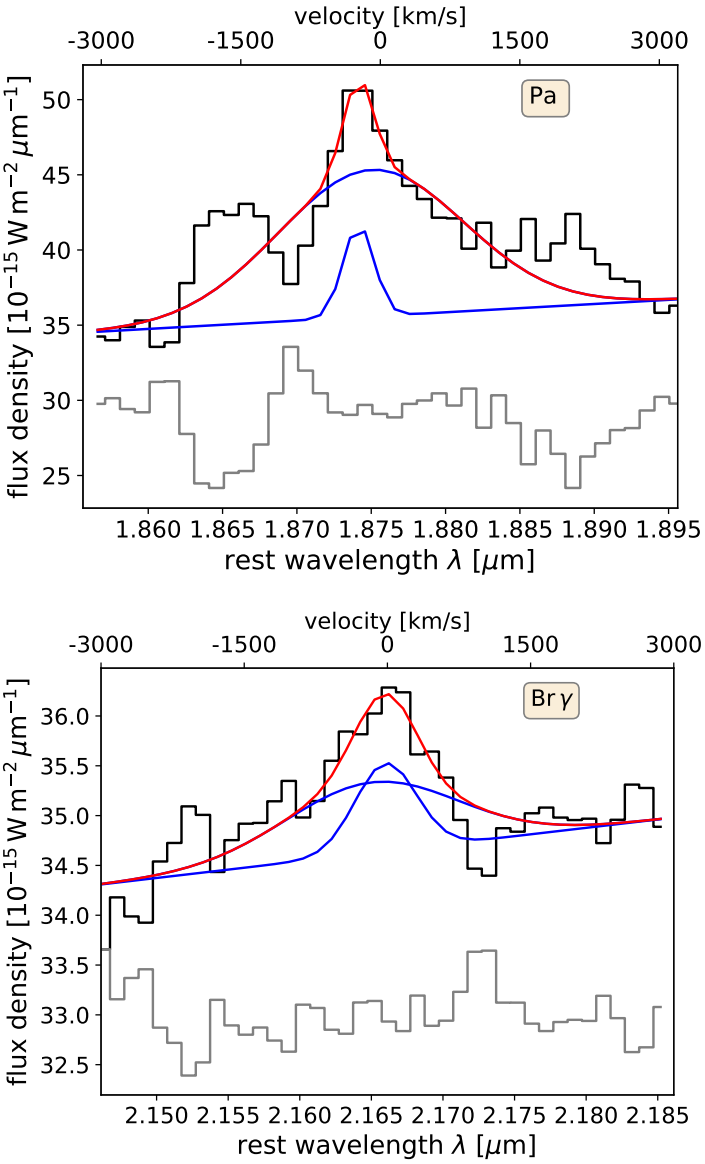

Figure A.3: (Cont.) Line fits of the Pα and Brγ line for object 76 (HE1346-3003). All components of the graphs have the same meaning as previously.

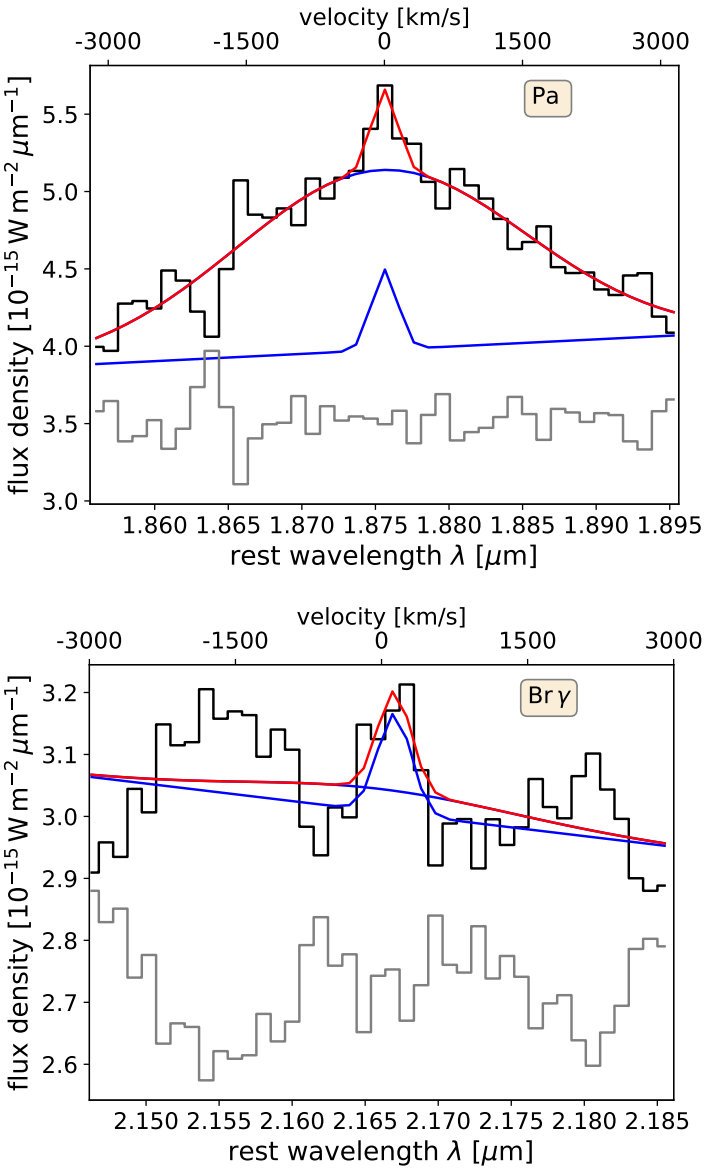

Figure A.3: (Cont.) Line fits of the Pα and Brγ line for object 78 (HE1353-1917). All components of the graphs have the same meaning as previously.

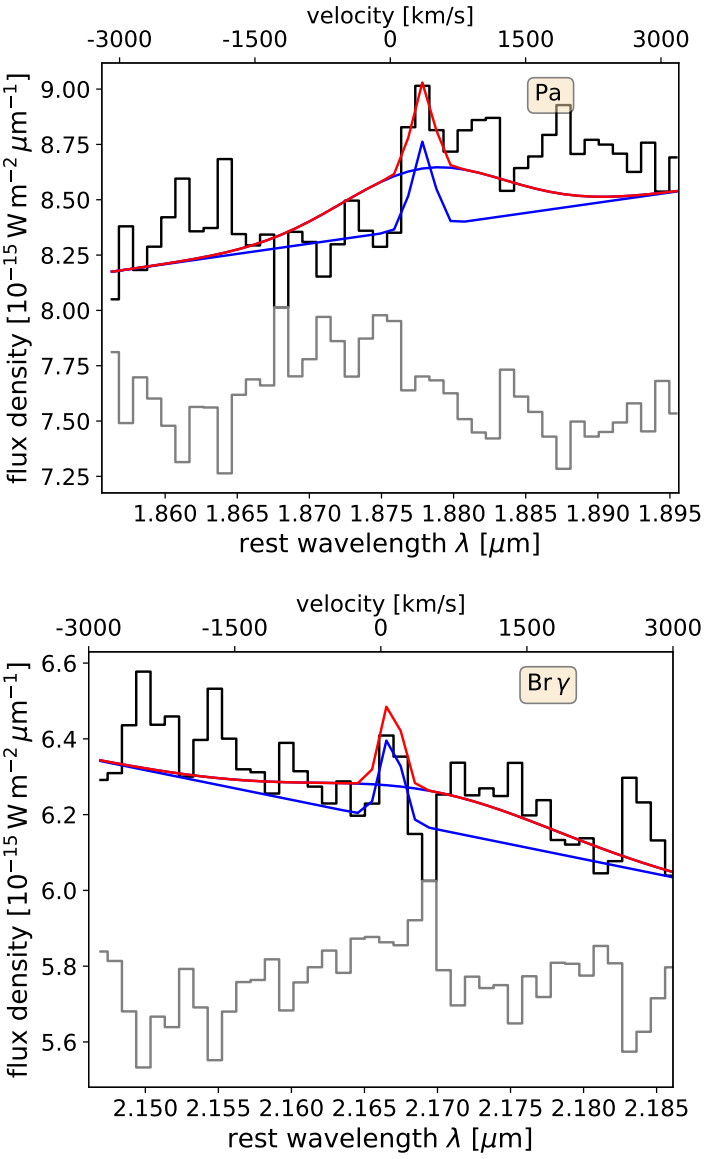

Figure A.3: (Cont.) Line fits of the Pα and Brγ line for object 95 (HE2322-3843). All components of the graphs have the same meaning as previously.

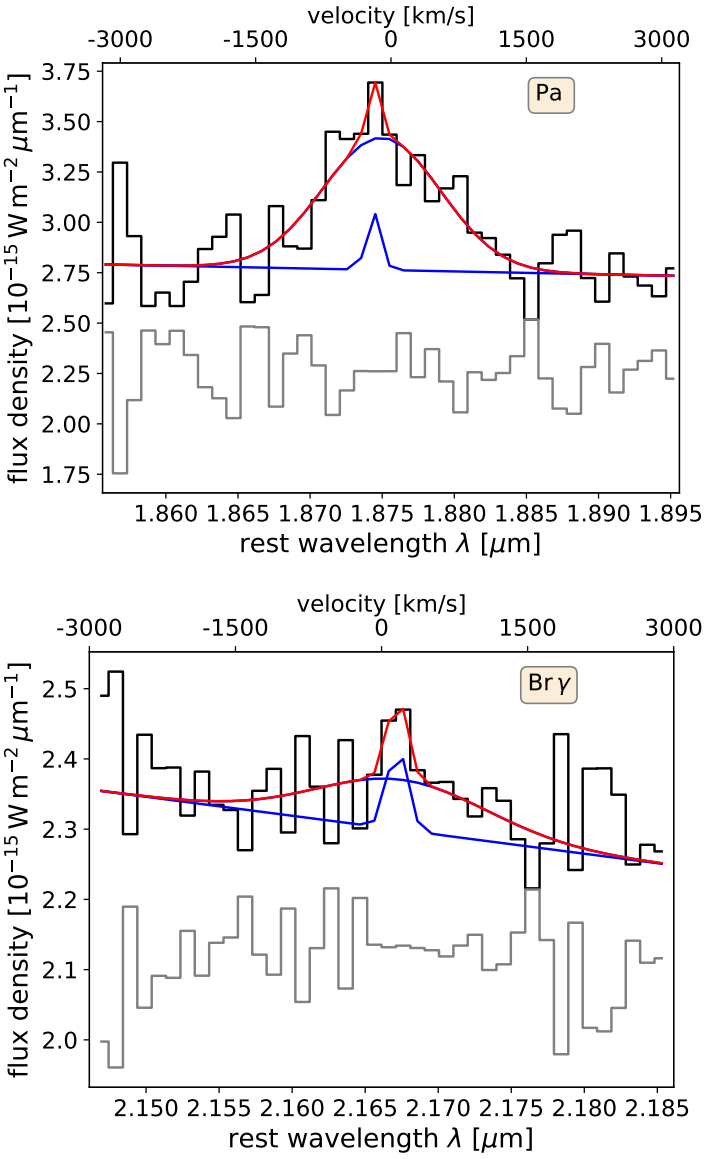

Figure A.3: (Cont.) Line fits of the Pα and Brγ line for object 99 (HE2354-3044). All components of the graphs have the same meaning as previously.

Table A.6: All objects with BH mass estimates from literature. The masses are given as $\log(M_{\rm BH}/{\rm M}_\odot)$. Column (1): Object ID from the LLQSO sample. Column (2): Chosen emission line for the BH mass estimate in this work. Column (3): BH mass estimate in this work. Column (4): Mass estimate scatter in this work. Column (5): Literature BH mass estimate.

ID	Line	BH Mass	Scatter	Lit. Mass
(1)	(2)	(3)	(4)	(5)
22	Pα	7.04	$6.90 - 7.17$	$7.7^{[a]}$, $7.99^{[b]}$, $8.09^{[c]}$, $8.39^{[d]}$
29	Pα	7.03	$6.91 - 7.14$	$6.71^{[e]}$
64	Brγ	6.56	$6.44 - 6.67$	$6.52^{[f,g]}$, $7.78^{[f,h]}$
66	Pα	7.78	$7.69 - 7.88$	$7.30^{[i,j]}$
67	Pα	7.62	$7.56 - 7.69$	$6.70^{[i,k]}$
71	Pα	7.39	$7.29 - 7.49$	$7.33^{[e]}$
77	Brγ	6.80	$6.64 - 6.96$	$6.30^{[e]}$
95	Pα	6.86	$6.70 - 7.01$	$8.22^{[f,g]}$, $6.95^{[f,h]}$
99	Pα	6.63	$6.48 - 6.78$	$6.5^{[l]}$

[a]: Greene and Ho (2007b, Tab. 1) via Hα; [b]: Shen et al. (2008, Tab. 1) via Hα; [c]: Woo and Urry (2002, Tab. 5) via stellar velocity dispersion; [d]: Benítez et al. (2008, Tab. 1) via M_R(bulge) magnitude; [e]: Busch et al. (2014, Tab. 7) (referring to private communication with another author) via Hβ line; [f]: Wang and Zhang (2007, Tab. 3), where the authors refer to [g] (Nelson and Whittle (1995) via Hβ) and [h] (Young et al. (1996) via [O III]/Hα); [i]: Laha et al. (2018, Tab. 1), where the authors refer to [j] (Vestergaard and Peterson (2006) via Hβ) and [k] (Winter et al. (2009) via 2MASS K-band stellar magnitudes); [l]: Schmidt et al. (2016, Tab. A.2) via Hα.

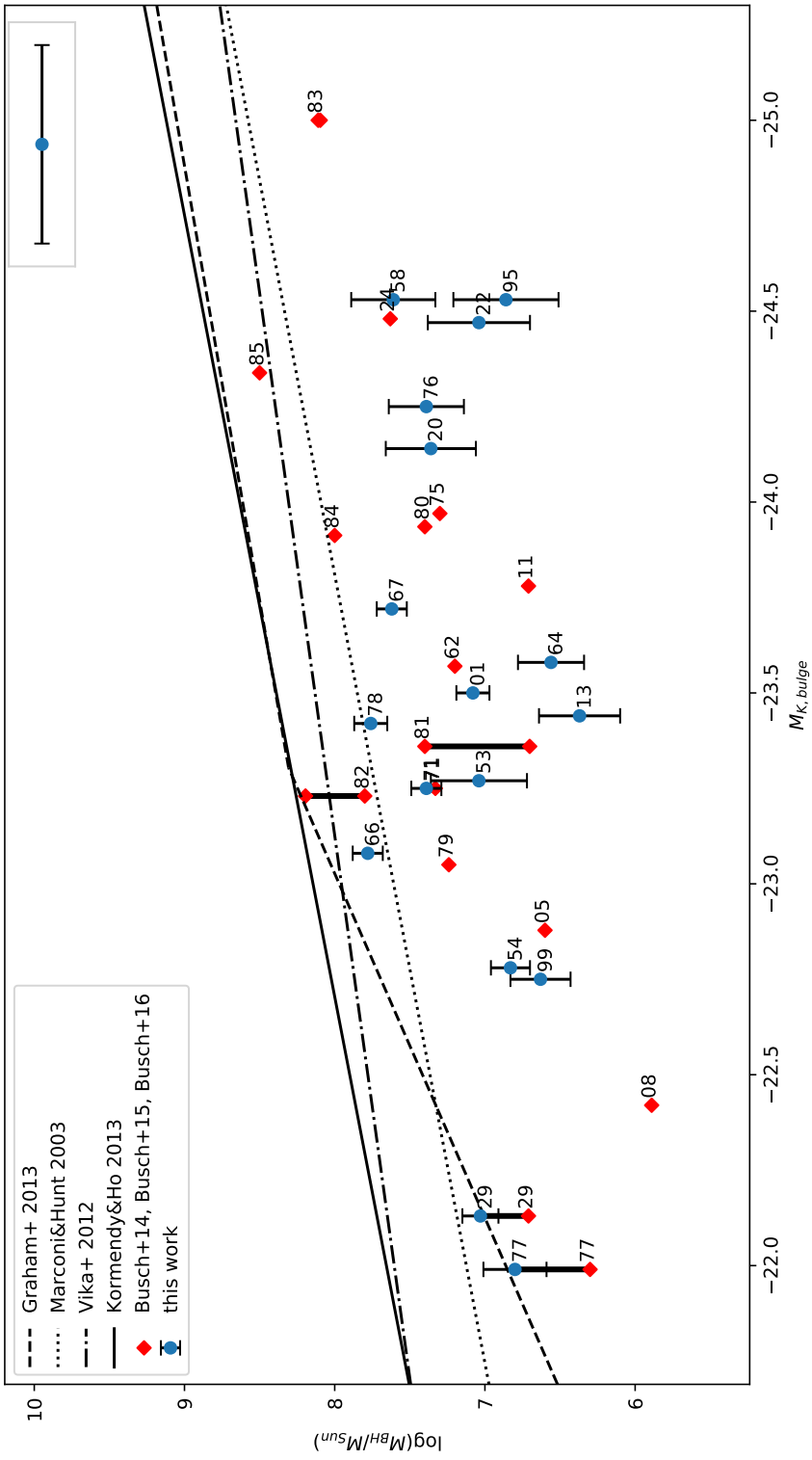

Figure A.4: In principle the same figure as Fig 4.2, but stretched and including the object IDs of the LLQSO sample.

A.2 Impact of a Varying Redshift

This section deals with a potential problem for line identifications, which is especially relevant for noise around the same level as a respective emission line.

In almost all cases literature provides different redshift values for the same object, depending on the source of the respective redshift. The amount of variation is almost always very small. However, larger deviations might influence the possibility to identify certain emission and absorption lines at the correct wavelength. In order to test the influence of the variations given by literature I choose object 22 (HE0203-0031). Literature provides several redshifts with a relatively large scatter in comparison to most other objects from the LLQSO sample. Additionally, its spectrum around the Pα emission line is rather noisy, which makes it harder to properly identify and fit this emission line (see Fig. A.5).

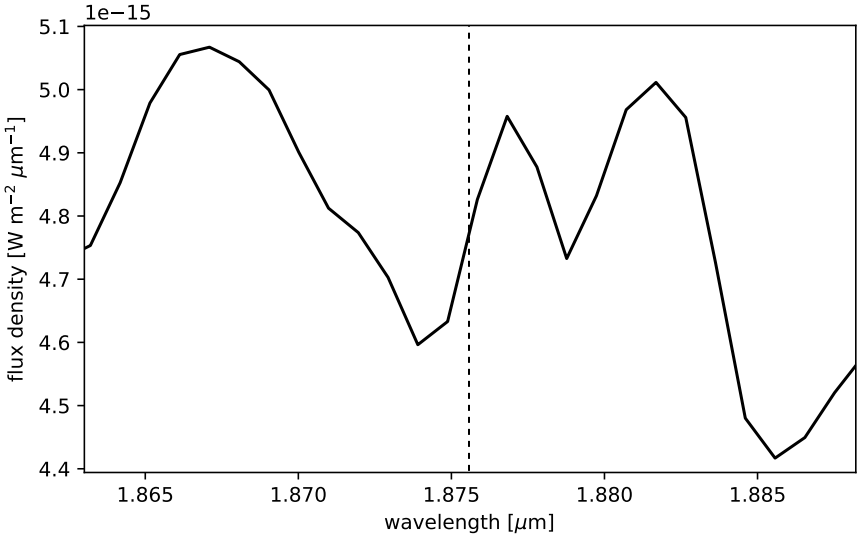

Figure A.5: A small part of the redshift-corrected spectrum of object 22 (HE0203-0031) for $z = 0.0424$, covering the wavelengths around $1.863 - 1.888\,\mu\text{m}$. For easier recognition of features the spectrum is smoothed by a Gaussian of $\sigma = 1.0$. The vertical, dashed line marks a wavelength of $1.87561\,\mu\text{m}$, i. e., the expected position of the Pα emission line.

The Pα line is expected to be at $1.87561\,\mu\text{m}$, which is roughly where the spectrum of object 22 shows a feature as a candidate for the Pα line. The estimated peak of the feature according to the diagram is at $\sim 1.8763\,\mu\text{m}$, i. e., a deviation from the expected wavelength of about $\Delta\lambda = 0.0007\,\mu\text{m}$. This feature is only about as strong as other nearby features and thus not a strong, distinctive candidate. In the context of line identification the question arises, whether another, close feature could be the actual Pα line, of which the wavelength is misaligned with the expected position due to an

erroneous redshift correction. It makes sense to consider at least the two closest features to the previously mentioned one.

The first feature is a strong bump that peaks at a lower wavelength of roughly 1.866 µm, i. e., in the diagram to the left of the supposed Pα emission line candidate. As the feature is larger, broader, and overall more prominent, it would be a candidate for an easier and probably better line fit than the more central feature. At a larger wavelength is the second feature, which peaks at roughly 1.882 µm and is of similar size as the central candidate. The difference between the estimated peak position of the left feature from the expected peak wavelength is then about 0.01 µm, while the difference for the right feature is about 0.006 µm. The right feature is a bit closer to the expected peak position and thus can be reached with a smaller deviation of the redshift, whereas the left feature is more pronounced than that on the right side. As a result, both features are further considered.

For an observed wavelength λ_o, the emitted wavelength λ_e (i. e., the assumed rest wavelength) and the redshift z, it is $\lambda_\mathrm{o}/\lambda_\mathrm{e} = 1 + z \;\Leftrightarrow\; \lambda_\mathrm{e} = \lambda_\mathrm{o}/(1 + z)$. The emitted wavelength of another redshift z' is accordingly λ'_e, which relates to the previous wavelength λ_e via $\lambda'_\mathrm{e} = \lambda_\mathrm{e} \cdot (1+z)/(1+z')$. Here, the assumed redshift of object 22 is 0.0424, while NED provides multiple redshift values for this object, which are mostly between 0.04 and 0.043[(1)]. Using the assumed redshift of $z = 0.0424$ together with the higher literature redshift value $z' = 0.043$ on the expected rest wavelength of $\lambda_\mathrm{e} = 1.87561$ µm results in the new, smaller wavelength $\lambda'_\mathrm{e} \approx 1.87453$ µm, i. e., a shift in wavelength of about 0.001 µm. This wavelength shift is only about a tenth of the previously found shift between the expected and the actual peak position of the left feature at ~ 1.866 µm.

When using the lowest redshift value provided by literature of $z' = 0.04$ instead, it is $\lambda'_\mathrm{e} \approx 1.87994$ µm, i. e., a larger shift in wavelength than previously of about $\Delta\lambda \approx 0.004$ µm. However, this still does not reach the right feature, but is in between the central and the right one. A reversed calculation shows that the redshift needed to reach 1.882 µm is $z' \approx 0.0389$. Additionally, this shows that the wavelength at the peak of the central feature is included within the given uncertainties of the literature redshift values, as the redshift z' necessary to go from the peak at $\lambda'_\mathrm{e} \approx 1.8763$ µm for $z = 0.0424$ to the expected position is $z' \approx 0.042$.

With these results in mind it is hard to argue that any other spectral feature besides that in the center at about the expected wavelength could be the actual Pα emission line instead. On the one hand, the scatter of redshift values from literature can be assumed to play only a minor role in finding the right emission line, if a feature close to the expected wavelength does exist, as the scatter usually appears to be negligible. On the other hand, if the only candidate for an emission line is a spectral feature that peaks very close to the expected wavelength, this could well be explained by a slight deviation in redshift.

[(1)] One exception is the redshift value 0.024256, which is left out as it appears to be a mistake of transposed digits.

A.3 Additional Line Identifications

The following contains information about possible line identifications in the redshift-corrected spectra, except for the Pα and the Brγ emission lines, as these are extensively studied in Sect. 4.2.1. Three different spectra are used for these identifications, the two centered spectra with aperture size factors of 0.5 and 1.5, as well as the off-center spectrum. Most line entries should be considered as potential candidates at best, as the spectra are often very noisy. Accordingly, sometimes part of the continuum noise might appear to show a feature that does not really exist. If any feature corresponds to the wavelength of one of the NIR lines given by Tokunaga, A. T. (2002), it is listed here. Candidates, that are especially strong and/or features that are distinct from the noise, are accompanied by a respective comment. The expected wavelength in μm trails the identifier of each feature.

01 HE0003-5023

- CO(6-3)band head@1.6189
- OH(2-0)@1.62646
- [Fe II]@1.644
- H I(11-4)(Br11)@1.68111
- H I(10-4)(Br10)@1.73669
- H I(8-4)(Brδ)@1.94509 (big, distinct feature with very broad base)
- [Si VI]@1.9634
- H_2(1-0)S(2)@2.03376
- H_2(1-0)S(0)@2.22329
- H_2(2-1)S(1)@2.24772
- CO(2-0)band head@2.29353

13 HE0108-4743 (Gaussian smoothing by $\sigma = 1.0$)

- H I(13-4)(Br13)@1.61137
- CO(6-3)band head@1.6189
- H I(11-4)(Br11)@1.68111
- H I(8-4)(Brδ)@1.94509
- H_2(1-0)S(3)@1.95756 (distincitve feature, but slightly off from the expected position)

- H_2(1-0)S(0)@2.22329
- CO(2-0)band head@2.29353
- CO(2-0)R(1)@2.34327

20 HE0149-3626 (Gaussian smoothing by $\sigma = 0.5$)

- H I(13-4)(Br13)@1.61137
- H I(11-4)(Br11)@1.68111
- H_2(1-0)S(3)@1.95756 (the left part of a distinct double-spiked feature)
- [Si VI]@1.9634 (the right part of a distinct double-spiked feature)
- H_2(1-0)S(2)@2.03376
- CO(2-0)band head@2.29353
- CO(4-2)band head@2.35246

22 HE0203-0031 (Gaussian smoothing by $\sigma = 1.0$)

- H I(13-4)(Br13)@1.61137
- H_2(1-0)S(3)@1.95756
- [Si VI]@1.9634
- H_2(2-1)S(1)@2.24772

29 HE0253-1641

- H I(13-4)(Br13)@1.61137
- [Fe II]@1.644 (big, distinct feature)
- H I(11-4)(Br11)@1.68111
- H I(10-4)(Br10)@1.73669
- H I(9-4)(Br9)@1.81791 (although located in the band gap, appears to be distinct)
- H I(8-4)(Brδ)@1.94509 (noisy, but distinct feature)
- H_2(1-0)S(3)@1.95756
- H_2(1-0)S(2)@2.03376
- H_2(1-0)S(1)@2.12183
- CO(2-0)band head@2.29353

53 HE0535-4224

- H I(8-4)(Brδ)@1.94509
- CO(2-0)P(2)
- CO(4-2)band head@2.35246

54 HE0608-5606 (Gaussian smoothing by $\sigma = 1.0$)

- CO(6-3)band head@1.6189
- OH(2-0)@1.62646
- [Fe II]@1.644
- H I(11-4)(Br11)@1.68111
- H I(10-4)(Br10)@1.73669
- [Si VI]@1.9634
- H_2(2-1)S(1)@2.24772
- CO(2-0)band head@2.29353
- CO(2-0)R(1)@2.34327

58 HE0949-0122

- [Fe II]@1.644
- H I(11-4)(Br11)@1.68111
- [Si VI]@1.9634 (strong, distinct feature)
- H_3^+@2.09326
- H_2(2-1)S(1)@2.24772

64 HE1108-2813

- CO(6-3)band head@1.6189
- [Fe II]@1.644
- H I(11-4)(Br11)@1.68111
- H I(8-4)(Brδ)@1.94509
- H_2(1-0)S(3)@1.95756
- H_2(1-0)S(1)@2.12183

- CO(2-0)band head@2.29353

66 HE1136-2304

- CO(6-3)band head@1.6189
- OH(2-0)@1.62646
- [Fe II]@1.644 (distinct feature)
- He II(12-7)@1.69230
- CO(2-0)band head@2.29353

67 HE1143-1810

- H I(13-4)(Br13)@1.61137
- CO(6-3)band head@1.61889
- [Fe II]@1.644 (broad feature that might include H I(13-4)(Br13)@1.61137)
- H I(11-4)(Br11)@1.68111 (quite distinct feature)
- H I(10-4)(Br10)@1.73669 (quite distinct feature)
- H I(8-4)(Brδ)@1.94509 (distinct feature)
- [Si VI]@1.9634
- He I@2.05869

70 HE1256-1805

- Fe II@1.74188
- H_2(1-0)S(1)@2.12183 (more pronounced in the spectrum from an aperture size factor of 1.5)

71 HE1310-1051

- Fe II@1.74188
- H I(8-4)(Brδ)@1.94509
- [Si VI]@1.9634
- H_2(2-1)S(1)@2.24772

74 HE1330-1013

- CO(6-3)band head@1.6189

- [Fe II]@1.644
- CO(5-3)band head@2.38295

76 HE1346-3003

- CO(6-3)band head@1.6189
- OH(2-0)@1.62646
- [Fe II]@1.644 (distinct feature)
- [Si VI]@1.9634 (strong, distinct feature)

77 HE1348-1758

- H I(13-4)(Br14)@1.61137
- CO(6-3)band head@1.6189
- H I(11-4)(Br11)@1.68111
- — @1.978 (All spectra, including the two aperture size factors 0.5 and 1.5, as well as the off-center spectrum, show a strong, distinct feature here, but the list of literature lines does not include any line there. It could be an artifact from the band gap noise, but as it is quite far out, this seems unlikely.)
- H_2(1-0)Q(1)@2.40659

78 HE1353-1917

- CO(6-3)band head@1.6189
- H I(11-4)(Br11)@1.68111
- [Si VI]@1.9634
- H_2(1-0)S(1)@2.12183
- CO(2-0)band head@2.29353

89 HE2236-3621

- H I(8-4)(Brδ)@1.94509
- [Si VI]@1.9634
- H_2(1-0)S(0)@2.22329

95 HE2322-3843

- CO(6-3)band head@1.6189

- H I(11-4)(Br11)@1.68111
- — @1.937 (All spectra show this feature, and it is one of the most distinct features beside the strong noise in the band gap. It is intriguing, that this feature is even more pronounced in the off-center spectrum. As there is no counterpart in the list of literature lines, its nature is unclear.)
- CO(2-0)band head@2.29353
- CO(3-1)band head@2.32265

99 HE2354-3044 (Gaussian smoothing by $\sigma = 1.0$)

- H I(13-4)(Br13)@1.61137
- CO(6-3)band head@1.6189
- H I(11-4)(Br11)@1.68111
- H I(8-4)(Brδ)@1.94509 (distinct feature)
- H_2(1-0)S(2)@2.03376
- Fe II@2.08938
- H_2(1-0)S(0)@2.22329
- H_2(2-1)S(1)@2.24772
- CO(2-0)band head@2.29353
- CO(2-0)band head@2.32265

Bibliography

Aird, J. et al. (Aug. 2015). "The evolution of the X-ray luminosity functions of unabsorbed and absorbed AGNs out to z$\sim$ 5". In: *"Monthly Notices of the Royal Astronomical Society"* 451.2, pp. 1892–1927. DOI: 10.1093/mnras/stv1062. arXiv: 1503.01120 [astro-ph.HE].

Alexander, D. M. and R. C. Hickox (June 2012). "What drives the growth of black holes?" In: *"New Astronomy Reviews"* 56.4, pp. 93–121. DOI: 10.1016/j.newar.2011.11.003. arXiv: 1112.1949 [astro-ph.GA].

Alonso-Herrero, Almudena et al. (Mar. 2003). "The [Fe II] 1.644 Micron Emission in M82 and NGC 253: Is It a Measure of the Supernova Rate?" In: *"The Astronomical Journal"* 125.3, pp. 1210–1225. DOI: 10.1086/367790. arXiv: astro-ph/0212142 [astro-ph].

Athanassoula, E. (Apr. 2005). "On the nature of bulges in general and of box/peanut bulges in particular: input from N-body simulations". In: *"Monthly Notices of the Royal Astronomical Society"* 358.4, pp. 1477–1488. DOI: 10.1111/j.1365-2966.2005.08872.x. arXiv: astro-ph/0502316 [astro-ph].

Bahcall, John N. et al. (Feb. 1972). "On the Time Dependence of Emission-Line Strengths from a Photoionized Nebula". In: *"The Astrophysical Journal"* 171, p. 467. DOI: 10.1086/151300.

Baldwin, J. A. et al. (Feb. 1981). "Classification parameters for the emission-line spectra of extragalactic objects." In: *"Publications of the Astronomical Society of the Pacific"* 93, pp. 5–19. DOI: 10.1086/130766.

Banik, Indranil and Hongsheng Zhao (June 2022). "From Galactic Bars to the Hubble Tension: Weighing Up the Astrophysical Evidence for Milgromian Gravity". In: *Symmetry* 14.7, p. 1331. DOI: 10.3390/sym14071331. arXiv: 2110.06936 [astro-ph.CO].

Benítez, E. et al. (Apr. 2008). "Black Hole Mass estimates in nearby AGN from Host-Bulge Properties". In: *Revista Mexicana de Astronomia y Astrofisica Conference Series*. Vol. 32. Revista Mexicana de Astronomia y Astrofisica Conference Series, pp. 173–173.

Bennert, Vardha N. et al. (Dec. 2011a). "The Relation between Black Hole Mass and Host Spheroid Stellar Mass Out to z ~2". In: *"The Astrophysical Journal"* 742.2, 107, p. 107. DOI: 10.1088/0004-637X/742/2/107. arXiv: 1102.1975 [astro-ph.CO].

Bennert, Vardha Nicola et al. (Jan. 2010). "Cosmic Evolution of Black Holes and Spheroids. IV. The M $_{BH}$-L $_{sph}$ Relation". In: *"The Astrophysical Journal"* 708.2, pp. 1507–1527. DOI: 10.1088/0004-637X/708/2/1507. arXiv: 0911.4107 [astro-ph.CO].

Bennert, Vardha Nicola et al. (Jan. 2011b). "A Local Baseline of the Black Hole Mass Scaling Relations for Active Galaxies. I. Methodology and Results of Pilot Study". In: *"The Astrophysical Journal"* 726.2, 59, p. 59. DOI: 10.1088/0004-637X/726/2/59. arXiv: 1008.4602 [astro-ph.CO].

Bennett, A. S. (Jan. 1962). "The revised 3C catalogue of radio sources." In: *"Memoirs of the Royal Astronomical Society"* 68, p. 163.

Bertram, T. et al. (Aug. 2007). "Molecular gas in nearby low-luminosity QSO host galaxies". In: *"Astronomy & Astrophysics"* 470.2, pp. 571–583. DOI: 10.1051/0004-6361:20077578. arXiv: 0706.2759 [astro-ph].

Blandford, R. D. and C. F. McKee (Apr. 1982). "Reverberation mapping of the emission line regions of Seyfert galaxies and quasars." In: *"The Astrophysical Journal"* 255, pp. 419–439. DOI: 10.1086/159843.

Blandford, R. D. and M. J. Rees (Jan. 1978). "Some comments on radiation mechanisms in Lacertids." In: *BL Lac Objects*. Ed. by A. M. Wolfe, pp. 328–341.

Bolton, J. G. et al. (July 1949). "Positions of Three Discrete Sources of Galactic Radio-Frequency Radiation". In: *"Nature"* 164.4159, pp. 101–102. DOI: 10.1038/164101b0.

Bongiorno, A. et al. (Sept. 2014). "The M_{BH}-M_* relation for X-ray-obscured, red QSOs at 1.2 ¡ z ¡ 2.6". In: *"Monthly Notices of the Royal Astronomical Society"* 443.3, pp. 2077–2091. DOI: 10.1093/mnras/stu1248. arXiv: 1406.6094 [astro-ph.GA].

Busch, G. et al. (Jan. 2012). "A low-luminosity type-1 QSO sample: Near-infrared study of nearby AGN host galaxies". In: *Proceedings of Nuclei of Seyfert galaxies and QSOs - Central engine & conditions of star formation (Seyfert 2012). 6-8 November*, 60, p. 60. DOI: 10.22323/1.169.0060. arXiv: 1307.1049 [astro-ph.CO].

Busch, G. et al. (Jan. 2014). "A low-luminosity type-1 QSO sample. I. Overluminous host spheroidals or undermassive black holes". In: *"Astronomy & Astrophysics"* 561, A140. DOI: 10.1051/0004-6361/201322486. arXiv: 1310.0272 [astro-ph.CO].

Busch, Gerold et al. (Mar. 2015). "A low-luminosity type-1 QSO sample. II. Tracing circumnuclear star formation in HE 1029-1831 with SINFONI". In: *"Astronomy & Astrophysics"* 575, A128, A128. DOI: 10.1051/0004-6361/201425261. arXiv: 1412.2069 [astro-ph.GA].

Busch, Gerold et al. (Mar. 2016). "A low-luminosity type-1 QSO sample. V. Overluminous host spheroids and their excitation mechanisms". In: *"Astronomy & Astrophysics"* 587, A138, A138. DOI: 10.1051/0004-6361/201526753. arXiv: 1511.00904 [astro-ph.GA].

Calzetti, Daniela (Jan. 1997). "Reddening and Star Formation in Starburst Galaxies". In: *"The Astronomical Journal"* 113, pp. 162–184. DOI: 10.1086/118242. arXiv: astro-ph/9610184 [astro-ph].

Cohen, Martin et al. (Oct. 1992). "Spectral Irradiance Calibration in the Infrared. I. Ground-Based and IRAS Broadband Calibrations". In: *"The Astronomical Journal"* 104, p. 1650. DOI: 10.1086/116349.

Cohen, Martin et al. (Aug. 2003). "Spectral Irradiance Calibration in the Infrared. XIV. The Absolute Calibration of 2MASS". In: *"The Astronomical Journal"* 126.2, pp. 1090–1096. DOI: 10.1086/376474. arXiv: astro-ph/0304350 [astro-ph].

Collin, S. et al. (Sept. 2006). "Systematic effects in measurement of black hole masses by emission-line reverberation of active galactic nuclei: Eddington ratio and inclination". In: *"Astronomy & Astrophysics"* 456.1, pp. 75–90. DOI: 10.1051/0004-6361:20064878. arXiv: astro-ph/0603460 [astro-ph].

Couderc, Paul (Jan. 1939). "Les auréoles lumineuses des Novæ (French) [The luminous halos of Novae]". In: *Annales d'Astrophysique* 2, p. 271.

Croton, Darren J. (July 2006). "Evolution in the black hole mass-bulge mass relation: a theoretical perspective". In: *"Monthly Notices of the Royal Astronomical Society"* 369.4, pp. 1808–1812. DOI: 10.1111/j.1365-2966.2006.10429.x. arXiv: astro-ph/0512375 [astro-ph].

de Nicola, Stefano et al. (Nov. 2019). "The fundamental relation between supermassive black holes and their host galaxies". In: *"Monthly Notices of the Royal Astronomical Society"* 490.1, pp. 600–612. DOI: 10.1093/mnras/stz2472. arXiv: 1909.01749 [astro-ph.GA].

de Vaucouleurs, Gerard (Jan. 1959). "Classification and Morphology of External Galaxies." In: *Handbuch der Physik* 53, p. 275. DOI: 10.1007/978-3-642-45932-0_7.

Dibai, E. A. (Feb. 1977). "Mass of the central bodies of active galaxy nuclei". In: *Soviet Astronomy Letters* 3, pp. 1–3.

Ding, Xuheng et al. (Nov. 2017). "H0LiCOW VII: cosmic evolution of the correlation between black hole mass and host galaxy luminosity". In: *"Monthly Notices of the Royal Astronomical Society"* 472.1, pp. 90–103. DOI: 10.1093/mnras/stx1972. arXiv: 1703.02041 [astro-ph.GA].

Ding, Xuheng et al. (Jan. 2020). "The Mass Relations between Supermassive Black Holes and Their Host Galaxies at 1 ¡ z ¡ 2 HST-WFC3". In: *"The Astrophysical Journal"* 888.1, 37, p. 37. DOI: 10.3847/1538-4357/ab5b90. arXiv: 1910.11875 [astro-ph.GA].

Eckart, A. and R. Genzel (Oct. 1996). "Observations of stellar proper motions near the Galactic Centre". In: *"Nature"* 383.6599, pp. 415–417. DOI: 10.1038/383415a0.

Edge, D. O. et al. (Jan. 1959). "A survey of radio sources at a frequency of 159 Mc/s." In: *"Memoirs of the Royal Astronomical Society"* 68, pp. 37–60.

ESO (Apr. 2014). *The ESO New Technology Telescope (website)*. European Southern Observatory. URL: http://www.eso.org/sci/facilities/lasilla/telescopes/ntt.html (visited on 03/22/2023).

— (Aug. 2019). *SOFI (website)*. European Southern Observatory. URL: https://www.eso.org/sci/facilities/lasilla/instruments/sofi.html (visited on 03/22/2023).

Fath, Edward Arthur (Jan. 1909). "The spectra of some spiral nebulae and globular star clusters". In: *Lick Observatory Bulletin* 149, pp. 71–77. DOI: 10.5479/ADS/bib/1909LicOB.5.71F.

Ferrarese, Laura and David Merritt (Aug. 2000). "A Fundamental Relation between Supermassive Black Holes and Their Host Galaxies". In: *"The Astrophysical Journal"* 539.1, pp. L9–L12. DOI: 10.1086/312838. arXiv: astro-ph/0006053 [astro-ph].

Fischer, S. et al. (June 2006). "Nearby AGN and their hosts in the near infrared". In: *"Astronomy & Astrophysics"* 452.3, pp. 827–837. DOI: 10.1051/0004-6361:20053158. arXiv: astro-ph/0603303 [astro-ph].

Gaffney, Niall I. et al. (Jan. 1995). "Measuring Stellar Kinematics in Galaxies with the Near-Infrared (2-0) 12CO Absorption Bandhead". In: *"Publications of the Astronomical Society of the Pacific"* 107, p. 68. DOI: 10.1086/133517.

García-Burillo, S. et al. (July 2014). "Molecular line emission in NGC 1068 imaged with ALMA. I. An AGN-driven outflow in the dense molecular gas". In: *"Astronomy & Astrophysics"* 567, A125, A125. DOI: 10.1051/0004-6361/201423843. arXiv: 1405.7706 [astro-ph.GA].

Gebhardt, Karl et al. (Aug. 2000). "A Relationship between Nuclear Black Hole Mass and Galaxy Velocity Dispersion". In: *"The Astrophysical Journal"* 539.1, pp. L13–L16. DOI: 10.1086/312840. arXiv: astro-ph/0006289 [astro-ph].

Glass, Ian S. (Oct. 1999). *Handbook of Infrared Astronomy*. Cambridge Observing Handbooks for Research Astronomers. Cambridge University Press. ISBN: 9780521633116.

Glikman, Eilat et al. (Apr. 2006). "A Near-Infrared Spectral Template for Quasars". In: *"The Astrophysical Journal"* 640.2, pp. 579–591. DOI: 10.1086/500098. arXiv: astro-ph/0511640 [astro-ph].

Graham, Alister W. and Simon P. Driver (Jan. 2007). "A Log-Quadratic Relation for Predicting Supermassive Black Hole Masses from the Host Bulge Sérsic Index". In: *"The Astrophysical Journal"* 655.1, pp. 77–87. DOI: 10.1086/509758. arXiv: astro-ph/0607378 [astro-ph].

Graham, Alister W. and Nicholas Scott (Feb. 2013). "The M_{BH}-$L_{spheroid}$ Relation at High and Low Masses, the Quadratic Growth of Black Holes, and Intermediate-mass Black Hole Candidates". In: *"The Astrophysical Journal"* 764.2, 151, p. 151. DOI: 10.1088/0004-637X/764/2/151. arXiv: 1211.3199 [astro-ph.CO].

— (Jan. 2015). "The (Black Hole)-bulge Mass Scaling Relation at Low Masses". In: *"The Astrophysical Journal"* 798.1, 54, p. 54. DOI: 10.1088/0004-637X/798/1/54. arXiv: 1412.3091 [astro-ph.GA].

Greene, Jenny E. and Luis C. Ho (Sept. 2005). "Estimating Black Hole Masses in Active Galaxies Using the Hα Emission Line". In: *"The Astrophysical Journal"* 630.1, pp. 122–129. DOI: 10.1086/431897. arXiv: astro-ph/0508335 [astro-ph].

— (Apr. 2006). "The M_{BH}-σ_* Relation in Local Active Galaxies". In: *"The Astrophysical Journal"* 641.1, pp. L21–L24. DOI: 10.1086/500507. arXiv: astro-ph/0512461 [astro-ph].

— (Nov. 2007a). "A New Sample of Low-Mass Black Holes in Active Galaxies". In: *"The Astrophysical Journal"* 670.1, pp. 92–104. DOI: 10.1086/522082. arXiv: 0707.2617 [astro-ph].

— (Sept. 2007b). "The Mass Function of Active Black Holes in the Local Universe". In: *"The Astrophysical Journal"* 667.1, pp. 131–148. DOI: 10.1086/520497. arXiv: 0705.0020 [astro-ph].

Greenstein, Jesse L. (Mar. 1963). "Red-Shift of the Unusual Radio Source: 3C 48". In: *"Nature"* 197.4872, pp. 1041–1042. DOI: 10.1038/1971041a0.

Greenstein, Jesse L. and Maarten Schmidt (July 1964). "The Quasi-Stellar Radio Sources 3C 48 and 3C 273." In: *"The Astrophysical Journal"* 140, p. 1. DOI: 10.1086/147889.

Gültekin, Kayhan et al. (June 2009). "The M-σ and M-L Relations in Galactic Bulges, and Determinations of Their Intrinsic Scatter". In: *"The Astrophysical Journal"* 698.1, pp. 198–221. DOI: 10.1088/0004-637X/698/1/198. arXiv: 0903.4897 [astro-ph.GA].

Gunn, James E. (Mar. 1971). "On the Distances of the Quasi-Stellar Objects". In: *"The Astrophysical Journal"* 164, p. L113. DOI: 10.1086/180702.

Hanbury Brown, R. et al. (Dec. 1952). "Apparent Angular Sizes of Discrete Radio Sources: Observations at Jodrell Bank, Manchester". In: *"Nature"* 170.4338, pp. 1061–1063. DOI: 10.1038/1701061a0.

Häring, Nadine and Hans-Walter Rix (Apr. 2004). "On the Black Hole Mass-Bulge Mass Relation". In: *"The Astrophysical Journal"* 604.2, pp. L89–L92. DOI: 10.1086/383567. arXiv: astro-ph/0402376 [astro-ph].

Hazard, C. et al. (Mar. 1963). "Investigation of the Radio Source 3C 273 By The Method of Lunar Occultations". In: *"Nature"* 197.4872, pp. 1037–1039. DOI: 10.1038/1971037a0.

Heckman, T. M. (July 1980). "An Optical and Radio Survey of the Nuclei of Bright Galaxies - Activity in the Normal Galactic Nuclei". In: *"Astronomy & Astrophysics"* 87, p. 152.

— (Jan. 1987). "The Nature of Liners". In: *Observational Evidence of Activity in Galaxies*. Ed. by E. E. Khachikian et al. Vol. 121, p. 421.

Heckman, Timothy M. and Philip N. Best (Aug. 2014). "The Coevolution of Galaxies and Supermassive Black Holes: Insights from Surveys of the Contemporary Universe". In: *"Annual Review of Astronomy and Astrophysics"* 52, pp. 589–660. DOI: 10.1146/annurev-astro-081913-035722. arXiv: 1403.4620 [astro-ph.GA].

Hey, J. S. et al. (Aug. 1946). "Fluctuations in Cosmic Radiation at Radio-Frequencies". In: *"Nature"* 158.4007, p. 234. DOI: 10.1038/158234a0.

Hickox, Ryan C. et al. (May 2009). "Host Galaxies, Clustering, Eddington Ratios, and Evolution of Radio, X-Ray, and Infrared-Selected AGNs". In: *"The Astrophysical Journal"* 696.1, pp. 891–919. DOI: 10.1088/0004-637X/696/1/891. arXiv: 0901.4121 [astro-ph.GA].

Ho, L. C. (Sept. 2008). "Nuclear activity in nearby galaxies." In: *"Annual Review of Astronomy and Astrophysics"* 46, pp. 475–539. DOI: 10.1146/annurev.astro.45.051806.110546. arXiv: 0803.2268 [astro-ph].

Ho, Luis (Jan. 1999). "Supermassive Black Holes in Galactic Nuclei: Observational Evidence and Astrophysical Consequences". In: *Observational Evidence for the Black*

Holes in the Universe. Ed. by Sandip K. Chakrabarti. Vol. 234. Astrophysics and Space Science Library, p. 157. DOI: 10.1007/978-94-011-4750-7_11.

Hubble, E. P. (Dec. 1926). "Extragalactic nebulae." In: *"The Astrophysical Journal"* 64, pp. 321–369. DOI: 10.1086/143018.

Jahnke, K. et al. (Aug. 2004). "Quasar host galaxy star formation activity from multi-colour data". In: *"Monthly Notices of the Royal Astronomical Society"* 352.2, pp. 399–415. DOI: 10.1111/j.1365-2966.2004.07933.x. arXiv: astro-ph/0311123 [astro-ph].

Jahnke, Knud et al. (Dec. 2009). "Massive Galaxies in COSMOS: Evolution of Black Hole Versus Bulge Mass but not Versus Total Stellar Mass Over the Last 9 Gyr?" In: *"The Astrophysical Journal"* 706.2, pp. L215–L220. DOI: 10.1088/0004-637X/706/2/L215. arXiv: 0907.5199 [astro-ph.CO].

Jansky, K.G. (1932). "Directional Studies of Atmospherics at High Frequencies". In: *Proceedings of the Institute of Radio Engineers* 20.12, pp. 1920–1932. DOI: 10.1109/JRPROC.1932.227477.

— (1933). "Electrical Disturbances Apparently of Extraterrestrial Origin". In: *Proceedings of the Institute of Radio Engineers* 21.10, pp. 1387–1398. DOI: 10.1109/JRPROC.1933.227458.

Jiang, Yan-Fei et al. (Aug. 2011). "Black Hole Mass and Bulge Luminosity for Low-mass Black Holes". In: *"The Astrophysical Journal"* 737.2, L45, p. L45. DOI: 10.1088/2041-8205/737/2/L45. arXiv: 1107.4103 [astro-ph.CO].

Joye, W. A. and E. Mandel (Jan. 2003). "New Features of SAOImage DS9". In: *Astronomical Data Analysis Software and Systems XII*. Ed. by H. E. Payne et al. Vol. 295. Astronomical Society of the Pacific Conference Series, p. 489.

Kaspi, Shai et al. (Apr. 2000). "Reverberation Measurements for 17 Quasars and the Size-Mass-Luminosity Relations in Active Galactic Nuclei". In: *"The Astrophysical Journal"* 533.2, pp. 631–649. DOI: 10.1086/308704. arXiv: astro-ph/9911476 [astro-ph].

Kaspi, Shai et al. (Aug. 2005). "The Relationship between Luminosity and Broad-Line Region Size in Active Galactic Nuclei". In: *"The Astrophysical Journal"* 629.1, pp. 61–71. DOI: 10.1086/431275. arXiv: astro-ph/0504484 [astro-ph].

Kauffmann, Guinevere et al. (Dec. 2003). "The host galaxies of active galactic nuclei". In: *"Monthly Notices of the Royal Astronomical Society"* 346.4, pp. 1055–1077. DOI: 10.1111/j.1365-2966.2003.07154.x. arXiv: astro-ph/0304239 [astro-ph].

Kennicutt Robert C., Jr. (May 1998). "The Global Schmidt Law in Star-forming Galaxies". In: *"The Astrophysical Journal"* 498.2, pp. 541–552. DOI: 10.1086/305588. arXiv: astro-ph/9712213 [astro-ph].

Kim, Dohyeong et al. (Nov. 2010). "New Estimators of Black Hole Mass in Active Galactic Nuclei with Hydrogen Paschen Lines". In: *The Astrophysical Journal* 724.1, pp. 386–399. DOI: 10.1088/0004-637X/724/1/386. arXiv: 1012.1112 [astro-ph.CO].

Kim, Minjin et al. (Nov. 2008). "The Origin of the Intrinsic Scatter in the Relation Between Black Hole Mass and Bulge Luminosity for Nearby Active Galaxies". In:

"The Astrophysical Journal" 687.2, pp. 767–827. DOI: 10.1086/591663. arXiv: 0807.1337 [astro-ph].

König, S. et al. (Mar. 2012). "A search for H_2O maser emission in nearby low-luminosity QSO host galaxies". In: *"Monthly Notices of the Royal Astronomical Society"* 420.3, pp. 2263–2270. DOI: 10.1111/j.1365-2966.2011.20191.x. arXiv: 1111.3245 [astro-ph.CO].

Kormendy, John and Luis C. Ho (Aug. 2013). "Coevolution (Or Not) of Supermassive Black Holes and Host Galaxies". In: *"Annual Review of Astronomy and Astrophysics"* 51.1, pp. 511–653. DOI: 10.1146/annurev-astro-082708-101811. arXiv: 1304.7762 [astro-ph.CO].

Kormendy, John and Douglas Richstone (Jan. 1995). "Inward Bound—The Search For Supermassive Black Holes In Galactic Nuclei". In: *"Annual Review of Astronomy and Astrophysics"* 33, p. 581. DOI: 10.1146/annurev.aa.33.090195.003053.

Kormendy, John et al. (Jan. 2011). "Supermassive black holes do not correlate with galaxy disks or pseudobulges". In: *"Nature"* 469.7330, pp. 374–376. DOI: 10.1038/nature09694. arXiv: 1101.3781 [astro-ph.GA].

Kozlowski, M. et al. (Jan. 1979). "Self-gravitating accretion disk models with realistic equations of state and opacities." In: *"Acta Astronomica"* 29.2, pp. 157–176.

Laha, Sibasish et al. (Oct. 2018). "An X-ray view of central engines of low-luminosity quasars (LLQSO) in the local Universe". In: *Monthly Notices of the Royal Astronomical Society* 480.2, pp. 1522–1546. DOI: 10.1093/mnras/sty1919. arXiv: 1807.07641 [astro-ph.GA].

Leggett, S. K. et al. (Dec. 2006). "JHK observations of faint standard stars in the Mauna Kea Observatories near-infrared photometric system". In: *"Monthly Notices of the Royal Astronomical Society"* 373.2, pp. 781–792. DOI: 10.1111/j.1365-2966.2006.11069.x. arXiv: astro-ph/0609461 [astro-ph].

Li, Yiming et al. (May 2013). "Star Formation Rates in Resolved Galaxies: Calibrations with Near- and Far-infrared Data for NGC 5055 and NGC 6946". In: *"The Astrophysical Journal"* 768.2, 180, p. 180. DOI: 10.1088/0004-637X/768/2/180. arXiv: 1304.1541 [astro-ph.CO].

Lidman, C. and Cuby J.-G. (Aug. 2019). *SOFI User's Manual*. Ed. by Vanzi L. et al. manual. Version Doc. No. LSO-MAN-ESO-40100-0004. European Southern Observatory. URL: https://www.eso.org/sci/facilities/lasilla/instruments/sofi/doc/manual/sofiman_2p50.pdf.

Lu, Ru-Sen et al. (Apr. 2023). "A ring-like accretion structure in M87 connecting its black hole and jet". In: *arXiv e-prints*, arXiv:2304.13252, arXiv:2304.13252. DOI: 10.48550/arXiv.2304.13252. arXiv: 2304.13252 [astro-ph.HE].

Magorrian, John et al. (June 1998). "The Demography of Massive Dark Objects in Galaxy Centers". In: *"The Astronomical Journal"* 115.6, pp. 2285–2305. DOI: 10.1086/300353. arXiv: astro-ph/9708072 [astro-ph].

Maiolino, R. et al. (Jan. 1996). "Correction of the Atmospheric Transmission in Infrared Spectroscopy". In: *"The Astronomical Journal"* 111, p. 537. DOI: 10.1086/117804.

Mandal, Amit Kumar et al. (Apr. 2021). "Estimation of the size and structure of the broad line region using Bayesian approach". In: *"Monthly Notices of the Royal Astronomical Society"* 502.2, pp. 2140–2157. DOI: 10.1093/mnras/stab012. arXiv: 2101.00802 [astro-ph.GA].

Marconi, Alessandro and Leslie K. Hunt (May 2003). "The Relation between Black Hole Mass, Bulge Mass, and Near-Infrared Luminosity". In: *"The Astrophysical Journal"* 589.1, pp. L21–L24. DOI: 10.1086/375804. arXiv: astro-ph/0304274 [astro-ph].

Mason, R. E. et al. (Mar. 2015). "The Nuclear Near-Infrared Spectral Properties of Nearby Galaxies". In: *"The Astrophysical Journal Supplement Series"* 217.1, 13, p. 13. DOI: 10.1088/0067-0049/217/1/13. arXiv: 1503.01836 [astro-ph.GA].

McLure, R. J. and J. S. Dunlop (Apr. 2002). "On the black hole-bulge mass relation in active and inactive galaxies". In: *"Monthly Notices of the Royal Astronomical Society"* 331.3, pp. 795–804. DOI: 10.1046/j.1365-8711.2002.05236.x. arXiv: astro-ph/0108417 [astro-ph].

Merloni, A. et al. (Jan. 2010). "On the Cosmic Evolution of the Scaling Relations Between Black Holes and Their Host Galaxies: Broad-Line Active Galactic Nuclei in the zCOSMOS Survey". In: *"The Astrophysical Journal"* 708.1, pp. 137–157. DOI: 10.1088/0004-637X/708/1/137. arXiv: 0910.4970 [astro-ph.CO].

Minkowski, R. (Nov. 1960). "A New Distant Cluster of Galaxies." In: *"The Astrophysical Journal"* 132, pp. 908–910. DOI: 10.1086/146994.

Moffat, A. F. J. (Dec. 1969). "A Theoretical Investigation of Focal Stellar Images in the Photographic Emulsion and Application to Photographic Photometry". In: *"Astronomy & Astrophysics"* 3, p. 455.

Moorwood, A. et al. (Mar. 1998). "SOFI sees first light at the NTT." In: *The Messenger* 91, pp. 9–13.

Morgan, W. W. (Aug. 1958). "A Preliminary Classification of the Forms of Galaxies According to Their Stellar Population". In: *"Publications of the Astronomical Society of the Pacific"* 70.415, p. 364. DOI: 10.1086/127243.

— (Oct. 1959). "Preliminary Classification of the Forms of Galaxies According to Their Stellar Population. II". In: *"Publications of the Astronomical Society of the Pacific"* 71.422, p. 394. DOI: 10.1086/127415.

Moser, Lydia et al. (Mar. 2016). "A low-luminosity type-1 QSO sample . IV. Molecular gas contents and conditions of star formation in three nearby Seyfert galaxies". In: *"Astronomy & Astrophysics"* 587, A137, A137. DOI: 10.1051/0004-6361/201526358. arXiv: 1707.01081 [astro-ph.GA].

Nelson, Charles H. and Mark Whittle (July 1995). "Stellar and Gaseous Kinematics of Seyfert Galaxies. I. Spectroscopic Data". In: *"The Astrophysical Journal Supplement Series"* 99, p. 67. DOI: 10.1086/192179.

Nelson, Charles H. et al. (Nov. 2004). "The Relationship Between Black Hole Mass and Velocity Dispersion in Seyfert 1 Galaxies". In: *"The Astrophysical Journal"* 615.2, pp. 652–661. DOI: 10.1086/424657. arXiv: astro-ph/0407383 [astro-ph].

Netzer, Hagai (2013). *The Physics and Evolution of Active Galactic Nuclei*. Cambridge University Press. DOI: 10.1017/CBO9781139109291.

Netzer, Hagai and Ari Laor (Feb. 1993). "Dust in the Narrow-Line Region of Active Galactic Nuclei". In: *"The Astrophysical Journal"* 404, p. L51. DOI: 10.1086/186741.

Norman, C. and J. Silk (Mar. 1983). "The dynamics and fueling of active nuclei". In: *"The Astrophysical Journal"* 266, pp. 502–515. DOI: 10.1086/160798.

Oke, J. B. (Mar. 1963). "Absolute Energy Distribution in the Optical Spectrum of 3C 273". In: *"Nature"* 197.4872, pp. 1040–1041. DOI: 10.1038/1971040b0.

Onken, Christopher A. et al. (Nov. 2004). "Supermassive Black Holes in Active Galactic Nuclei. II. Calibration of the Black Hole Mass-Velocity Dispersion Relationship for Active Galactic Nuclei". In: *"The Astrophysical Journal"* 615.2, pp. 645–651. DOI: 10.1086/424655. arXiv: astro-ph/0407297 [astro-ph].

Osterbrock, D.E. and G.J. Ferland (2006). *Astrophysics Of Gas Nebulae and Active Galactic Nuclei*. University Science Books. ISBN: 9781891389344. URL: https://books.google.de/books?id=HgfrkDjBD98C.

Osterbrock, Donald E. (Feb. 1978). "Observational Model of the Ionized Gas in Seyfert and Radio-Galaxy Nuclei". In: *Proceedings of the National Academy of Science* 75.2, pp. 540–544. DOI: 10.1073/pnas.75.2.540.

Peng, Chien Y. et al. (Oct. 2006a). "Probing the Coevolution of Supermassive Black Holes and Galaxies Using Gravitationally Lensed Quasar Hosts". In: *"The Astrophysical Journal"* 649.2, pp. 616–634. DOI: 10.1086/506266. arXiv: astro-ph/0603248 [astro-ph].

Peng, Chien Y. et al. (Mar. 2006b). "Probing the Coevolution of Supermassive Black Holes and Quasar Host Galaxies". In: *"The Astrophysical Journal"* 640.1, pp. 114–125. DOI: 10.1086/499930. arXiv: astro-ph/0509155 [astro-ph].

Penston, M. V. and E. Perez (Nov. 1984). "An evolutionary link between Seyfert I and II galaxies." In: *"Monthly Notices of the Royal Astronomical Society"* 211, 33P–39. DOI: 10.1093/mnras/211.1.33P.

Persson, S. E. et al. (Nov. 1998). "A New System of Faint Near-Infrared Standard Stars". In: *"The Astronomical Journal"* 116.5, pp. 2475–2488. DOI: 10.1086/300607.

Peterson, B. M. et al. (Oct. 2004). "Central Masses and Broad-Line Region Sizes of Active Galactic Nuclei. II. A Homogeneous Analysis of a Large Reverberation-Mapping Database". In: *"The Astrophysical Journal"* 613.2, pp. 682–699. DOI: 10.1086/423269. arXiv: astro-ph/0407299 [astro-ph].

Peterson, Bradley M. (1997). *An Introduction to Active Galactic Nuclei*.

Peterson, Bradley M. and Amri Wandel (Aug. 1999). "Keplerian Motion of Broad-Line Region Gas as Evidence for Supermassive Black Holes in Active Galactic Nuclei". In: *"The Astrophysical Journal"* 521.2, pp. L95–L98. DOI: 10.1086/312190. arXiv: astro-ph/9905382 [astro-ph].

Planck Collaboration et al. (Sept. 2016). "Planck 2015 results. XIII. Cosmological parameters". In: *"Astronomy & Astrophysics"* 594, A13, A13. DOI: 10.1051/0004-6361/201525830. arXiv: 1502.01589 [astro-ph.CO].

Reber, Grote (Feb. 1940a). "Cosmic Static". In: *Proceedings of the IRE* 28, pp. 68–70. DOI: 10.1109/JRPROC.1940.228921.

Reber, Grote (June 1940b). "Notes: Cosmic Static." In: *"The Astrophysical Journal"* 91, pp. 621–624. DOI: 10.1086/144197.

— (Nov. 1944). "Cosmic Static." In: *"The Astrophysical Journal"* 100, p. 279. DOI: 10.1086/144668.

Richstone, D. et al. (Oct. 1998). "Supermassive black holes and the evolution of galaxies." In: *"Nature"* 385.6701, A14. DOI: 10.48550/arXiv.astro-ph/9810378. arXiv: astro-ph/9810378 [astro-ph].

Riffel, R. et al. (Oct. 2006). "A 0.8-2.4 μm spectral atlas of active galactic nuclei". In: *"Astronomy & Astrophysics"* 457.1, pp. 61–70. DOI: 10.1051/0004-6361:20065291. arXiv: astro-ph/0605463 [astro-ph].

Riffel, Rogemar A. et al. (Aug. 2015). "Feeding versus feedback in active galactic nuclei from near-infrared integral field spectroscopy - X. NGC 5929". In: *"Monthly Notices of the Royal Astronomical Society"* 451.4, pp. 3587–3605. DOI: 10.1093/mnras/stv1129. arXiv: 1505.04052 [astro-ph.GA].

Ryle, M. and F. G. Smith (Sept. 1948). "A New Intense Source of Radio-Frequency Radiation in the Constellation of Cassiopeia". In: *"Nature"* 162.4116, pp. 462–463. DOI: 10.1038/162462a0.

Sakimoto, P. J. and F. V. Coroniti (July 1981). "Accretion disk models for QSOs and active galactic nuclei - The role of magnetic viscosity". In: *"The Astrophysical Journal"* 247, pp. 19–31. DOI: 10.1086/159005.

Sani, E. et al. (May 2011). "The Spitzer/IRAC view of black hole-bulge scaling relations". In: *"Monthly Notices of the Royal Astronomical Society"* 413.2, pp. 1479–1494. DOI: 10.1111/j.1365-2966.2011.18229.x. arXiv: 1012.3073 [astro-ph.CO].

Schmidt, E. O. et al. (Dec. 2016). "Spectral nuclear properties of NLS1 galaxies". In: *"Astronomy & Astrophysics"* 596, A95, A95. DOI: 10.1051/0004-6361/201629343. arXiv: 1608.02396 [astro-ph.GA].

Schmidt, M. (Mar. 1963). "3C 273 : A Star-Like Object with Large Red-Shift". In: *"Nature"* 197.4872, p. 1040. DOI: 10.1038/1971040a0.

Schmidt, M. and R. F. Green (June 1983). "Quasar evolution derived from the Palomar bright quasar survey and other complete quasar surveys." In: *"The Astrophysical Journal"* 269, pp. 352–374. DOI: 10.1086/161048.

Schneider, Peter (2015). *Extragalactic Astronomy and Cosmology: An Introduction*. 2nd ed. Springer Verlag Berlin Heidelberg, pp. XVIII, 626. ISBN: 978-3-642-54082-0. DOI: https://doi.org/10.1007/978-3-642-54083-7.

Schulze, A. and L. Wisotzki (Nov. 2011). "Selection effects in the black hole-bulge relation and its evolution". In: *"Astronomy & Astrophysics"* 535, A87, A87. DOI: 10.1051/0004-6361/201117564. arXiv: 1109.2787 [astro-ph.CO].

Schulze, Andreas and Lutz Wisotzki (Mar. 2014). "Accounting for selection effects in the BH-bulge relations: no evidence for cosmological evolution". In: *"Monthly Notices of the Royal Astronomical Society"* 438.4, pp. 3422–3433. DOI: 10.1093/mnras/stt2457. arXiv: 1312.5610 [astro-ph.CO].

Scott, Nicholas et al. (May 2013). "The Supermassive Black Hole Mass-Spheroid Stellar Mass Relation for Sérsic and Core-Sérsic Galaxies". In: *"The Astrophysical Jour-*

nal" 768.1, 76, p. 76. DOI: 10.1088/0004-637X/768/1/76. arXiv: 1303.5490 [astro-ph.CO].

Seigar, Marc S. et al. (May 2008). "Discovery of a Relationship between Spiral Arm Morphology and Supermassive Black Hole Mass in Disk Galaxies". In: *"The Astrophysical Journal"* 678.2, p. L93. DOI: 10.1086/588727. arXiv: 0804.0773 [astro-ph].

Sérsic, J. L. (Feb. 1963). "Influence of the atmospheric and instrumental dispersion on the brightness distribution in a galaxy". In: *Boletin de la Asociacion Argentina de Astronomia La Plata Argentina* 6, pp. 41–43.

Seyfert, Carl K. (Jan. 1943). "Nuclear Emission in Spiral Nebulae." In: *"The Astrophysical Journal"* 97, p. 28. DOI: 10.1086/144488.

Shen, Jiajian et al. (Mar. 2008). "The Black Hole-Bulge Relationship in Luminous Broad-Line Active Galactic Nuclei and Host Galaxies". In: *"The Astronomical Journal"* 135.3, pp. 928–946. DOI: 10.1088/0004-6256/135/3/928. arXiv: 0712.1630 [astro-ph].

Shields, Gregory A. (June 1999). "A Brief History of Active Galactic Nuclei". In: *"Publications of the Astronomical Society of the Pacific"* 111.760, pp. 661–678. DOI: 10.1086/316378. arXiv: astro-ph/9903401 [astro-ph].

Slipher, V. M. (Jan. 1917). "The spectrum and velocity of the nebula N.G.C. 1068 (M 77)". In: *Lowell Observatory Bulletin* 3, pp. 59–62.

Somerville, Rachel S. et al. (Dec. 2008). "A semi-analytic model for the co-evolution of galaxies, black holes and active galactic nuclei". In: *"Monthly Notices of the Royal Astronomical Society"* 391.2, pp. 481–506. DOI: 10.1111/j.1365-2966.2008.13805.x. arXiv: 0808.1227 [astro-ph].

Tokunaga, A. T. (2002). "Infrared Astronomy". In: *Allen's Astrophysical Quantities*. Ed. by Cox, Arthur N. New York, NY: Springer New York, pp. 143–167. ISBN: 978-1-4612-1186-0. DOI: 10.1007/978-1-4612-1186-0_7. URL: https://doi.org/10.1007/978-1-4612-1186-0_7.

Tremaine, Scott et al. (Aug. 2002). "The Slope of the Black Hole Mass versus Velocity Dispersion Correlation". In: *"The Astrophysical Journal"* 574.2, pp. 740–753. DOI: 10.1086/341002. arXiv: astro-ph/0203468 [astro-ph].

Tremou, E. et al. (Aug. 2015). "A low-luminosity type-1 QSO sample. III. Optical spectroscopic properties and activity classification". In: *"Astronomy & Astrophysics"* 580, A113, A113. DOI: 10.1051/0004-6361/201525707. arXiv: 1506.09053 [astro-ph.GA].

Urrutia, Tanya et al. (Oct. 2012). "Spitzer Observations of Young Red Quasars". In: *"The Astrophysical Journal"* 757.2, 125, p. 125. DOI: 10.1088/0004-637X/757/2/125. arXiv: 1208.4585 [astro-ph.CO].

Urry, C. Megan and Paolo Padovani (Sept. 1995). "Unified Schemes for Radio-Loud Active Galactic Nuclei". In: *"Publications of the Astronomical Society of the Pacific"* 107, p. 803. DOI: 10.1086/133630. arXiv: astro-ph/9506063 [astro-ph].

Vestergaard, Marianne and Bradley M. Peterson (Apr. 2006). "Determining Central Black Hole Masses in Distant Active Galaxies and Quasars. II. Improved Optical and UV Scaling Relationships". In: *"The Astrophysical Journal"* 641.2, pp. 689–709. DOI: 10.1086/500572. arXiv: astro-ph/0601303 [astro-ph].

Viegas-Aldrovandi, S. M. and M. Contini (Apr. 1989). "A Guideline to the Interpretation of the Narrow Emission-Line Spectra of Active Galactic Nuclei". In: *"The Astrophysical Journal"* 339, p. 689. DOI: 10.1086/167328.

Vika, Marina et al. (Jan. 2012). "The near-IR M_{bh}-L and M_{bh}-n relations". In: *"Monthly Notices of the Royal Astronomical Society"* 419.3, pp. 2264–2292. DOI: 10.1111/j.1365-2966.2011.19881.x. arXiv: 1110.1275 [astro-ph.CO].

Wandel, A. (Nov. 2004). "The black hole-bulge relations in active galactic nuclei". In: *The Interplay Among Black Holes, Stars and ISM in Galactic Nuclei*. Ed. by Thaisa Storchi-Bergmann et al. Vol. 222, pp. 65–69. DOI: 10.1017/S1743921304001474. arXiv: astro-ph/0407399 [astro-ph].

Wandel, A. et al. (Dec. 1999). "Central Masses and Broad-Line Region Sizes of Active Galactic Nuclei. I. Comparing the Photoionization and Reverberation Techniques". In: *"The Astrophysical Journal"* 526.2, pp. 579–591. DOI: 10.1086/308017. arXiv: astro-ph/9905224 [astro-ph].

Wang, Jian-Min and En-Peng Zhang (May 2007). "The Unified Model of Active Galactic Nuclei. II. Evolutionary Connection". In: *The Astrophysical Journal* 660.2, pp. 1072–1092. DOI: 10.1086/513685. arXiv: astro-ph/0702279 [astro-ph].

Ward, M. J. et al. (Aug. 1978). "Optical identifications of extragalactic X-ray sources." In: *"The Astrophysical Journal"* 223, pp. 788–797. DOI: 10.1086/156311.

Weedman, D. W. (Aug. 1976). "Luminosities of Seyfert galaxies and QSOs." In: *"The Astrophysical Journal"* 208, pp. 30–36. DOI: 10.1086/154577.

Wenger, M. et al. (Apr. 2000). "The SIMBAD astronomical database. The CDS reference database for astronomical objects". In: *Astronomy and Astrophysics Supplement* 143, pp. 9–22. DOI: 10.1051/aas:2000332. arXiv: astro-ph/0002110 [astro-ph]. URL: http://simbad.u-strasbg.fr/simbad/ (visited on 08/20/2020).

Winter, Lisa M. et al. (Jan. 2009). "X-Ray Spectral Properties of the BAT AGN Sample". In: *"The Astrophysical Journal"* 690.2, pp. 1322–1349. DOI: 10.1088/0004-637X/690/2/1322. arXiv: 0808.0461 [astro-ph].

Wisotzki, L. et al. (June 2000). "The Hamburg/ESO survey for bright QSOs. III. A large flux-limited sample of QSOs". In: *Astronomy and Astrophysics* 358, pp. 77–87. arXiv: astro-ph/0004162 [astro-ph].

Woo, Jong-Hak and C. Megan Urry (Nov. 2002). "Active Galactic Nucleus Black Hole Masses and Bolometric Luminosities". In: *"The Astrophysical Journal"* 579.2, pp. 530–544. DOI: 10.1086/342878. arXiv: astro-ph/0207249 [astro-ph].

Woo, Jong-Hak et al. (June 2010). "The Lick AGN Monitoring Project: The M_{BH}-σ_* Relation for Reverberation-mapped Active Galaxies". In: *"The Astrophysical Journal"* 716.1, pp. 269–280. DOI: 10.1088/0004-637X/716/1/269. arXiv: 1004.0252 [astro-ph.CO].

Yesuf, Hassen M. et al. (Jan. 2020). "The Activation of Galactic Nuclei and Their Accretion Rates Are Linked to the Star Formation Rates and Bulge-types of Their Host Galaxies". In: *"The Astrophysical Journal"* 889.1, 14, p. 14. DOI: 10.3847/1538-4357/ab5fe1. arXiv: 1912.03633 [astro-ph.GA].

Young, S. et al. (Aug. 1996). "Polarimetry and modelling of narrow-line active galaxies". In: *"Monthly Notices of the Royal Astronomical Society"* 281.4, pp. 1206–1242. DOI: 10.1093/mnras/281.4.1206.

List of Figures

List of Tables

List of Acronyms

2MASS	Two Micron All-Sky Survey
ADU	Analog-Digital Unit
AGN	active galactic nucleus
BB	black body
BH	black hole
BLR	broad-line region
BLRG	broad-line radio galaxy
DIMM	differential image motion monitor
DIT	detector integration time
EHT	Event Horizon Telescope
EHTC	Event Horizon Telescope Collaboration
ENLR	extended narrow-line region
ESO	European Southern Observatory
FIR	far-infrared
FITS	Flexible Image Transport System
FOV	field of view
FWHM	full width at half maximum
HDU	Header/Data Unit
HES	Hamburg/ESO Survey
ID	identifier
IPAC	Infrared Processing and Analysis Center

IR	infrared
IRAF	Image Reduction and Analysis Facility
IRSA	Infrared Science Archive
ISAAC	Infrared Spectrometer And Array Camera
JWST	James Webb Space Telescope
LEDA	Lyon-Meudon Extragalactic Database
LINER	low-ionization nuclear emission-line region
LLQSO	low-luminosity type-1 quasi-stellar object
LM	Levenberg-Marquardt
LOS	line-of-sight
MIR	mid-infrared
MW	Milky Way
NASA	National Aeronautics and Space Administration
NED	NASA/IPAC Extragalactic Database
NIR	near-infrared
NIST	National Institute of Standards and Technology
NLR	narrow-line region
NLRG	narrow-line radio galaxy
NOAO	National Optical Astronomy Observatory
NTT	New Technology Telescope
OB	observation block
OVV	optically violent variable
PID	program identifier
PSF	point spread function
QSO	quasi-stellar object
RM	reverberation mapping
S/N	signal-to-noise ratio

SED	spectral energy distribution
SF	star formation
SFR	star formation rate
SIMBAD	Set of Identifications, Measurements and Bibliography for Astronomical Data
SMBH	supermassive black hole
SOFI	Son of ISAAC
STScI	Space Telescope Science Institute
UV	ultraviolet
VLT	Very Large Telescope

Acknowledgments

First and foremost, I like to thank Prof. Dr. Andreas Eckart, not only for the opportunity to work on my project, but the guidance over many years by now, which covers my bachelor thesis, my master thesis, and essentially all my work related to astrophysics. Moreover, his personal anecdotes to virtually all topics are always a nice diversion from physics.

I also want to thank Prof. Dr. Anton Zensus for agreeing to be the second examiner and Prof. Dr. Boris Braun for agreeing to be the chair of the thesis defense committee.

I will never forget the friendly atmosphere and fun moments I experienced being part of the workgroup of Prof. Eckart. Obviously, this involves all colleagues from the workgroup that I had the honor to meet, but also includes members of other workgroups and the staff at the institute as well. I would like to mention especially the workgroup of Prof. Dr. Lucas Labadie from the same institute, as well as people from workgroups in Prague with whom our workgroup interacted often. While it would be too much to list all people, I feel that I have to mention at least a few names, such as Florian Peißker, Matthias Subroweit, Fabio Eupen, Moritz Wiegand, Persis Misquitta, Harshitha Bhat, S. Elaheh Hosseini, Basel Ali, Alexander Wojtczak, and Christian Straubmeier. I can only emphasize that there could and should be many more names here, as all these people made my time at the institute as worthwhile as it was.

Additionally, there are people that I got to know through studying physics that I can now call my friends. They helped me in many ways – from talking about their or my projects to multiple recreational activities, which kept me sane in some critical moments. A lot of thanks to Micah Bowles, Sebastian Vider, Dorian Kürschner, Fabian Holling, and Maurizio Titz.

Naturally, I would not be where I am today without the (often more indirect) support from my family and other friends, i. e., people that are not necessarily trapped in the urge to study a natural science.

Finally, I want to thank 那菜 for supporting and taking care of me. You are a beacon of light to me. いつもありがとうございます。

Thank you so much.

*

Erklärung zur Dissertation
gemäß der Promotionsordnung vom 12. März 2020

"Hiermit versichere ich an Eides statt, dass ich die vorliegende Dissertation selbstständig und ohne die Benutzung anderer als der angegebenen Hilfsmittel und Literatur angefertigt habe. Alle Stellen, die wörtlich oder sinngemäß aus veröffentlichten und nicht veröffentlichten Werken dem Wortlaut oder dem Sinn nach entnommen wurden, sind als solche kenntlich gemacht. Ich versichere an Eides statt, dass diese Dissertation noch keiner anderen Fakultät oder Universität zur Prüfung vorgelegen hat; dass sie – abgesehen von unten angegebenen Teilpublikationen und eingebundenen Artikeln und Manuskripten – noch nicht veröffentlicht worden ist sowie, dass ich eine Veröffentlichung der Dissertation vor Abschluss der Promotion nicht ohne Genehmigung des Promotionsausschusses vornehmen werde. Die Bestimmungen dieser Ordnung sind mir bekannt. Darüber hinaus erkläre ich hiermit, dass ich die Ordnung zur Sicherung guter wissenschaftlicher Praxis und zum Umgang mit wissenschaftlichem Fehlverhalten der Universität zu Köln gelesen und sie bei der Durchführung der Dissertation zugrundeliegenden Arbeiten und der schriftlich verfassten Dissertation beachtet habe und verpflichte mich hiermit, die dort genannten Vorgaben bei allen wissenschaftlichen Tätigkeiten zu beachten und umzusetzen. Ich versichere, dass die eingereichte elektronische Fassung der eingereichten Druckfassung vollständig entspricht."

Teilpublikationen: —

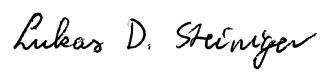

30. April 2023, Lukas Dominik Steiniger

*